RADIATION FROM COUPLED OPEN-ENDED WAVEGUIDES

by

Peter F. Driessen

B.Sc., University of British Columbia, 1976

A THESIS SUBMITTED IN PARTIAL FULFILMENT OF

THE REQUIREMENTS FOR THE DEGREE OF

DOCTOR OF PHILOSOPHY

in the Department

of

Electrical Engineering

We accept this thesis as conforming

to the required standard

THE UNIVERSITY OF BRITISH COLUMBIA

February 1981

In presenting this thesis in partial fulfilment of the requirements for an advanced degree at the University of British Columbia, I agree that the Library shall make it freely available for reference and study. I further agree that permission for extensive copying of this thesis for scholarly purposes may be granted by the head of my department or by his or her representatives. It is understood that copying or publication of this thesis for financial gain shall not be allowed without my written permission.

Department of Electrical Engineering

The University of British Columbia
2075 Wesbrook Place
Vancouver, Canada
V6T 1W5

Date 29 April 1981

ABSTRACT

Ray-optical methods are used to calculate the coupling between open-ended parallel-plate waveguides, as well as the radiation patterns of finite arrays of coupled parallel-plate waveguides with only the central guide driven. These methods require extensive ray tracing, particularly for the larger arrays, to take into account the many possible ray paths.

The coupling coefficients between both two and three guides in isolation agreed remarkably well with those previously derived in the presence of other guides, groundplanes etc., indicating a general lack of sensitivity of the coupling coefficients to the details of the surrounding structure.

The calculated patterns were compared with experimental patterns using an H-plane sectoral horn to simulate the parallel-plate waveguide array. Radiation patterns of both three and five element arrays with all waveguide edges in the aperture plane, as well as that of a three element staggered array with the outer edges not in the aperture plane agreed well with the experimental patterns. A wide variety of patterns could be obtained by varying the width, depth, and number of the outer guides in the array. Ray-optical methods may thus be useful in the development of waveguide antennas for a variety of applications.

TABLE OF CONTENTS

LIST OF TABLES

LIST OF FIGURES

ACKNOWLEDGEMENTS

The author is thankful to Dr. Edward V. Jull, who first perceived this investigation, for his supervision of this thesis and his many valuable comments and suggestions as the work progressed.

Thanks are also due to Dave Fletcher for constructing the sectoral horn antenna, to Dr. J.Y. Wong and W. Lavrench of the National Research Council of Canada Division of Electrical Engineering for permission to use their antenna range, and to John Hazell for assisting with the measurements.

The author gratefully acknowledges the financial support of the National Sciences and Engineering Research Council of Canada.

Chapter 1

INTRODUCTION AND MOTIVATION

1.1 INTRODUCTION

The calculation of the electromagnetic fields in coupled open-ended parallel-plate waveguides is a basic problem whose solution may assist in the design of antenna arrays with waveguide elements. Waveguide antenna arrays have been used in a variety of applications, including phased arrays whose pattern can be changed by altering the amplitude and phase of the fields in each element, and parasitic arrays whose pattern is fixed by the antenna dimensions. In both phased and parasitic arrays, the coupling between elements will excite new fields which will alter the radiation pattern from that if the coupling were ignored. The radiation pattern of a parasitic array can be modified by changing the number, width and depth of the parasitic guides surrounding a central driven guide. The possible range of adjustment is somewhat less than for a phased array , because the energy in the parasitic elements relative to the driven element is fixed by the coupling between them. For many purposes the range of adjustment available with a parasitic array is adequate, and thus the added complexity of feeding each element separately with the associated power dividers and phase shifters is avoided.

One possible application of a coupled waveguide array is as a feed antenna for a parabolic reflector. For this

case, a sector-shaped radiation pattern is usually desirable, i.e. a pattern which provides a constant power level over a given angular range and is zero elsewhere (Fig.1.1). A sector-shaped pattern is nearly optimum (except for space attenuation) because it illuminates the entire reflector surface almost uniformly but does not spill over the sides (Fig.1.2). This provides maximum directivity while avoiding noise and interference pickup including the thermal noise from the ground. Thus the gain/noise temperature ratio, the figure of merit for a satellite earth station antenna, is maximized.

A parallel-plate waveguide array with a small number of elements (Fig.1.3) potentially satisfies these requirements for two-dimensional fields. The aperture field at the open end of the array may be made to approximate a truncated (sin x)/x curve by adjusting the array parameters (width, depth and number of parasitic guides surrounding the central driven guide). The radiation pattern, which is the Fourier transform of the aperture field, will then approximate the required sector shape.

The parameters of this parallel-plate array may be applied directly to the design of line feeds for parabolic cylinder reflectors (Fig.1.4). These parameters may also be used as a guide in achieving the same sector-shaped radiation pattern with an array of concentric circular guides (Fig.1.5). Such an antenna has produced reasonably good patterns by empirical adjustment of the parameters [25].

Good patterns have also been obtained using an array where the edges are not all in the same plane, but staggered slightly [13] (Fig.1.6). Measurements of various types of feed antennas [15] has shown that there is little difference in the resulting pattern between an array of staggered circular guides (Fig.1.6) and a four-ring corrugated surface [15] (Fig.1.7) when both arrays are the same size. The amount of stagger is an additional parameter which can be adjusted to optimize the pattern.

The design of waveguide feeds with parasitic elements has been mainly empirical to date. Thus the analysis of an array of parallel-plate waveguides may assist in the development of optimum feeds for reflector antennas, at least for two dimensional structures. The results of this analysis could be applied not only to feed design, but to any coupled waveguide antenna.

1.2 LITERATURE REVIEW

Many different types of open-ended parallel-plate waveguide structures have been analyzed using a variety of methods. The structures include infinite arrays of parallel-plate waveguides, finite arrays in isolation or embedded in a groundplane or other surface (Figs.1.8-1.17), and closed region problems including bi,tri and N-furcated waveguides (Fig.1.18).

The fields in coupled open-ended waveguides cannot always be found rigorously except for certain geometries,

because the resulting boundary value problem does not have a known closed form solution. Hence for many cases approximate methods have been developed to obtain the fields.

When rigorous solutions can be found, the methods used include both the Wiener-Hopf technique and mode matching techniques [37]. These methods can also be used to find approximate solutions for those cases where the resulting integral or infinite matrix equations cannot be solved exactly. Approximate solutions are also obtained using ray-optical techniques based on the geometrical theory of diffraction [26], modified residue calculus and function theoretic techniques [38], and numerical techniques based on moment methods [21].

The choice of method to be applied to a given problem depends on the particular geometry. Rigorous methods are generally limited to very specific geometries, ray-optical methods are most suitable for structures whose characteristic dimensions are on the order of a wavelength or greater, and numerical methods can be used with any geometry in principle, but are generally suitable only for relatively small structures. The literature of parallel-plate waveguide structures is reviewed below.

A single parallel plate waveguide in isolation (Fig.1.8) has been used as a test geometry for exact, numerical and ray-optical methods, particularly for several refinements of ray-optical techniques. The exact solution for the reflection coefficient was given by Weinstein [45] and Heins [22] using the Wiener-Hopf technique. The

reflection coefficient was found using moment methods by Wu and Chow [48] and was improved by Gardiol and Haldemann [20]. Montgomery and Chang [38] found it using modified residue calculus. Rudduck and Tsai [40] calculated the reflection coefficient using a ray-optical procedure but depending also on a reciprocity argument. Yee, Felsen and Keller [50] found the reflection coefficient by tracing rays directly and using a ray-to-mode conversion formula. They improved their solution for low frequencies in [18] and [49]. Bowman [8] [9] pointed out that the ray-optical solution of [50] did not agree with the asymptotic form of the exact solution. The ray-optical solution was improved by Boersma [3] [4] using the uniform asymptotic theory of Ahluwalia et al.[1]. Boersma's results showed much improvement in the mode transition regions and recovered the asymptotic form of the exact solution. Lee [30] [31] derived a modified diffraction coefficient which includes interactions between the two half-plane edges automatically, so that these interactions need not be explicitly calculated. This method recovered the exact solution for the reflection coefficient. The coupling between two separated waveguides (Fig.1.9) was calculated using edge diffraction theory by Dybdal,Rudduck and Tsai [17] and also using residue calculus by Montgomery and Chang [38].

The exact radiation pattern of a parallel plate waveguide was given by Weinstein [45] and Heins [22] using the Wiener-Hopf technique. Yee and Felsen [19] [49] used ray-optical methods to derive a radiation pattern which

agreed well with the exact solution except in the aperture plane. Rudduck and Wu [41] improved the pattern in the aperture plane by using a slope diffraction coefficient. Lee [30] recovered the exact solution using his method of modified diffraction coefficient. The aperture fields and gain were calculated by Jull [24].

The fields along the shadow boundary of a parallel-plate waveguide when a plane wave is normally incident on it from outside the guide were calculated by Lee and Boersma [32] using both the uniform asymptotic theory and the modified diffraction coefficient. They also found the fields for a line source incident on two staggered parallel plates (Fig.1.10). Boersma [5] also considers a plane wave incident on a staggered guide. Rahmat-Samii and Mittra [39] use a spectral domain approach for this problem. The radiation pattern of a staggered guide using wedge diffraction was found by Ryan and Rudduck [42].

Parallel plate waveguides embedded in a groundplane and/or surrounded by other waveguides have also been analyzed using rigorous, numerical and ray-optical methods. The reflection coefficient from a single waveguide embedded in an infinite groundplane (Fig.1.11a) and a flanged waveguide with arbitrary angle of flange (Fig.1.11b) was calculated by Rudduck and Tsai [40] and Yee, Felsen and Keller [50] using ray-optical methods and by Lee [30] using his modified diffraction coefficient. The radiation pattern of the flanged waveguide was calculated by Mittra and Lee [37] using Weiner-Hopf techniques, by Yee and Felsen [49]

using ray-optical methods ,by Lee [30] using a modified diffraction coefficient and by Wu and Chow [48] using moment methods. The coupling between two and three such guides embedded in a groundplane (Fig.1.12) was calculated numerically by Wu [47]. The coupling between adjacent and separated guides in both a finite (Fig.1.13) and an infinite (Fig.1.14) array of parallel plate waveguides has been calculated by Lee [29] using the Weiner-Hopf technique and by Montgomery and Chang [38] using modified residue calculus. Radiation patterns were calculated by Mittra and Lee [37] for an infinite array with all guides excited and with only one guide excited using both the Weiner-Hopf and mode-matching techniques. Radiation patterns were also calculated by Lee [29] for a finite array embedded in a simulated groundplane (Fig.1.15) with only one guide excited , by Montgomery and Chang [38] for a finite array in isolation (Fig.1.17) and by Burnside et al. [10] for the same array but with all guides excited. Luzwick and Harrington [35] [36] found the radiation pattern for a finite array with thick walls embedded in a groundplane with the central guide excited and the outer guides reactively loaded (Fig.1.16).

The coupling between waveguides in a closed region (bi,tri and N-furcated waveguide) (Fig.1.18) has been calculated by Mittra and Lee [37] using the Weiner-Hopf technique and by Montgomery and Chang [38] using modified residue calculus.

1.3 APPROACH TO THE PROBLEM

It appears that the small parallel plate waveguide array in isolation (Fig.1.3 and 1.6) to be considered here may be effectively analyzed using ray-optical techniques. Similar waveguide structures have been analyzed successfully using these methods, and it may be expected that these previous results will be useful for the problem at hand. There is no exact solution for this geometry, and numerical methods would require very large matrices because of the relatively large size of the array in terms of wavelengths.

Ray-optical methods using the geometrical theory of diffraction have as their canonical basis the exact solution for plane wave diffraction by a perfectly conducting half-plane. The parallel-plate waveguide arrays of Fig.1.3 and 1.6 consist of several half-plane edges and so ray-optical methods appear to be a natural choice for their analysis.

Ray-optical methods can be used to solve for electromagnetic fields in the presence of diffracting edges provided the characteristic dimensions of the structure are of the order of a wavelength or more. These methods assume that the fields travel in straight lines called rays. The geometrical theory of diffraction (GTD) is an extension of geometrical optics which accounts for diffraction [26]. It is postulated that diffracted rays are produced when incident rays strike the edges of conductors (Fig.1.19). A diffraction coefficient is introduced based on the asymptotic form of the exact solution for diffraction of a

plane wave by a perfectly conducting half-plane [7]. Diffraction is a local effect; the diffraction coefficient is determined by the edge alone, and is not dependent on other parts of the structure. The diffracted field appears to emanate from the diffracting edge which for a straight edge looks like a line source of rays.

One major flaw in GTD is that the diffraction coefficient is not uniformly valid in the asymptotic limit, and becomes infinite at the boundaries between light and shadow. Various uniform theories have been advocated [1] [28] to overcome this difficulty, but with some sacrifice in simplicity of application.

Ray-optical methods have been extended to allow fields more general than plane waves to be incident on the half-plane [50] [6]. These extensions are required in the analysis when a diffracted field is in turn diffracted by another half-plane edge.

A ray-optical analysis may begin by tracing ray paths corresponding to the fields. Incident fields may be reflected from a surface, or diffracted from an edge. The resulting fields may be again reflected or diffracted. The ray-optical analysis of the parallel-plate waveguide arrays of Figs. 1.3 and 1.6 require that many ray paths be traced to represent the fields. Fields excited by the source transmitter travel down the central waveguide and are diffracted at the open end. The diffracted fields will excite fields in the outer parasitic guides surrounding the central driven guide. The magnitude of these fields may be

calculated. These fields will travel down the outer guides, be reflected at the shorted end, and diffracted at the open end. These diffracted fields will in turn excite more diffracted fields and the process continues. The radiation pattern is the sum of all these diffracted fields.

The analysis thus divides naturally into several parts:

1- coupling between two adjacent parallel-plate waveguides (Fig.1.20)

2- coupling between two separated guides (Fig.1.9)

3- reflection from the open end of a single guide (Fig.1.8)

4- radiation pattern of single guide (Fig.1.8)

5- radiation pattern of multi-element waveguide array (Fig.1.3)

6- coupling between two adjacent staggered parallel-plate waveguides (Fig.1.20)

7- reflection from open end of single staggered guide (Fig.1.10)

8- radiation pattern of single staggered guide (Fig,1.10)

9- radiation pattern of multi-element staggered waveguide array (Fig.1.6).

Parts 1,2,3 and 4 are needed to solve 5 and similarly parts 6,7, and 8 are needed to solve 9. Parts 2,3,4,7 and 8 have been considered in the literature, however, some of the solutions presented here (parts 2, 8) constitute improvements to these earlier results.

1.4 EXPERIMENTAL ARRANGEMENT

It would be very desirable to confirm the analysis by comparing the numerical results to those obtained by experimental measurement. Measurement of coupling and reflection coefficients of two dimensional structures is very difficult to perform accurately, but is possible [17]. However, approximate radiation patterns of a two-dimensional array of parallel-plate waveguides may be measured if the third dimension (perpendicular to the page in Figs.1.3 and 1.6) of the guides is large enough. If a rectangular waveguide is flared in one dimension to form an H-plane sectoral horn (Fig.1.22), a TE_{10} mode in the guide approximates a two-dimensional TEM mode in the center of the antenna aperture. Thus the E-plane radiation pattern of an H-plane sectoral horn approximates that of a parallel-plate waveguide of the same width. Appendages to the horn simulate the outer parallel-plate guides.

The horn used for the measurements had a total flare angle of 30° with an aperture of 1.016 x 50 cm, and was fed with WR-90 waveguide. The outer guides were 1.016 cm wide and of various depths. Radiation pattern measurements were performed at X-band on the outdoor antenna range described in Appendix D.

1.5 SUMMARY

The calculation of radiation patterns of small arrays of parallel plate waveguides is potentially useful in designing antennas with waveguide elements. Exact, numerical and ray-optical methods have been used to analyze various parallel plate waveguide structures, however the ray-optical method appears to be well suited to the three and five element arrays to be considered here. The analysis divides naturally into several parts which are considered in turn in the following chapters. The theoretical patterns will be compared to experimental measurements made with a wide angle H-plane sectoral horn.

When the analysis is complete and the results verified by experiment the width, depth, number and amount of stagger of the elements of the parallel plate waveguide array may be adjusted to optimize the pattern for particular applications. A wide variety of patterns may be obtained because of the many parameters available. The results are expected to be useful for the design of several types of waveguide antennas.

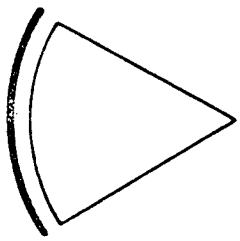

Fig. 1.1
sector-shaped
radiation pattern

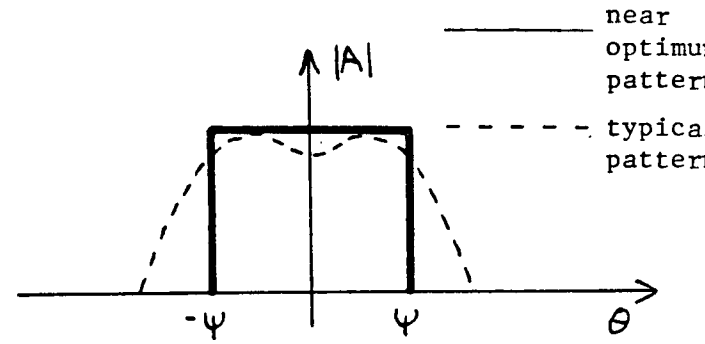

Fig. 1.2
near optimum and typical radiation patterns
for a feed antenna

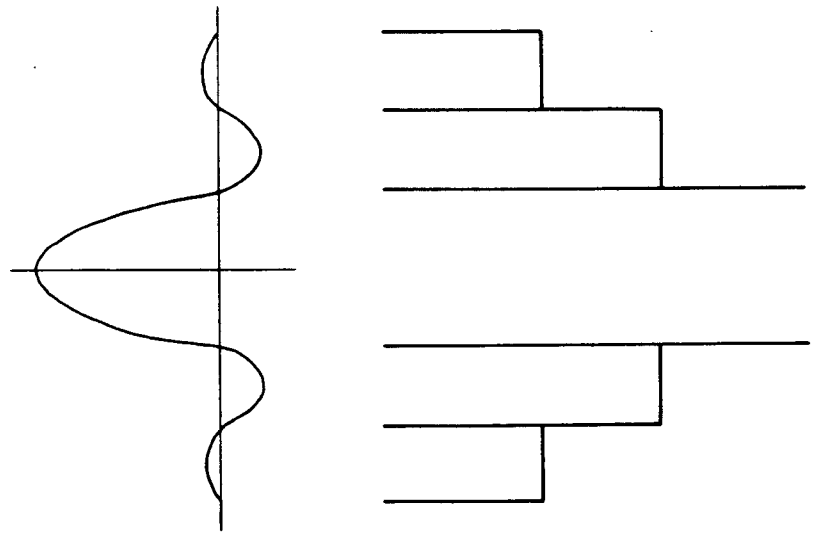

Fig. 1.3
parallel plate waveguide array
with desired aperture field

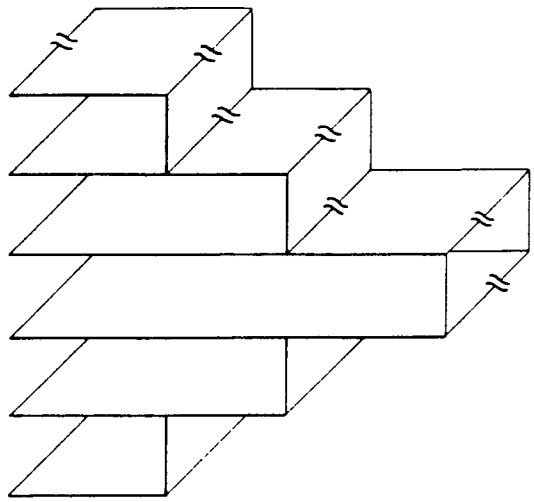

Fig 1.4
line feed for a parabolic
cylinder reflector

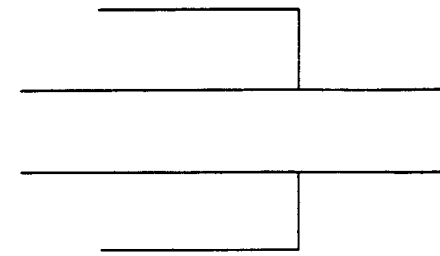

Fig. 1.6
staggered array of parallel
plate waveguides

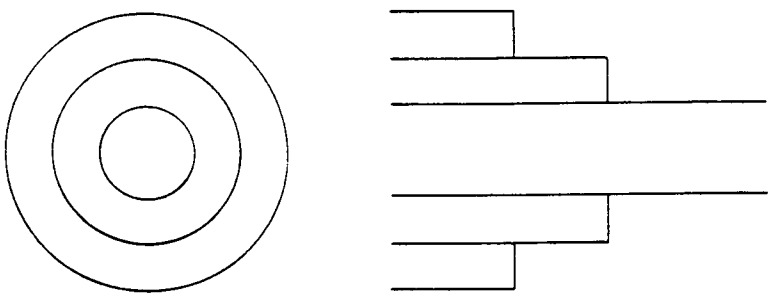

Fig. 1.5
array of concentric circular
waveguides

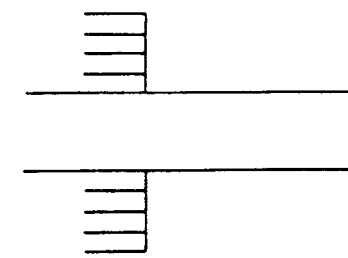

Fig. 1.7
cross-section of
concentric circular
waveguide feed

Fig. 1.8
parallel plate waveguide

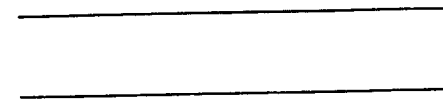

Fig. 1.9
two separated parallel plate waveguides

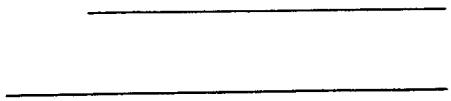

Fig. 1.10
staggered parallel plate waveguide

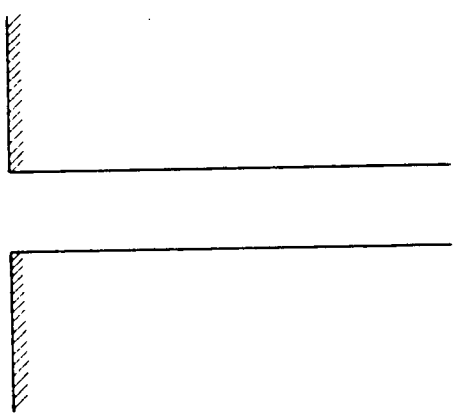

a b

Fig. 1.11
flanged parallel plate waveguides

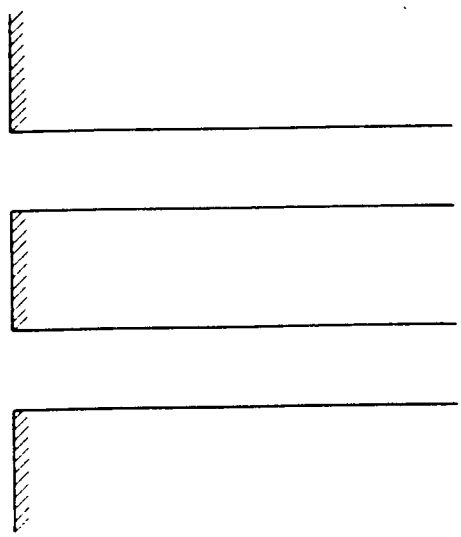

Fig. 1.12
two separated flanged
parallel plate waveguides

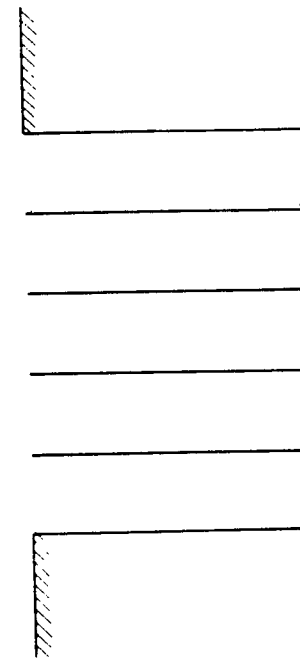

Fig. 1.13
finite array of parallel
plate waveguides embedded
in a groundplane

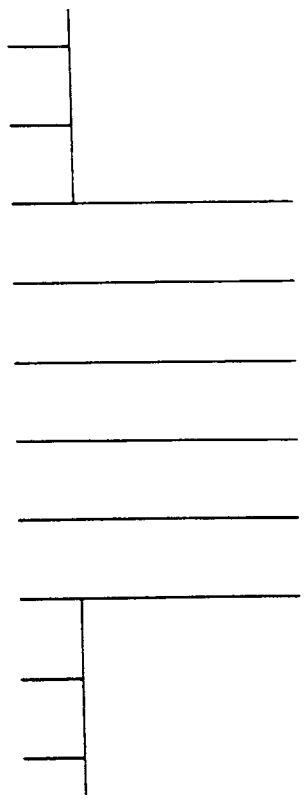

Fig. 1.15
finite array of parallel
plate waveguides embedded
in a simulated groundplane

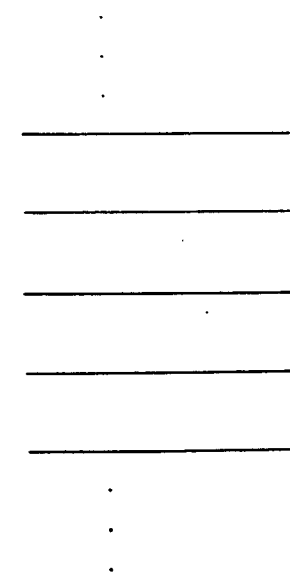

Fig. 1.14
infinite array of
parallel plate waveguides

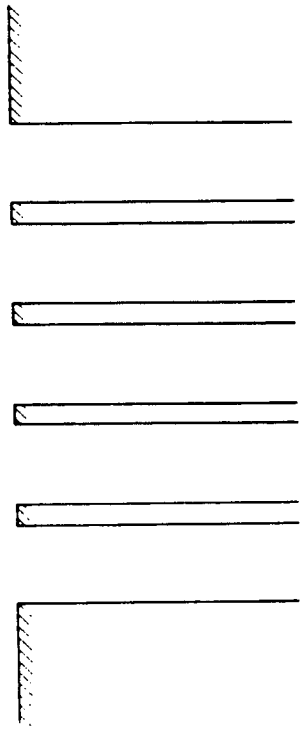

Fig. 1.16
finite array of parallel
plate waveguides with thick
walls embedded in a groundplane

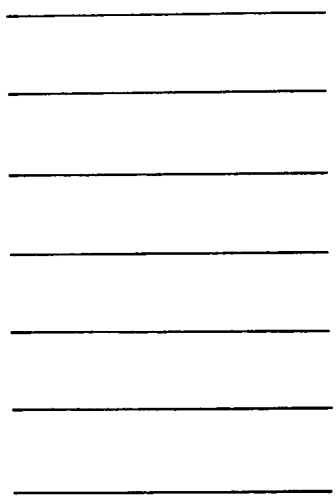

Fig. 1.17
finite array of parallel
plate waveguides in isolation

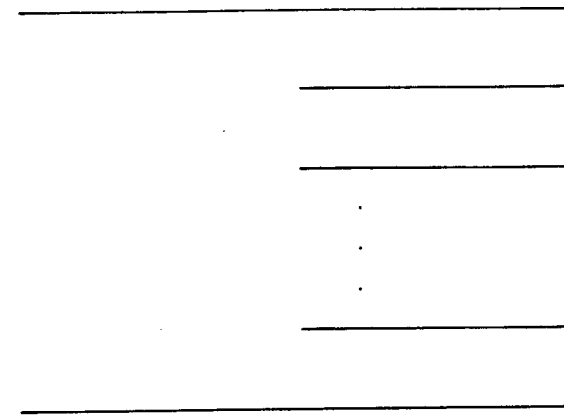

Fig. 1.18
N-furcated waveguide

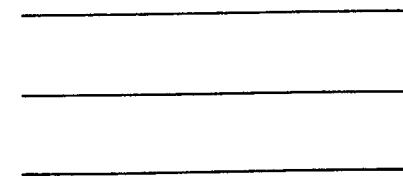

Fig. 1.20
two adjacent parallel
plate waveguides

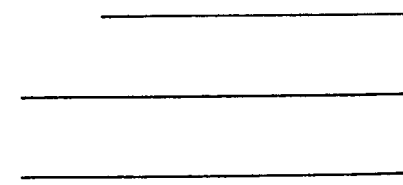

Fig. 1.21
two adjacent staggered
parallel plate waveguides

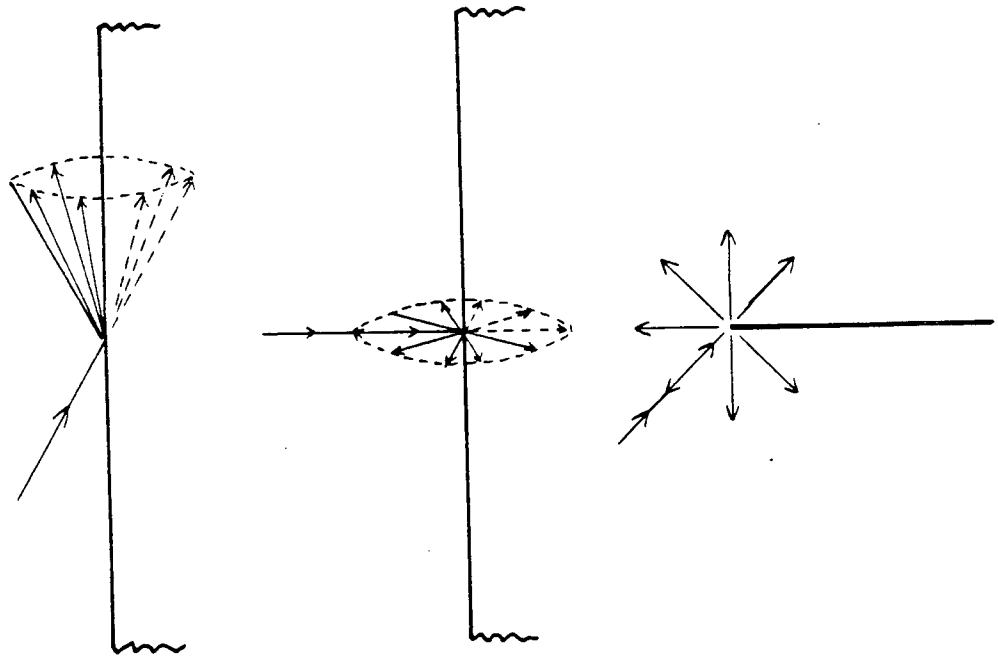

Fig. 1.19
diffracted rays

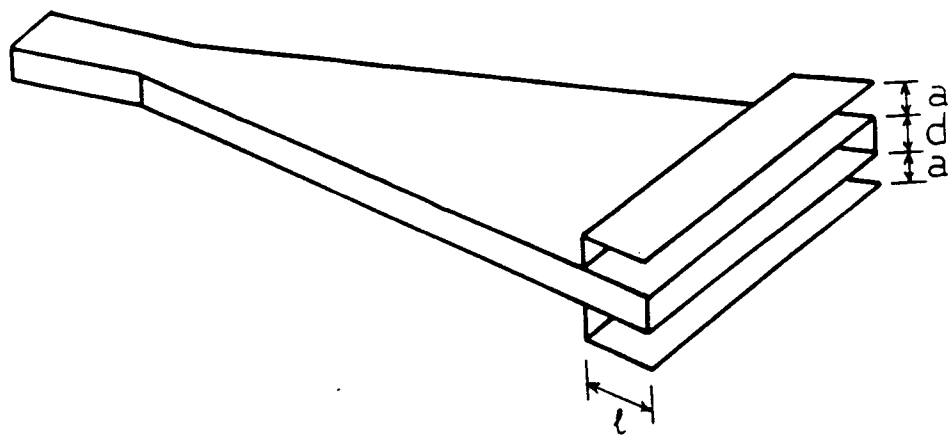

Fig. 1.22
H-plane sectoral horn

Chapter 2

METHOD OF ANALYSIS

2.1 GENERAL DESCRIPTION

In this chapter the ray-optical analysis procedure used to calculate coupling coefficients or radiation patterns of waveguide antennas will be described in general, and some canonical problems upon which ray-optical methods are based will be discussed. In later chapters each of the parts of the analysis mentioned in Chapter 1 will be considered in turn. The numerical results will be compared with those obtained by others for similar or related geometries, and in the case of radiation patterns will be compared to the experimental results.

The ray-optical analysis of any part of the analysis begins by following essentially the procedure in [50] for analysis of the reflection for a single guide. First the mode in the incident driven guide is decomposed into two plane waves which diffract from the edges of the open end of the waveguide. At distances $kr \gg 1$ from an edge the diffracted fields appear to emanate from a line source centred at the edge. These line source fields are in turn diffracted from other edges, thus exciting additional line source fields at the edges. These additional fields are again diffracted, and in principle the process continues indefinitely. In practice only a few diffractions are usually adequate. These same line source fields also excite

modes in the outer parasitic guides and also radiate into space. The complex amplitudes of these waveguide modes relative to the incident mode corresponds to the coupling coefficient between guides. The sum of all the line source fields at the edges as observed at a distant point produces the radiation pattern of the waveguide array.

The totality of rays associated with all these fields can be divided into groups, each group corresponding to a particular sequence of rays, or ray path. To find the coupling between guides the ray path would start in one guide and end in another. To find the radiation pattern, the ray path would start in a guide and end up radiating into space. The alternate paths possible when a ray strikes an edge are traced individually. The number of possible ray paths is infinite, but only the first few contribute significantly to the coupling coefficients or radiation patterns.

All ray paths to be considered for each of the problems mentioned above will be traced explicitly and their contribution to coupling or radiation will be calculated (Figs. 3.2, 4.2, 5.1, 6.3-6.6, 7.3-7.7, 8.3, 9.2, 10.3-10.5, and 10.7). To facilitate these computations, the fields represented by the various combinations of two successive rays which occur in these ray paths will be calculated first. The field represented by any ray in a particular sequence or ray path can then be found from the field of the ray preceding it. In this way the field represented by all rays can be found. From this the total field solution, the

coupling coefficients and radiation patterns can be derived. This approach gives rise to a series of diffraction problems of two successive rays in a sequence, which are solved in the following sections as they are required. The canonical solutions will then be used to assemble the solutions to each of the coupled waveguide problems listed at the end of Chapter 1.

2.2 CANONICAL PROBLEMS

Ray-optical methods have as their canonical basis the exact solution for plane wave diffraction by a perfectly conducting half-plane. This problem was originally solved by Sommerfeld [43] and was solved more simply by Clemmow [14] and others.

Consider the half-plane y=0, z>0 and a $\frac{TM}{TE}$ field

$$\begin{matrix} H_x^i \\ E_x^i \end{matrix} = u_i = e^{-ikr\cos(\theta-\theta_0)} \tag{2.1}$$

incident on it at an arbitrary angle θ_0 (Fig.2.1), where $k = 2\pi/\lambda$ is the free space wavenumber. In this and all subsequent equations a time factor $e^{-i\omega t}$ is implied and suppressed, where $\omega = 2\pi f$ is the angular frequency of the wave. The total field at all points (x,y,z) in space in the presence of the half-plane is given by

$$\begin{matrix} H_x^t \\ H_x^t \end{matrix} = u_t = G(r,\theta_0,\theta), \tag{2.2}$$

where $G(r,\theta_0,\theta) = \frac{e^{-i\pi/4}}{\sqrt{\pi}} \{e^{-ikr\cos(\theta-\theta_0)} F[-\sqrt{2kr}\cos(\frac{\theta-\theta_0}{2})]$

$$\pm e^{-ikr\cos(\theta-\theta_0)} F[-\sqrt{2kr}\cos(\frac{\theta+\theta_0}{2})]\}, \qquad (2.3)$$

$$F(\alpha) = \int_{\alpha}^{\infty} e^{ix^2} dx, \qquad (2.4)$$

$$F(-\alpha) = \sqrt{\pi}\, e^{+i\pi/4} - F(\alpha), \qquad (2.5)$$

and the top(bottom) signs refer to TM(TE) fields. This result can be evaluated for kr>>1 using the asymptotic form of the Fresnel integral

$$F(\alpha) \sim \frac{ie^{i\alpha^2}}{2\alpha}, \quad \alpha >> 1, \qquad (2.6)$$

to obtain

$$u_t = u_g + D(\theta_0,\theta)E(r), \qquad (2.7)$$

where u_g is the geometrical optics field given by

$$u_g = \begin{cases} e^{-ikr\cos(\theta-\theta_0)} \pm e^{-ikr\cos(\theta+\theta_0)} & \text{for } 0\le\theta<\pi-\theta_0 \\ e^{-ikr\cos(\theta-\theta_0)} & \text{for } \pi-\theta_0<\theta<\pi+\theta_0 \\ 0 & \text{for } \pi+\theta_0<\theta\le 2\pi \end{cases} \qquad (2.8)$$

and $D(\theta_0,\theta)E(r)$ is the diffracted field given by

$$D(\theta_0,\theta) = -\frac{e^{+i\pi/4}}{2\sqrt{2\pi}} \{\sec(\frac{\theta-\theta_0}{2}) \pm \sec(\frac{\theta+\theta_0}{2})\} \qquad (2.9)$$

and $E(r) = e^{ikr}/\sqrt{kr}$. (2.10)

This asymptotic result shows that the total field is made up of the incident field and a reflected field which are both plane waves, and a diffracted field which is a cylindrical

wave (Fig.2.2). $D(\theta_0,\theta)$ can be interpreted as a diffraction coefficient giving the magnitude of the cylindrical wave $E(r)$ emanating from the half-plane edge. The diffracting edge thus appears like a line source of the diffracted field.

Unfortunately the asymptotic expression (2.7) is not uniformly valid, and becomes infinite along the shadow boundaries between the lit and shadowed regions at $\theta = \pi \pm \theta_0$ (Fig.2.1). However, (2.7) does characterize the diffracted field as a line source at the edge and can be used to predict the diffracted field away from the shadow boundary.

The expression (2.7) can be made uniformly valid by introducing a transition function that precisely cancels the infinity at $\theta = \pi \pm \theta_0$ [49]. This is in fact equivalent to rewriting (2.2) for an observation point at r=a from the edge. Then the total field at r=a is

$$u_t = G(a,\theta_0,\theta)\frac{E(r)}{E(a)} \tag{2.11}$$

which looks like a line source field and is uniformly valid for all θ .

To predict the fields when a diffracted field is diffracted again a second time requires an expression for the fields when a line source is diffracted by a half-plane.

It has been shown [7] that for an isotropic line source $u_i = E(r)$ in the presence of a half-plane (Fig.2.3) the total field for $k(r_o+r)>>1$ is given by

$$u_t \sim \sqrt{\frac{2}{\pi}}\, e^{-i\pi/4} \left\{ \frac{e^{ikR}}{\sqrt{k(r_0+r+R)}} F[-2\sqrt{\frac{kr_0 r}{r_0+r+R}}\cos(\frac{\theta-\theta_0}{2})]\right.$$

$$\pm \frac{e^{ikS}}{\sqrt{k(r_0+r+S)}} F[-2\sqrt{\frac{kr_0 r}{r_0+r+S}} \cos(\frac{\theta+\theta_0}{2})]\} \qquad (2.12)$$

If $r>>r_0$ and $\cos(\frac{\theta\pm\theta_0}{2})\neq 0$ (2.12) becomes

$$u_t \sim G(r_0,\theta_0,\theta)E(r) \qquad (2.13)$$

Note that (2.13) is simply the plane wave solution (2.2) multiplied by $E(r)$.

(2.12) and (2.13) can be used to predict multiply diffracted fields. A field which has already been diffracted at least once before looks like a line source $f(\theta)E(r)$ incident on another diffracting edge (if that edge is not on the shadow boundary of the first edge). If this field is approximated by an isotropic line source $f(\phi)E(r)$, where ϕ is the direction from the line source to the other diffracting edge, then the doubly diffracted field can be predicted using (2.12). This approximation has been used successfully by others [24] [50] and gives acceptable results, except where the second edge lies on the shadow boundary of the first.

2.3 LIMITATIONS OF THE METHOD

When a diffracted field from an edge is again diffracted by another edge near the shadow boundary of the first edge, the resultant field cannot be accurately calculated using this isotropic line source approximation. Consider a line source field incident on two parallel half-planes in Fig.2.4, where the observation point and half-

plane edges are all collinear. The essence of the difficulty is that the field which is diffracted from the first edge and incident on the second edge is not a "ray field" [33], i.e. is not of the form

$$\sum_{m=0}^{\infty} A_m \frac{e^{ikf(r)}}{(ik)^m} \tag{2.14}$$

near the shadow boundary (i.e. within a parabola with focus at the first edge and axis along the shadow boundary [39]). The ray methods used here and their uniform extensions are only valid when the incident field is a ray field. Thus using the solution for diffraction of an anisotropic line source by a half-plane [6] is not accurate either. This difficulty along the shadow boundary may be expected to compromise the accuracy of some of the parts of the analysis mentioned on page 10.

If both a singly and doubly diffracted field in any ray path lie on the shadow boundary, then the doubly diffracted field is not a ray field, and the triply diffracted field cannot be calculated accurately using the line source approximation, so that all triply and higher order diffracted fields are potentially inaccurate. However, this does not appear to be serious because, unless the triply diffracted field is itself along the shadow boundary, it contributes very little numerically to the final result. Thus for the coupling between adjacent guides (parts 1 and 6) and the reflection and radiation from a single guide (parts 3,4,7,8) this method should yield acceptable results.

However, for the coupling between two separated guides (part 2) the triply and higher order diffracted fields affect the shape of the coupling versus guide width curve and make a significant contribution to the result. The radiation patterns of the multi-element non-staggered arrays (part 5) is expected to be inaccurate near the aperture plane because of the many interactions along the shadow boundary. The errors are cumulative because the diffracted fields are repeatedly calculated as if the incident fields are ray fields.

In certain cases this difficulty may be overcome by expanding the (non-ray) field in a Taylor series with each term representing a cylindrical wave of the form (2.14), and then applying the method of [50] on a term-by-term basis. However, when there are three or more half-planes, the fields in the aperture plane can no longer be neatly represented by an infinite sum of n times diffracted fields. In the two half-plane case, each n times diffracted field when in turn diffracted produces only one (n+1) times diffracted field. By contrast, in the three half-plane case, an n times diffracted field which is diffracted from the central half-plane edge produces two (n+1) times diffracted fields. To represent all diffracted fields of all orders incident on a given edge requires a much more complex summation of the type derived in Appendix B. When there are only two half-planes, the field u_{n+1} is determined by applying UAT to u_n on a term-by-term basis. The expression for the field is then compared with an Ansatz and leads to a

set of recurrence relations which must be solved. This process may be greatly complicated in the three half-plane case because there are many fields u_n to be considered. Ignoring the fact that the fields are not ray fields and mechanically applying the theory to very high orders of diffraction as was done by Ciarkowski [12] and also in Appendix B leads in both cases to reflection and coupling versus guide width curves with an apparently random fine structure which never approaches the known shape of the exact solution, regardless of the number of terms considered.

A similar difficulty occurs if the plates are staggered. Consider a line source field incident on two staggered parallel plates (Fig.2.5). The diffracted field u_1 in these figures is not a ray field in the neighborhood of the second edge, because the edge is on the incident or reflected shadow boundary. Hence (8.1) is not valid and the term-by-term approach may be used.

The approximation of [24] [50] is thus not expected to yield accurate results near a shadow boundary along which there are three or more half-plane edges, and triple or higher order diffraction terms contribute significantly to the numerical result. The accuracy of this approximation is expected to be acceptable away from the shadow boundaries and near the shadow boundary if there are only two half-plane edges on it.

2.4 SUMMARY

The ray-optical analysis of any parallel plate waveguide structure requires that many ray paths be traced. The fields represented by these rays are calculated from the canonical problems of a plane wave or a line source incident on a half-plane. This method is inaccurate for field calculations on or near shadow boundaries, which limits its application to situations where accuracy is not required along shadow boundaries. The solutions for plane wave and line source diffraction by a half-plane will be used in succeeding chapters to find the fields represented by the various combinations of two successive rays in a ray path, and thus the coupling coefficients and radiation patterns.

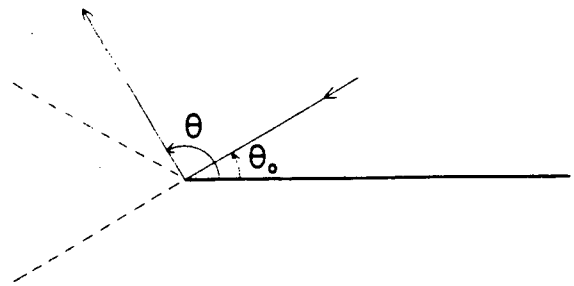

Fig. 2.1
incident and reflected shadow boundaries

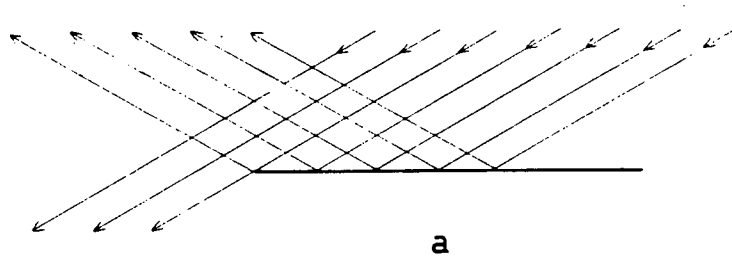

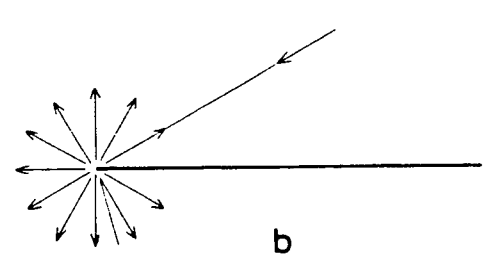

Fig. 2.2
incident, reflected and diffracted fields

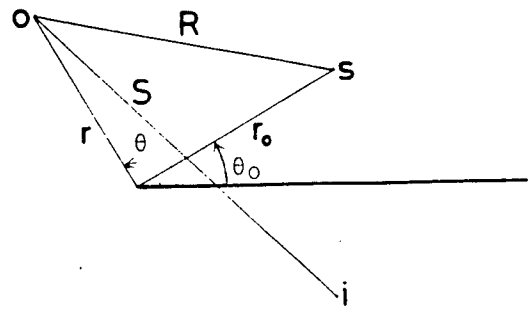

Fig. 2.3
line source incident on a
half-plane

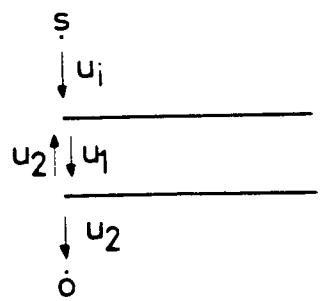

Fig. 2.4
line source incident on
two parallel half-planes

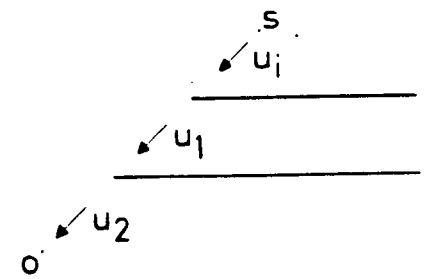

Fig. 2.5
line source incident on
two staggered half-planes

Chapter 3

COUPLING BETWEEN TWO ADJACENT WAVEGUIDES

3.1 FORMULATION

The first problem to be solved is that of the coupling between two adjacent parallel plate waveguides (Fig.3.1). The ray paths from the lower driven guide to the upper parasitic guide are determined by inspection and shown in Fig.3.2 .

Consider two adjacent semi-infinite parallel plate waveguides consisting of the three perfectly conducting parallel half planes in $z>0$ at $y=-d$, $y=0$, $y=a$ (Fig.3.1). We wish to determine the field coupled from the driven guide ($-d<y<0$; $z>0$) into the parasitic guide ($0<y<a$; $z>0$) . An incident field

$$\begin{matrix} H_x^i \\ E_x^i \end{matrix} = e^{-ik_N z} \begin{matrix} \cos \\ \sin \end{matrix} \left(\frac{N\pi y}{d}\right) \tag{3.1}$$

in the driven guide will excite fields of the form

$$\begin{matrix} H_x^c \\ E_x^c \end{matrix} = \sum_{\substack{n=0 \\ 1}}^{\infty} A_{Nn} e^{+ik_n z} \begin{matrix} \cos \\ \sin \end{matrix} \left(\frac{n\pi y}{a}\right) \tag{3.2}$$

in the parasitic guide. The coupling coefficient A_{Nn} is the relative amplitude and phase of the nth mode in the parasitic guide to the Nth mode in the incident guide at

z=0. The propagation constants k_N, k_n are given by

$$k_N = \sqrt{k^2-(\pi N/d)^2} \tag{3.3}$$

$$k_n = \sqrt{k^2-(\pi n/a)^2} \tag{3.4}$$

Here we use the ray-optical method of Yee, Felsen and Keller [50] to find A_{Nn} .

Following [50] the incident field (3.1) is decomposed into two plane waves

$$\begin{matrix} H_x^i \\ E_x^i \end{matrix} = u_i = \frac{1}{2q}\{e^{-i(k_N z - N\pi y/d)} + \tau e^{-i(k_N z + N\pi y/d)}\} \tag{3.5}$$

traveling in the directions $\pi \pm \theta_N$ relative to the half plane guide boundaries, where

$$\sin\theta_N = N\pi/kd\ , \tag{3.6}$$

$$q = \begin{cases} 1 & \text{TM fields} \\ i & \text{TE fields} \end{cases}, \tag{3.7}$$

$$\tau = q^2\ . \tag{3.8}$$

The first term in (3.5) is a plane wave traveling in the direction $\pi - \theta_N$ which has the value

$$u_i = \frac{1}{2q} \tag{3.9}$$

at the edge y=0, z=0 The other term, a plane wave in the direction $\pi + \theta_N$ has the value

$$u_i = \frac{(-1)^N \tau}{2q} \tag{3.10}$$

at the edge y=-d, z=0. These two plane waves are represented by the incident rays in the lower guide of Fig. 3.1.

The fields excited by diffraction into the parasitic guide appear to originate from line sources of the form

$$u_d \sim f(\theta)E(r) \tag{3.11}$$

located at the edges z=0; y=0 or a. In (3.11) r is the distance from the edge and $f(\theta)$ is the radiation pattern of the diffracted field. Radiation in the direction $\theta = \theta_n$ excites the nth waveguide mode in z>0; 0<y<a. The fields excited in the parasitic guide due to a line source (3.11) at one of its edges are [50]

$$\begin{matrix} H_x^c \\ E_x^c \end{matrix} = u_d = \sum_{n=0}^{\infty} \frac{q\varepsilon_n \sqrt{\pi} e^{i\pi/4}}{\sqrt{2k_n a}} f(\theta) e^{-in\pi y_0/a} e^{ik_n z} \begin{matrix} \cos \\ \sin \end{matrix} \left(\frac{n\pi y}{a}\right) , \tag{3.12}$$

$$\varepsilon_n = \begin{cases} 1 & \text{if } n = 0 \\ 2 & \text{if } n \neq 0 \end{cases} , \tag{3.13}$$

$$y_0 = 0 \text{ or } a .$$

Comparison of (3.12) with (3.2) immediately yields the coupling coefficient A_{Nn}.

Throughout this chapter, the following notations are employed to represent the fields, where the superscript x refers to the letter of the figure showing the particular ray path under consideration.

u_i is a plane wave in the driven guide.

u_1^x is a line source field arising from diffraction of the incident field u_i (ie u_1^x is a singly diffracted field).

u_m^x is a line source field arising from diffraction of a linesource u_{m-1}^x (ie u_m^x is an m times multiply diffracted field).

$A_{Nn}^{(j)}$ is the contribution to A_{Nn} of (3.2) arising from fields diffracted j times.

3.2 SINGLE DIFFRACTION

The coupling contribution due to single diffraction is calculated from the solution for diffraction of a plane wave by a half plane. One of the two plane waves comprising the field in the driven guide is incident on the edge y=0,z=0 at an angle $\theta_o = 2\pi - \theta_N$ (see Fig.3.2a). At distances kr>>1 from this edge, the diffracted field is given by

$$u_1^a = \frac{1}{2q} D(2\pi-\theta_N,\theta_n) E(r), \tag{3.14}$$

where $D(\theta_0,\theta)$ is given by (2.9). Substituting

$$\sin \theta_n = n\pi/ka \tag{3.15}$$

we find

$$u_1^a = \frac{1}{2q} \frac{e^{+i\pi/4}}{\sqrt{2\pi}} \frac{\sqrt{k+\tau k_N}\ \sqrt{k+\tau k_n}}{(k_N+k_n)} E(r). \tag{3.16}$$

The radiation pattern $f(\theta)$ of (3.16) is obtained by comparison with (3.11). Putting this into (3.12), the contribution to the coupling coefficient of (3.2) for single diffraction only is

$$A_{Nn}^{(1)} = \frac{i\epsilon_n}{4k_n a} \frac{\sqrt{k+\tau k_N}\ \sqrt{k+\tau k_n}}{k_N+k_n} . \tag{3.17}$$

3.3 MULTIPLE DIFFRACTION

The contributions to the coupling coefficient for multiple diffraction are obtained separately for each ray

path in Fig.3.2. First the individual diffraction problems of two successive rays in a sequence will be solved, and then pieced together to find the coupling contributed by the fields in each ray path and the total coupling. The pairs of successive rays which will be considered are shown in Figs.3.3, 3.4 and 3.5.

In Fig.3.3 a plane wave u_i is incident on a half-plane edge at $\theta_0 = \theta_N$ or $\theta_0 = 2\pi - \theta_N$. The diffracted field in the direction $\theta = \frac{\pi}{2}$ or $\theta = \frac{3\pi}{2}$ at a point r=a away from the edge is, from (2.11)

$$u_1 = u_i \tau_1 C_N'(a) , \tag{3.18}$$

where

$$C_N'(a) = C_N(a)/E(a) , \tag{3.19}$$

$$C_N(a) = \frac{e^{-i\pi/4}}{\sqrt{\pi}} \{e^{+i\sqrt{k^2-k_N^2}\,a} F[\sqrt{\frac{a}{2}}\,(\sqrt{k+k_N} - \sqrt{k-k_N})]$$

$$+ \tau e^{-i\sqrt{k^2-k_N^2}\,a} F[\sqrt{\frac{a}{2}}\,(\sqrt{k+k_N} + \sqrt{k+k_N})]\} \tag{3.20}$$

and

$$\tau_1 = \begin{cases} -\tau & \text{if } |\theta-\theta_0|<\pi/2 \\ 1 & \text{otherwise} \end{cases} . \tag{3.21}$$

For ka>>1 (3.18) simplifies to

$$u_1 = u_i \tau_1 C_N E(r) , \tag{3.22}$$

where

$$C_N = \frac{e^{+i\pi/4}}{\sqrt{2\pi}} \frac{\sqrt{k}\,\sqrt{k+\tau k_N}}{k_N} . \tag{3.23}$$

In Fig.3.4 an isotropic line source $u_{m-1} = E(r)$

located at S, a distance r_0 from a guide wall is incident on that edge at $\theta_0 = \pi/2$ or $3\pi/2$. The total field in the directions $\theta = \pi/2$ or $3\pi/2$ is found from (2.12).

The results for Figs.3.4a and 3.4c are found to be the same. Consider the two cases $r>r_0$ and $r<r_0$. If $r>r_0$ substitute in (2.12): R=r-d, S=r+d, $\cos(\frac{\theta-\theta_0}{2}) = 1$ $\cos(\frac{\theta+\theta_0}{2}) = 0$ to find

$$u_m = \frac{e^{ik(r-r_0)}}{\sqrt{kr}} - \frac{e^{-i\pi/4}}{\sqrt{\pi}} \frac{e^{ik(r-r_0)}}{\sqrt{kr}} F[\sqrt{2kr_0}] + \frac{1}{2} E(r+r_0) . \qquad (3.24)$$

If $r<r_0$, R=d-r, S=r+d, and

$$u_m = \frac{e^{ik(r_0-r)}}{\sqrt{kr}} - \frac{e^{-i\pi/4}}{\sqrt{\pi}} \frac{e^{ik(r_0-r)}}{\sqrt{kr_0}} F[\sqrt{2kr}] + \frac{1}{2} E(r+r_0) . \qquad (3.25)$$

If $kr_0 \gg 1$ and $kr \gg 1$, and the field from the incident line source is subtracted out, both (3.24) and (3.25) become

$$u_m = + \frac{1}{2} E(r+r_0) - \frac{e^{+i\pi/4}}{2\sqrt{2\pi}} E(r_0)\, E(r) . \qquad (3.26)$$

This field has two components: the field of the image of the original line source reduced in amplitude by half, plus a field diffracted by the edge. These two line sources originate at different points in space, one at the location of image of the original line source at distance r_0 from the edge, and the other at the edge.

The results for Figs.3.4b and 3.4d also are found to be the same. Consider the two cases $r>r_0$ and $r<r_0$. If $r>r_0$ substitute in (2.12): R=r+d, S=r-d, $\cos(\frac{\theta-\theta_0}{2}) = 0$, $\cos(\frac{\theta+\theta_0}{2}) = -1$ to find

$$u_m = \frac{1}{2} E(r+r_0) + \tau \frac{e^{-i\pi/4}}{\sqrt{\pi}} \frac{e^{ik(r-r_0)}}{\sqrt{kr}} F[\sqrt{2kr_0}] \quad . \tag{3.27}$$

If $r<r_0$, $R=r+d$, $S=d-r$, and

$$u_m = \frac{1}{2} E(r+r_0) + \tau \frac{e^{-i\pi/4}}{\sqrt{\pi}} \frac{e^{ik(r_0-r)}}{\sqrt{kr_0}} F[\sqrt{2kr}] \quad . \tag{3.28}$$

If $kr_0>>1$ and $kr>>1$ both (3.27) and (3.28) become

$$u_m = \frac{1}{2} E(r+r_0) + \tau \frac{e^{+i\pi/4}}{2\sqrt{2\pi}} E(r_0)E(r) \quad . \tag{3.29}$$

This field has two components: the original line source field reduced in amplitude by half, plus a field diffracted by the edge. These two line sources originate at different points in space, one at the location of the original line source at distance r_o from the edge, and the other at the edge.

In Fig.3.5a and 3.5b an isotropic line source $u_{m-1} = E(r)$ located at S, at a distance r_o from the edge is incident on that edge at an angle $\theta_0 = \pi/2$ or $3\pi/2$. This field is diffracted into a waveguide of width a at an angle $\Theta = \Theta_n$ or $2\pi - \theta_n$. From (3.18), the diffracted field u_m is, for $kr>>1$

$$u_m = \tau_1 C_n(r_0)E(r), \tag{3.30}$$

where $C_n(r_0)$ is given by (3.20). For $kr_o>>1$ (3.30) simplifies to

$$u_m = \tau_1 C_n E(r_0)E(r) \quad . \tag{3.31}$$

3.4 CALCULATION OF THE COUPLING COEFFICIENT

The fields represented by various combinations of two successive rays as presented above will now be used to calculate the coupling between two adjacent parallel-plate waveguides. The ray paths for these calculations, shown in Fig.3.2, represent all possible combinations of rays up to and including triple diffraction, and one combination with quadruple diffraction.

For each sequence of rays in Fig.3.2, the fields u_m associated with the mth ray can be calculated from the fields u_{m-1} of the (m-1) ray. The amplitude of the modes in the upper parasitic guide excited by last ray is calculated by comparison of (3.11), (3.12) and (3.2).

The doubly diffracted fields are represented by Figures 3.2b and c. In Fig. 3.2b the incident field , given by (3.9), is diffracted at the edge y=z=0. From (3.18), as observed at y=a,z=0, the diffracted field is a line source

$$u_1^b = \frac{1}{2q} C_N'(a) E(r) \tag{3.32}$$

located at the diffracting edge. This field is again diffracted at the edge y=a, z=0, and from (3.30) gives a line source

$$u_2^b = \frac{-\tau}{2q} C_N'(a) C_n(a) E(r) \tag{3.33}$$

located at the diffracting edge. In Fig. 3.2c the incident field , given by (3.10), is diffracted at the edge y=-d, z=0. From (3.18), as observed at y=z=0, the diffracted field

is a line source

$$u_1^C = \frac{-(-1)^N}{2q} C_N'(d)E(r) \tag{3.34}$$

located at the diffracting edge. This field is again diffracted at the edge y=z=0, and from (3.30) gives a line source

$$u_2^C = \frac{-(-1)^N}{2q} C_N'(d)C_n(d)E(r) \tag{3.35}$$

located at the diffracting edge. The total contribution to the coupling coefficient A_{Nn} from double diffraction is found by treating (3.33) and (3.35) as line sources and using (3.11), (3.12) and (3.2). Thus

$$A_{Nn}^{(2)} = \frac{-\sqrt{\pi}e^{i\pi/4}}{2\sqrt{2}k_n a} [(-1)^n C_N'(a)C_n(a) + (-1)^N C_N'(d)C_n(d)] . \tag{3.36}$$

The triply diffracted fields are represented by Figures 3.2d, e and f. In Fig. 3.2d the incident field , given by (3.10), is diffracted at the edge y=z=0. From (3.18), as observed at y=-d,z=0, the diffracted field is a line source

$$u_i^d = \frac{-\tau}{2q} C_N'(d)E(r) \tag{3.37}$$

located at the diffracting edge. This field is again diffracted at the edge y=-d, z=0, and from (3.26) the resultant field is

$$u_2^d = \frac{-1}{4q} C_N'(d)E(d+r) + \frac{\tau}{4q} \frac{e^{+i\pi/4}}{\sqrt{2\pi}} C_N'(d)E(d)E(r) . \tag{3.38}$$

u_2^d is made up of two line source fields, one centered at y=-2d, z=0, the other at y=-d, z=0. This field is again diffracted at the edge y=z=0, and from (3.30) gives two line

sources

$$u_3^d = \frac{-1}{4q} C_N'(d)C_n(2d)E(r) + \frac{\tau}{4q} \frac{e^{+i\pi/4}}{\sqrt{2\pi}} C_N'(d)C_n(d)E(d)E(r) \qquad (3.39)$$

located at the diffracting edge. In Fig.3.2e the incident field is given by (3.9) and the field u_i^e is given by (3.32). This field is again diffracted at y=a, z=0 and from (3.26) the resultant field is

$$u_2^e = \frac{\tau}{4q} C_N'(a)E(a+r) - \frac{1}{4q} \frac{e^{+i\pi/4}}{\sqrt{2\pi}} C_N'(a)E(a)E(r) . \qquad (3.40)$$

u_2^e is made up of two line source fields, one centered at y=2a, z=0, the other at y=a, z=0. This field is again diffracted at y=z=0 and from (3.30) the resultant field is

$$u_3^e = \frac{-1}{4q} C_N'(a)C_n(2a)E(r) + \frac{\tau}{4q} \frac{e^{+i\pi/4}}{\sqrt{2\pi}} C_N'(a)C_n(a)E(a)E(r) . \qquad (3.41)$$

In Fig.3.2f the incident field is given by (3.10) and the field u_1^f is given by (3.34). This field is again diffracted at y=z=0 and from (3.29) the resultant field is

$$u_2^f = \frac{-(-1)^N}{4q} C_N'(d)E(d+r) - \frac{\tau(-1)^N}{4q} \frac{e^{+i\pi/4}}{\sqrt{2\pi}} C_N'(d)E(d)E(r) . \qquad (3.42)$$

u_2^f is made up of two line source fields, one centered at y=-d, z=0, the other at y=z=0. This field is again diffracted at y=a, z=0 and from (3.30) the resultant field is

$$u_3^f = \frac{\tau(-1)^N}{4q} C_N'(d)C_n(d+a)E(r) + \frac{(-1)^N}{4q} \frac{e^{+i\pi/4}}{\sqrt{2\pi}} C_N'(d)C_n(a)E(d)E(r), \qquad (3.43)$$

The total contribution to the coupling coefficient A_{Nn} from triple diffraction is found by treating (3.39), (3.41) and (3.43) as line sources and using (3.11), (3.12) and (3.2). Thus

$$A_{Nn}^{(3)} = \frac{\varepsilon_n \sqrt{\pi} e^{+i\pi/4}}{4\sqrt{2k_n a}} [-C_N'(d)C_n(2d) - C_N'(a)C_n(2a) + (-1)^{N+n} C_N'(d)C_n(d+a)]$$

$$+ \frac{\varepsilon_n i\tau}{8k_n a} [C_N'(d)C_n(d)E(d) + C_N'(a)C_n(a)E(a) + (-1)^{N+n} C_N'(d)C_n(a)E(d)] . \tag{3.44}$$

A quadruply diffracted field is represented in Fig.3.2g. Here u_2^g is given by (3.38). Both line source fields in (3.38) are diffracted independently by the edge y=0, z=0, so that from (3.29), u_3^g consists of four line source fields centered at (-2d,0),(0,0),(-d,0) and (0,0) respectively. Note that one of these fields in u_3^g is $O(k^{-3/2})$ which is of the same order as the second term in the asymptotic expansion of the half plane diffraction solution. If terms of $O(k^{-3/2})$ are to be included in A_{Nn} then consistency requires that higher order terms be added to the Keller diffraction coefficient (2.9) and also in (3.23),(3.26),(3.29) and (3.31). Thus the $O(k^{-3/2})$ contributions due to quadruple and higher order diffraction are not expected to be meaningful within the ray-optical theory used here. It turns out that these $O(k^{-3/2})$ terms contribute very little numerically.

From (3.26) and (3.29) the field amplitudes are reduced by only half when diffracted along the shadow boundary. The number of terms arising from quadruple and higher order diffraction grows rapidly for each successively higher order, but only the $O(k^{-1/2})$ and $O(k^{-1})$ terms from higher order diffraction may be expected to contribute significantly to the value of the coupling coefficient.

Contributions to A_{Nn} from higher order diffraction of $O(k^{-1/2})$, calculated for the special case of TEM-TEM coupling ($\tau=1$, N=0, n=0), are given in Appendix B.

3.5 NUMERICAL RESULTS

Numerical values for the coupling coefficient A_{Nn} were calculated for various guide widths a and d for both TM and TE polarizations. Contributions to A_{Nn} due to single, double, and triple diffraction were included.

The amplitude and phase of A_{oo} ,the coupling from a TEM mode in the driven guide to a TEM mode in the parasitic guide, is shown in Fig.3.6, 3.7 and 3.8 for guide widths a=d, a=d/2 and a=2d respectively. Values of A_{11} (TE_1-TE_1 coupling) are plotted in Fig.3.9. Figs.3.10 and 3.11 show coupling from the TM and TE fundamental modes into higher order modes.

When both driven and parasitic guides are the same width the single diffraction term provides the average behaviour of the coupling coefficient. Adding the double diffraction terms reveals a fine structure with minima near the cutoff widths of the various modes. The triple diffraction terms provide some correction to this fine structure ,especially near the cutoff widths, but do not alter the basic shape of the curve.

When in the TEM case the parasitic guide is half the width of the driven guide (a=d/2) (Fig.3.7) the minima near

the mode transition widths are reduced in depth. When the parasitic guide is double the width of the driven guide (a=2d) (Fig.3.8) minima appear at the mode transition widths for the parasitic guide at a=n or d=n/2 (n=1,2,3...). In both cases adding triple diffraction terms provides a more substantial correction to the double diffraction result as compared to the case where a=d.

Exact results for the coupling coefficient $A_{N\Lambda}$ are not available for comparison. However, ray-optical expressions for the reflection coefficient $R_{N\Lambda}$ for a single guide [50] with the low frequency correction [18] show good agreement with the exact result for guide widths as small as 0.1 wavelengths for TEM-TEM coupling and 0.6 wavelengths for TE_1-TE_1 coupling. The values of $A_{N\Lambda}$ presented here may be expected to have accuracy comparable to [50] and [18] because the same method of calculation has been used.

The TEM and TE_1 coupling coefficients for low frequencies near mode cutoff calculated using the asymptotic approximation (3.22) are compared with the non-asymptotic results obtained using (3.18) in Figs.3.12 and 3.13. The asymptotic results begin to deviate significantly at guide widths less than 0.3λ in the TEM case and 0.7λ in the TE_1 case. This appears to be consistent with the results of [18] where a similar comparison was made for the reflection coefficients. When the asymptotic approximation (3.31) is used also, the results deviate even more.

Higher order terms of $O(k^{-1/2})$ and $O(k^{-1})$ were calculated

but they were found to give only small contributions. It has also been noted that in the calculation of scattering by a single open-ended parallel plate waveguide the quadruple and higher order diffracted fields are likely to be in error, since they do not agree with the asymptotic expansion of the exact solution [9].

Note that all the curves of coupling versus guide width have minima at widths slightly below the mode transition widths ($n\lambda$ for TM modes and $(2n-1)\lambda/2$ for TE modes). The depth of these minima (nulls) increases and the null moves closer to the mode transition width as higher orders of diffraction are taken into account (Figs.3.6 and 3.9). This behaviour is similar to that found by Yee et al. [50] for the reflection coefficient of a single waveguide. It might be surmised that taking still more terms would eventually give a sharp null exactly at the mode transition width.

It turns out that the known exact solution for the reflection coefficient of a single waveguide [45] has sharp cusps with discontinuous first derivative at the mode transition widths. The ray-optical solution [50] however does not have any cusps, even when very large numbers of diffraction terms are taken into account. Similarly in the coupling case, no cusps are found in the ray-optical solution, even with many terms (see Appendix B). An exact solution for the coupling case is not available for comparison, however it is reasonable to assume that it also will contain cusps. It appears that the ray-optical method used here is unable to provide an accurate solution near the

mode transition widths where cusps are expected, but is acceptable elsewhere.

Some consideration has been given to applying the uniform asymptotic theory (UAT) [1] to this problem. In the case of reflection from a single open-ended parallel-plate waveguide the final expression for the reflection coefficient is similar to that obtained by this ray-optical method [3, eqns.(35),(36)] [4, eqns.(8.7),(8.8)] for terms of $O(k^{-1/2})$ and $O(k^{-1})$. However this series solution is slowly convergent; up to 50 terms are required to provide essentially full agreement with the exact values near the mode transition widths for the guides (though this convergence may be accelerated). Each term in the series represents interaction between edges of the guide and with two adjacent guides there is a rapid growth in the number of interactions that have to be included. Since a general expression for all terms of $O(k^{-1})$ was not found even with the simpler ray-optical method (see Appendix B), a UAT solution for $A_{N\Lambda}$ providing better numerical accuracy would appear to be very difficult to find. It is, however, only at the mode transition widths that the UAT may be expected to provide substantial improvement. Only marginal, if any, improvement occurs near cutoff of the fundamental mode [3, Fig. 2] [4, Fig.2]

No other calculations of the coupling between adjacent guides in isolation has been found; however it is interesting to compare the coupling coefficients obtained here with those for adjacent guides in the presence of other

guides. Montgomery and Chang [38] calculated the coupling between adjacent guides for the closed region geometry in Fig.1.18 using function theoretic techniques. Lee [29] found the coupling coefficients for the structure of Fig. 1.15 using Weiner-Hopf techniques. The structures are sufficiently similar to that under consideration that a reasonable comparison might be expected.

The results for each case, listed in Table I , are very similar. The coupling coefficient in the presence of other guides is quite insensitive to which pair of adjacent guides in the array is considered. It is thus not unexpected that the coupling coefficient derived here in the absence of other guides agrees quite well with these other results. The ray-optical coupling gives the best agreement when the asymptotic form of the Fresnel integral scattering functions (3.23),(3.26), (3.29) and (3.31) are used.

3.6 SUMMARY

Coupling between adjacent parallel plate waveguides has been calculated by first tracing sequences of rays from the driven guide to the parasitic guide and then adding the contributions to the amplitude of the mode excited in the parasitic guide from the final ray in each sequence. The number of different sequences of rays grows rapidly as the number of rays in each sequence increases. However, useful results are obtained even when only three such sequences of rays (single and double diffraction) are considered. An

exact solution for this geometry is not available for comparison, however, the coupling coefficients obtained here agree remarkably well with those obtained by other methods when the two guides are surrounded by other guides or halfplanes. This agreement indicates a general lack of sensitivity of the coupling coefficients to the nature of the surrounding structure, and gives confidence that these results are applicable in the context of the complete waveguide array.

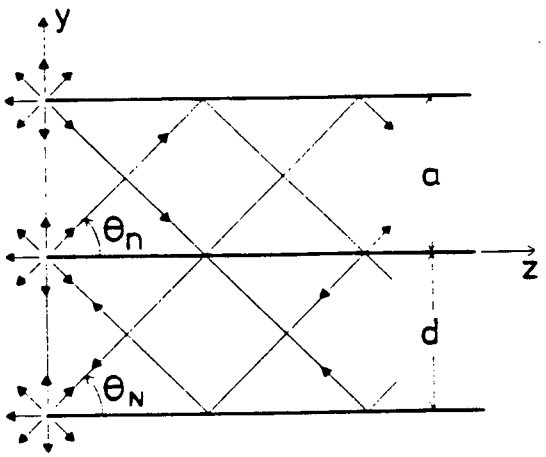

Fig. 3.1
ray paths of mode fields in two
adjacent parallel plate waveguides

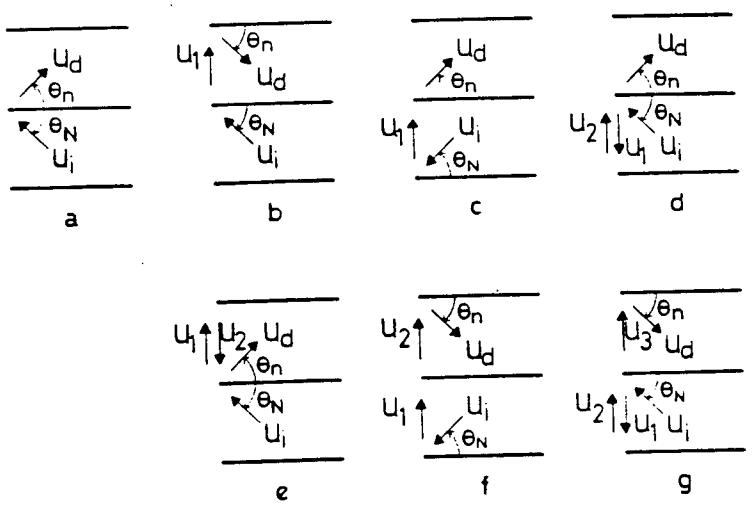

Fig. 3.2
ray paths from the driven guide
to the parasitic guide

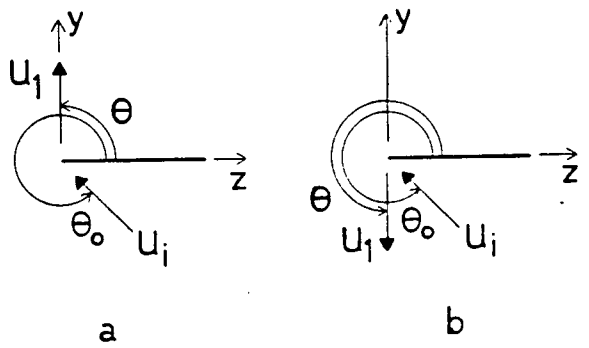

Fig. 3.3
two successive rays in a ray path
from the driven guide to a guide aperture

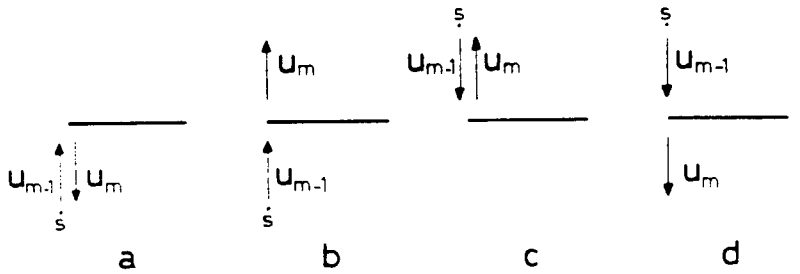

Fig. 3.4
two successive rays in a ray path, both
rays in a guide aperture

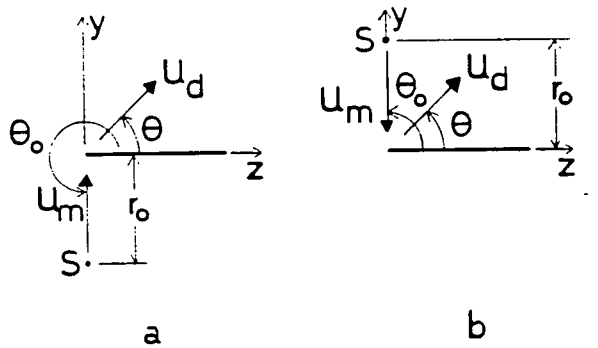

Fig. 3.5
two successive rays in a ray path from
the guide aperture to the parasitic guide

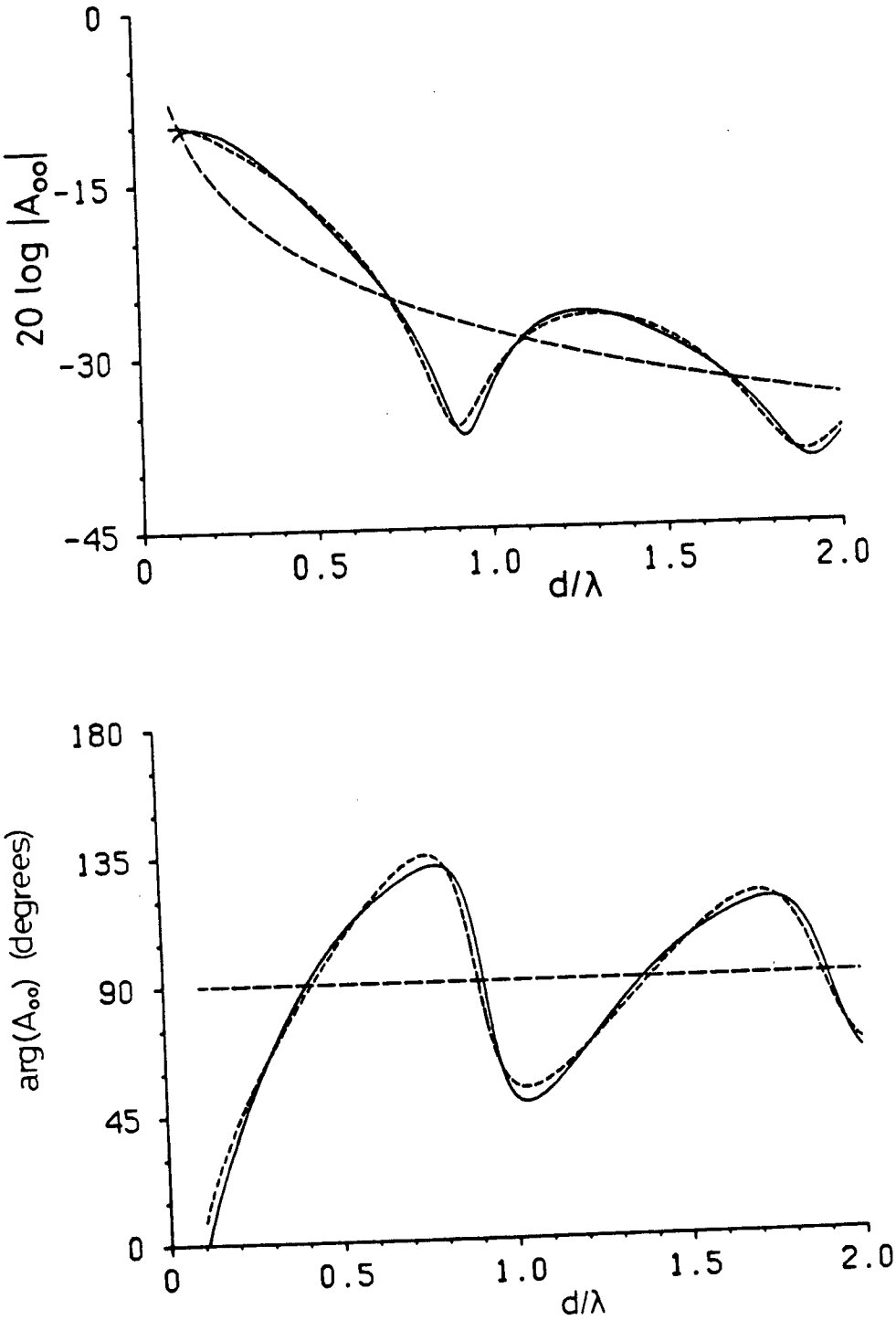

Fig. 3.6 TEM-TEM coupling between adjacent waveguides (a=d).

—— single diffraction
---- single and double diffraction
——— single and double and triple diffraction

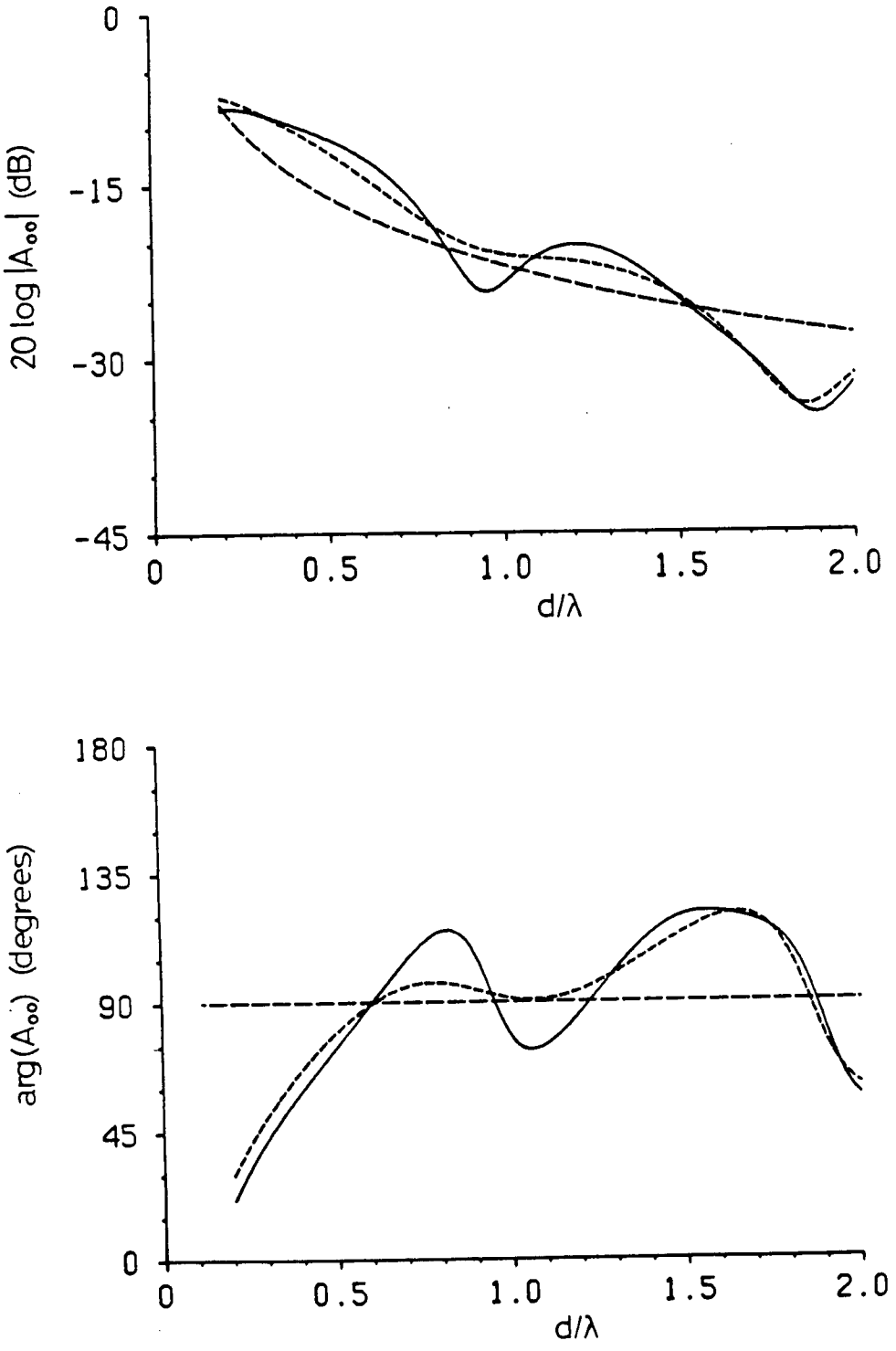

Fig. 3.7 TEM-TEM coupling between adjacent waveguides (a=d/2).

— — single diffraction
---- single and double diffraction
—— single and double and triple diffraction

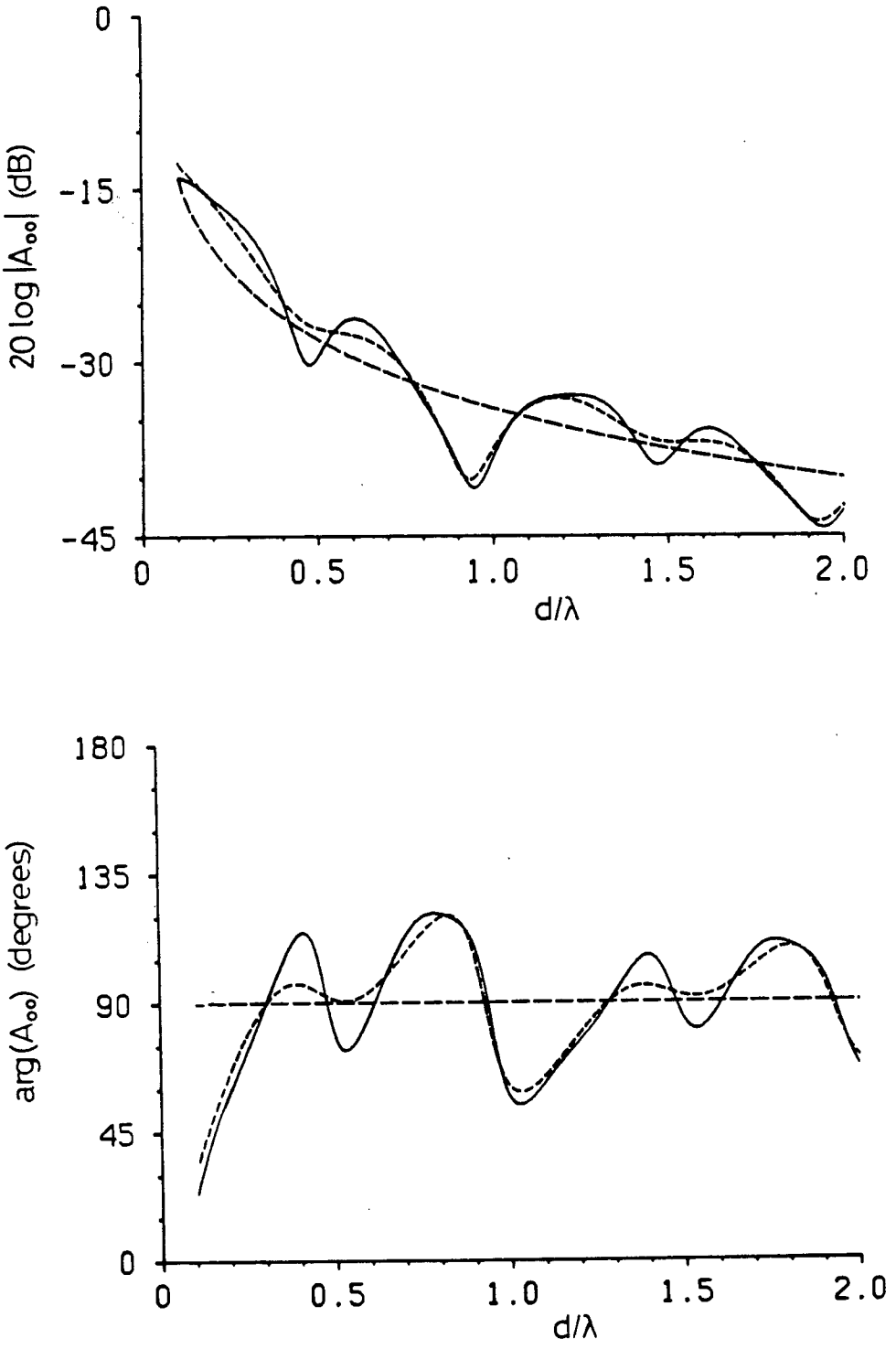

Fig. 3.8 TEM-TEM coupling between adjacent waveguides (a=2d).

— — single diffraction
- - - - single and double diffraction
—— single and double and triple diffraction

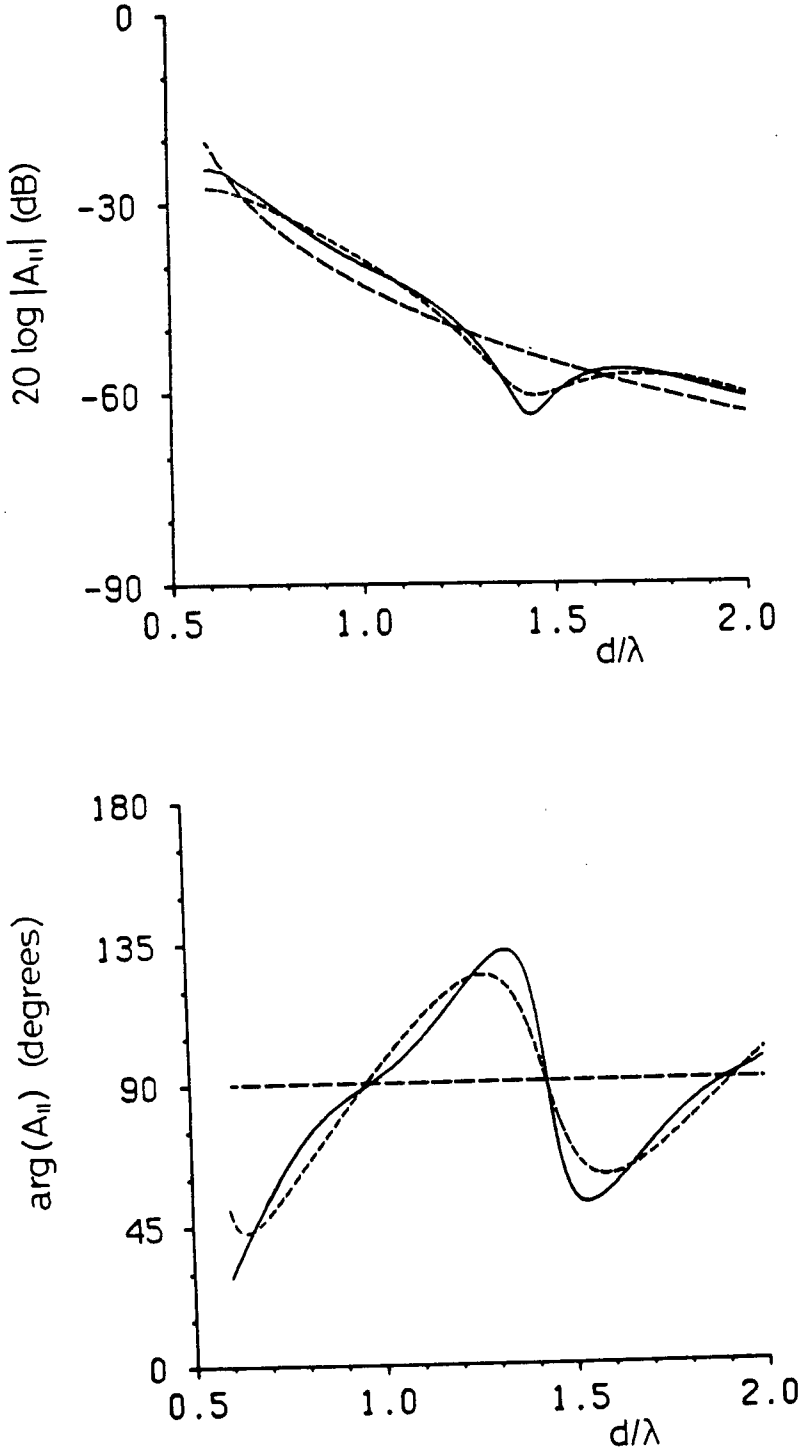

Fig. 3.9 TE_1-TE_1 coupling between adjacent waveguides (a=d).
— — single diffraction
---- single and double diffraction
—— single and double and triple diffraction

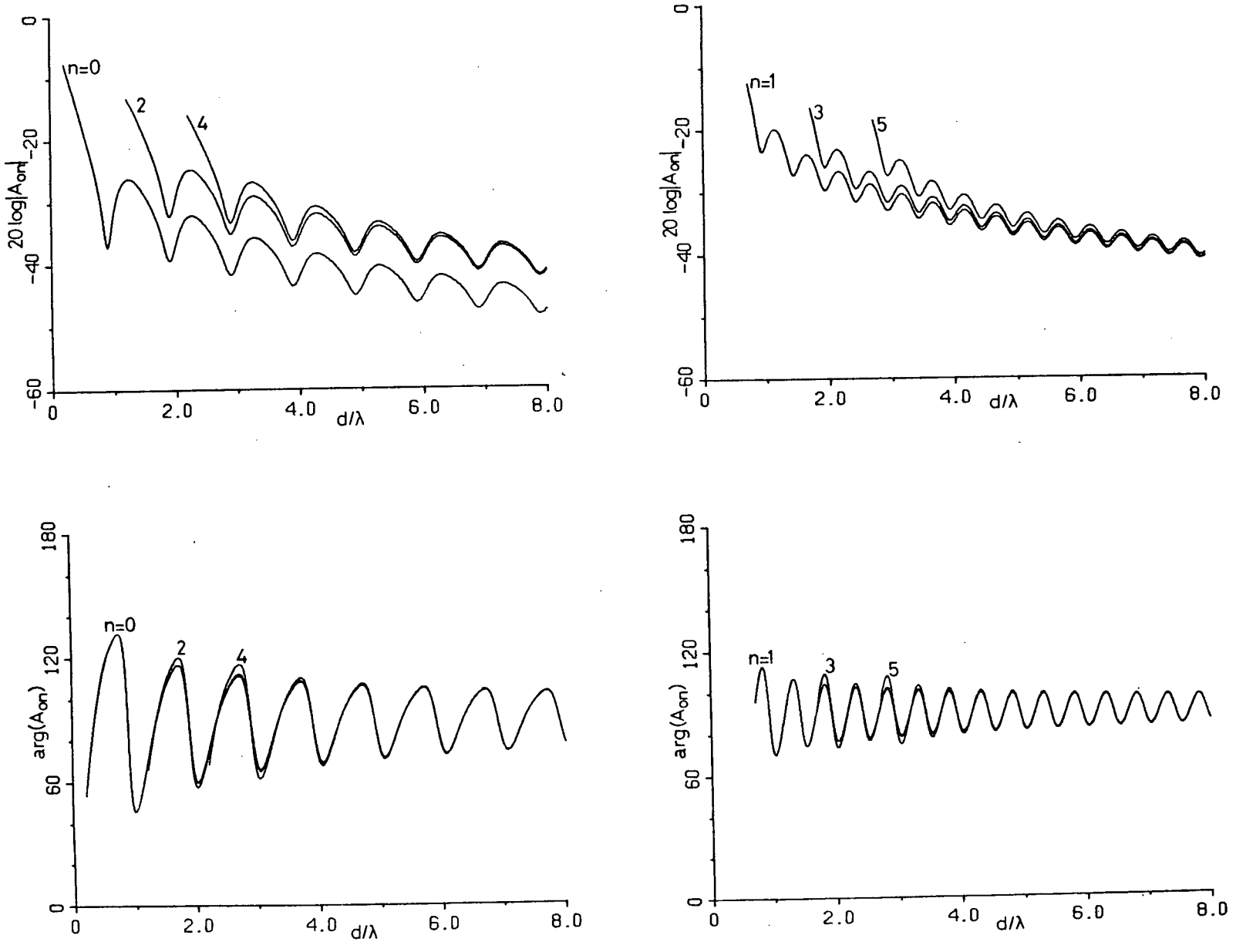

Fig. 3.10 TEM-TM_n coupling coefficient (a=d, N=0).

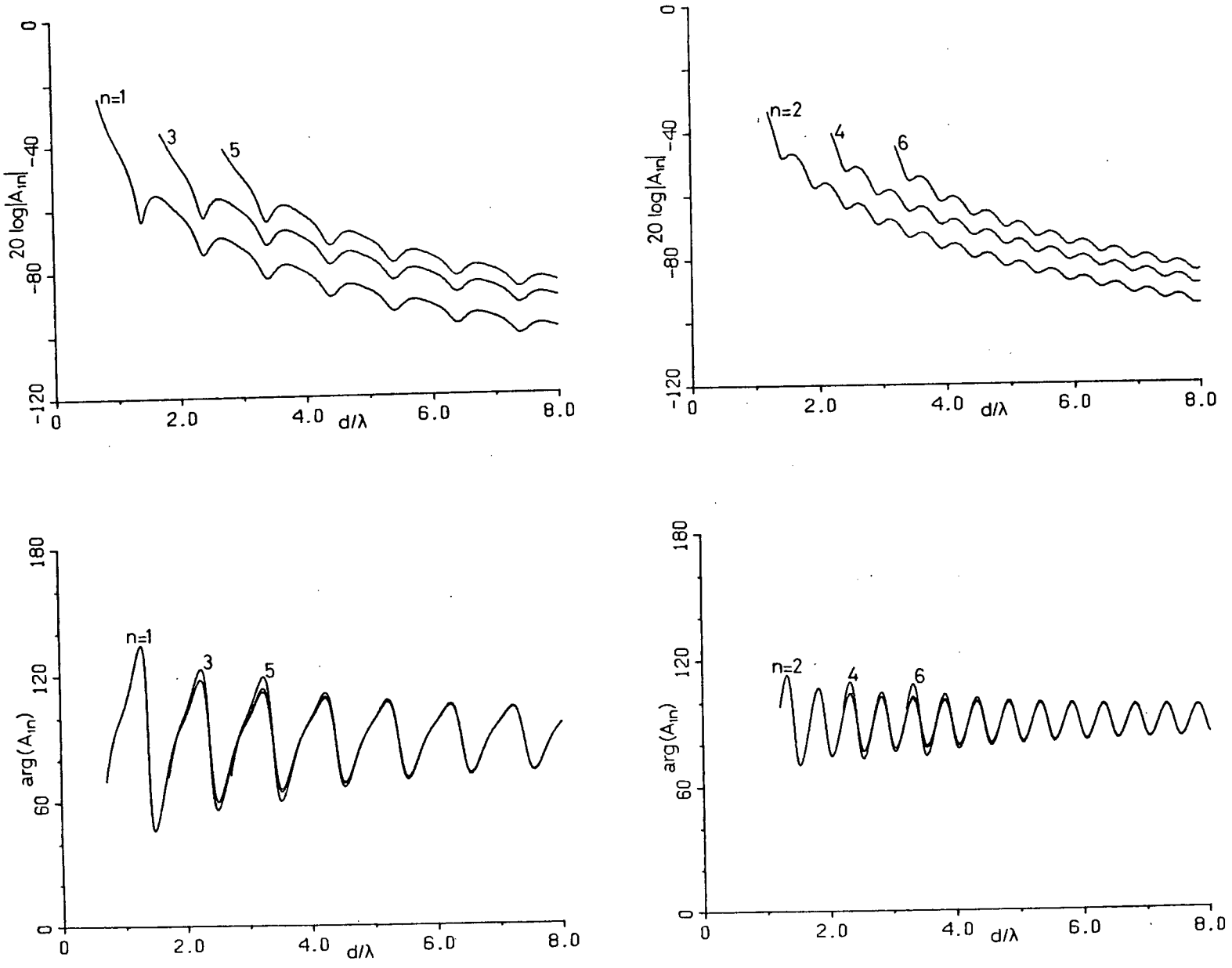

Fig. 3.11 TE_1-TE_n coupling coefficient (a=d, N=1).

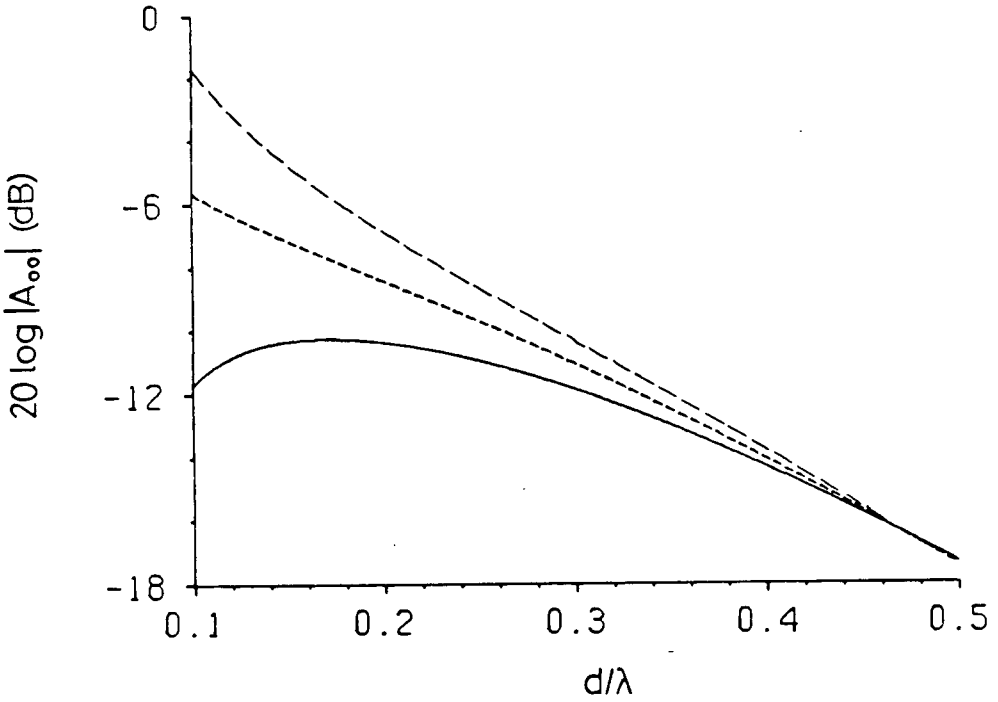

Fig. 3.12 TEM-TEM coupling at low frequencies.

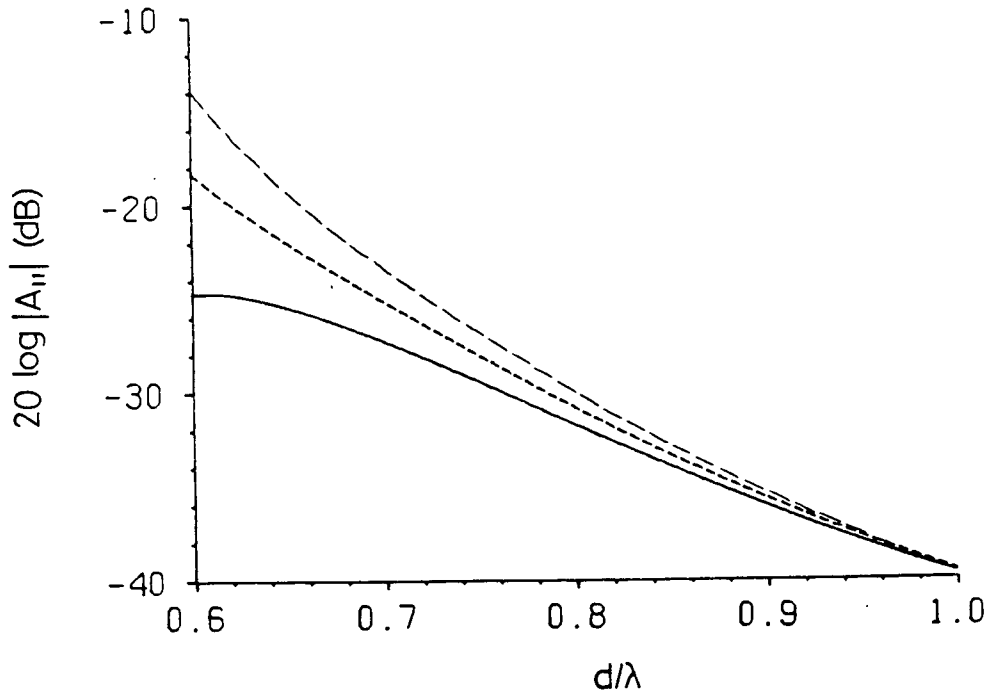

Fig. 3.13 TE_1-TE_1 coupling at low frequencies.

——— non-asymptotic form

---- asymptotic form (3.18)

— — asymptotic form (3.18) and (3.31)

TABLE I

Coupling Coefficients $A_\infty(d,a)$
Between Adjacent Parallel Plate Waveguides
$a = d = 0.45\ \lambda$

# excited →# coupled into	Montgomery [38]		Lee [29]		this theory using the asymptotic form (3.22)		this theory using the non-asymptotic form (3.17)	
	20 log|A| (dB)	∠A (degrees)	20 log|A| (dB)	∠A (degrees)	20 log|A| (dB)	∠A (degrees)	20 log|A| (dB)	∠A (degrees)
1→2 & 2→1	-15.32	+105.2	-15.76	+102.3				
3→2 & 3→4	-15.57	+107.8	-15.78	+106.8	-15.74	+102.3	-15.80	+97.7
2→3	-15.33	+105.3	-15.78	+106.8				

Chapter 4

COUPLING BETWEEN SEPARATED GUIDES

4.1 CALCULATION OF THE COUPLING COEFFICIENT

The coupling between two separated guides (Fig.4.1) will be found in a manner similar to that for adjacent guides. First all possible ray paths up to and including quadruple diffraction are determined by inspection (Fig.4.2). The fields represented by each ray is calculated from the fields of the ray preceding it using the expressions derived in Chapter 2. In this way the fields represented by all rays in Fig.4.2 are found and hence the coupling coefficient. The results will be compared to those found previously by Dybdal et al. [17] using edge diffraction and a reciprocity argument and Montgomery and Chang [38] using modified residue calculus.

Consider three adjacent semi-infinite parallel-plate waveguides consisting of four perfectly conducting half-planes in $z>0$ at $y=-d-b$, $y=-d$, $y=0$ and $y=a$, so that the widths of the three guides are b, d and a respectively (Fig.4.1). We wish to determine the field coupled from the transmitting guide $-d-b<y<-d$, $z>0$ into the parasitic guide $0<y<a$, $z>0$. As in Chapter 3 the incident mode in the driven guide is decomposed into two plane waves, with value given by (3.9) at the edge $y=-d$, $z=0$ and by (3.10) at $y=-d-b$, $z=0$. These plane waves are incident on the half-plane edges at $\theta_0 = 2\pi - \theta_N$ and $\theta_0 = \theta_N$ respectively where θ_N is given by (3.6).

The doubly diffracted fields are represented by Fig.4.2a. The incident field , given by (3.9) is diffracted at the edge y=-d, z=0. From (3.18) as observed at y=z=0 the diffracted field is a line source

$$u_1^a = \frac{1}{2q} C_N'(d)E(r) \tag{4.1}$$

located at the diffracting edge. This field is again diffracted at the edge y=z=0 and from (3.30) gives a line source

$$u_2^a = \frac{1}{2q} C_N'(d)C_n(d)E(r) . \tag{4.2}$$

The coupling coefficient from double diffraction is found by treating (4.2) as a line source and using (3.11), (3.12) and (3.2). Thus

$$A_{Nn}^{(2)} = \frac{\varepsilon_n \sqrt{\pi}\, e^{+i\pi/4}}{2\sqrt{2}\, k_n a} C_N'(d)C_n(d) . \tag{4.3}$$

The triply diffracted fields are represented by Figs.4.2b and c. In Fig.4.2b the incident field u_i is given by (3.9) and the singly diffracted field u_1^b is given by (4.1). This field is again diffracted at the edge y=z=0 and from (3.29) the resultant field is

$$u_2^b = \frac{1}{4q} C_N'(d)E(d+r) + \frac{\tau}{4q} \frac{e^{+i\pi/4}}{\sqrt{2\pi}} C_N'(d)E(d)E(r) . \tag{4.4}$$

u_2^b is made up of two line sources, one centred at y=-d, z=0, the other at y=z=0. This field is again diffracted at y=a, z=0 and from (3.30) the resultant field is

$$u_3^b = \frac{-\tau}{4q} C'_N(d) C_n(d+a) E(r) - \frac{1}{4q} \frac{e^{+i\pi/4}}{\sqrt{2\pi}} C'_N(d) C_n(a) E(d) E(r) . \quad (4.5)$$

In Fig.4.2c the incident field u_i is given by (3.10). From (3.18), as observed at y=-d, z=0, the diffracted field is a line source

$$u_1^c = \frac{-(-1)^N}{2q} C'_N(b) E(r) \quad (4.6)$$

located at the diffracting edge. This field is again diffracted at the edge y=-d, z=0 and from (3.29) the resultant field u_2^c is

$$u_2^c = \frac{-(-1)^N}{4q} C'_N(b) E(b+r) - \tau \frac{(-1)^N}{4q} \frac{e^{+i\pi/4}}{\sqrt{2\pi}} C'_N(b) E(b) E(r) . \quad (4.7)$$

u_2^c is made up of two line sources, one centred at y=-d-b, z=0, the other at y=-d, z=0. This field is again diffracted at y=z=0 and from (3.30) the resultant field is

$$u_3^c = \frac{-(-1)^N}{4q} C'_N(b) C_n(b+d) E(r) - \tau \frac{(-1)^N}{4q} \frac{e^{+i\pi/4}}{\sqrt{2\pi}} C'_N(b) C_n(d) E(b) E(r) . \quad (4.8)$$

The total contribution to A_{Nn} from triple diffraction is found by treating (4.5) and (4.8) as line sources and using (3.11), (3.12) and (3.2). Thus

$$A_{Nn}^{(3)} = \frac{\varepsilon_n \sqrt{\pi}\, e^{+i\pi/4}}{4\sqrt{2}\, k_n a} [-(-1)^n C'_N(d) C_n(d+a) - (-1)^N C'_N(b) C_n(b+d)]$$

$$+ \frac{\varepsilon_n i \tau}{8 k_n a} [-(-1)^n C'_N(d) C_n(a) E(d) - (-1)^N C'_N(b) C_n(d) E(b)] . \quad (4.9)$$

The quadruply diffracted fields are represented in Figs.4.2d, e, f and g. In Fig.4.2d u_i is given by (3.10), u_1^d is given by (4.6) and u_2^d is given by (4.7). The field u_2^d is

again diffracted at y=z=0 and from (3.29) the resultant field is

$$u_3^d = \frac{-(-1)^N}{8q} C_N'(b)E(b+d+r) - \tau \frac{(-1)^N}{8q} \frac{e^{+i\pi/4}}{\sqrt{2\pi}} C_N'(b)E(b+d)E(r)$$

$$- \tau \frac{(-1)^N}{8q} \frac{e^{+i\pi/4}}{\sqrt{2\pi}} C_N'(b)E(b)E(d+r) . \qquad (4.10)$$

Note that the term of $O(k^{-3/2})$ has been deleted for the reasons mentioned in Chapter 3. u_3^d is made up of three line sources at y=-d-b, z=0; y=z=0; and y=-d, z=0 respectively. This field u_3^d is again diffracted at y=a, z=0 and from (3.30) the resultant field is

$$u_4^d = (-1)^N \frac{\tau}{8q} C_N'(b)C_n(b+d+a)E(r) + \frac{(-1)^N}{8q} \frac{e^{+i\pi/4}}{\sqrt{2\pi}} C_N'(b)E(b+d)C_n(a)E(r)$$

$$+ \frac{(-1)^N}{8q} \frac{e^{+i\pi/4}}{\sqrt{2\pi}} C_N'(b)E(b)C_n(d+a)E(r) . \qquad (4.11)$$

u_4^d consists of three line sources all centred at y=a, z=0. The contribution to A_{Nn} from this quadruply diffracted field is found by treating (4.11) as line sources and using (3.11), (3.12) and (3.2). Thus

$$A_{Nn}'^{(4)} = \frac{\varepsilon_n \sqrt{\pi}\, e^{+i\pi/4}}{8\sqrt{2}\, k_n a} [(-1)^{N+n} C_N'(b)C_n(b+d+a)]$$

$$+ \frac{\varepsilon_n i\tau(-1)^{N+n}}{16 k_n a} [C_N'(b)E(b+d)C_n(a) + C_N'(b)E(b)C_n(d+a)]. \qquad (4.12)$$

In Fig.4.2e u_i is given by (3.9) and u_1^e is given by (4.1). This field u_1^e is again diffracted at the edge y=z=0, and from (3.26) the resultant field is

$$u_2^e = \frac{\tau}{4q} C_N'(d)E(d+r) - \frac{1}{4q} \frac{e^{+i\pi/4}}{\sqrt{2\pi}} C_N'(d)E(d)E(r) . \qquad (4.13)$$

u_2^e is made up of two line sources, one at y=d, z=0, the

other at y=z=0. This field u_2^e is again diffracted at the edge y=-d, z=0, and from (3.26) the resultant field is

$$u_3^e = \frac{1}{8q} C_N'(d)E(2d+r) - \tau \frac{e^{+i\pi/4}}{\sqrt{2\pi}} C_N'(d)E(2d)E(r)$$

$$- \tau \frac{e^{+i\pi/4}}{\sqrt{2\pi}} C_N'(d)E(d)E(d+r) . \qquad (4.14)$$

u_3^e is made up of three line sources at y=-3d, z=0, y=-d, z=0, and y=-2d, z=0 respectively. Again the term of $O(k^{-3/2})$ has been deleted. This field u_3^e is again diffracted at the edge y=z=0, and from (3.30), treating each line source separately, the resultant field is

$$u_4^e = \frac{1}{8q} C_N'(d)C_n(3d)E(r) - \frac{\tau}{8q} \frac{e^{+i\pi/4}}{\sqrt{2\pi}} C_N'(d)E(2d)C_n(d)E(r)$$

$$- \frac{\tau}{8q} \frac{e^{+i\pi/4}}{\sqrt{2\pi}} C_N'(d)E(d)C_n(2d)E(r) . \qquad (4.15)$$

In Fig.4.2f the incident field given by (3.9) is diffracted at the edge y=-d, z=0. From (3.18), as observed at y=-d-b, z=0, the diffracted field is a line source

$$u_1^f = -\frac{\tau}{2q} C_N'(b)E(r) \qquad (4.16)$$

located at the diffracting edge. This field is again diffracted at the edge y=-d-b, z=0, and from (3.26) the resultant field is

$$u_2^f = -\frac{1}{4q} C_N'(b)E(b+r) + \frac{\tau}{4q} \frac{e^{+i\pi/4}}{\sqrt{2\pi}} C_N'(b)E(b)E(r) . \qquad (4.17)$$

u_2^f is made up of two line sources, one at y=-2b-d, z=0, the other at y=-d-b, z=0. This field is again diffracted at the edge y=-d, z=0, and from (3.29) the resultant field is

$$u_3^f = \frac{-1}{8q} C_N'(b)E(2b+r) - \frac{\tau}{8q}\frac{e^{+i\pi/4}}{\sqrt{2\pi}} C_N'(b)E(2b)E(r)$$

$$+ \frac{\tau}{8q}\frac{e^{+i\pi/4}}{\sqrt{2\pi}} C_N'(b)E(b)E(b+r) . \qquad (4.18)$$

u_3^f is made up of three line sources at y=-2b-d, z=0, y=-d, z=0, and y=-d-b, z=0 respectively. This field u_3^f is again diffracted at the edge y=z=0, and from (3.30), treating each line source separately, the resultant field is

$$u_4^f = \frac{1}{8q} C_N'(b)C_n(2b+d)E(r) - \frac{\tau}{8q}\frac{e^{+i\pi/4}}{\sqrt{2\pi}} C_N'(b)E(2b)C_n(d)E(r)$$

$$+ \frac{\tau}{8q}\frac{e^{+i\pi/4}}{\sqrt{2\pi}} C_N'(b)E(b)C_n(b+d)E(r) . \qquad (4.19)$$

In Fig.4.2g the incident field is given by (3.9), u_1^g is given by (4.1), and u_2^g is given by (4.4). This field u_2^g is again diffracted at the edge y=a, z=0, and from (3.26) the resultant field is

$$u_3^g = \frac{\tau}{8q} C_N'(d)E(d+a+r) - \frac{1}{8q}\frac{e^{+i\pi/4}}{\sqrt{2\pi}} C_N'(d)E(d+a)E(r)$$

$$+ \frac{1}{8q}\frac{e^{+i\pi/4}}{\sqrt{2\pi}} C_N'(d)E(d)E(a+r) . \qquad (4.20)$$

u_3^g is made up of three line sources at y=2a+d, z=0, y=a, z=0, and y=2a, z=0 respectively. This field u_3^g is again diffracted at the edge y=z=0, and from (3.30), treating each line source separately, the resultant field is

$$u_4^g = -\frac{1}{8q} C_N'(d)C_n(d+2a)E(r) + \frac{\tau}{8q}\frac{e^{+i\pi/4}}{\sqrt{2\pi}} C_N'(d)E(d+a)C_n(a)E(r)$$

$$- \frac{\tau}{8q}\frac{e^{+i\pi/4}}{\sqrt{2\pi}} C_N'(d)E(d)C_n(2a)E(r) , \qquad (4.21)$$

The contributions to A_{Nn} from these quadruply

diffracted fields is found by treating (4.15), (4.19) and (4.21) as line sources and using (3.11), (3.12) and (3.2). Thus

$$A_{Nn}^{''(4)} = \frac{\varepsilon_n \sqrt{\pi}\, e^{+i\pi/4}}{8\sqrt{2}\, k_n a} [C_N'(d) C_n(3d) - C_N'(b) C_n(2b+d) - C_N'(d) C_n(d+2a)]$$

$$+ \frac{\varepsilon_n i\tau}{16 k_n a} [- C_N'(d) E(2d) C_n(d) - C_N'(d) E(d) C_n(2d) - C_N'(b) E(2b) C_n(d) + C_N'(b) E(b) C_n(b+d) + C_N'(d) E(d+a) C_n(a) - C_N'(d) E(d) C_n(2a)] \quad (4.22)$$

The total contribution to A_{Nn} from quadruple diffraction is

$$A_{Nn}^{(4)} = A_{Nn}^{'(4)} + A_{Nn}^{''(4)} \quad (4.23)$$

The sum of (4.3), (4.9), (4.12) and (4.22) is the coupling coefficient A_{Nn} between separated waveguides up to and including quadruple diffraction.

4.2 ANALYTICAL AND NUMERICAL RESULTS

The coupling coefficients are calculated for various guide widths and separations and compared with the results of others. The expressions (4.3), (4.9), (4.12) and (4.22) were compared with those of Dybdal et al. [17]. Their results were obtained by considering the transmitting guide as a line source incident on the receiving parasitic guide. A reciprocity argument was used to obtain the response of the guide to the line source.

It turns out that Dybdal's method gives virtually identical results to those derived here, if only the ray paths in Figs.4.2a, b, c and d are considered, i.e. in the TEM case

$$\frac{I}{I_0} \sim A_{00}^{(2)} + A_{00}^{(3)} + A_{00}^{'(4)} \tag{4.24}$$

and in the TE_1 case

$$\frac{V}{V_0} \sim A_{11}^{(2)} + A_{11}^{(3)} + A_{11}^{'(4)} \tag{4.25}$$

Dybdal's expressions neglect the interaction between guides shown in the ray paths of Figs.4.2e,f, and g.

The numerical values for the coupling coefficients A_{oo} and A_{11} were calculated as a function of the separation between the guides, and compared with the results of Dybdal et al.[17], Montgomery and Chang [38] and Lee [29].

The amplitude of A_{oo} for TEM coupling is shown in Fig.4.3 and 4.4, and for TE_1 coupling in Fig.4.5 for guide widths of 0.338λ and 0.761λ and separation between guides ranging from 0.4λ to 2.0λ. If interaction between the guides is neglected, the coupling decreases monotonically as the separation between guides is increased. Addition of the interaction terms neglected by Dybdal show an oscillation with period $\lambda/2$, which becomes more pronounced as more interaction terms are added.

The limitations of this ray-optical method are illustrated in Fig.4.3 in which Montgomery's results are compared to those obtained here. Montgomery's results in the TEM case have cusps at guide separations of $n\lambda/2, (n=1,2,...)$,

but the ray-optical results obtained here show only approximate agreement. Higher order diffraction terms add an oscillation to the curve in phase with the cusps. However, the cusps were not obtained with this ray-optical theory, even with a large number of terms.

While the addition of the interaction terms gives a qualitative agreement with Montgomery's results, the quantitative agreement is less for some values of guide separation. These interaction terms are all quadruple and higher order diffraction and cannot be calculated accurately along the shadow boundary with this ray-optical theory. Assuming that Montgomery's results are accurate, the ray-optical theory underestimates the coupling by about 0 - 2 dB. This is a measure of the error which may be expected in the calculation of the fields along the shadow boundary.

The method used here predicts that the singly diffracted field along the shadow boundary will be one-half the incident field and the doubly diffracted field will be one-quarter the incident field (equations (3.26) or (3.29) applied twice). These results are incorrect in view of the analysis of Lee and Boersma [32] and Lee et al. [33]. Lee and Boersma [32] find the fields on the shadow boundary of two parallel plates for two cases: a plane wave normally incident on two non-staggered parallel plates (Fig.4.11) and a line source incident on two staggered parallel plates (Fig.2.5). In both of these two cases the doubly diffracted field is somewhat greater than one-quarter of the incident field. Even though Lee and Boersma do not consider the

specific case which arises here (line source incident on two parallel plates, Fig.2.3 or 4.2d), their results ([32], Fig.(4)) indicate that the analysis used here underestimates the fields near the shadow boundary. Their results also indicate that enhanced coupling will occur at $d=n\lambda/2$ ($n=1,2,...$), which is consistent with the results of Montgomery and Chang [38]. The application of the method of [32] to the problem at hand is not trivial, and may be intractable for the three half-plane case (Fig.4.12) which arises in later chapters.

The coupling is also calculated for the case that all three guides are of the same width and this width is varied from 0.4λ to 2.0λ (Figs.4.6-4.10). The results are similar to those for two guides of the same width (Fig.3.6-3.9), but with some important differences:

1- the addition of higher order diffraction terms makes more difference to the shape of the curve especially at the mode transition widths.

2- the minima are exactly at the mode transition widths and much deeper when up to five times diffraction is taken into account. However, if interaction between the guides is neglected these minima are quite shallow and broad.

These results for the case $a=d=b=0.45\lambda$ are compared with those of Montgomery et al. [38] and Lee [29] in Table II. Both these authors considered five adjacent waveguides and calculated coupling between each pair of separated guides. Montgomery's array was in free space (Fig.1.17) and Lee's array was embedded in a simulated groundplane

(Fig.1.15).

As in the case for adjacent guides the coupling coefficients are insensitive to which pair of separated guides is considered. The coupling derived here in the absence of other guides agrees quite well with these results in the presence of other guides.

This similarity of the coupling between two separated guides in isolation, in the presence of other guides and embedded in a simulated groundplane indicates a general lack of sensitivity of the coupling coefficients to the nature of the surrounding structure.

4.3 SUMMARY

The coupling between two separated parallel plate waveguides has been calculated by the same method used for adjacent waveguides. To obtain an approximately correct shape of the curve of coupling versus guide width it was necessary to include terms up to at least quadruple diffraction, as compared to only double diffraction for adjacent guides.

The coupling coefficients obtained here agree very well with those calculated by Dybdal et al.[17] if interaction between the guides is neglected. Including those interactions shows only approximate agreement with the results of Montgomery and Chang [38]. Thus the inaccuracy of the ray-optical method when there are four edges along a shadow boundary is apparent. However, the results obtained

here are similar to those for guides in the presence of other guides or a groundplane. Thus the coupling coefficients between separated guides may be used in the calculations involving the array of Fig.1.3 without considering the details of the other guides in the array.

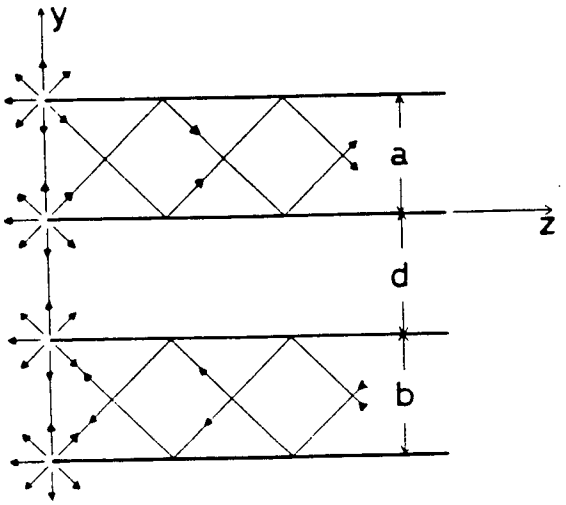

Fig 4.1
ray paths of mode fields in two
separated parallel plate waveguides

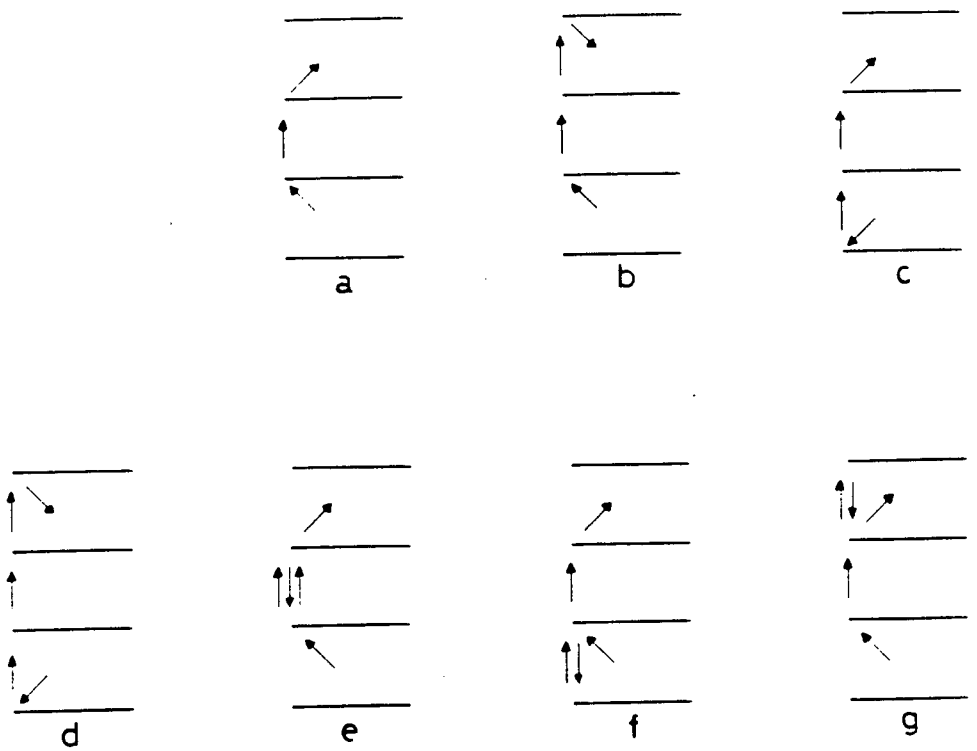

Fig. 4.2
ray path from the driven guide
to the parasitic guide

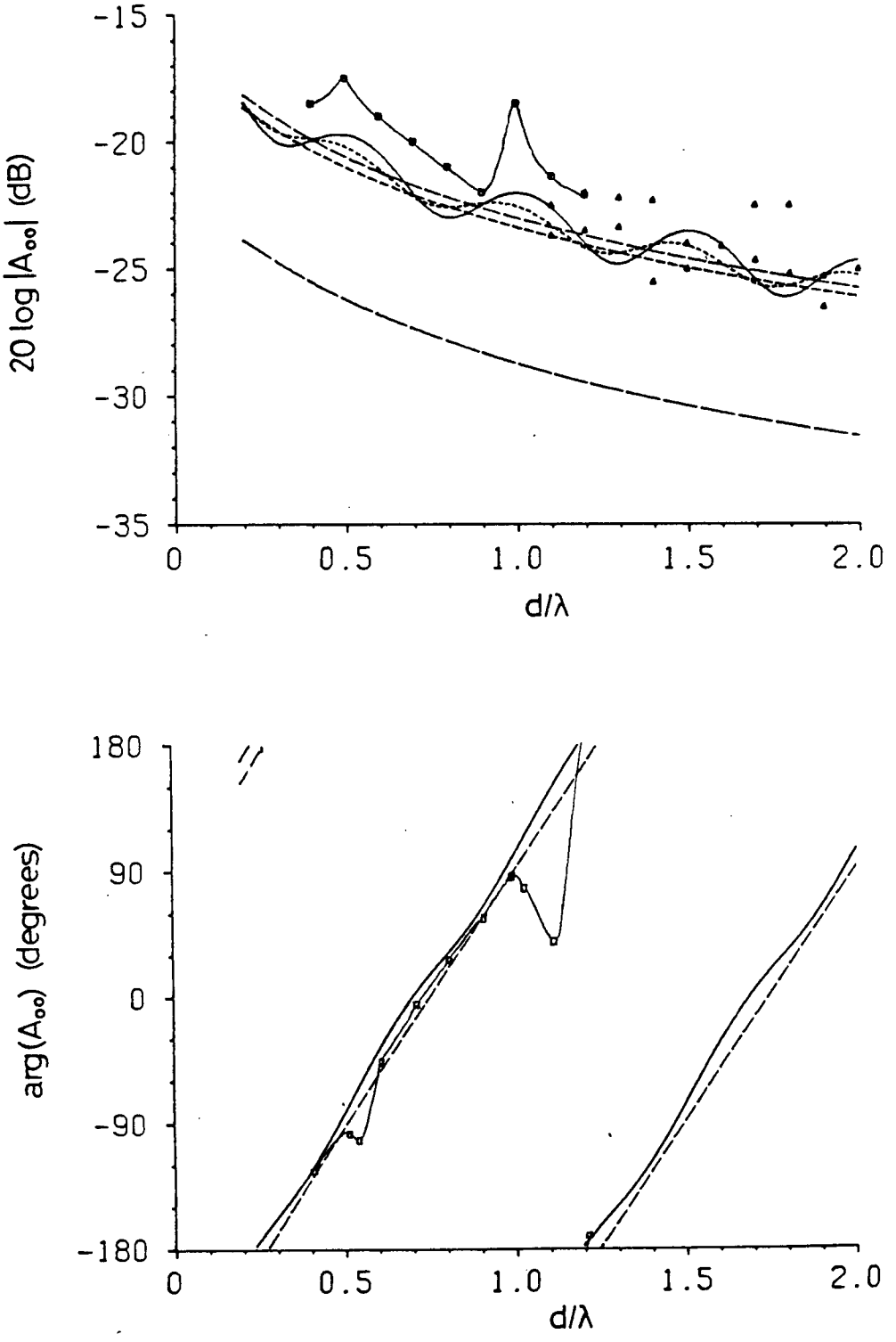

Fig. 4.3 TEM-TEM coupling between separated waveguides (a=b=0. 338λ).

For Figs. 4.3 - 4.9 as applicable:

- —— $A_{\infty}^{(2)}$
- ------ $A_{\infty}^{(2)}+A_{\infty}^{(3)}$
- ---- $A_{\infty}^{(2)}+A_{\infty}^{(3)}+A'^{(4)}_{\infty}$
- ..... $A_{\infty}^{(2)}+A_{\infty}^{(3)}+A_{\infty}^{(4)}$
- —— $A_{\infty}^{(2)}+A_{\infty}^{(3)}+A_{\infty}^{(4)}+A_{\infty}^{(5)}$
- —o— Montgomery and Chang [38]
- ▲ Dybdal et al. [17] (measured)

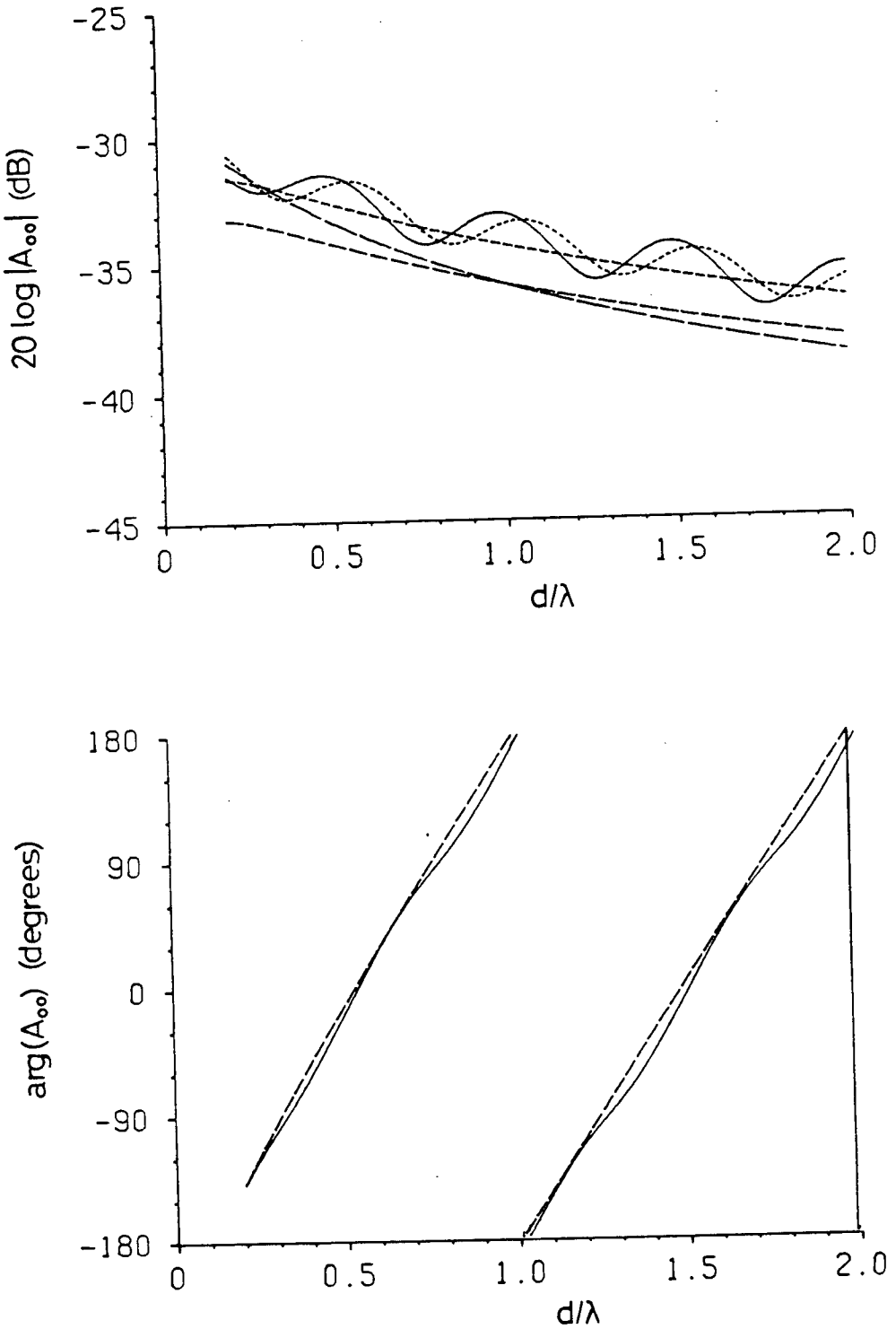

Fig. 4.4 TEM-TEM coupling between separated waveguides (a=b=0. 761λ).

See Fig. 4.3 for key.

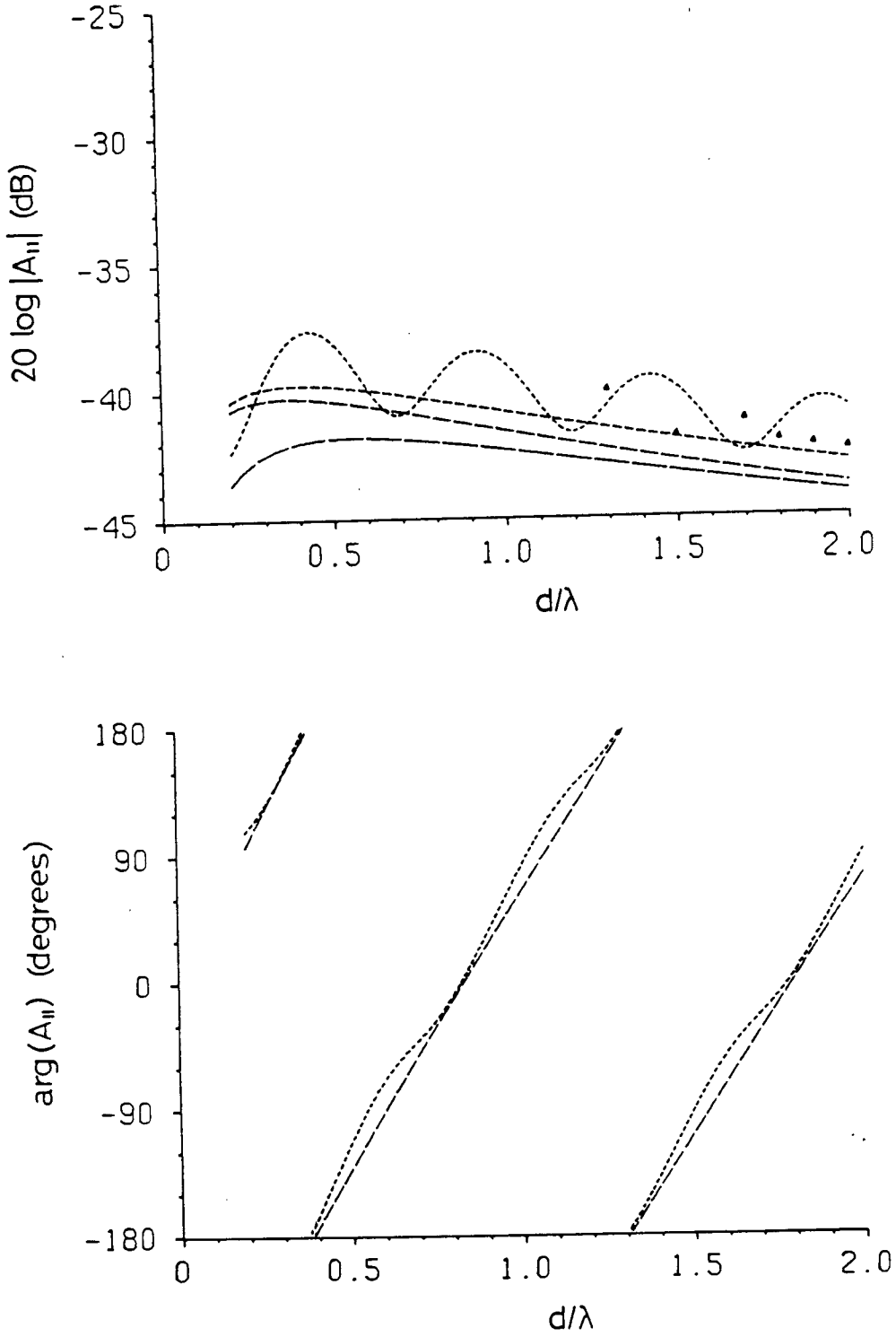

Fig. 4.5 TE_1-TE_1 coupling between separated waveguides (a=b=0.761λ).
See Fig. 4.3 for key.

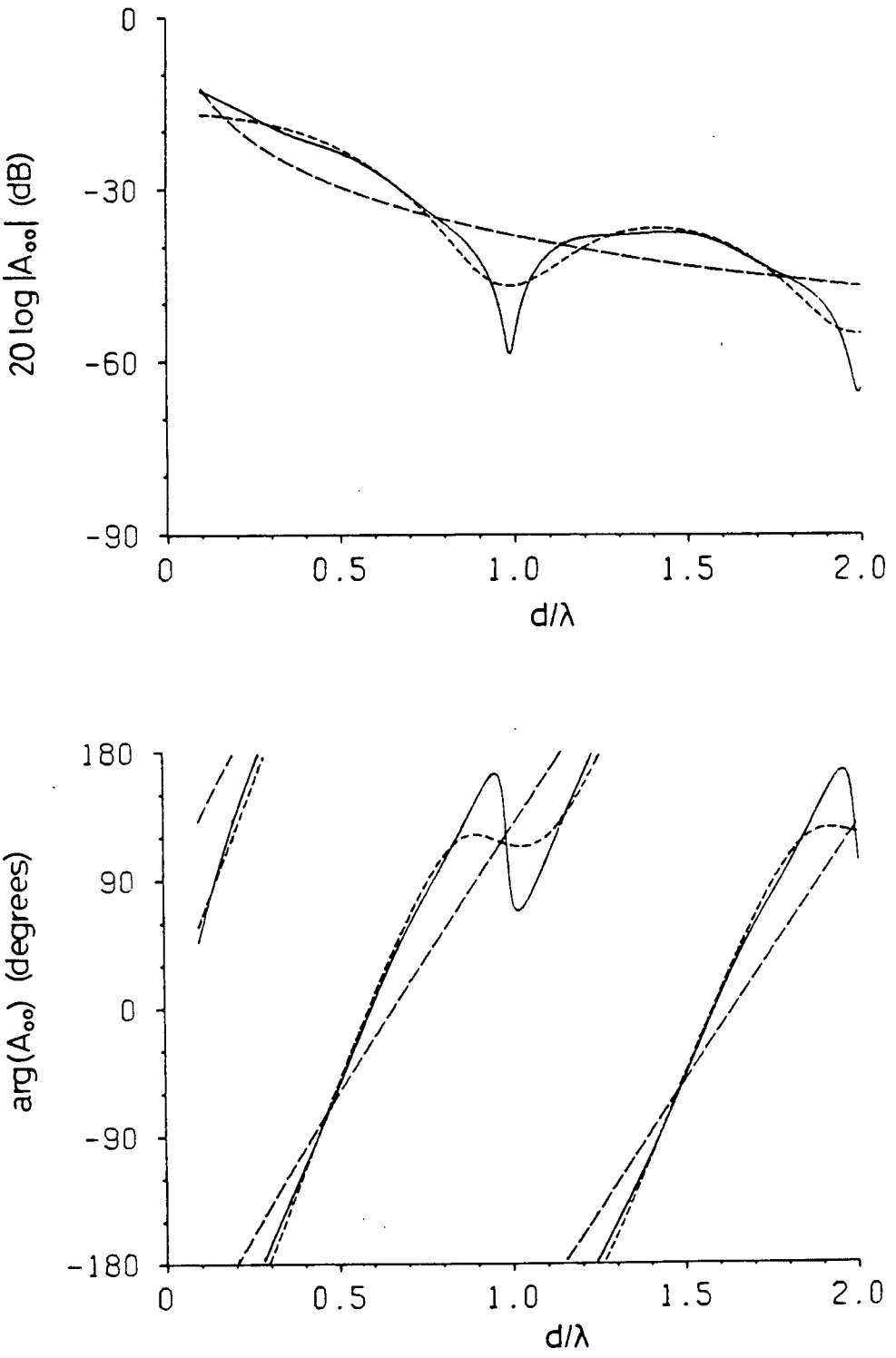

Fig. 4.6 TEM-TEM coupling between separated waveguides (d=a=b). See Fig. 4.3 for key.

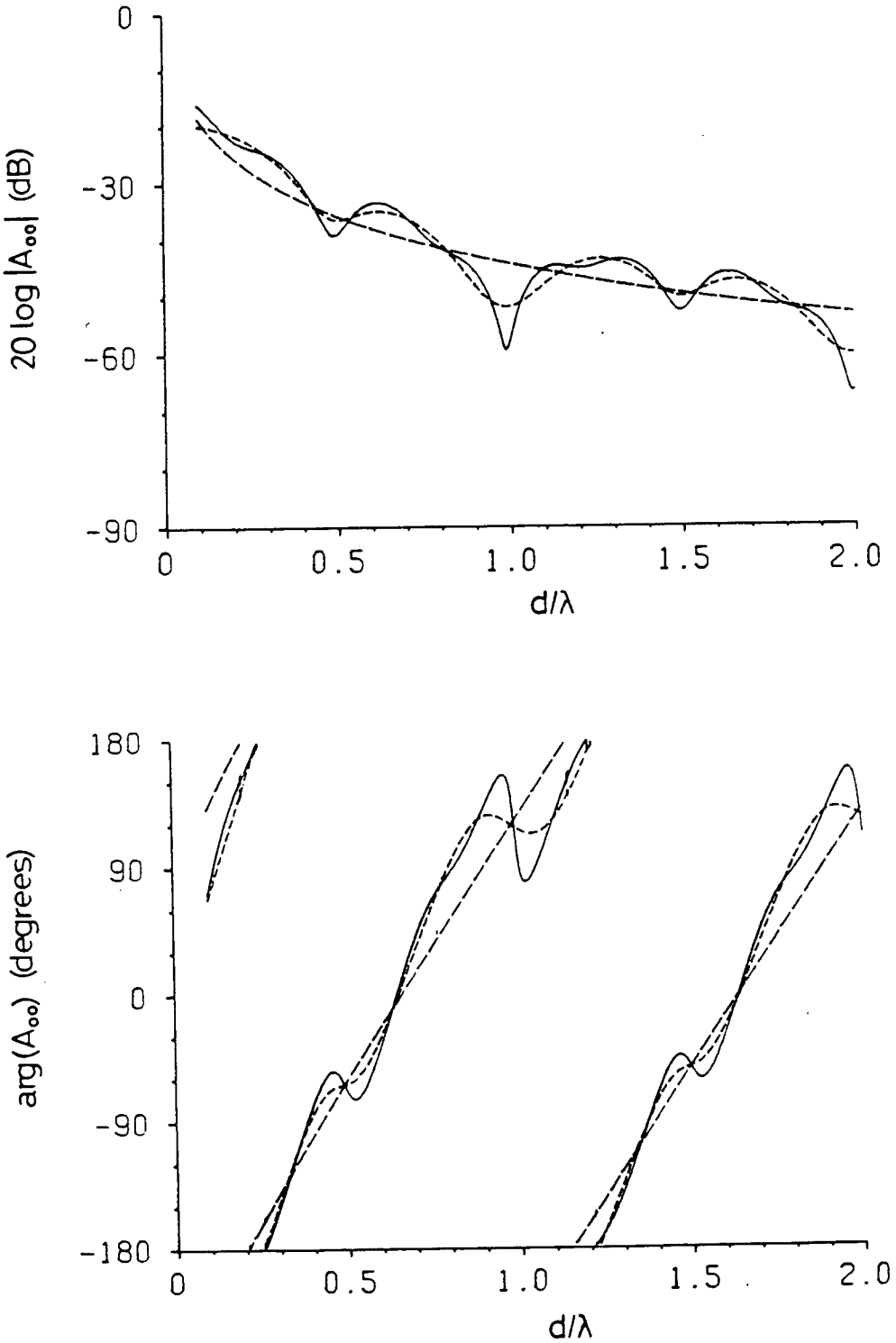

Fig. 4.7 TEM-TEM coupling between separated waveguides (a=2d, b=d).

See Fig. 4.3 for key.

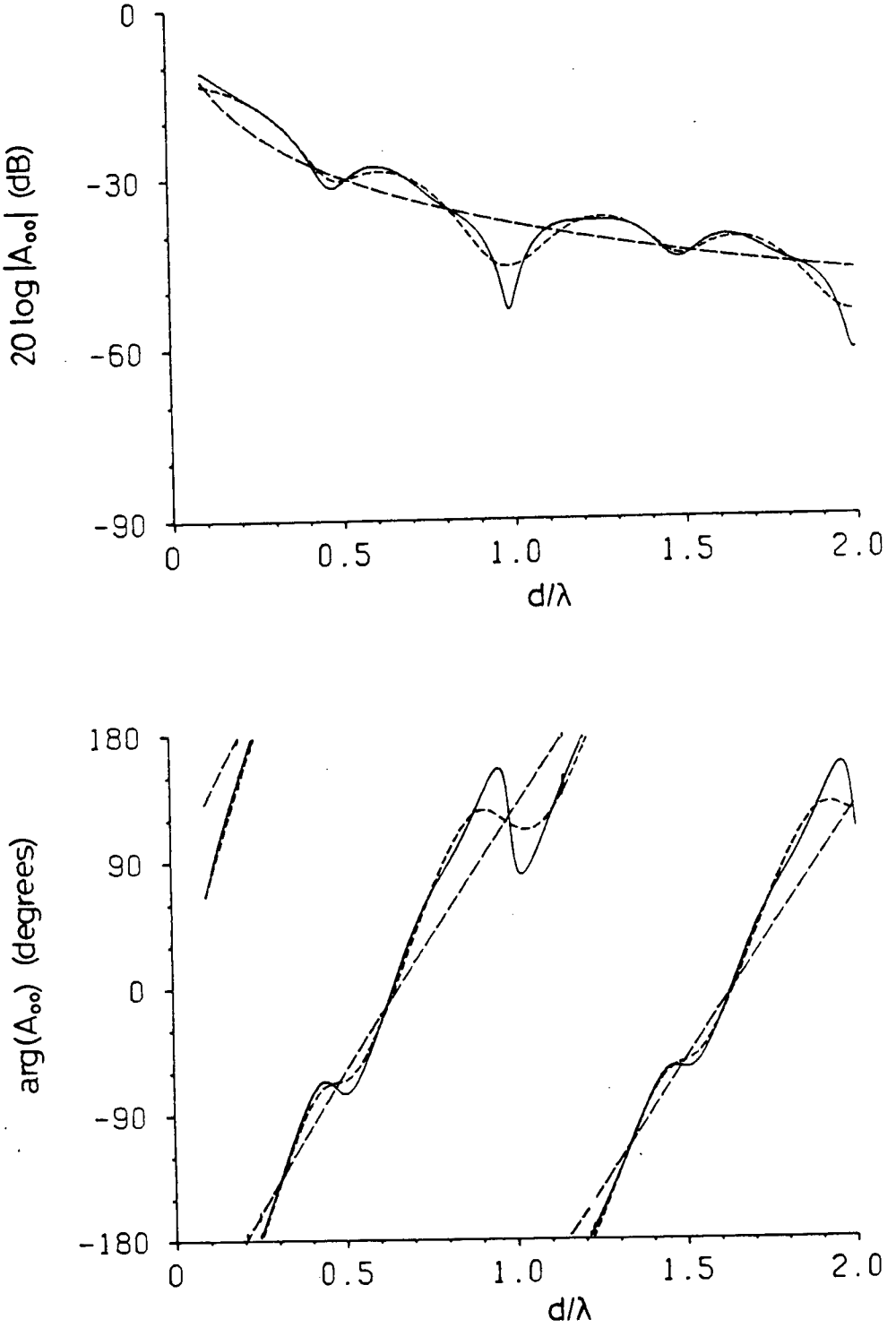

Fig. 4.8 TEM-TEM coupling between separated waveguides (a=d, b=2d).

See Fig. 4.3 for key.

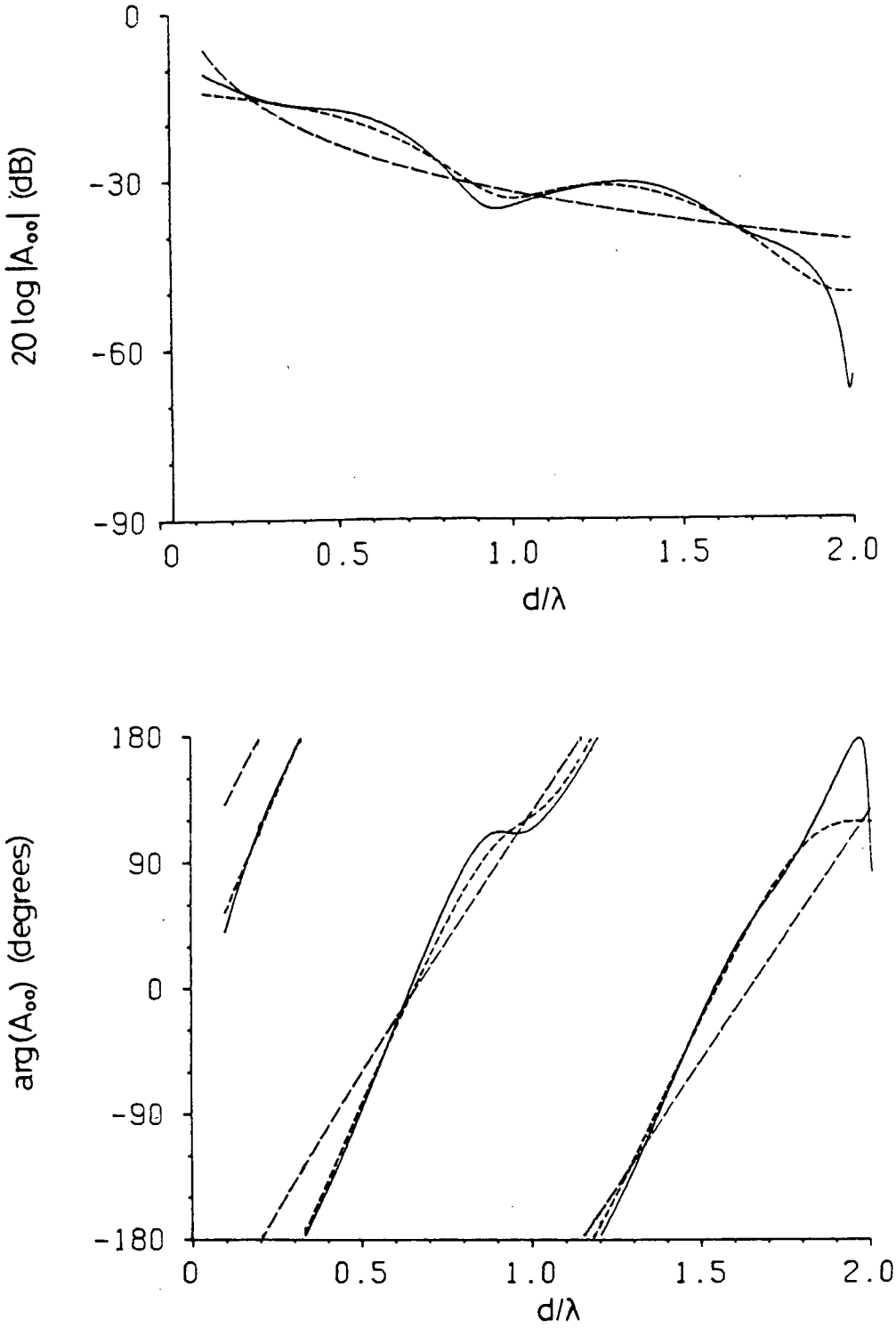

Fig. 4.9 TEM-TEM coupling between separated waveguides (a=d/2, b=d).

See Fig. 4.3 for key.

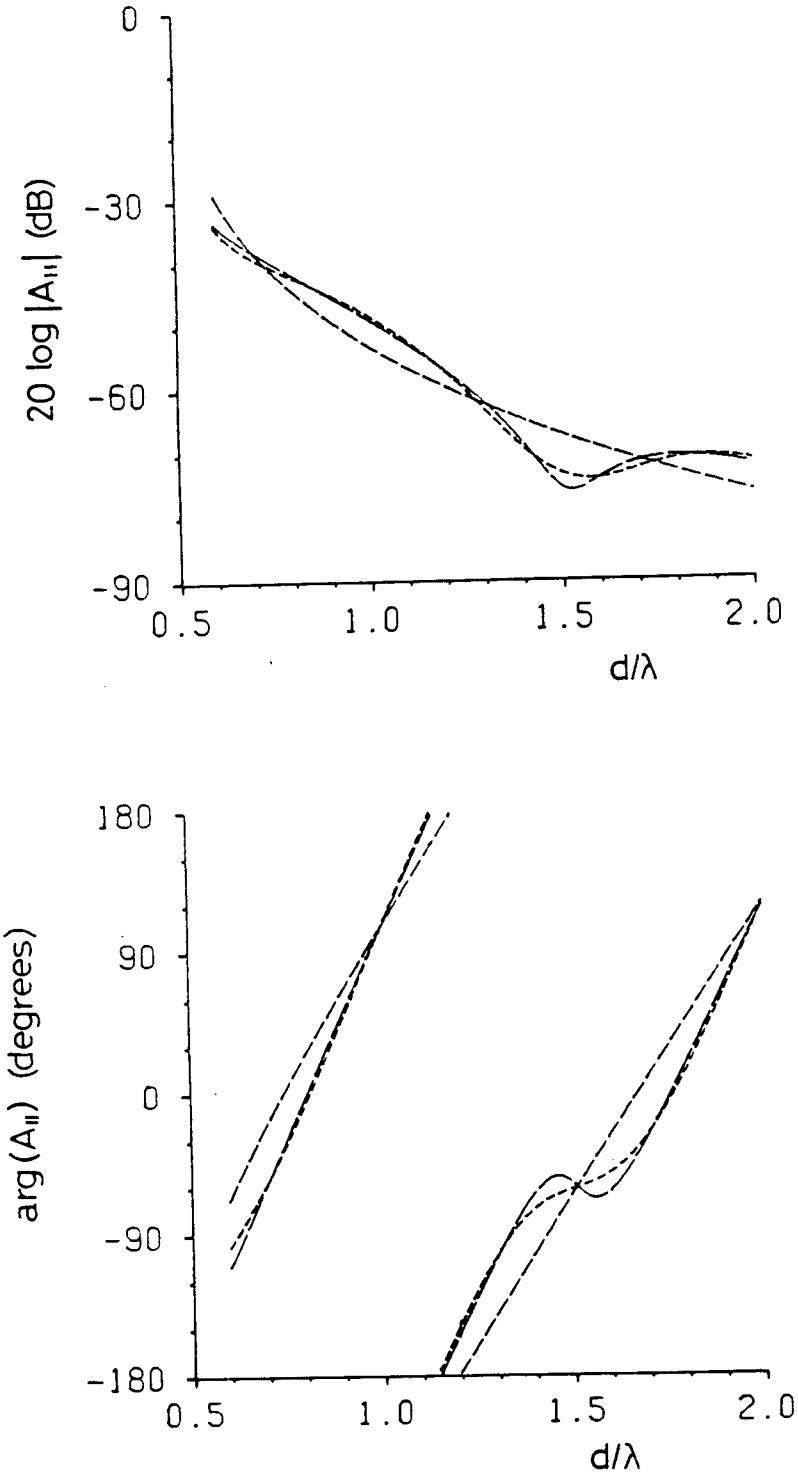

Fig. 4.10 TE_1-TE_1 coupling between separated waveguides (a=d=b).

—— $A_{11}^{(2)}$

---- $A_{11}^{(2)}+A_{11}^{(3)}+A_{11}^{(4)}$

—— $A_{11}^{(2)}+A_{11}^{(3)}+A_{11}^{(4)}$

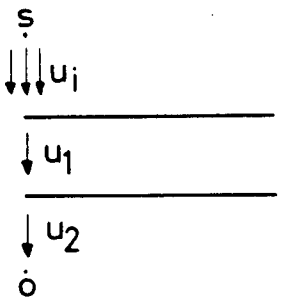

Fig. 4.11
plane wave normally incident
on two non-staggered parallel
plates

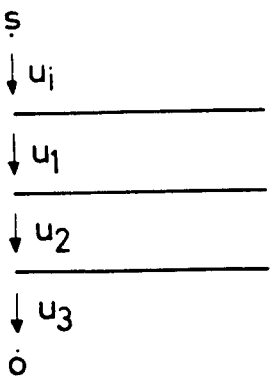

Fig. 4.12
line source normally incident
on three non-staggered parallel
plates

TABLE II

Coupling Coefficients $A_{\infty}(b,d,a)$
Between Separated Parallel Plate Waveguides
$a = d = b = 0.45\ \lambda$

# excited →# coupled into	Montgomery [38]		Lee [29]		Dybdal [17]		this theory using the asymptotic form (3.17)		this theory using the non-asymptotic form (3.22)	
	20 log|A| (dB)	∠A (degrees)	20 log|A| (dB)	∠A (degrees)	20 log|A| (dB)	∠A (degrees)	20 log|A| (dB)	∠A (degrees)	20 log|A| (dB)	∠A (degrees)
3→1 & 3→5	-20.69	-74.8	-21.27	-77.7						
1-3	-20.69	-74.9	-21.27	-77.7	-21.34	-74.6	-22.26	-75.8	-22.64	-84.6
2→4	-20.83	-72.4	-21.24	-73.8						

Chapter 5

RADIATION PATTERN OF A SINGLE GUIDE

5.1 INTRODUCTION

The radiation pattern of a single open-ended parallel-plate waveguide is found by ray-optical methods similar to those employed for the coupling analysis. This radiation pattern was previously obtained by Yee and Felsen [49]. Because many parts of this analysis will be required to find the radiation pattern of the multi-element waveguide array, it is repeated here for convenience. The analysis will be restricted to the TEM case.

The fields radiated from the waveguide are made up of fields diffracted from the waveguide edges. These diffracted fields are calculated by tracing ray paths from the mode in the guide to the edge under consideration (Fig.5.1). The fields represented by successive rays in a ray path are calculated in turn. The final ray in each ray path represents fields radiated into space. Several different ray paths can be traced from the mode in the guide to a particular edge. The total radiation pattern is made up of the sum of the fields represented by all ray paths leading to both edges of the waveguide.

5.2 CANONICAL PROBLEMS

The fields represented by some of the various combinations of two successive rays in the ray paths of Fig.5.1 have been calculated in Chapter 3. Thus the fields represented by any ray in a sequence can be found from the fields of the ray immediately preceding it. Other needed combinations (Fig.5.2 and 5.3) were not included and are presented here.

In Fig.5.2a a plane wave $u_i = 1/2$ is incident on a waveguide edge y=z=0 at $\theta_o = 0$. From (2.7), the diffracted field in the direction θ is given by

$$u_1 = u_i D(0,\theta)E(r) = -u_i \frac{e^{+i\pi/4}}{\sqrt{2\pi}} \sec(\frac{\theta}{2})E(r) , \qquad (5.1)$$

In Fig 5.2b a plane wave $u_i = 1/2$ is incident on the edge y=a,z=0 at $\theta_0 = 2\pi$. From (2.7), the diffracted field in the direction θ is given by

$$u_1 = u_i D(2\pi,\theta)E(r) = +u_i \frac{e^{+i\pi/4}}{\sqrt{2\pi}} \sec(\frac{\theta}{2})E(r) . \qquad (5.2)$$

In Fig 5.3a an isotropic line source $u_m = E(r)$ located a distance r_o from a guide wall is incident on that edge at an angle $\theta_0 = 3\pi/2$. From (2.12), the diffracted (not the total) field in the direction θ is given by

$$u_{m+1} = G(r_0,\theta)E(r), \qquad (5.3)$$

where for $0 < \theta < \pi/2$

$$G(r_0,\theta) = \frac{e^{-i\pi/4}}{\sqrt{\pi}} \{+e^{+ikr_0\sin\theta} F[\sqrt{kr_0}\ (\cos\frac{\theta}{2} - \sin\frac{\theta}{2})]$$

$$+e^{-ikr_0\sin\theta} F[\sqrt{kr_0}\,(\cos\tfrac{\theta}{2} + \sin\tfrac{\theta}{2})]\}\,, \qquad (5.4a)$$

for $\pi/2 < \theta < 3\pi/2$

$$G(r_0,\theta) = \frac{e^{-i\pi/4}}{\sqrt{\pi}}\{-e^{+ikr_0\sin\theta} F[\sqrt{kr_0}\,(-\cos\tfrac{\theta}{2} + \sin\tfrac{\theta}{2})]$$

$$+e^{-ikr_0\sin\theta} F[\sqrt{kr_0}\,(\cos\tfrac{\theta}{2} + \sin\tfrac{\theta}{2})]\} \qquad (5.4b)$$

and for $3\pi/2 < \theta < 2\pi$

$$G(r_0,\theta) = \frac{e^{-i\pi/4}}{\sqrt{\pi}}\{-e^{+ikr_0\sin\theta} F[\sqrt{kr_0}\,(-\cos\tfrac{\theta}{2} + \sin\tfrac{\theta}{2})]$$

$$-e^{-ikr_0\sin\theta} F[\sqrt{kr_0}\,(-\cos\tfrac{\theta}{2} - \sin\tfrac{\theta}{2})]\}\,, \qquad (5.4c)$$

for $kr_0 >> 1$

$$G(r_0,\theta) \sim \frac{e^{+i\pi/4}}{\sqrt{\pi}} E(r_0)\,\frac{\cos(\theta/2)}{\cos\theta}\,, \qquad (5.5)$$

In Fig 5.3b an isotropic line source $u_m = E(r)$ located a distance r_o from a guide wall is incident on that edge at an angle $\theta_0 = \pi/2$. From (2.12), the diffracted (not the total) field in the direction θ is given by

$$u_{m+1} = -G(r_0,\theta)E(r) , \tag{5.6}$$

5.3 CALCULATION OF RADIATION PATTERN

The total radiation pattern $P_0(d)$ of a parallel-plate waveguide of width d is calculated here. Consider a semi-infinite parallel-plate waveguide consisting of the two perfectly conducting parallel half-planes in z>0 at y=-d/2 and y=+d/2. We wish to determine the fields radiated into the space outside the guide.

As before, the incident field

$$u_i = e^{-ikz} \tag{5.7}$$

in the guide is decomposed into two plane waves incident on the top and bottom edges at $\theta_0 = 0$ or 2π respectively, whose value is

$$u_i = \frac{1}{2} \tag{5.8}$$

at both edges.

The singly diffracted fields are shown in Fig 5.1a and e. In Fig.5.1a the incident field (5.8) is diffracted by the edge y=+d/2, z=0. From (5.2) the diffracted field is

$$u_1^a = \frac{1}{2} D(2\pi,\theta)E(r) . \tag{5.9}$$

In Fig.5.1b the incident field (5.8) is diffracted by the edge y=-d/2, z=0. From (3.18), as observed at y=+d/2,

z=0 the diffracted field u_1^b is a line source

$$u_1^b = -\frac{1}{2} C_0'(d)E(r) \tag{5.10}$$

located at the diffracting edge, where from (3.19) and (3.20)

$$C_0'(d) = \frac{e^{-i\pi/4}}{\sqrt{\pi}} \frac{2F(\sqrt{kd})}{E(d)} . \tag{5.11}$$

If kd>>1,

$$C_0'(d) \sim \frac{e^{+i\pi/4}}{\sqrt{\pi}} . \tag{5.12}$$

This line source is again diffracted at the edge y=+d/2, z=0 and from (5.3) gives a field

$$u_2^b = \frac{-C_0'(d)}{2} G(d,\theta)E(r) . \tag{5.13}$$

In Fig.5.1c the incident field (5.8) is diffracted by the edge y=+d/2, z=0. From (3.18), as observed at y=+d/2, z=0 the diffracted field u_1^c is a line source

$$u_1^c = \frac{-C_0'(d)}{2} E(r) \tag{5.14}$$

located at the diffracting edge. This field is again diffracted at the edge y=-d/2, z=0 and from (3.26) the resultant field is

$$u_2^c = \frac{-C_0'(d)}{4} E(d+r) + \frac{e^{+i\pi/4}}{4\sqrt{2\pi}} C_0'(d)E(d)E(r) . \tag{5.15}$$

u_2^c is made up of two line sources, one at y=-3d/2, z=0, the other at y=-d/2, z=0. This field is again diffracted at the edge y=+d/2, z=0 and from (5.3) the resultant field is

$$u_3^c = \frac{-C_0'(d)}{4} G(2d,\theta)E(r) + \frac{e^{+i\pi/4}}{4\sqrt{2\pi}} C_0'(d)E(d)G(d,\theta)E(r) \quad (5.16)$$

which looks like two line sources at the diffracting edge.

In Fig 5.1d the incident field u_i is given by (5.8) and the field u_1^d is given by (5.10). This field is again diffracted at the edge y=+d/2, z=0 and from (3.26) the resultant field is

$$u_2^d = \frac{-C_0'(d)}{4} E(d+r) + \frac{e^{+i\pi/4}}{4\sqrt{2\pi}} C_0'(d)E(d)E(r) . \quad (5.17)$$

u_2^d is made up of two line sources, one at y=+3d/2, z=0, the other at y=+d/2, z=0. This field is again diffracted at the edge y=-d/2, z=0 and from (3.26) the resultant field is

$$u_3^d = \frac{-C_0'(d)}{8} E(2d+r) + \frac{e^{+i\pi/4}}{8\sqrt{2\pi}} C_0'(d)E(2d)E(r)$$

$$+ \frac{e^{+i\pi/4}}{8\sqrt{2\pi}} C_0'(d)E(d)E(d+r) . \quad (5.18)$$

u_3^d is made up of three line sources at y=-5d/2, y=-d/2 and y=-3d/2, z=0 respectively. This field is again diffracted at the edge y=+d/2, z=0 and from (5.3) the resultant field is

$$u_4^d = \frac{-C_0'(d)}{8} G(3d,\theta)E(r) + \frac{e^{+i\pi/4}}{8\sqrt{2\pi}} C_0'(d)E(2d)G(d,\theta)E(r)$$

$$+ \frac{e^{+i\pi/4}}{8\sqrt{2\pi}} C_0'(d)E(d)G(2d,\theta)E(r) \quad (5.19)$$

which looks like three line sources at the diffracting edge.

The total fields P_0' diffracted from the edge y=+d/2, z=0 up to quadruple diffraction are given by the sum of (5.9), (5.13), (5.16) and (5.19). These fields appear like line sources at the edge. The field P_0'' diffracted from the edge y=-d/2, z=0 and radiated into space is calculated

similarly using the ray paths in Fig.5.1e,f,g,h, and is given by

$$P_0'' = -P_0' . \tag{5.20}$$

The radiation pattern formed by these apparent line sources at the two edges of the waveguide is given by

$$P_0 = P_0' e^{\frac{-ikd}{2}\sin\theta} + P_0'' e^{\frac{+ikd}{2}\sin\theta} \tag{5.21}$$

in the second quadrant $(\pi/2 < \theta < \pi)$, where the exponential terms are the array factors which adjust for the different path lengths from the edges to a distant observation point. In the first quadrant $(0 < \theta < \pi/2)$, one of the edges is shadowed and

$$P_0 = P_0' e^{\frac{-ikd}{2}\sin\theta} . \tag{5.22}$$

The pattern is symmetrical about $\theta = \pi$ so that

$$P_0(d,2\pi-\theta) = P_0(d,\theta) . \tag{5.23}$$

The radiation pattern $P_0^{(1)}$ for single diffraction may be written

$$P_0^{(1)} = \frac{e^{+i3\pi/4}}{\sqrt{2\pi}} \sec(\tfrac{\theta}{2}) \sin(\tfrac{kd}{2}\sin\theta) E(r) . \tag{5.24}$$

Note that at $\theta = \pi$ the value of $P_0^{(1)}$ is finite and is given by

$$P_0^{(1)}(d,\theta=\pi) = \frac{e^{+i3\pi/4}}{\sqrt{2\pi}} kd\, E(r) , \tag{5.25}$$

so that the maximum radiation is proportional to the guide width. For $0 < \theta < \pi/2$

$$P_0^{(1)} = -\frac{1}{2}\frac{e^{+i\pi/4}}{\sqrt{2\pi}}\sec(\frac{\theta}{2})e^{\frac{-ikd}{2}\sin\theta} . \quad (5.26)$$

At $\theta = \pi/2$ there is a discontinuity in the single diffraction radiation pattern, because u_1^e is shadowed for $\theta < \pi/2$. This discontinuity can be reduced by taking higher order diffraction into account. The addition of double diffraction term u_2^b eliminates this discontinuity because it can been shown that (Fig.5.4a)

$$u_1^e(\frac{\pi+}{2})e^{\frac{+ikd}{2}\sin\theta} + u_2^b(\frac{\pi+}{2})e^{\frac{-ikd}{2}\sin\theta} = u_2^b(\frac{\pi-}{2})e^{\frac{-ikd}{2}\sin\theta} \quad (5.27)$$

if the asymptotic form of (5.12) is used. The discontinuity in the double diffraction radiation pattern at $\theta = \pi/2$ is given by the remaining double diffraction term $u_2^f(\frac{\pi-}{2})e^{\frac{+ikd}{2}\sin\theta}$ which is about half of $u_1^e(\frac{\pi-}{2})d^{\frac{+ikd}{2}\sin\theta}$ [49]. The addition of triple diffraction term u_2^c eliminates the discontinuity in the double diffraction radiation pattern at $\theta = \pi/2$ because similarly it can be shown that (Fig.5.4b)

$$u_2^f(\frac{\pi+}{2})e^{\frac{+ikd}{2}\sin\theta} + u_2^c(\frac{\pi+}{2})e^{\frac{-ikd}{2}\sin\theta} = u_2^c(\frac{\pi-}{2})e^{\frac{-ikd}{2}\sin\theta} . \quad (5.28)$$

The discontinuity in the triple diffraction radiation pattern at $\theta = \pi/2$ is given by $u_3^g(\frac{\pi-}{2})e^{\frac{+ikd}{2}\sin\theta}$ which is about half of $u_2^f(\frac{\pi-}{2})e^{\frac{+ikd}{2}\sin\theta}$ [49]. Thus by taking successively higher order diffraction terms, the discontinuity at $\theta = \pi/2$ may be reduced. Similar reasoning applies to the discontinuity at $\theta = 3\pi/2$.

5.4 NUMERICAL AND EXPERIMENTAL RESULTS

The radiation pattern of a single parallel-plate waveguide calculated by ray-optical methods is compared with the known exact pattern[Weinstein, 1969] and the measured E-plane pattern of the H-plane sectoral horn (section 1.4). These patterns are shown for various guide widths in Fig.5.5 and 5.6. The radiation patterns are calculated for $0 < \theta < 2\pi$ in radian measure, but are plotted for $-180° < \theta' < 180°$. $(\theta' = \theta - \pi)$

The radiation patterns of a parallel plate waveguide consist of only a single lobe. As might be expected, the gain increases and the beamwidth decreases as the width of the guide is increased. The phase is essentially constant in the forward direction $(-90° < \theta' < 90°)$.

The maximum error between the ray-optical and the exact pattern is never more then 1 dB and is less then 0.5 dB in the forward direction (Fig. 5.5a). The discontinuity at $\theta = \pi/2$ is less then 1 dB when quadruple diffraction is taken into account. The ray-optical pattern is more accurate at the shadow boundary when the asymptotic form of (5.12) is used throughout (Fig. 5.5b). The discontinuity at $\theta = \pi/2$ is also much smaller since the continuity relations (5.27) and (5.28) are true only for the asymptotic form, and may be reduced to an arbitrarily small value by considering still higher order terms. Each successive interaction reduces the discontinuity by approximately one-half.

The experimental pattern is also within 1 dB of the exact pattern for guide widths from 0.339λ to 0.441λ (f=10-

13 GHz) and over the entire angular range, except for $\theta' > 150^{\circ}$, where the patterns could not be measured accurately because of blockage by the antenna mounting arrangement (Figs.5.6a,b,c,d).

5.5 SUMMARY

The radiation pattern of a single non-staggered parallel plate waveguide is found by ray-optical methods and compared to experimental patterns obtained with an H-plane sectoral horn. The discontinuity expected along the shadow boundary in the aperture plane is less then 1 dB when terms up to quadruple diffraction are taken into account and can be reduced still further by taking the asymptotic form of the expression and/or adding higher order diffraction terms.

The good agreement between the exact and experimental results confirms that the E-plane pattern of the H-plane sectoral horn simulates that of a parallel-plate waveguide quite well, and gives an estimate of the accuracy of this approximation. The good agreement between exact, ray-optical and experimental patterns suggests that both the ray-optical and experimental methods may be extended with confidence to more complex structures to be considered in the following chapters.

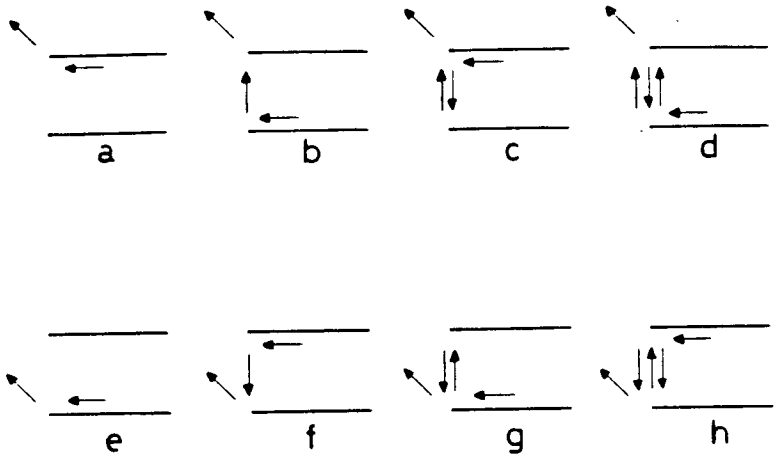

Fig. 5.1
ray paths in a parallel plate waveguide

Fig. 5.2
ray path (see text)

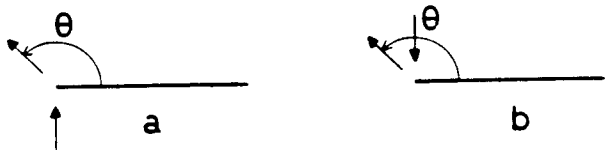

Fig. 5.3
ray path (see text)

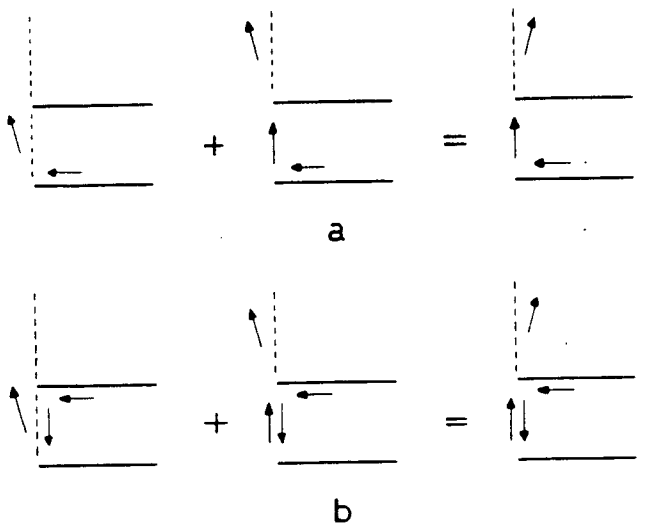

Fig. 5.4
continuity of fields across shadow boundary
see eqns. (5.27) and (5.28).

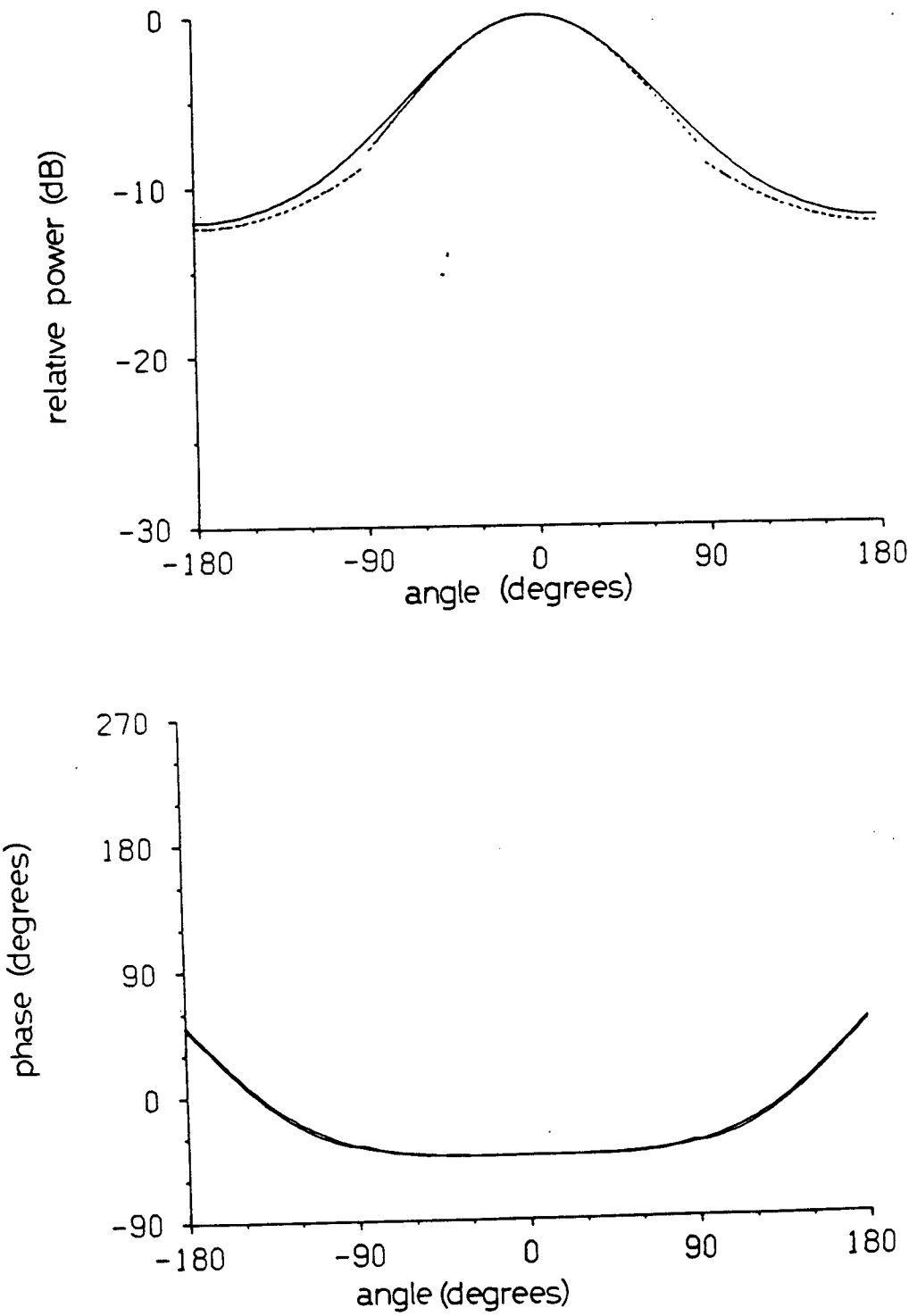

Fig. 5.5a Ray-optical and exact radiation patterns for a parallel plate waveguide (a=0. 45λ). using (5.11)

—— exact

----- ray-optical

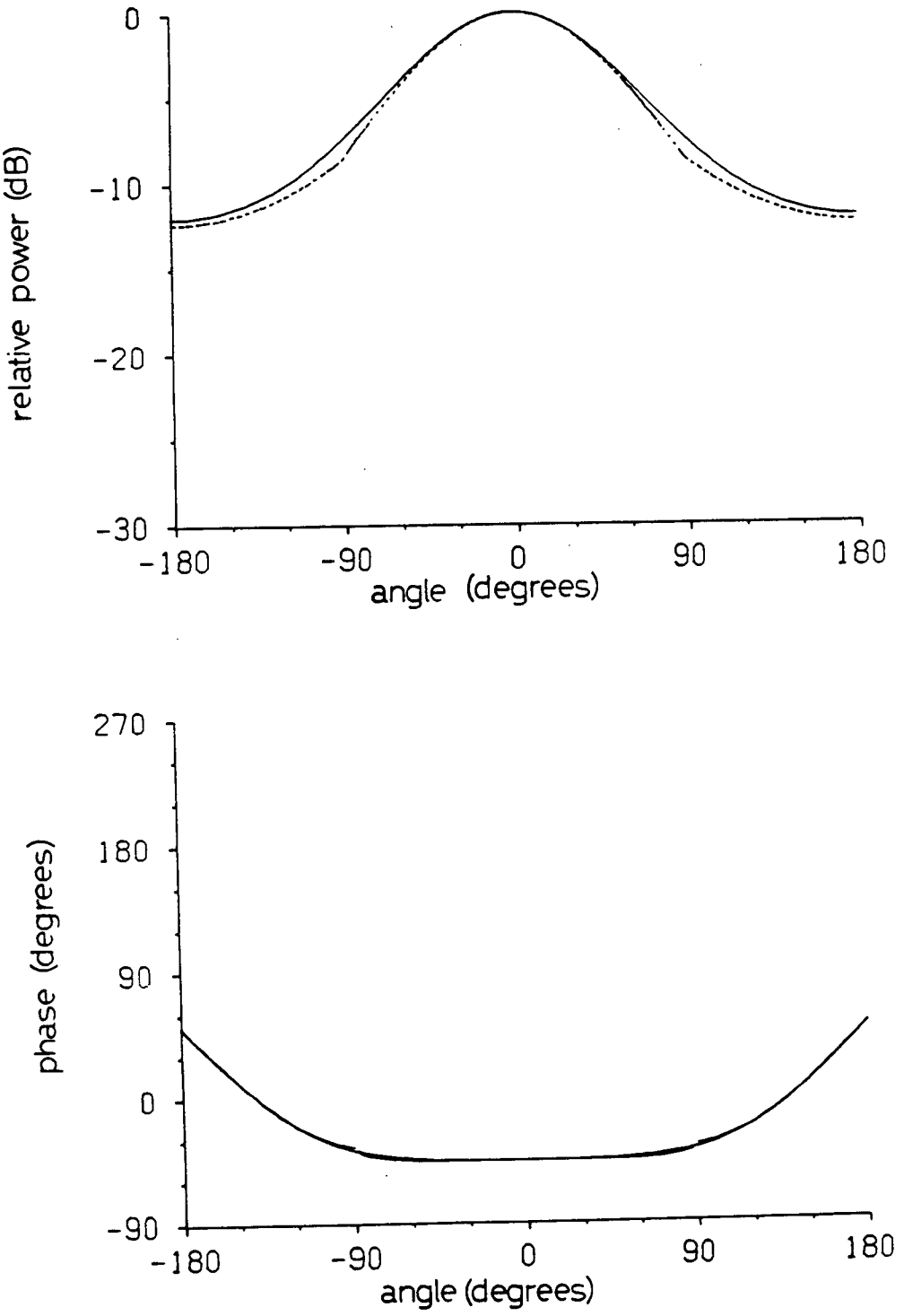

Fig. 5.5b Ray-optical and exact radiation patterns for a parallel plate waveguide (a=0. 45λ). using asymptotic form (5.12)

——— exact

····· ray-optical

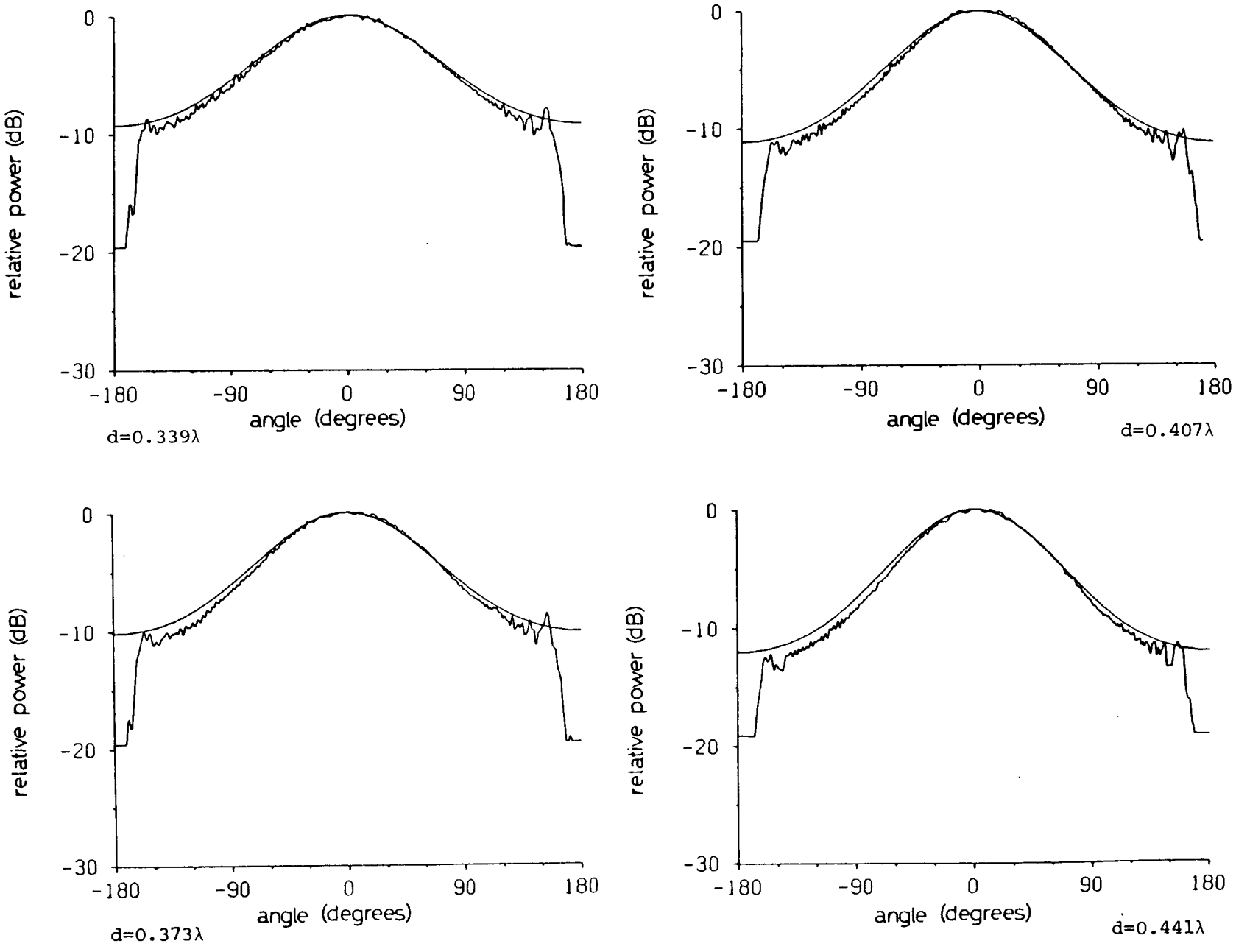

Fig. 5.6 Exact radiation patterns for a parallel plate waveguide compared with measured E-plane patterns of H-plane sectoral horn.

Chapter 6

RADIATION PATTERN OF THREE ELEMENT WAVEGUIDE ARRAY

6.1 INTRODUCTION

In this chapter the radiation pattern of a multi-element waveguide array (Fig.6.1) is found by methods similar to those used for a single waveguide, and will be compared to experimental results using the H-plane sectoral horn.

Calculation of the radiation pattern of the parallel-plate waveguide array begins by first calculating the pattern for the case when all three guides are of infinite depth (Fig.6.2). All edges of the resulting array of parallel-plate waveguides are excited by the central driven guide. The fields diffracted by these edges are calculated to yield the radiation pattern.

If the parasitic guides are of finite depth, the fields coupled into them also contribute to the total radiation pattern. For this case, the coupling coefficient between the central driven guide and the parasitic guide on either side must be calculated. The coupled fields are reflected between open and closed ends of the parasitic guide and eventually radiated from the open end. The total radiation pattern of the waveguide array is calculated by adding the fields radiated from the edges excited by the central driven guide and the fields radiated from the outer guides.

In the TE_1 case the coupling between adjacent guides is

very weak, and not enough power is coupled into the parasitic guide for its radiation to significantly affect the pattern. For this reason the analysis is restricted to the TEM case where the coupling is much stronger.

6.2 RAY-OPTICAL FORMULATION

Consider three adjacent semi-infinite parallel-plate waveguides consisting of four perfectly conducting infinitely thin half-planes in $z>0$ at $y=-d/2-a$, $y=-d/2$, $y=d/2$, $y=d/2+a$ (Fig.6.2). As in Chapter 5 the incident TEM mode in the central driven guide $-d/2<y<d/2$, $z>0$, given by (5.7) is decomposed into two plane waves incident on the top and bottom edges at $\theta = 0$ or 2π respectively. These plane waves both have the value

$$u_i = \frac{1}{2} \tag{6.1}$$

at the edge $y=d/2$, $z=0$, and $y=-d/2$, $z=0$, and are represented by the incident rays in the central guide of Fig.6.2.

These plane waves are diffracted by the waveguide edges. The resulting diffracted fields may be radiated or may be diffracted again by another waveguide edge. Thus all four waveguide edges are excited by the fields in the central driven guide and contribute to the radiation pattern. Sequences of rays called ray paths trace the fields as they are diffracted from various edges and eventually radiated into space.

Fig.6.1 shows some of the ray paths which must be

considered to calculate the radiation pattern of the central driven guide in the absence of the outer guides. Fig.6.3 and 6.4 shows some of the ray paths which must be considered to calculate the additional diffraction from the waveguide edges excited by the central driven guide when the waveguides of infinite depth are added.

6.3 RADIATION PATTERN WITH GUIDES OF INFINITE DEPTH

The total radiation pattern P_t of the array of three parallel plate waveguides with only the center guide driven is calculated. The field P_t is made up of the sum of the fields scattered from all the edges. $P_0(d)$ represents the field scattered from the open end of the central guide, and P_n (n=1,2,3,4) represents the total field scattered from the nth edge (as labelled in Fig.6.2) not already included in P_0.

The total radiation pattern P_t for the array of Fig.6.2 is given by the sum of the fields from all the edges. In the rear halfspace all but the outermost edges are shadowed, so that for angles $0 < \theta < \pi/2$ only the edge at y=(d+2a)/2, z=0 is visible, and

$$P_t = P_3 e^{-ik(\frac{d+2a}{2})\sin\theta} \qquad (6.2)$$

For angles $\pi/2 < \theta < \pi$ all edges are visible and

$$P_t = P_3 e^{-ik(\frac{d+2a}{2})\sin\theta}$$

$$+ P_1 e^{-ik\frac{d}{2}\sin\theta}$$

$$+ P_0(d)$$

$$+ P_2 e^{+ik\frac{d}{2}\sin\theta}$$

$$+ P_4 e^{+ik(\frac{d+2a}{2})\sin\theta} \quad . \qquad (6.3)$$

The pattern is symmetrical about $\theta = \pi$.

The field P_0 was calculated in Chapter 5 using the ray paths in Fig.5.1. The field P_1 is calculated using the ray paths in Fig.6.3. The field P_3 is calculated using the ray paths in Fig.6.4. The ray paths used to calculate P_2 and P_4 are the image about the z-axis of those shown in Figs.6.3 and 6.4.

The solution for the fields represented by two successive rays in the ray paths of Figs.6.3 and 6.4 can now be used to calculate all the fields associated with a ray path and thus the contributions P_n (n=1,2,3,4) from the waveguide edges. Note that there are several different ray paths (labelled a,b,c,etc. in Figs. 6.3 and 6.4) which contribute to any P_n . The following notations are employed to represent the fields, where the superscript x refers to the letter of the figure showing the particular ray path under consideration.

u_i = an incident field in the central driven guide

u^x_{nm} = a field in a ray path contributing to P_n which has been diffracted m times.

The field P_0 has been calculated in Chapter 5.

To calculate contributions to P_3, consider the ray diagrams in Fig.6.4. In Fig.6.4a the incident field u_i, given by (6.1), is diffracted at the edge y=d/2, z=0. From (3.18), as observed at y=d/2+a, z=0 the diffracted field u_{31}^a is a line source

$$u_{31}^a = \frac{C_0'(a)}{2} E(r) \tag{6.4}$$

located at the diffracting edge. This field is again diffracted at the edge y=d/2+a, z=0, and from (5.3) the resultant field is

$$u_{32}^a = \frac{C_0'(a)}{2} G(a,\theta)E(r) \tag{6.5}$$

from the edge.

In Fig.6.4b the incident field u_i, given by (6.1), is diffracted at the edge y=-d/2, z=0. From (3.18) as observed at y=+d/2, z=0 the diffracted field u is a line source

$$u_{31}^b = \frac{-C_0'(d)}{2} E(r) \tag{6.6}$$

at the edge. This line source is again diffracted at the edge y=d/2, z=0 and from (3.29) the resultant doubly diffracted field is

$$u_{32}^b = \frac{-C_0'(d)}{4} E(d+r) - \frac{e^{i\pi/4}}{4\sqrt{2\pi}} C_0'(d)E(d)E(r). \tag{6.7}$$

u_{32}^b is made up of two line source fields, one centred at y=-d/2, z=0, the other at y=d/2, z=0. The field (6.7) is again diffracted at y=(d+2a)/2, z=0, and from (5.3) the resultant field is

$$u_{33}^{b} = \frac{-C_0'(d)}{4} G(d+a,\theta)E(r) - \frac{e^{i\pi/4}}{4\sqrt{2\pi}} C_0'(d)E(d)G(a,\theta)E(r), \quad (6.8)$$

In Fig.6.4c the incident field u_i is given by (6.1) and the field u_{31}^{c} is given by (6.4). This field is again diffracted at the edge y=+d/2+a, z=0 and from (3.26) the resultant field is

$$u_{32}^{c} = \frac{C_0'(a)}{4} E(a+r) - \frac{e^{i\pi/4}}{4\sqrt{2\pi}} C_0'(a)E(a)E(r). \quad (6.9)$$

u_{32}^{c} is made up of two line source fields centred at y=+d/2+2a, z=0 and y=+d/2+a, z=0 respectively. This field is again diffracted at y=+d/2, z=0 and from (3.26) the resultant field is

$$u_{33}^{c} = \frac{C_0'(a)}{8} E(2a+r) - \frac{e^{i\pi/4}}{8\sqrt{2\pi}} C_0'(a)E(2a)E(r)$$

$$- \frac{e^{i\pi/4}}{8\sqrt{2\pi}} C_0'(a)E(a)E(a+r). \quad (6.10)$$

u_{33}^{c} is made up of three line source fields centred at y=+d/2-2a, y=+d/2 and y=+d/2-a, z=0 respectively. This field is again diffracted at the edge y=+d/2+a, z=0 and from (5.3) the resultant field is

$$u_{34}^{c} = \frac{C_0'(a)}{8} G(3a,\theta)E(r) - \frac{e^{i\pi/4}}{8\sqrt{2\pi}} C_0'(a)E(2a)G(a,\theta)E(r)$$

$$- \frac{e^{i\pi/4}}{8\sqrt{2\pi}} C_0'(a)E(a)G(2a,\theta)E(r) \quad (6.11)$$

which appears as three line sources all centred at the diffracting edge. The sum of (6.5), (6.8), and (6.11) represents the total field P_3 from the edge y=+d/2+a, z=0 up to and including quadruple diffraction.

To calculate contributions to P_1 consider the ray diagrams in Fig.6.3. In Fig.6.3a the incident field u_i is given by (6.1), the singly diffracted field u_{11}^a is given by (6.4) and u_{12}^a is given by (6.9). This field is diffracted at the edge y=+d/2, z=0, and from (5.3) the resultant field is

$$u_{13}^a = \frac{-C_0'(a)}{4} G(2a,\theta)E(r) + \frac{e^{i\pi/4}}{4\sqrt{2\pi}} C_0'(a)E(a)G(a,\theta)E(r). \qquad (6.12)$$

In Fig.6.3b the incident field u_i is given by (6.1), the field u_{11}^b is given by (6.6) and u_{12}^b is given by (6.7). This field is again diffracted at the edge y=+d/2+a, z=0 and from (3.26) the resultant field is

$$u_{13}^b = \frac{-C_0'(d)}{8} E(d+a+r) + \frac{e^{i\pi/4}}{8\sqrt{2\pi}} C_0'(d)E(d+a)E(r)$$

$$- \frac{e^{i\pi/4}}{8\sqrt{2\pi}} C_0'(d)E(d)E(a+r). \qquad (6.13)$$

u_{13}^b consists of three line source fields at y=+3d/2+2a, y=+d/2+a and y=+d/2+2a, z=0 respectively. This field is again diffracted at the edge y=+d/2, z=0 and from (5.3) the resultant field is

$$u_{14}^b = \frac{C_0'(d)}{8} G(d+2a,\theta)E(r) - \frac{e^{i\pi/4}}{8\sqrt{2\pi}} C_0'(d)E(d+a)G(a,\theta)E(r)$$

$$+ \frac{e^{i\pi/4}}{8\sqrt{2\pi}} C_0'(d)E(d)G(2a,\theta)E(r). \qquad (6.14)$$

In Fig.6.3c the incident field given by (6.1) is diffracted at the edge y=-d/2, z=0. From (3.18), as observed at the edge y=-d/2-a, z=0 the field u_{11}^c is given by a line source

$$u_{11}^{c} = \frac{C_0'(a)}{2} E(r) \tag{6.15}$$

located at the diffracting edge. This field is again diffracted at the edge y=-d/2-a, z=0 and from (3.26) the resultant field is

$$u_{12}^{c} = \frac{C_0'(a)}{4} E(a+r) - \frac{e^{i\pi/4}}{4\sqrt{2\pi}} C_0'(a)E(a)E(r) . \tag{6.16}$$

u_{12}^{c} consists of two line source fields at y=-d/2-2a, z=0 and y=-d/2-a, z=0 respectively. This field is again diffracted at the edge y=-d/2, z=0 and from (3.29) the resultant field is

$$u_{13}^{c} = \frac{C_0'(a)}{8} E(2a+r) + \frac{e^{i\pi/4}}{8\sqrt{2\pi}} C_0'(a)E(2a)E(r) - \frac{e^{i\pi/4}}{8\sqrt{2\pi}} C_0'(a)E(a)E(a+r) . \tag{6.17}$$

u_{13}^{c} consists of three line source fields at y=-d/2-2a, y=-d/2 and y=-d/2-a, z=0 respectively. This field is again diffracted at the edge y=+d/2, z=0 and from (5.3) the resultant field is

$$u_{14}^{c} = \frac{C_0'(a)}{8} G(2a+d,\theta)E(r) + \frac{e^{i\pi/4}}{8\sqrt{2\pi}} C_0'(a)E(2a)G(d,\theta)E(r) - \frac{e^{i\pi/4}}{8\sqrt{2\pi}} C_0'(a)E(a)G(a+d,\theta)E(r) . \tag{6.18}$$

The sum of (6.12), (6.14) and (6.18) represents the field P_1 from the edge y=d/2, z=0 up to and including quadruple diffraction.

Similar calculations for the fields P_2 scattered from the edge y=-d/2, z=0 and P4 from y=-d/2-a, show that

$$P_2 = -P_1 \tag{6.19}$$

$$P_4 = -P_3 \,. \tag{6.20}$$

The results for P_n are substituted in (6.2) and (6.3) to give the total radiation pattern of the array of Fig.6.2 with parasitic guides of infinite depth.

6.4 RADIATION WITH OUTER GUIDES SHORTED

Consider the array of Fig.6.1, which is equivalent to the array of Fig.6.2 except that the outer guides are now of finite depth. The fields coupled into these guides will be reflected from the far end and reradiated. Adjusting the depth of the guides will change the relative phase of their radiation and thus alter the radiation pattern.

The coupling coefficient $A_{00}(d,a)$ between the central driven guide of width d and the adjacent parasitic guide of width a has been calculated in Chapter 3. The coupled fields travel down the outer guide and are reflected at the shorted end. The fields then travel towards the open end ,where part is reflected back and part is radiated.

The value A of the fields in the outer guides at the aperture plane z=0 relative to those from the central driven guide is the sum of a geometric series

$$A = A_{00}e^{i2ks} + A_{00}R_{00}e^{i4ks} + A_{00}R_{00}^{2}e^{i6ks} + \ldots = \frac{A_{00}e^{i2ks}}{1-R_{00}e^{i2ks}} \tag{6.21}$$

where R_{00} is the reflection coefficient at the open end of the parallel plate waveguide [45] [50], and s is the depth of

the outer guide.

The total radiation pattern of the array of Fig.6.1 is calculated by adding the radiation field caused by the finite depth of the outer guides to the fields radiated from the array of Fig.6.2. The additional fields consist of fields radiated directly from the outer guides (Fig.5.1), and fields from other edges excited by fields in a shorted guide (Figs.6.5 and 6.6). Since all fields in the outer guides have been diffracted at least once, the ray paths in Figs.6.5 and 6.6 represent fields including quadruple diffraction.

Radiation from the outer guides shown in Fig.5.1 is simply the pattern $P_0(a)$ in (5.21) and (5.22) of a parallel-plate waveguide multiplied by A of (6.21). Scattering from other edges due to radiation from the outer guides is calculated by considering the ray paths in Figs.6.5 and 6.6.

In Fig.6.5a the field from the edge y=d/2, z=0 is

$$u_{1'2}^{a} = \frac{C_0'(d)}{2} G(d,\theta)E(r). \tag{6.22}$$

In Fig.6.5b the field from the same edge is

$$u_{1'3}^{b} = \frac{C_0'(d)}{4} G(2d,\theta)E(r) - \frac{e^{i\pi/4}}{4\sqrt{2\pi}} C_0'(d)E(d)G(d,\theta)E(r). \tag{6.23}$$

In Fig.6.5c the field from the same edge is

$$u_{1'3}^{c} = \frac{-C_0'(a)}{4} G(d+a,\theta)E(r) - \frac{e^{i\pi/4}}{4\sqrt{2\pi}} C_0'(a)E(a)G(d,\theta)E(r). \tag{6.24}$$

In Fig.6.6 the field from the edge y=(d+2a)/2, z=0 is

$$u_{3'3} = \frac{C_0'(d)}{4} G(d+a,\theta)E(r) + \frac{e^{i\pi/4}}{4\sqrt{2\pi}} C_0'(d)E(d)G(a,\theta)E(r). \tag{6.25}$$

The fields (6.22), (6.23) and (6.24) must be added to give the field P_1' from the edge y=d/2, z=0 excited by radiation from the outer guides. Similarly (6.25) gives the field P_3' from the edge y=d/2+a, z=0. Similar calculations of the fields P_2' from the edge y=-d/2, z=0, and P_4' from y=-d/2-a, z=0 show that

$$P_2' = -P_1' \tag{6.26}$$

$$P_4' = -P_3' \,. \tag{6.27}$$

The ray paths used to calculate P_2' and P_4' are the image about the z-axis of those shown in Fig.6.5 and 6.6.

The radiation caused by the finite depth of the outer guides is the array sum of P_0 and P_n' multiplied by the coupling coefficient A. This radiation must be added to P_t in (6.2) and (6.3) to obtain the complete radiation pattern P_{total} for the array of Fig.6.1.

In the first quadrant for $0 < \theta < \pi/2$ all edges except that at y=d/2+a, z=0 are shadowed and do not contribute to the radiated fields, so that

$$P_{total} = P_k + AP_3' e^{-ik(\frac{d+2a}{2})\sin\theta} + AP_0 e^{-ik(\frac{d+a}{2})\sin\theta} \,. \tag{6.28}$$

In the second quadrant for $\pi/2 < \theta < \pi$

$$P_{total} = P_t + AP'_3\, e^{-ik(\frac{d+2a}{2})\sin\theta} + AP_0(a)\, e^{-ik(\frac{d+a}{2})\sin\theta} + AP'_1\, e^{-ik\frac{d}{2}\sin\theta} + AP'_2\, e^{+ik\frac{d}{2}\sin\theta} + AP_0(a)\, e^{+ik(\frac{d+a}{2})\sin\theta} + AP'_4\, e^{+ik(\frac{d+2a}{2})\sin\theta} \quad (6.29)$$

This pattern is symmetrical about $\theta = \pi$ so that $P_{total}(2\pi-\theta) = P_{total}(\theta)$.

6.5 NUMERICAL AND EXPERIMENTAL RESULTS

The radiation pattern of a three element array of parallel plate waveguides calculated by ray-optical methods is compared to measured E-plane patterns of an H-plane sectoral horn with appendages added to simulate the outer guides (Fig. 1.2). The patterns are plotted for $-180° < \theta' < 180°$ ($\theta' = \theta-\pi$).

When the outer guides are of infinite depth (Fig.6.2), the radiation pattern P_t, given by (6.2) and (6.3), has a somewhat narrower beamwidth then a single guide.

The addition of the outer guides altered the radiation pattern of the central driven guide in different ways depending on their depth. Adjustment of the depth of the outer guides varies the phase of A in (6.21).

The pattern of the three-element array with outer

guides shorted shows a pronounced reduction of the beamwidth compared to that of a single guide when the radiation from all three guides is in phase (arg A = 0) (Fig.6.8). Adjustment of the frequency such that this phase difference is near 180° produces a pattern with a null on the beam axis and two main lobes to either side (Figs.6.9,6.13) These pattern shapes with varying A are what would be expected from a Fourier transform of the aperture fields [27]. For another value of this phase the pattern amplitude was essentially constant over an angular sector of about ± 60° (Fig.6.10). In all cases the phase of the pattern is relatively constant in the forward direction and the back radiation is substantially reduced compared to that of a single guide. Thus this parallel-plate waveguide can produce a variety of patterns by adjustment of the depth of the outer guides or the frequency.

The calculated patterns are expected to be least accurate at about $\theta' = 90°$ off the beam axis near the shadow boundary in the aperture plane for the reasons mentioned in Chapter 2. At angles slightly greater then 90° only the outermost edge contributes to the radiation (6.28), whereas at angles less then 90° all edges contribute (6.29), and consequently a discontinuity in the pattern is found at $\theta' = 90°$. This discontinuity may be reduced by including more ray paths along the shadow boundary. Terms up to quadruple diffraction appear to be sufficient, since more terms do not reduce the discontinuity significantly, and the number of terms grows very rapidly for higher orders of diffraction.

The discontinuity at $\theta' = 90^\circ$ varies between -4dB and +4dB depending on the depth of the outer guides and the frequency. The problems on the shadow boundaries were discussed in more detail in Chapter 2.

To effect a significant improvement in the pattern accuracy using ray-optical techniques may require that the method of Lee and Boersma [32] be applied to find the fields near the shadow boundary. A solution for the diffraction problem of a line source incident on two non-staggered half-planes is needed, where the source, observation point and half-plane edges are all collinear. Such a ray-optical solution, which would be used to evaluate the fields in Figs.6.3b, 6.3c, 6.4b, 6.5c and 6.6, is not presently available.

The experimental patterns were generally within 1 dB of the calculated results up to $\theta' = \pm 60^\circ$, and within 3dB up to $\theta' = \pm 150^\circ$. Any pattern asymmetry and the small oscillations are caused by site reflections. The patterns near $\theta' = 180^\circ$ could not be measured accurately because of blockage by the antenna mounting arrangement.

6.6 SUMMARY

Radiation from a finite, rather than an infinite aperiodic array of open-ended parallel plate waveguides has been analyzed by ray-optical methods. Only small arrays are tractable however for the numbers of ray required for reasonable accuracy rapidly increases with the number of

diffracting edges. Here a three-element array has been analyzed with triple diffraction by the four edges included.

The calculated results contain a discontinuity at 90° off the beam axis because most of the diffracting edges are shadowed in the backward direction. This discontinuity can be reduced by taking more ray paths into account, but cannot be eliminated for all values of d,a and s , even with a larger number of rays.

The ray-optical analysis is only valid for waveguide dimensions of moderate and large width. Inaccuracies are expected when the dimensions are reduced to $\lambda/3$ or less, particularly in the calculation of the fields in the aperture plane along the shadow boundary.

The experimental patterns generally agree with those calculated ones, so that the H-plane sectoral horn with appendages appears to simulate a parallel-plate waveguide array in the TEM mode reasonably well. The outer guides increased or decreased the beamwidth depending on the dimensions of the guides and the frequency. Thus the pattern of this waveguide antenna array may be adjusted to suit the application.

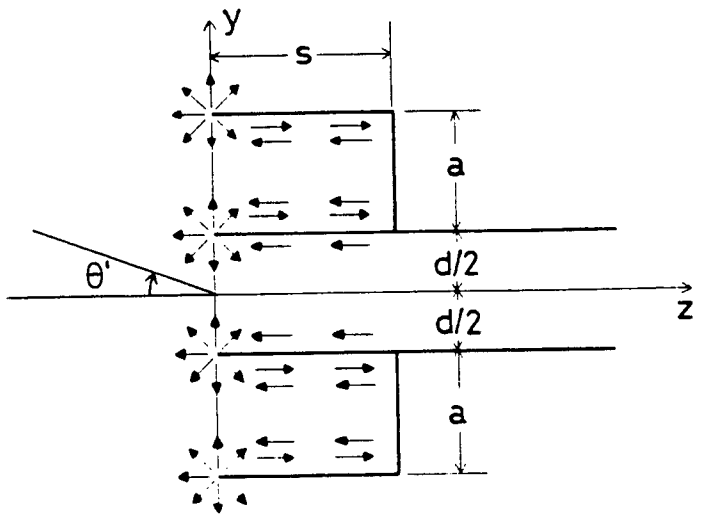

Fig. 6.1
three element array of parallel plate waveguides with outer guides shorted

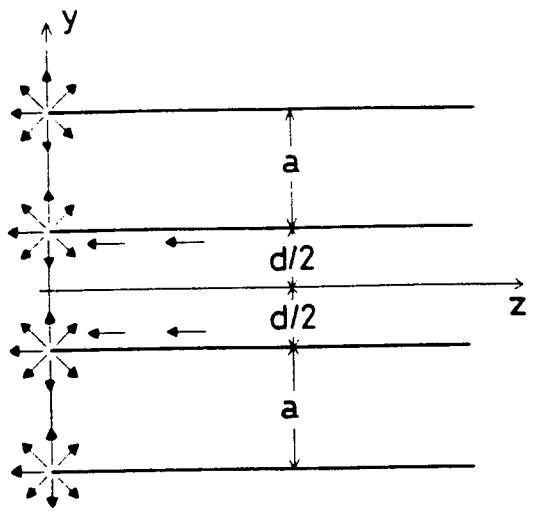

Fig. 6.2
three element array of parallel plate waveguides with outer guides of infinite depth

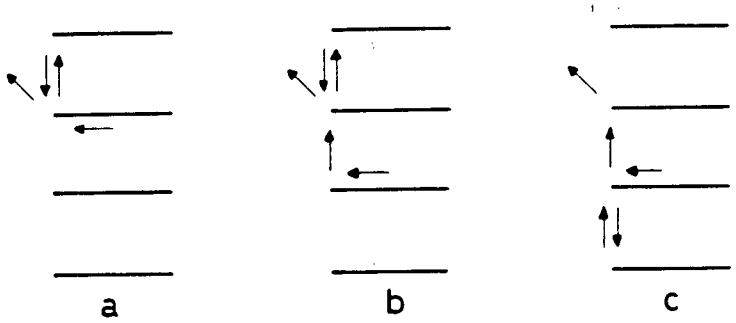

Fig. 6.3
ray paths from central
guides to edge 1

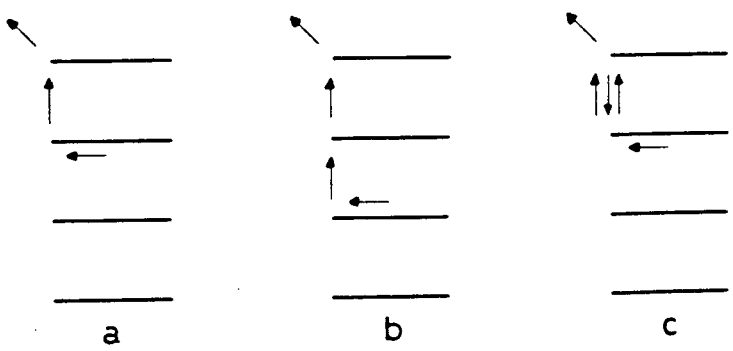

Fig. 6.4
ray paths from central guide
to edge 3

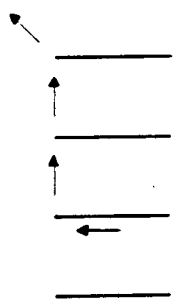

Fig. 6.6
ray path from outer
guide to edge 3

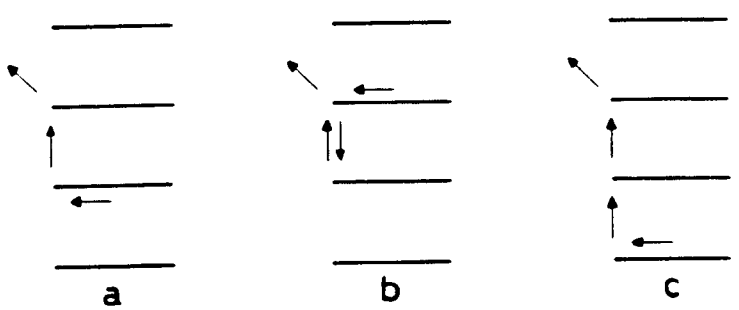

Fig. 6.5
ray paths from outer guides to edge 1

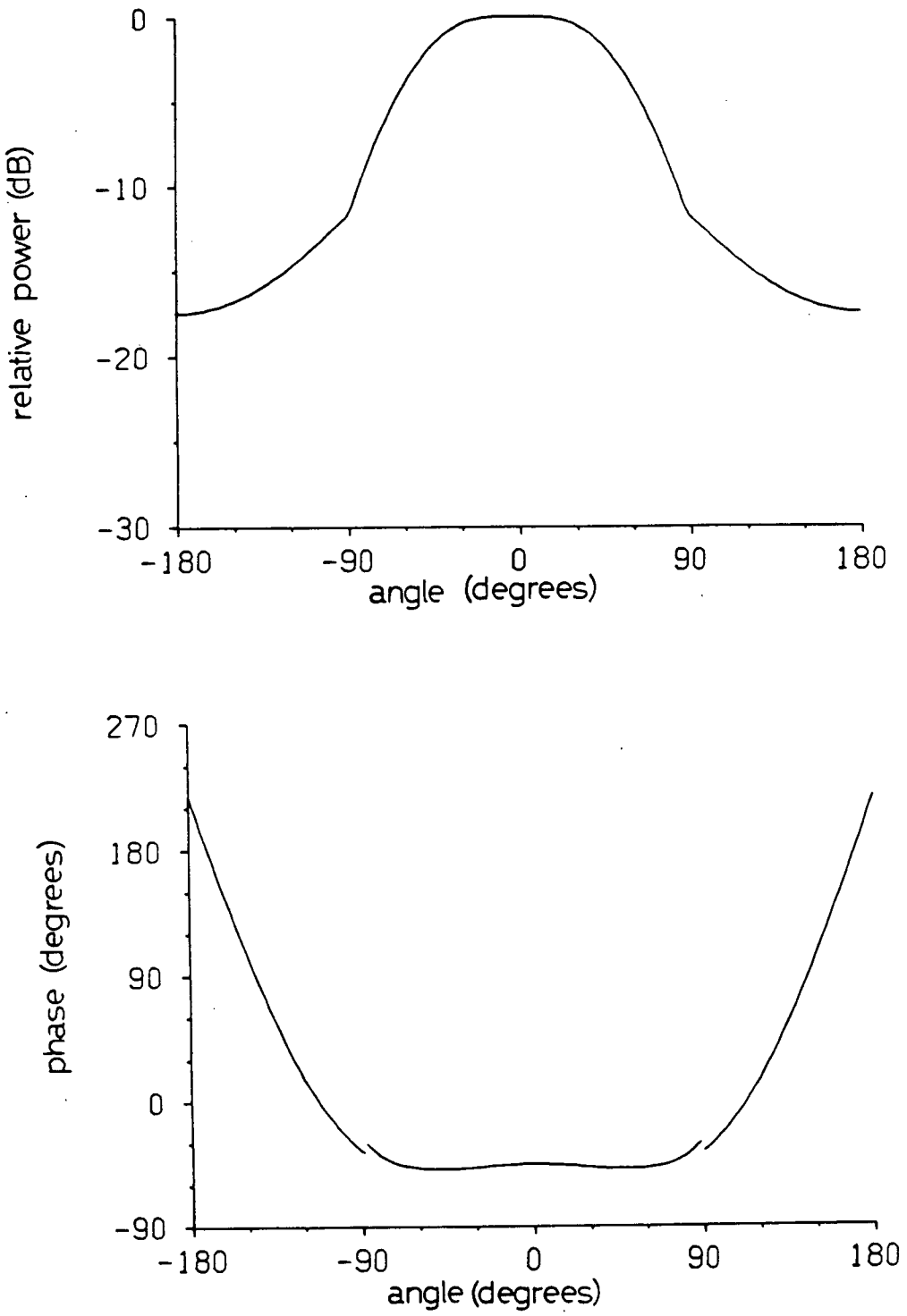

Fig. 6.7 Radiation pattern of three element array with outer guides of infinite depth (a=d=0. 407λ).

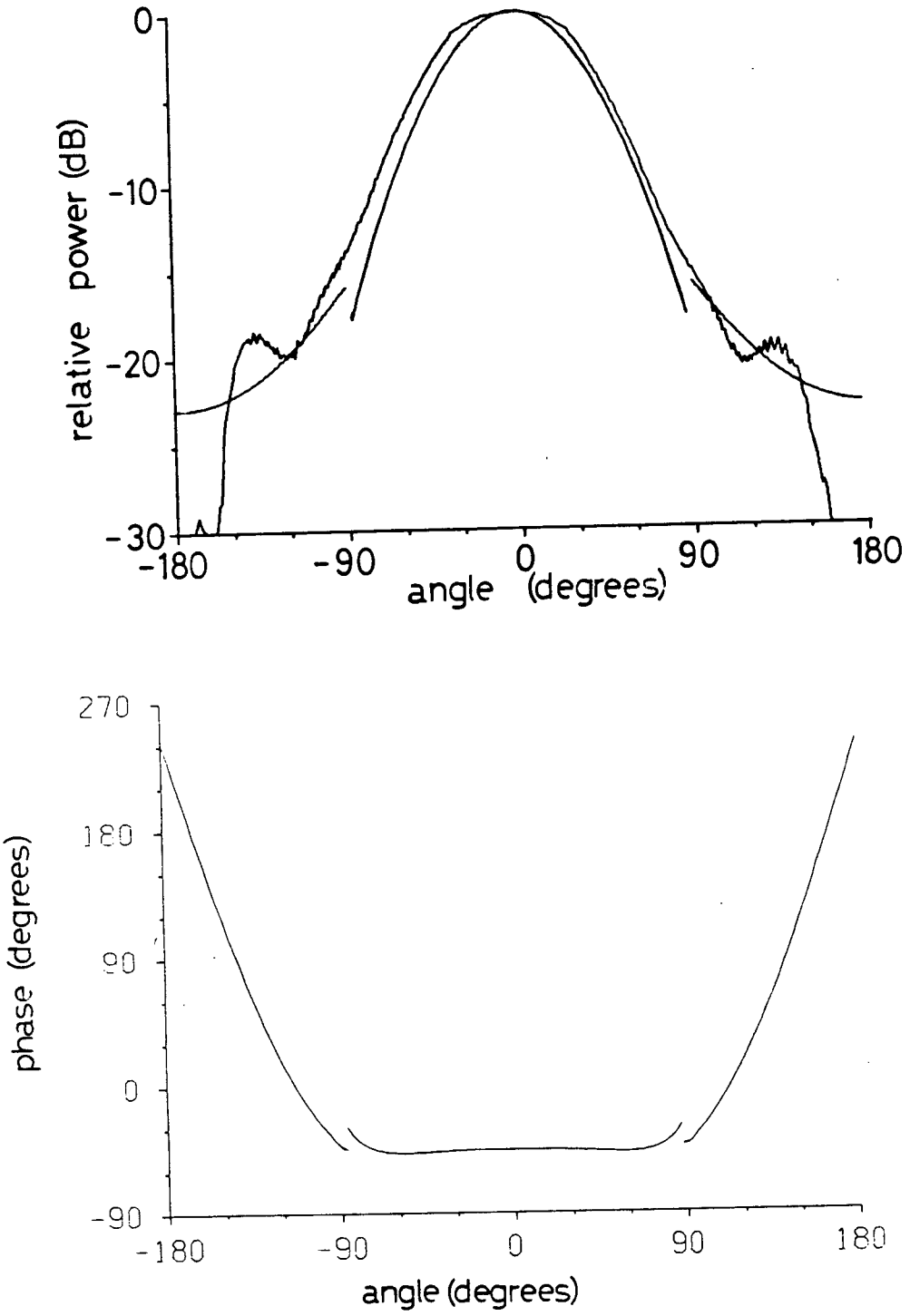

Fig. 6.8 Radiation pattern of three element array
a=d=0. 450λ s=0. 856λ A=0.131 ∠ 0°.

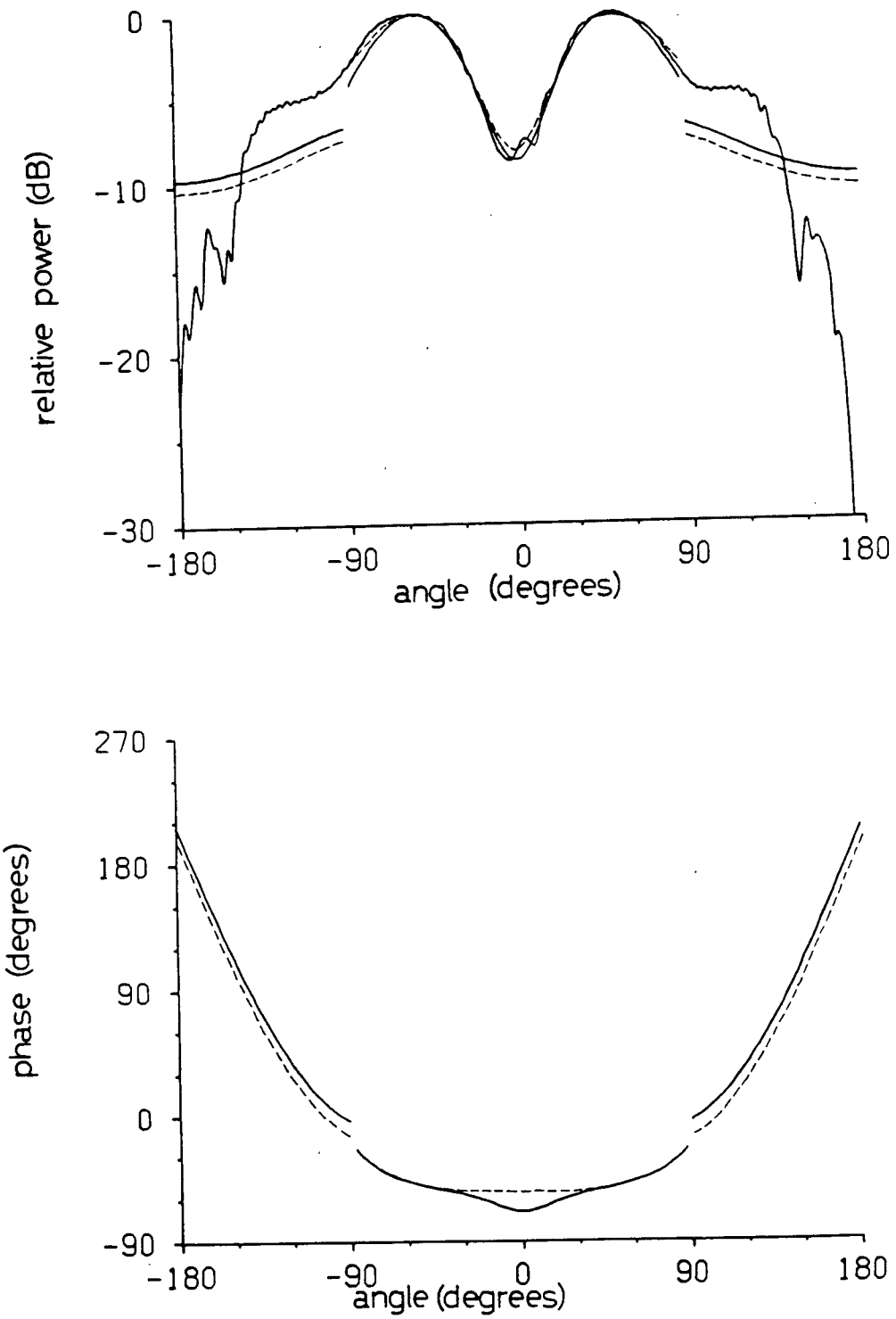

Fig. 6.9 Radiation pattern of three element array
a=d=0. 339λ s=0. 645λ A=0. 371 ∠ -171°

——— using (5.12)
- - - - using (5.11)

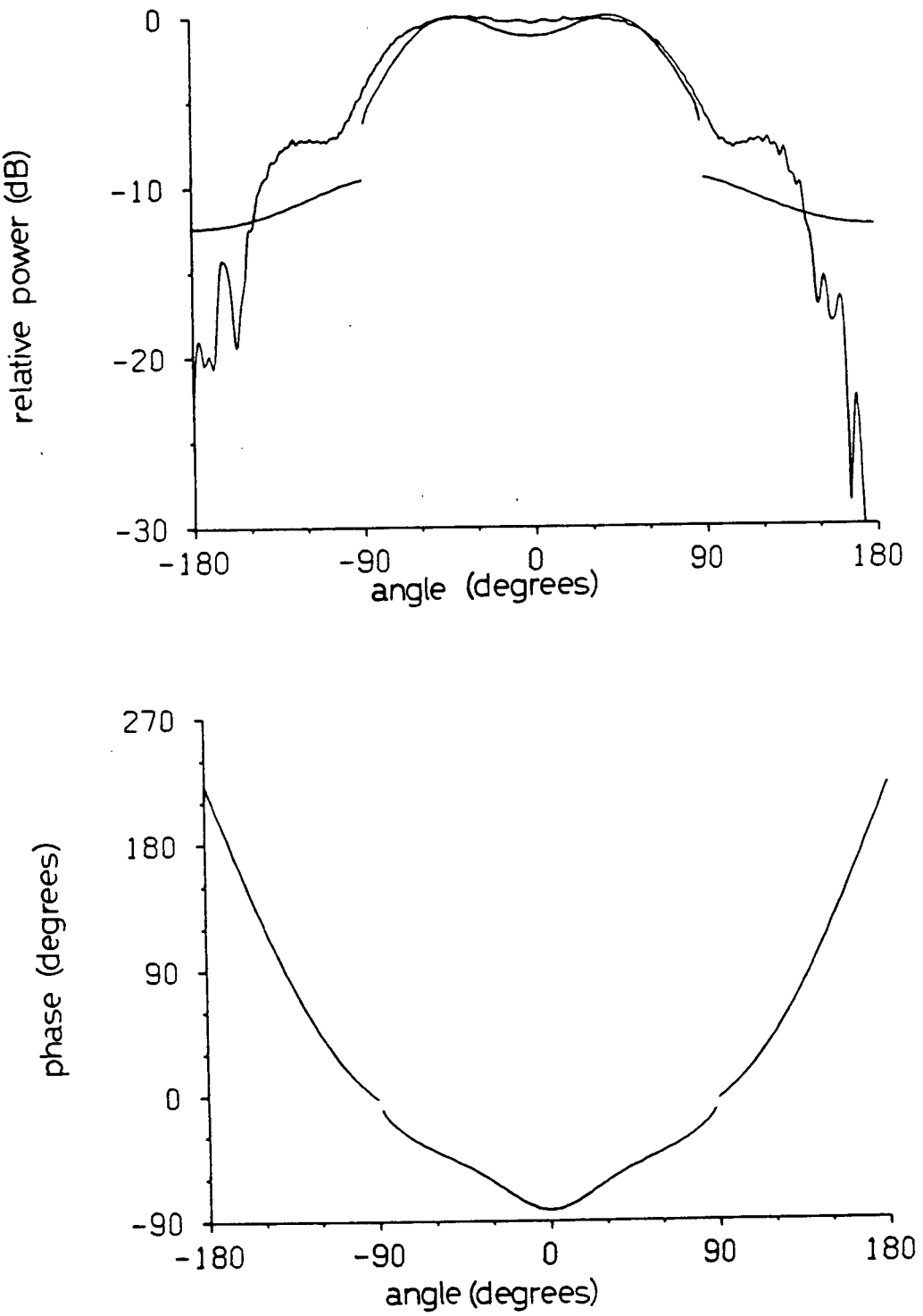

Fig. 6.10 Radiation pattern of three element array
a=d=0. 356λ s=0. 677λ A=0. 308 ∠ -134°.

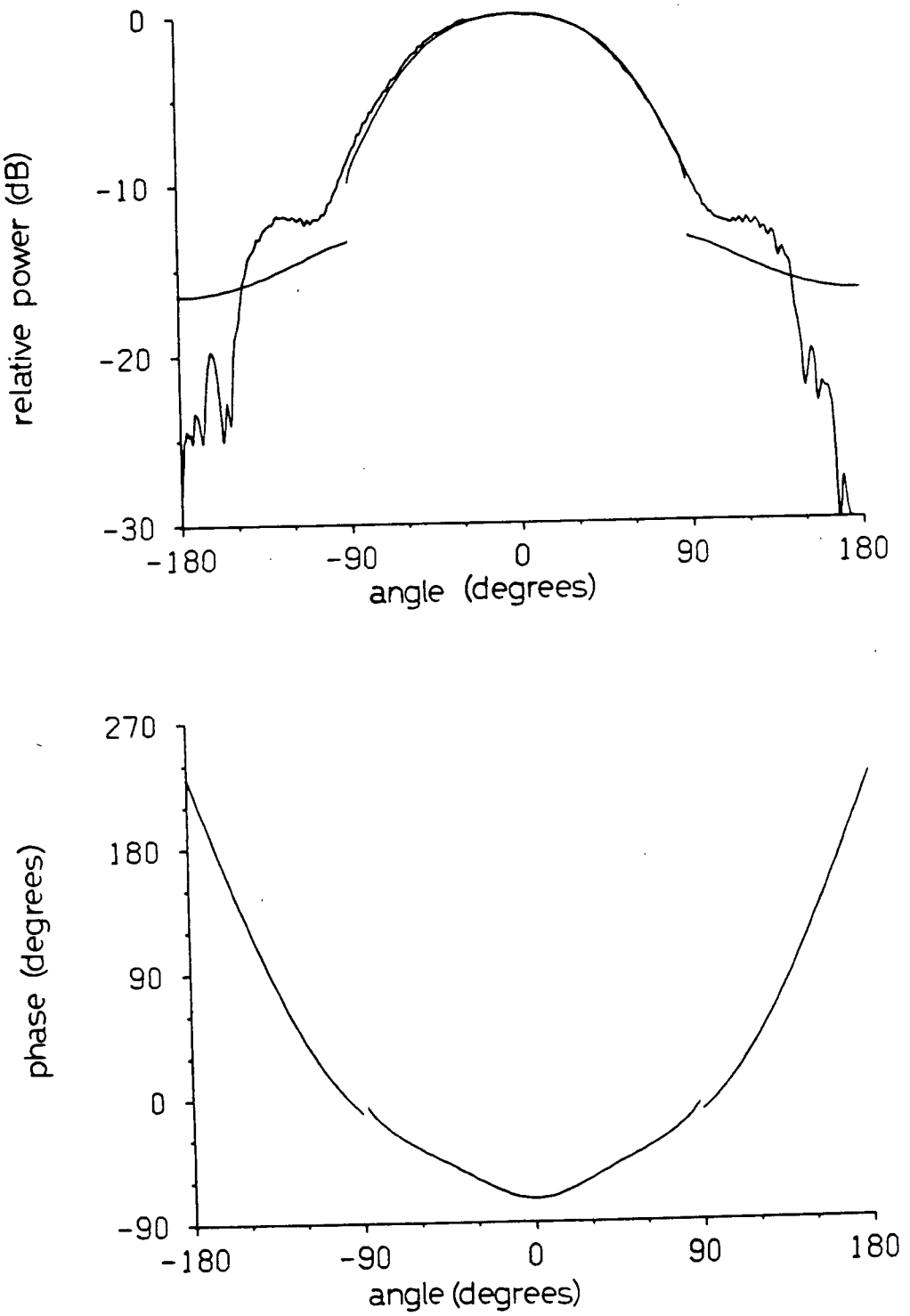

Fig. 6.11 Radiation pattern of three element array
a=d=0. 373λ s=0. 709λ A=0. 247 ∠ +104°.

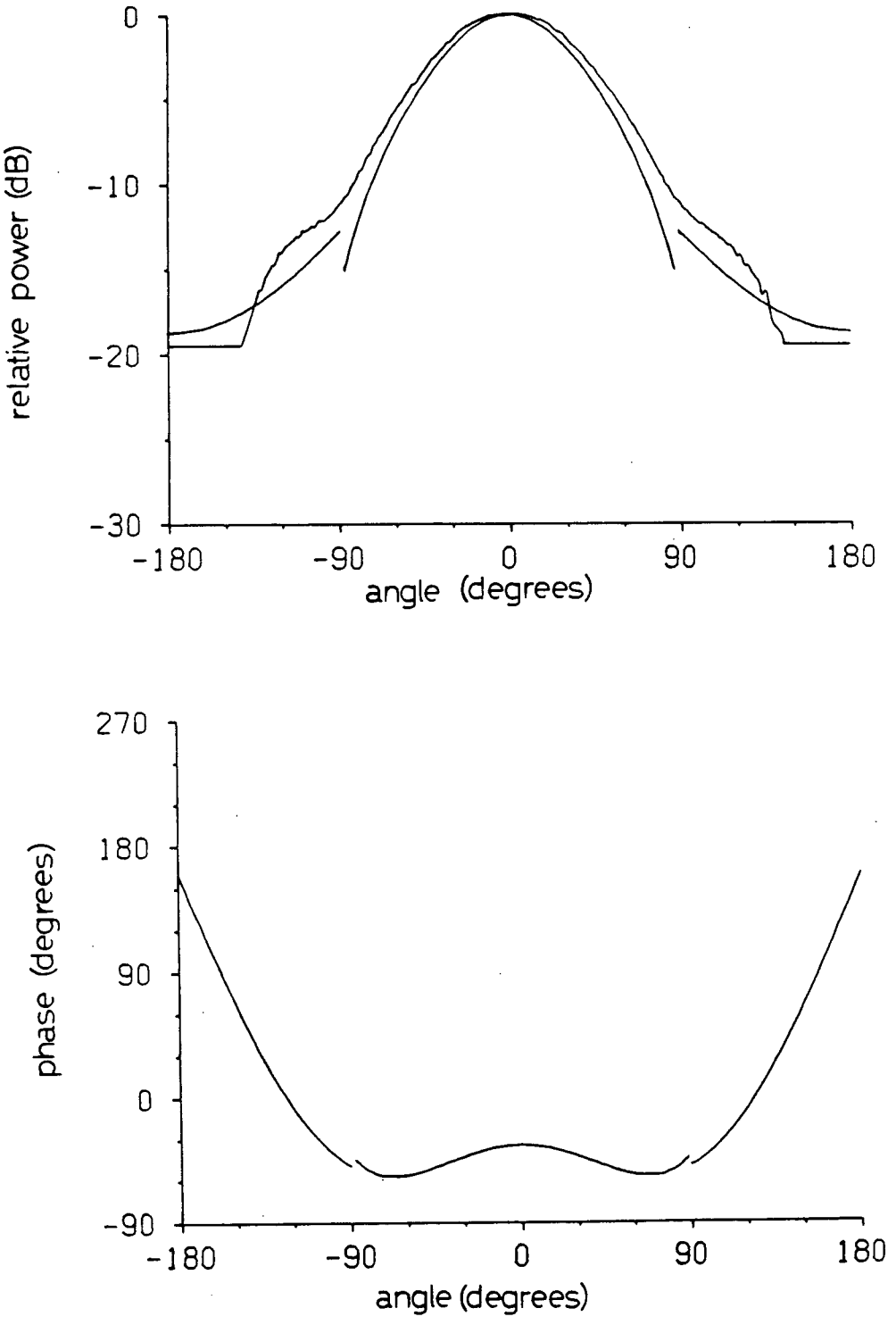

Fig. 6.12 Radiation pattern of three element array
a=d=0. 389λ s=0. 459λ A=0. 199 ∠ +38°.

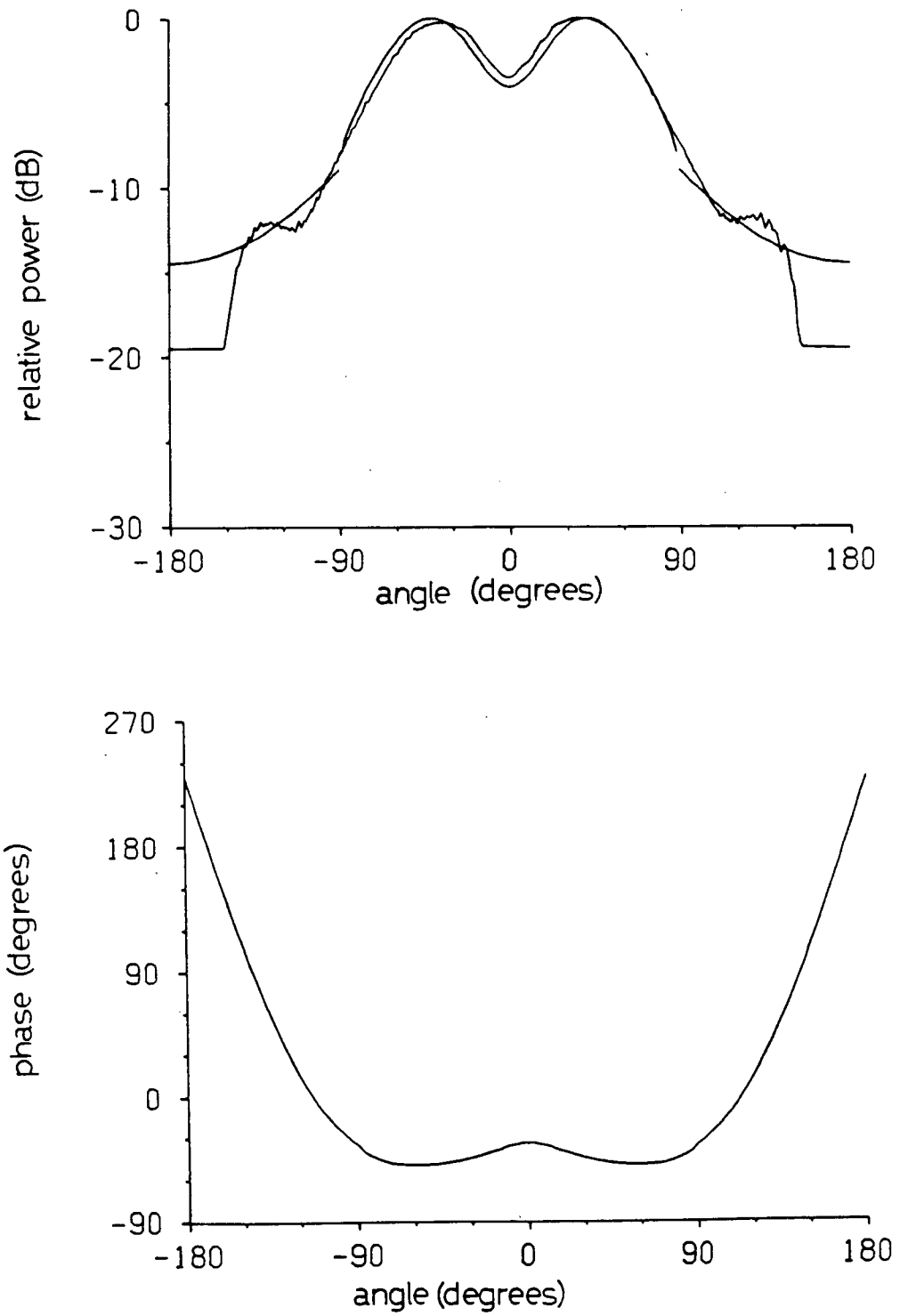

Fig. 6.13 Radiation pattern of three element array
a=d=0. 441λ s=0. 597λ A=0. 223 ∠ +166°.

Chapter 7

RADIATION PATTERN OF FIVE ELEMENT WAVEGUIDE ARRAY

7.1 RAY-OPTICAL FORMULATION

The radiation pattern of a five element parallel plate waveguide array (Fig.7.1,7.2) may be found by extending the results for the three element array considered in Chapter 6. The additional outer guides in the five element array allow the formation of many more ray paths which must be taken into account. The patterns will be calculated for outer guides of both infinite (Fig.7.2) and finite (Fig.7.1) depth and will be compared with results found by other methods [29] [38] and experimental results respectively.

Consider five adjacent semi-infinite parallel plate waveguides consisting of six perfectly conducting half-planes in $z>0$ at $y=-d/2-2a$, $y=-d/2-a$, $y=-d/2$, $y=+d/2$, $d=+d/2+a$ and $y=d/2+2a$ (Fig.7.2). As in Chapter 6 the incident mode in the central guide $-d/2<y<+d/2$, $z>0$, given by (5.7), is decomposed into two plane waves each with amplitude

$$u_i = \frac{1}{2} \tag{7.1}$$

at the edges $y=-d/2$, $z=0$ and $y=+d/2$, $z=0$. These two plane waves are represented by the incident rays in the central guide of Fig.7.2. Many of the ray paths which must be considered to calculate the radiation pattern are shown in Chapter 6. The additional ray paths which occur in the five

element array but not in the three element array are shown in Figs.7.3-7.7.

7.2 RADIATION PATTERN WITH OUTER GUIDES OF INFINITE DEPTH

The total radiation pattern P_t for the array of Fig.7.2 is given by the sum of the fields from all edges. In the first quadrant all but the outermost edges are shadowed so that for $0<\theta<\pi/2$ only the edge y=d/2+2a, z=0 is visible and

$$P_t = P_5 \, d^{-ik(\frac{d+4a}{2})\sin\theta} \tag{7.2}$$

In the second quadrant ($\pi/2<\theta<\pi$) all edges are visible and

$$\begin{aligned} P_t = {} & P_5 \, e^{-ik(\frac{d+4a}{2})\sin\theta} \\ & + P_3 \, d^{-ik(\frac{d+2a}{2})\sin\theta} \\ & + P_1 \, d^{-ik\frac{d}{2}\sin\theta} \\ & + P_0 \\ & + P_2 \, e^{+ik\frac{d}{2}\sin\theta} \\ & + P_4 \, e^{+ik(\frac{d+2a}{2})\sin\theta} \\ & + P_6 \, e^{+ik(\frac{d+4a}{2})\sin\theta} \end{aligned} \tag{7.3}$$

where P_n is a field radiated from edge #n. The pattern is symmetrical about $\theta = \pi$ so that $P_t(2\pi-\theta) = P_t(\theta)$.

The fields P_3 and P_4 calculated in Chapter 6 must now be modified to take into account additional ray paths created by the presence of the new outer guides (Fig.7.3). The fields P_1 and P_2 need not be modified because there are no additional ray paths up to quadruple diffraction. The fields P_5 and P_6 are new and must be calculated using the ray paths in Fig.7.4.

To calculate the additional contribution to P_3 consider the ray diagram of Fig.7.3. The incident field u_i given by (7.1) is diffracted at the edge y=+d/2, z=0. From (3.18) as observed at y=d/2+a, z=0 the diffracted field is a line source

$$u_{31}^{a} = \frac{C_0'(a)}{2} E(r) \tag{7.4}$$

located at the diffracting edge. This field is again diffracted at y=d/2+a, z=0 and from (3.29) the resultant field is

$$u_{32}^{a} = \frac{C_0'(a)}{4} E(a+r) + \frac{e^{i\pi/4}}{4\sqrt{2\pi}} C_0'(a)E(a)E(r). \tag{7.5}$$

u_{32}^{a} is made up of two line sources, one centred at y=+d/2, z=0, the other at y=+d/2+a, z=0. This field is again diffracted at y=+d/2+2a, z=0 and from (3.26) the resultant field is

$$u_{33}^{a} = \frac{C_0'(a)}{8} E(a+b+r) - \frac{e^{i\pi/4}}{8\sqrt{2\pi}} C_0'(a)E(a+b)E(r)$$

$$+ \frac{e^{i\pi/4}}{8\sqrt{2\pi}} C_0'(a)E(a)E(b+r). \tag{7.6}$$

This field is again diffracted at y=+d/2+a, z=0 and from (5.3) the resultant field is

$$u_{34}^{a} = \frac{-C_0'(a)}{8} G(a+2b,\theta)E(r) + \frac{e^{i\pi/4}}{8\sqrt{2\pi}} C_0'(a)E(a+b)G(b,\theta)E(r)$$

$$- \frac{e^{i\pi/4}}{8\sqrt{2\pi}} C_0'(a)E(a)G(2b,\theta)E(r) , \qquad (7.7)$$

u_{34}^{a} must be added to P_3 in Chapter 6 to give the field P_3 in (7.3) which represents the field from the edge y=d/2+a,z=0 up to and including quadruple diffraction.

To calculate the field P_5 consider the ray diagrams of Fig.7.4. In Fig.7.4a the incident field u_i is given by (7.1), u_{51}^{a} is given by (7.4) and u_{52}^{a} is given by (7.5). This field is again diffracted at y=+d/2+a, z=0 and from (5.3) the resultant field is

$$u_{53}^{a} = \frac{C_0'(a)}{8} G(a+b,\theta)E(r) + \frac{e^{i\pi/4}}{8\sqrt{2\pi}} C_0'(a)E(a)G(b,\theta)E(r). \qquad (7.8)$$

In Fig.7.4b the incident field u_i given by (7.1) is diffracted at the edge y=-d/2,z=0. From (3.18) as observed at y=+d/2,z=0 the diffracted field is a line source

$$u_{51}^{b} = \frac{-C_0'(d)}{2} E(r) \qquad (7.9)$$

located at the diffracting edge. This field u_{51}^{b} is again diffracted at y=+d/2, z=0 and from (3.29) the resultant field is

$$u_{52}^{b} = \frac{-C_0'(d)}{4} E(d+r) - \frac{e^{i\pi/4}}{4\sqrt{2\pi}} C_0'(d)E(d)E(r) . \qquad (7.10)$$

u_{52}^{b} is made up of two line sources, one centred at y=-

d/2,z=0, the other at y=+d/2, z=0. This field is again diffracted at y=+d/2+a, z=0 and from (3.29) the resultant field is

$$u_{53}^{b} = \frac{-C_0'(d)}{8} E(d+a+r) - \frac{e^{i\pi/4}}{8\sqrt{2\pi}} C_0'(d)E(d+a)E(r)$$

$$- \frac{e^{i\pi/4}}{8\sqrt{2\pi}} C_0'(d)E(d)E(a+r) . \qquad (7.11)$$

u_{53}^{b} is made up of three line sources at y=-d/2, y=+d/2+a and y=+d/2 respectively. This field is again diffracted at y=+d/2+2a, z=0 and from (5.3) the resultant field is

$$u_{54}^{b} = \frac{-C_0'(d)}{8} G(d+a+b,\theta)E(r) - \frac{e^{i\pi/4}}{8\sqrt{2\pi}} C_0'(d)E(d+a)G(b,\theta)E(r)$$

$$- \frac{e^{i\pi/4}}{8\sqrt{2\pi}} C_0'(d)E(d)G(a+b,\theta)E(r) . \qquad (7.12)$$

The sum of (7.8) and (7.12) represents the field P_5 from the edge y=d/2+2a,z=0 up to and including quadruple diffraction.

Similar calculations for P_6 and the additional contributions to P_4 show that

$$P_4 = -P_3 \qquad (7.13)$$

$$P_6 = -P_5 . \qquad (7.14)$$

The ray paths used to calculate P_6 and the additional contributions to P_4 are the image about the z-axis of those in Figs.7.3 and 7.4.

The results for P_n are substituted in (7.2) and (7.3) to give the total radiation pattern of the array of Fig.7.2 with parasitic guides of infinite depth.

7.3 RADIATION WITH OUTER GUIDES SHORTED

Consider the array of Fig.7.1 which is equivalent to Fig.7.2 except that the outer guides are now of finite depth. The fields coupled into these guides will now be reflected from the shorted end and reradiated. The TEM coupling coefficient $A_{00}(d,a)$ between adjacent guides of width d and a and $B_{00}(d,a,b)$ between guides of width b and a separated by distance d were calculated in Chapters 3 and 4 respectively. These coupling coefficients are used to determine the values A_1 and A_2 of the fields in the outer guides at the aperture plane relative to the fields from the central driven guide.

The value A_1 of the fields in the first outer guide $+d/2<y<+d/2+a$ is, from (6.21) given by

$$A_1 = \frac{A_{00}(d,a)\, e^{i2ks_1}}{1-R_{00}(a)\, e^{i2ks_1}} , \qquad (7.15)$$

where $R_{00}(a)$ is the reflection coefficient at the open end of the guide of width a, and s_1 is the depth of the first outer guide. To determine the value A_2 of the fields in the second outer guide $+d/2+a<y<+d/2+a+b$, the coupling from both the driven guide and the first outer guide into the second outer guide must be taken into account. The energy coupled into the second outer guide is given by

$$B_{00}(d,a,b) + A_1 A_{00}(a,b) \qquad (7.16)$$

The value of the field A_2 at the aperture plane is the sum of a geometric series

$$A_2 = \frac{[B_{00}(d,a,b) + A_1 A_{00}(a,b)]e^{iks_2}}{1-R_{00}(b)\, e^{iks2}} , \tag{7.17}$$

where S_2 is the depth of the second outer guide.

The total radiation pattern of the array of Fig.7.1 is calculated by adding the radiation field caused by the finite depth of the outer guides to the fields radiated from the array of Fig.7.2. The additional fields consist of fields radiated directly from the outer guides (Fig.5.1), and fields from other edges excited by fields in a shorted guide (Fig.7.5-7.7) Radiation from the outer guides shown in Fig.5.1 is simply the pattern P_0 in (5.21) and (5.22) of a parallel plate waveguide multiplied by A_1 or A_2 Scattering from other edges due to radiation from the outer guides is calculated by considering the ray paths in Fig.7.5-7.7.

In Fig.7.5a the field $u_{5"2}^{a}$ from the edge y=+d/2+a+b,z=0 is given by

$$u_{5"2}^{a} = \frac{C_0'(b)}{2} G(b,\theta)E(r) . \tag{7.18}$$

In Fig.7.5b the field $u_{5"3}^{a}$ from the edge y=+d/2+a+b,z=0 is given by

$$u_{5"3}^{b} = \frac{-C_0'(a)}{4} G(a+b,\theta)E(r) - \frac{e^{i\pi/4}}{4\sqrt{2\pi}} C_0'(a)E(a)G(b,\theta)E(r) . \tag{7.19}$$

The fields $u_{5"2}^{a}$ and $u_{5"3}^{b}$ are added to give the field $P_5"$ from the edge y=+d/2+a+b,z=0 excited by radiation from the first outer guide. In Fig.7.6a the field

$u_{3"3}^{a}$ from the edge y=+d/2+a,z=0 is given by

$$u_{3"3}^{a} = \frac{-C_0'(b)}{4} G(2b,\theta)E(r) + \frac{e^{i\pi/4}}{4\sqrt{2\pi}} C_0'(b)E(b)G(b,\theta)E(r) . \qquad (7.20)$$

In Fig.7.6b the field $u_{3"3}^{b}$ from the edge y=+d/2+a,z=0 is given by

$$u_{3"3}^{b} = \frac{C_0'(a)}{4} G(2a,\theta)E(r) - \frac{e^{i\pi/4}}{4\sqrt{2\pi}} C_0'(a)E(a)G(a,\theta)E(r) . \qquad (7.21)$$

$u_{3"3}^{a}$ is the field P_{31}'' from the edge y=+d/2+a,z=0 excited by radiation from the first outer guide in the presence of the second outer guide, and would not be present if the second outer guide was missing. $u_{3"3}^{b}$ is the field P_{32}'' from the same edge excited by radiation from the second outer guide.

In Fig.7.7a the field $u_{1"2}^{a}$ from the edge y=+d/2,z=0 is given by

$$u_{1"2}^{a} = \frac{-C_0'(a)}{2} G(a,\theta)E(r) . \qquad (7.22)$$

In Fig.7.7b the field $u_{1"3}^{b}$ from the edge y=+d/2,z=0 is given by

$$u_{1"3}^{b} = \frac{C_0'(b)}{4} G(a+b,\theta)E(r) + \frac{e^{i\pi/4}}{4\sqrt{2\pi}} C_0'(b)E(b)G(a,\theta)E(r) . \qquad (7.23)$$

In Fig.7.7c the field $u_{1"3}^{c}$ from the edge y=+d/2,z=0 is given by

$$u_{1"3}^{c} = \frac{C_0'(a)}{4} G(a+d,\theta)E(r) + \frac{e^{i\pi/4}}{4\sqrt{2\pi}} C_0'(a)E(a)G(d,\theta)E(r) . \qquad (7.24)$$

The fields (7.22), (7.23) and (7.24) are added to give the field P_1'' from the edge y=+d/2,z=0 excited by radiation from the second outer guide which would not be present with only one outer guide.

Similar calculations from the fields P''_2 for the edge y=-d/2,z=0, P''_{41} and P''_{42} from the edge y=-d/2-a,z=0 and P''_6 from the edge y=-d/2-a-b show that

$$P''_2 = -P''_1 \tag{7.25}$$

$$P''_{41} = -P''_{31} \tag{7.26}$$

$$P''_{42} = -P''_{42} \tag{7.27}$$

$$P''_6 = -P''_5 \tag{7.28}$$

The ray paths used to calculate P''_2, P''_{41}, P''_{42} and P''_6 are the image about the z-axis of those shown in Figs.7.5,7.6 and 7.7. The radiation caused by the finite depth of the outer guides is the array sum of $P_0(a)$, $P_0(b)$ and P''_n multiplied by the appropriate coefficient A_1 or A_2. This radiation must be added to P_t of (7.2) and (7.3) to obtain the complete radiation pattern P_{total} of the array of Fig.7.1.

In the first quadrant $0 < \theta < \pi/2$ all edges except that at y=+d/2+a+b are shadowed and do not contribute to the radiated field so that

$$P_{total} = P_{t1} + A_1 P''_5 e^{-ik(\frac{d+2a+2b}{2})\sin\theta} + A_2 P_0(b)\, e^{-ik(\frac{d+2a+b}{2})\sin\theta} . \tag{7.29}$$

In the second quadrant for $\pi/2 < \theta < \pi$

$$P_{total} = P_t + A_1 P''_5 e^{-ik(\frac{d+2a+2b}{2})\sin\theta}$$

$$+ A_2 P_0(b)\, e^{-ik\left(\frac{d+2a+b}{2}\right)\sin\theta}$$

$$+ [A_1 P'_3 + A_1 P''_{31} + A_2 P''_{32}] e^{-ik\left(\frac{d+2a}{2}\right)\sin\theta}$$

$$+ A_1 P_0(a)\, e^{-ik\left(\frac{d+a}{2}\right)\sin\theta}$$

$$+ [A_1 P'_1 + A_2 P''_1] e^{-ik\frac{d}{2}\sin\theta}$$

$$+ [A_1 P'_2 + A_2 P''_2] e^{+ik\frac{d}{2}\sin\theta}$$

$$+ A_1 P_0(a)\, e^{+ik\left(\frac{d+a}{2}\right)\sin\theta}$$

$$+ [A_1 P'_4 + A_1 P''_{41} + A_2 P''_{42}] e^{+ik\left(\frac{d+2a}{2}\right)\sin\theta}$$

$$+ A_2 P_0(b)\, e^{+ik\left(\frac{d+2a+b}{2}\right)\sin\theta}$$

$$+ A_1 P''_6\, e^{+ik\left(\frac{d+2a+2b}{2}\right)\sin\theta} \quad . \tag{7.30}$$

where P'_n are given in Chapter 6. The pattern is symmetrical about $\theta = \pi$ so that $P_{total}(2\pi-\theta) = P_{total}(\theta)$.

7.4 NUMERICAL AND EXPERIMENTAL RESULTS

The radiation patterns of a five element waveguide array are compared with other theoretical results and the measured E-plane patterns of an H-plane sectoral horn with appendages to simulate the outer guides $(\theta' = \theta - \pi)$.

When the outer guides are of infinite depth the pattern consists of a single lobe (Fig.7.8,7.9). The fields are essentially constant over an angular range of about 90-120° degrees depending on the frequency. There is a small discontinuity (<1dB) at $\theta' = 90°$ off the beam axis in the aperture plane along the shadow boundary.

The patterns calculated here are compared to that found by residue calculus methods [38] in Fig.7.10. The patterns agree to within a fraction of a dB at all angles in the forward direction except near $\theta' = 90°$ in the aperture plane. Taking higher order diffraction terms reduces but does not eliminate this discrepancy on the shadow boundary.

In Fig.7.11 the ray-optical pattern is compared to that calculated for the case that the five element array is embedded in a simulated groundplane [29]. Over an angular range of 45° in the forward direction the two patterns agree remarkably well, despite the presence of the simulated groundplane. As expected, agreement is not so good for larger angles, because the groundplane requires the field to be zero at $\theta' = \pm 90°$.

When the guides are of finite depth it is possible to control the phase of the aperture field in the parasitic guides relative to that in the driven guide. Hence the radiation pattern may be adjusted to suit a particular application (Figs.7.12-7.18). More control of the pattern is possible for the five element array considered here as compared to the three element array, because there are more parameters which may be adjusted. In general the five

element patterns have a smaller beamwidth and steeper slopes then the three element patterns. The five element patterns may be adjusted to produce two adjacent nulls about the beam axis, whereas the three element patterns can produce only a single null at the beam axis. The phase of the five element patterns is generally more constant in the forward direction and the back radiation is less then the three element patterns.

As in the three element case, the patterns are least accurate at 90° off the beam axis along the shadow boundary. The discontinuity in the patterns is reduced by taking more ray paths into account; however no significant improvement is noted beyond quadruple diffraction. The discontinuity varies between +3dB and -3dB depending on the array parameters, which is larger then for the infinite depth case. The shadow boundary difficulties were discussed in more detail in Chapter 2. Because of the larger number of edges in a five element array, these difficulties may be expected to be greater here then for the three element array discussed in the preceding chapter.

The experimental patterns for the five element array (Figs.7.12-7.15) generally agree with the calculated ones to within an accuracy not quite as good as the three element patterns (1 dB up to $\theta'=60^\circ$ and 3dB up to $\theta'=150^\circ$), but still comparable. Thus the accuracy of the ray-optical pattern calculation appears to be degraded slightly when the array is made larger.

Additional calculations are performed for arrays for

which the guide depth was chosen to make the aperture fields in the parasitic guides exactly in phase or exactly out of phase with the driven guide. The aperture fields and the corresponding radiation patterns are shown in Figs.7.16-7.18). Relevant parameters of these patterns are tabulated in Table III.

Note that the pattern has the narrowest 3dB beamwidth when all aperture fields are in phase (Fig.7.17), as might be expected. However, the beam is not very flat across the top. When the aperture fields in the parasitic guide are out of phase (Fig.7.16) there is a deep null on the beam axis and two lobes at $\theta' = \pm 38^\circ$. When the aperture field is alternating in sign (Fig. 7.18) the pattern is a good approximation to a sector shape, considering the small size of the array. This is not surprising because the aperture fields for this case are a crude approximation of a truncated (sin x)/x curve (Fig.1.3), whose radiation pattern is expected to approximate a sector shape.

Note that the amplitude and phase of the aperture field are determined by the array dimensions and cannot be adjusted independently. A further improvement in the patterns would require that each element be excited as in a phased array.

7.5 SUMMARY

The radiation from a five element finite array of parallel plate waveguides has been analyzed the same ray-

optical methods used for the three element array in Chapter 6. The radiation pattern calculation is more complex however, because there are more diffracting edges and hence more ray paths to be taken into account.

When the outer guides are of infinite depth the agreement between the ray-optical result and that calculated by the residue calculus method is quite good, which gives confidence that the ray-optical method can give acceptable results for this size of array. The pattern also agrees quite well with that calculated by the Wiener-Hopf technique. for the array embedded in a simulated groundplane, which indicates a general lack of sensitivity of the pattern in the forward direction to the type of surrounding structure.

When the outer guides are of finite depth the calculated and experimental patterns do not agree quite as well as for the three element array, indicating a slight degradation of accuracy of the ray-optical method as the complexity of the structure increases. The five element array can produce a wider variety of patterns then the three element by adjustment of the parameters, including a good approximation to a sector shaped pattern for such a small array.

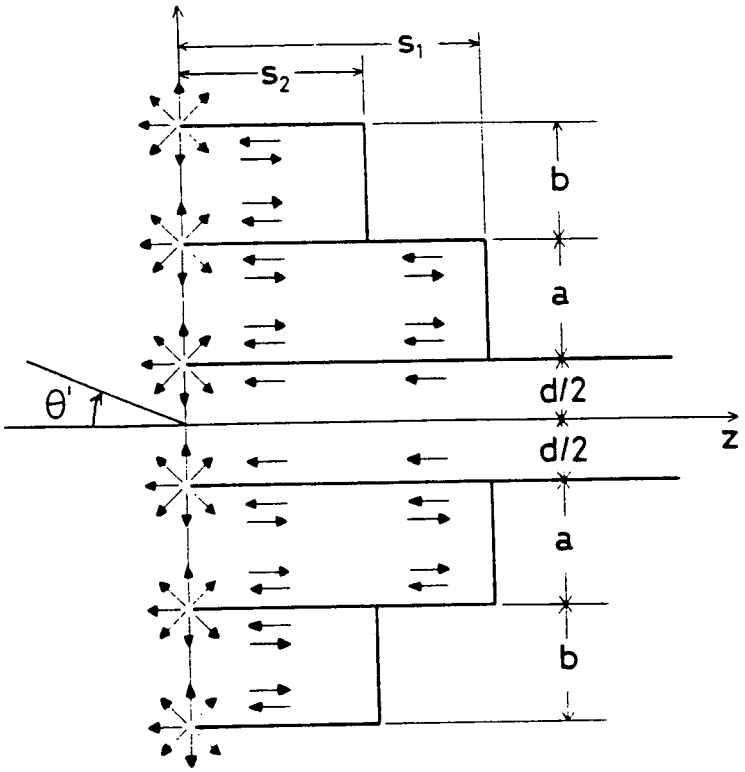

Fig. 7.1
five element array of
parallel plate waveguides
with outer guides shorted

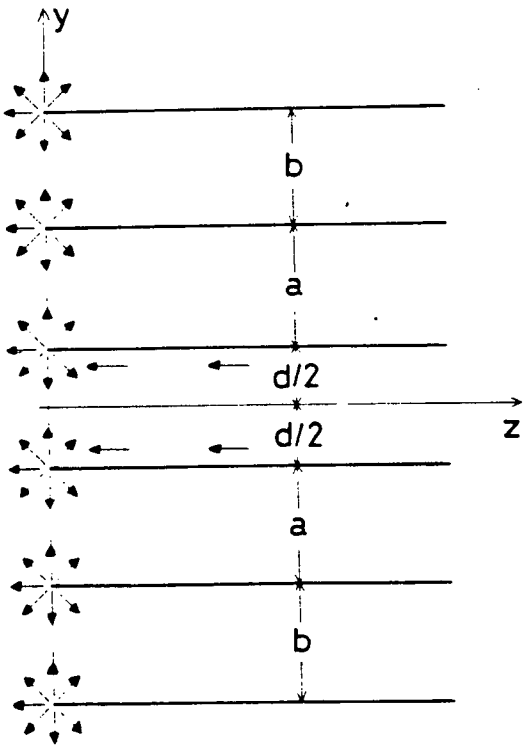

Fig. 7.2
five element array of
parallel plate waveguides
with outer guides of infinite
depth

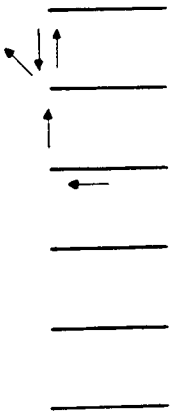

Fig. 7.3
ray path (see text)

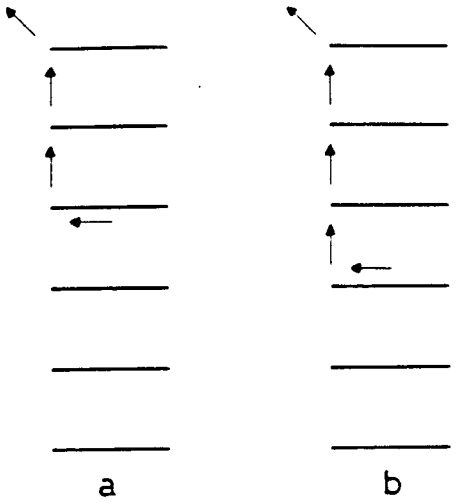

Fig. 7.4
ray paths(see text)

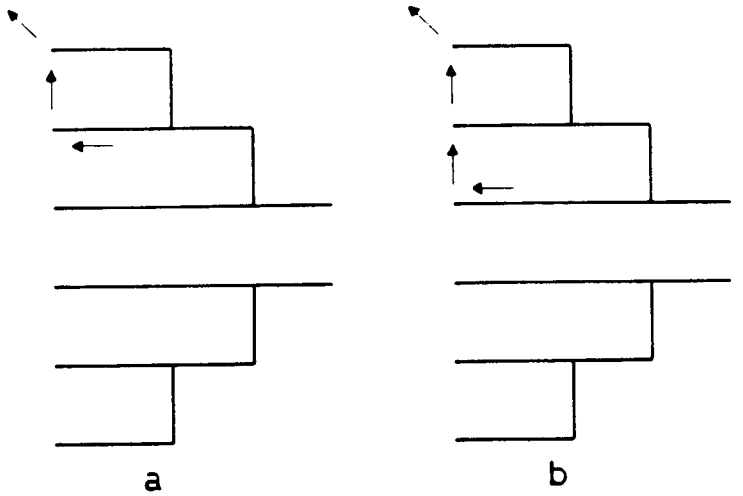

Fig. 7.5
ray paths(see text)

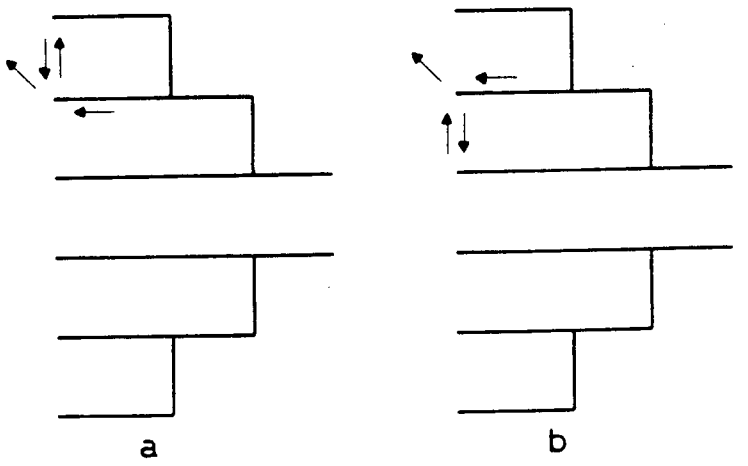

Fig. 7.6
ray paths (see text)

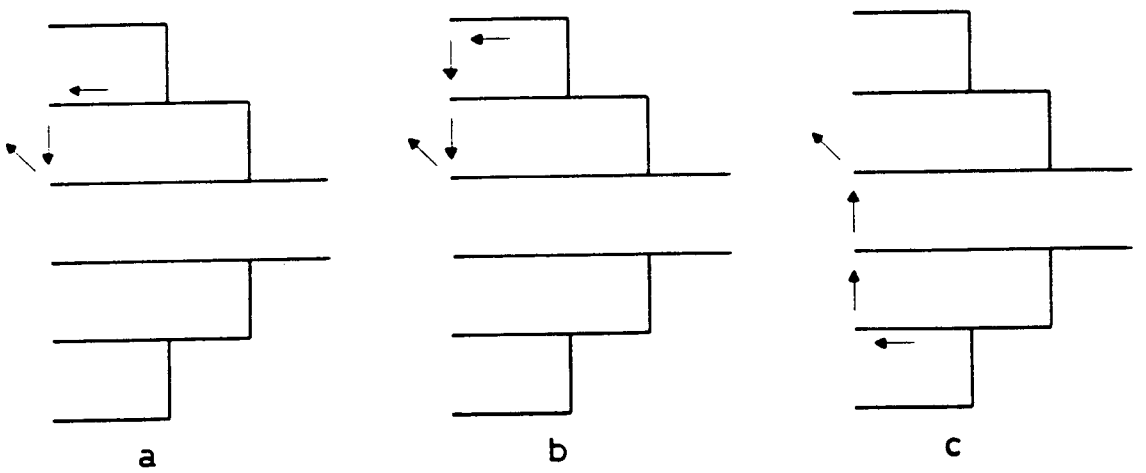

Fig. 7.7
ray paths (see text)

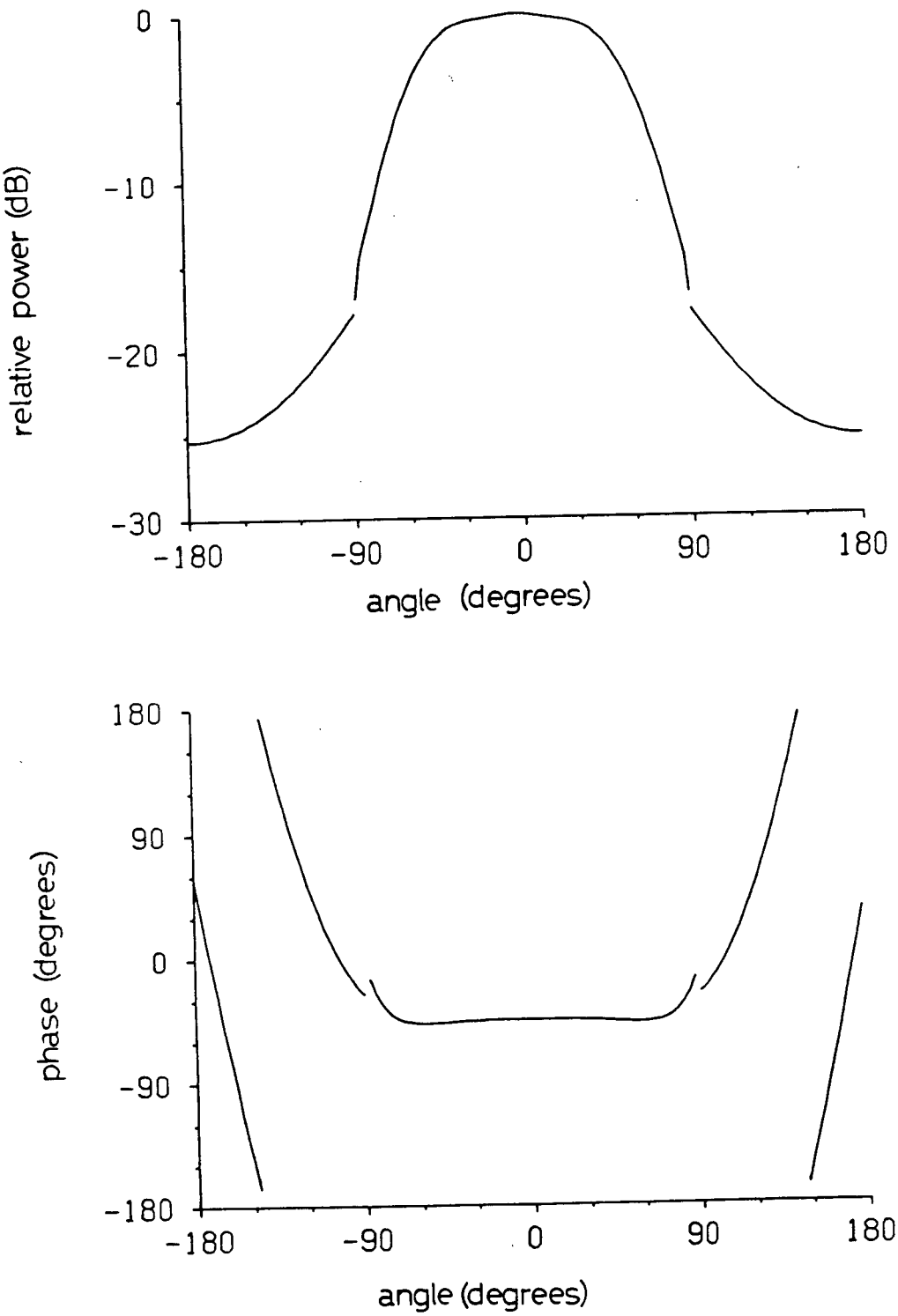

Fig. 7.8 Radiation pattern of five element array with outer guides of infinite depth d=a=b=0. 450λ.

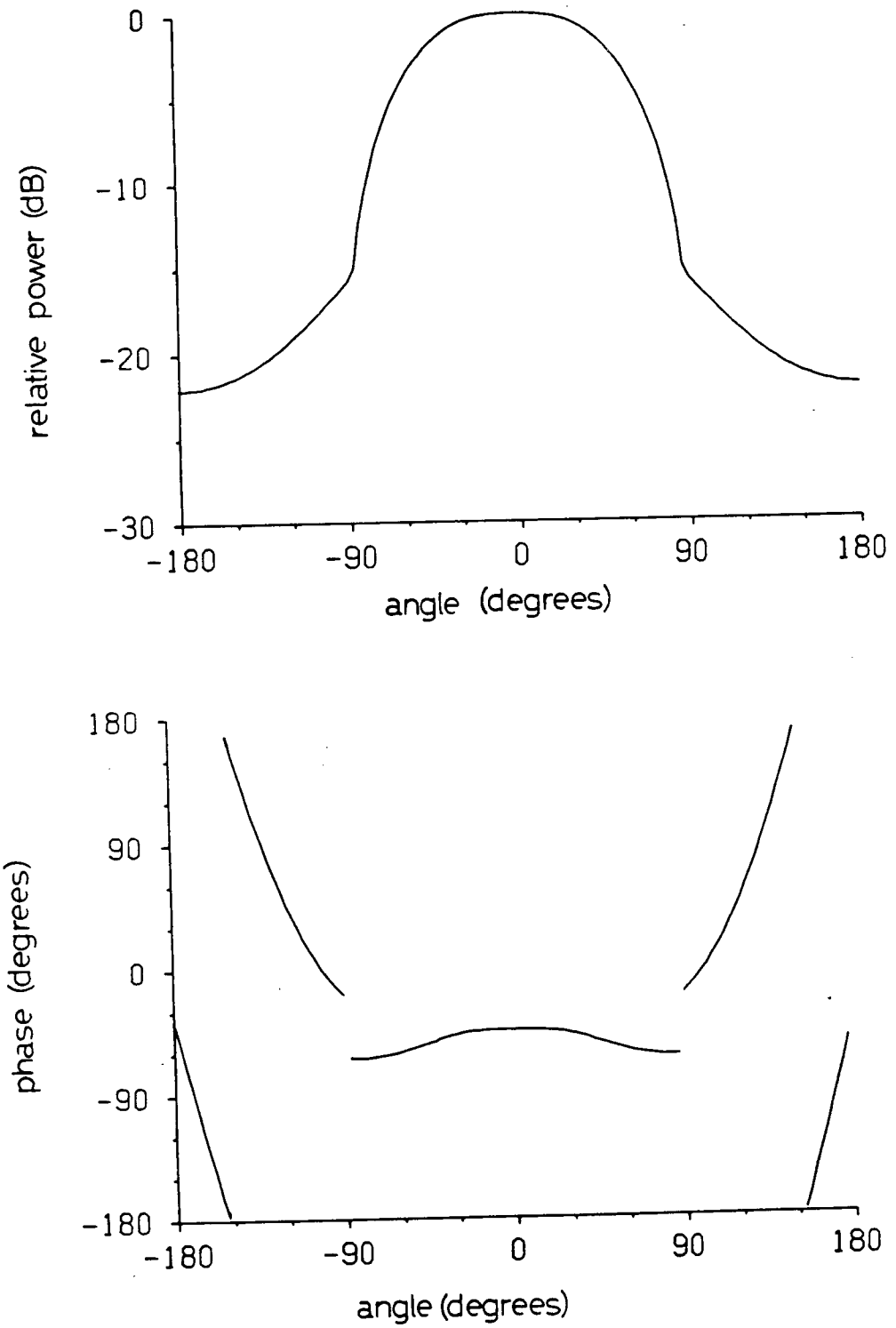

Fig. 7.9 Radiation pattern of five element array with outer guides of infinite depth d=a=b=0. 339λ.

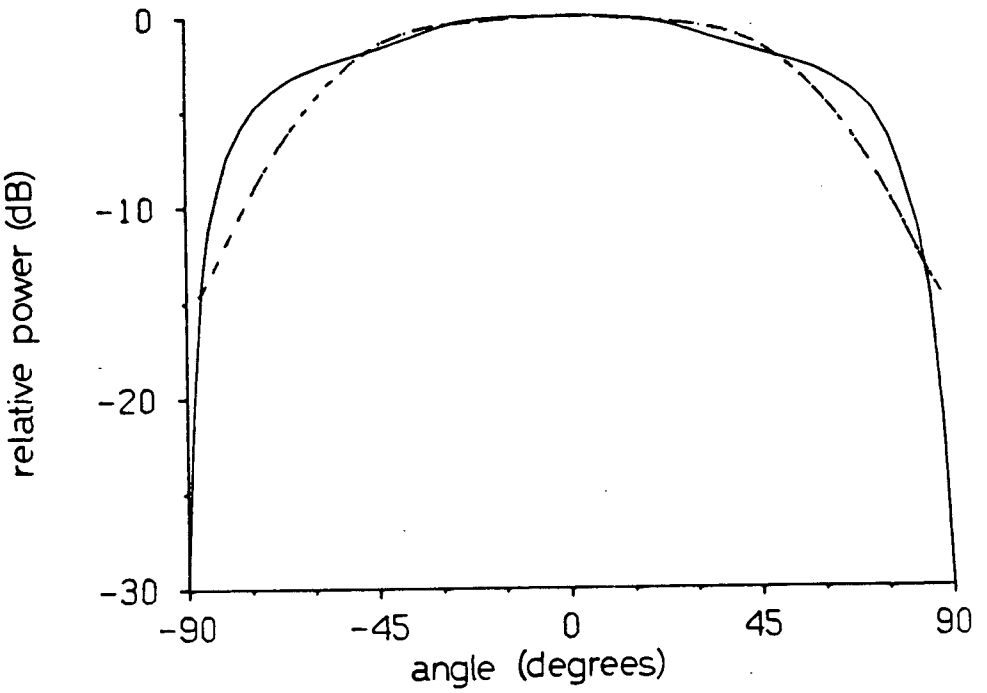

Fig. 7.11 Radiation pattern of five element array with outer guides of infinite depth, d=a=b=0. 450λ, comparison with [29].

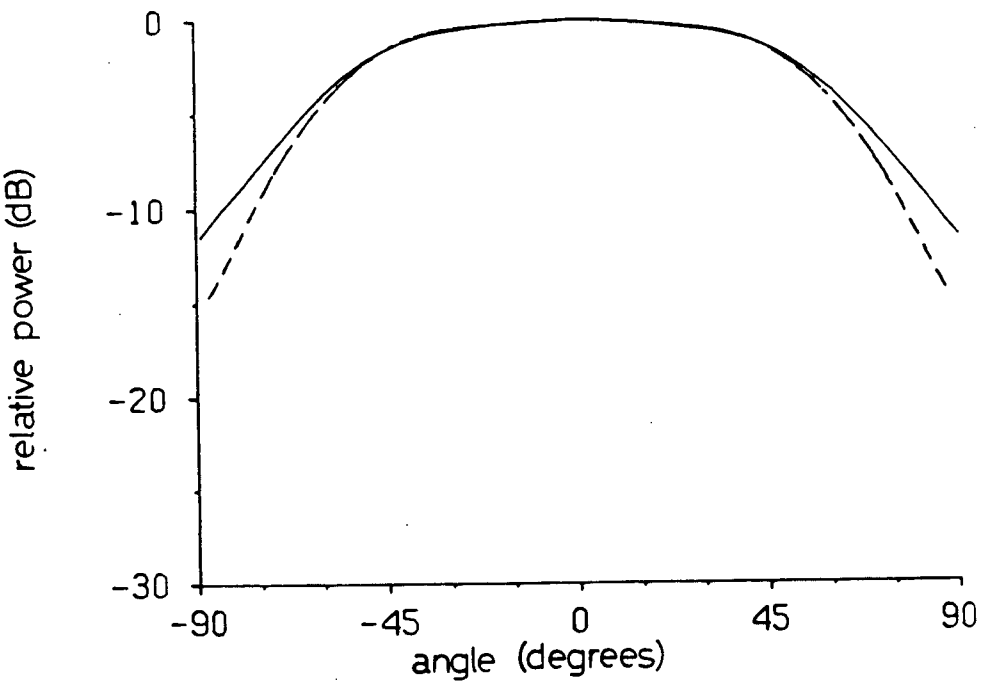

Fig. 7.10 Radiation pattern of five element array with outer guides of infinite depth, d=a=b=0.450λ, comparison with [38].

— — — this theory
——— comparison

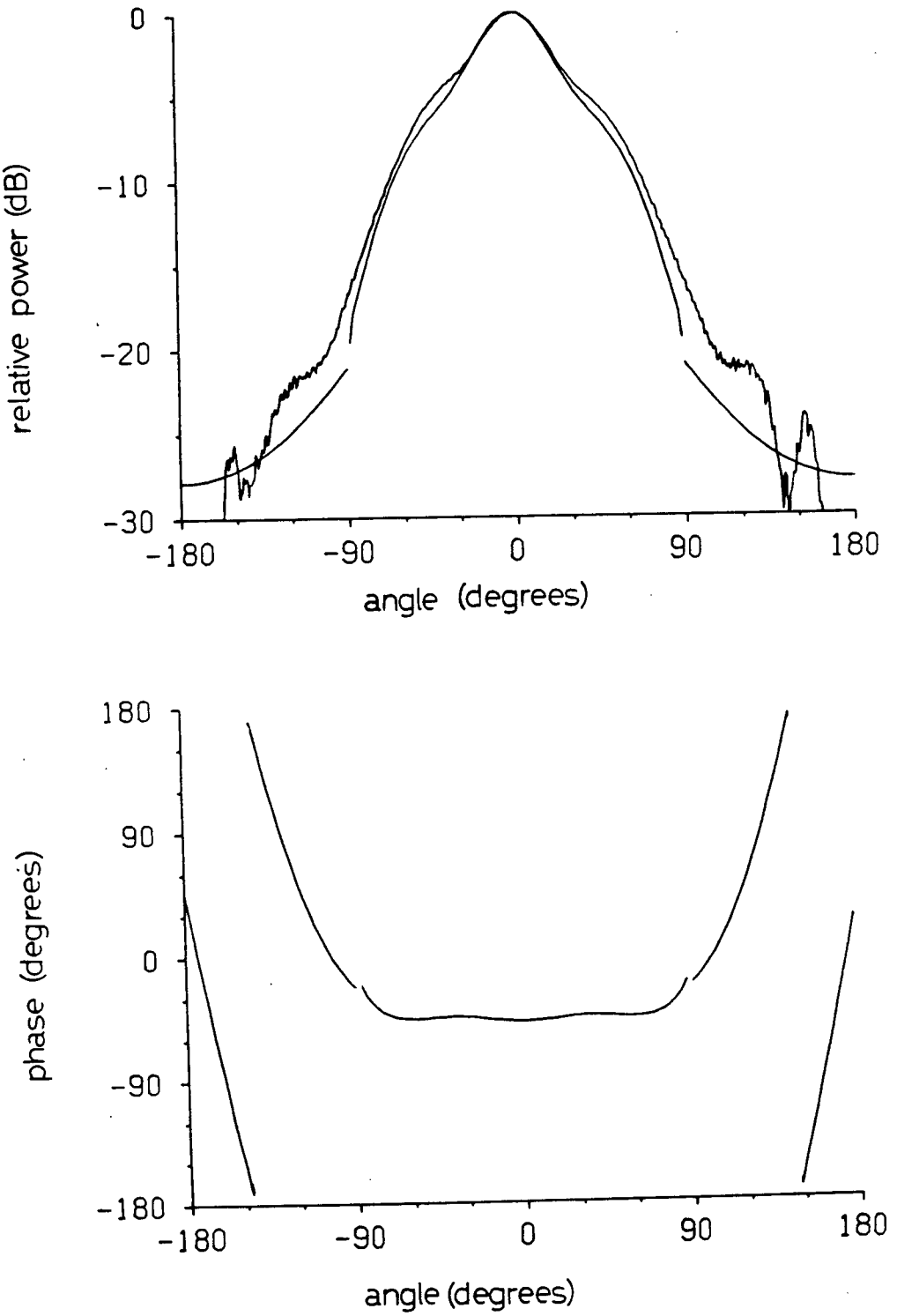

Fig. 7.12 Radiation pattern of five element array
$d=a=b=0.441\lambda$ $s_1=0.838\lambda$ $s_2=0.597\lambda$.
$A_1=0.137 \angle -12°$ $A_2=0.074 \angle -12°$.

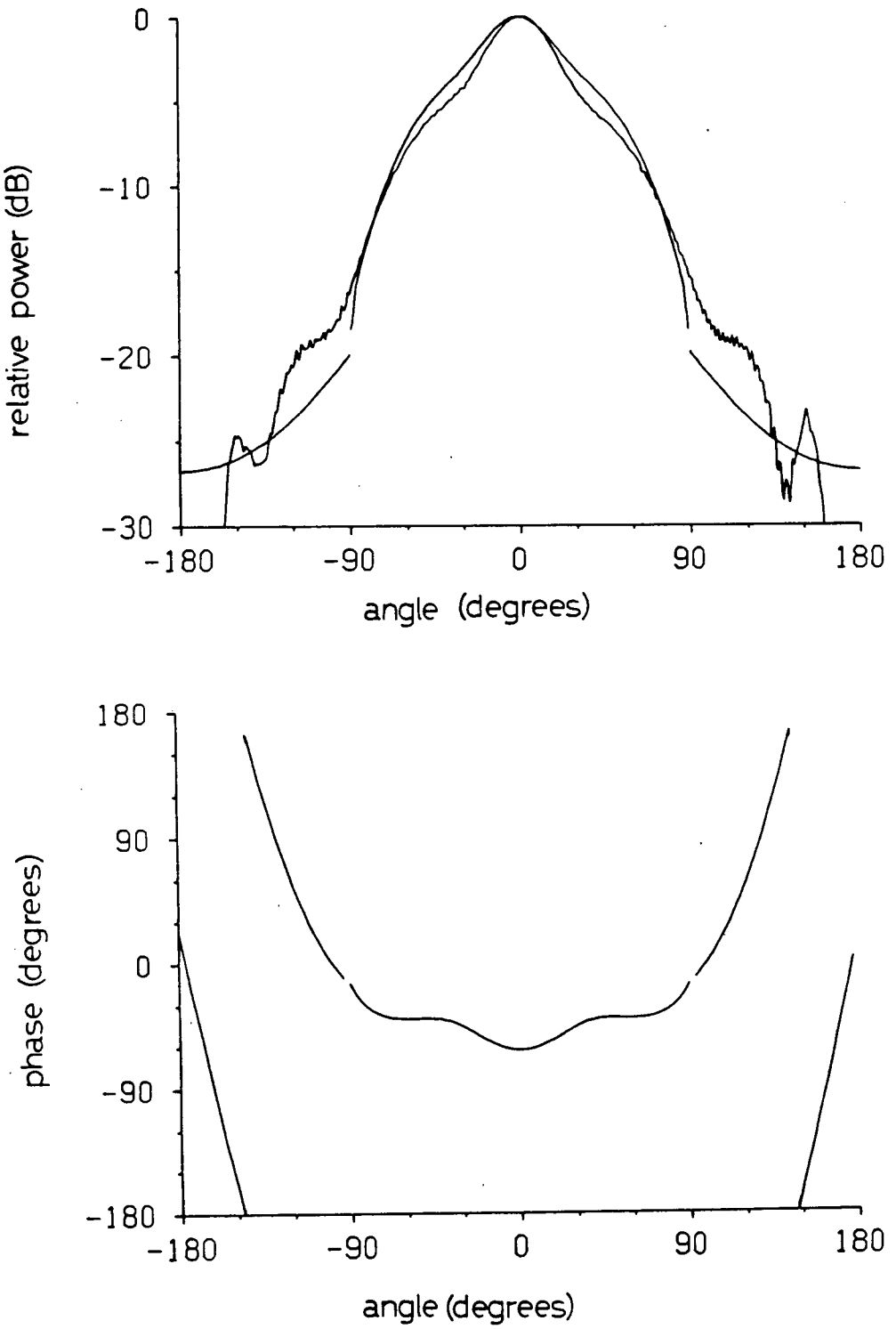

Fig. 7.13 Radiation pattern of five element array
$d=a=b=0.407\lambda$ $s_1=0.774\lambda$ $s_2=0.551\lambda$
$A_1=0.171 \angle -55°$ $A_2=0.076 \angle -57°$.

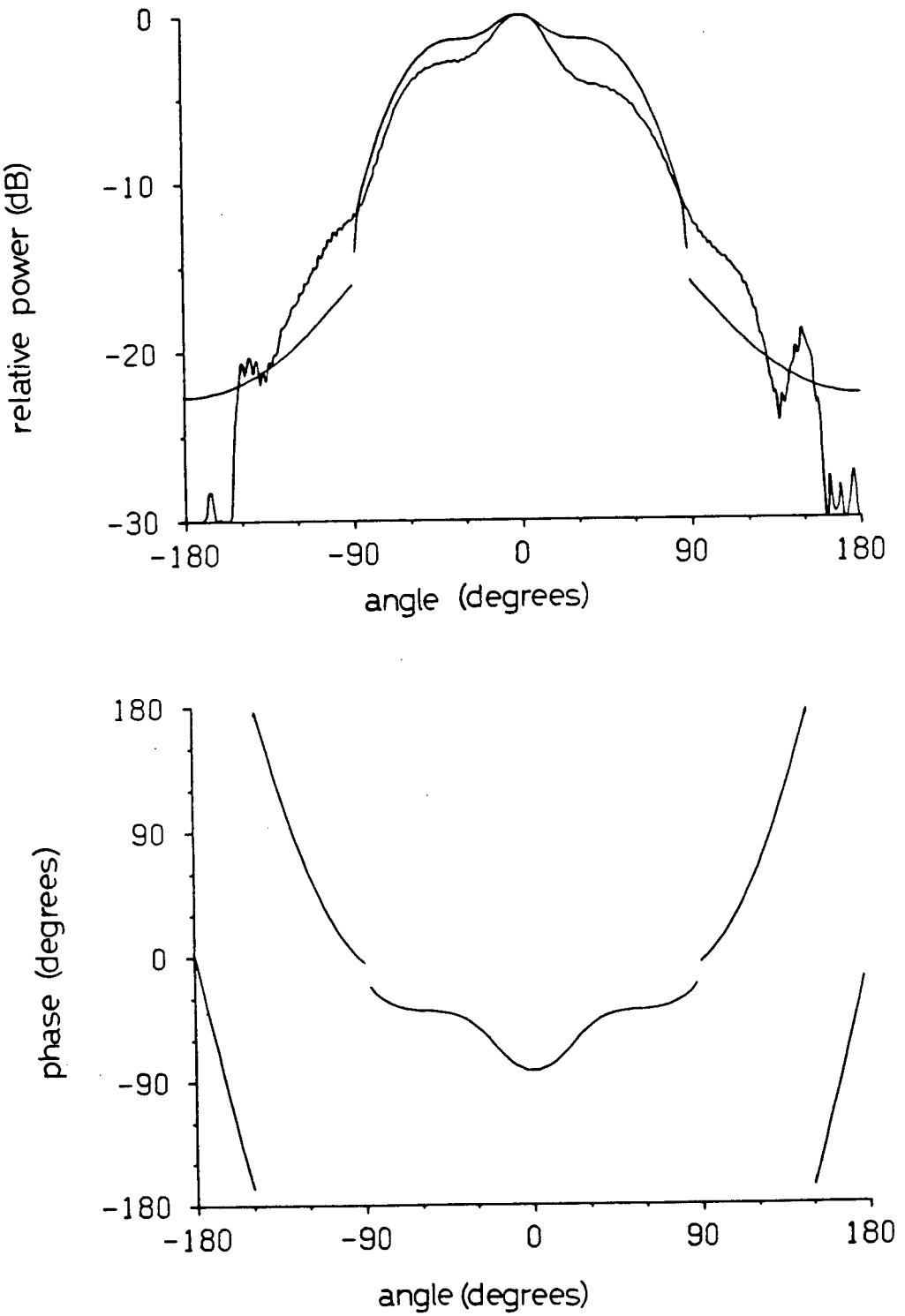

Fig. 7.14 Radiation pattern of five element array
$d=a=b=0.373\lambda$ $s_1=0.709\lambda$ $s_2=0.505\lambda$
$A_1=0.247 \angle -103^\circ$ $A_2=0.096 \angle -98^\circ$.

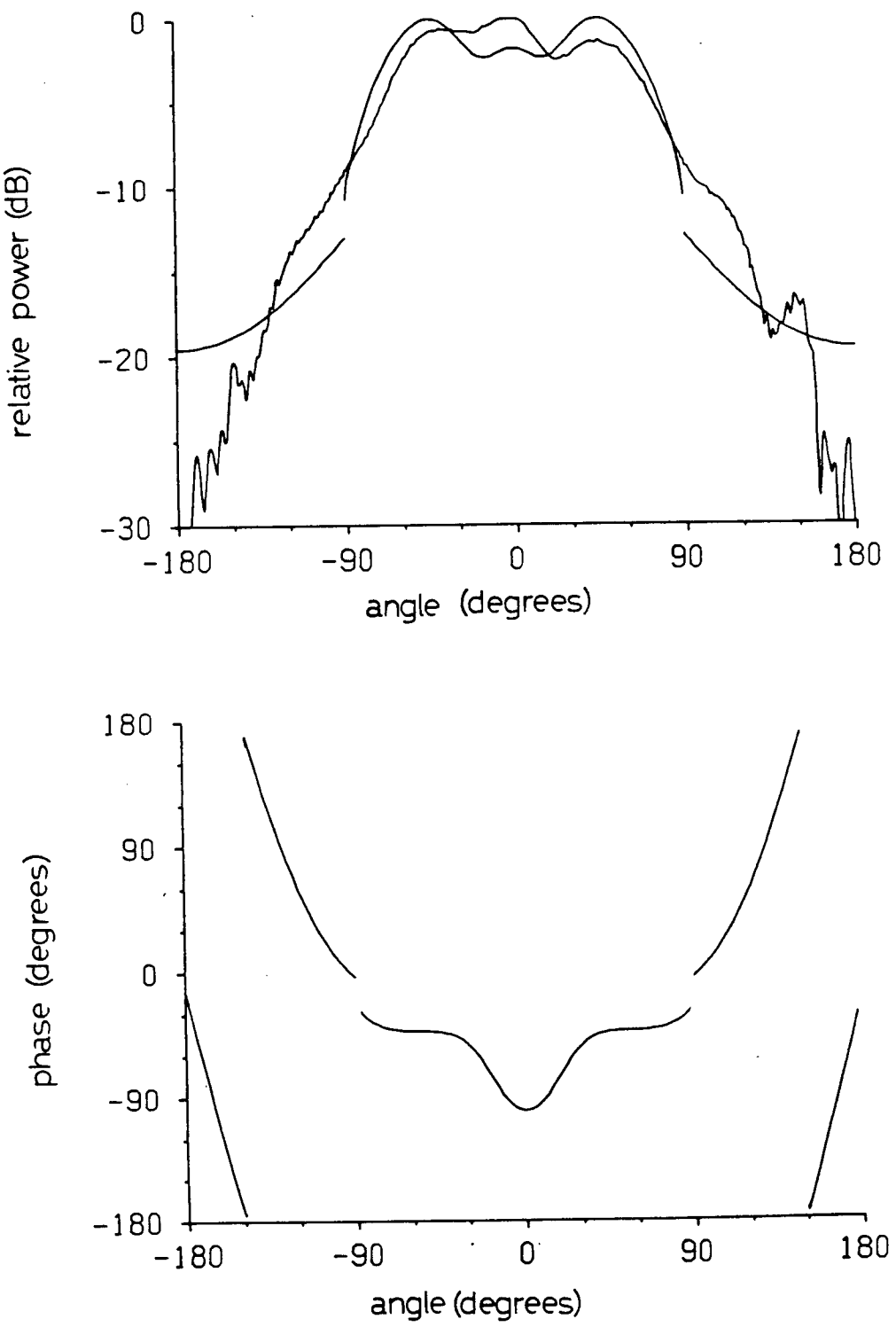

Fig. 7.15 Radiation pattern of five element array
$d=a=b=0.356\lambda$ $s_1=0.677\lambda$ $s_2=0.487\lambda$
$A_1=0.308 \angle -134°$ $A_2=0.126 \angle -123°$.

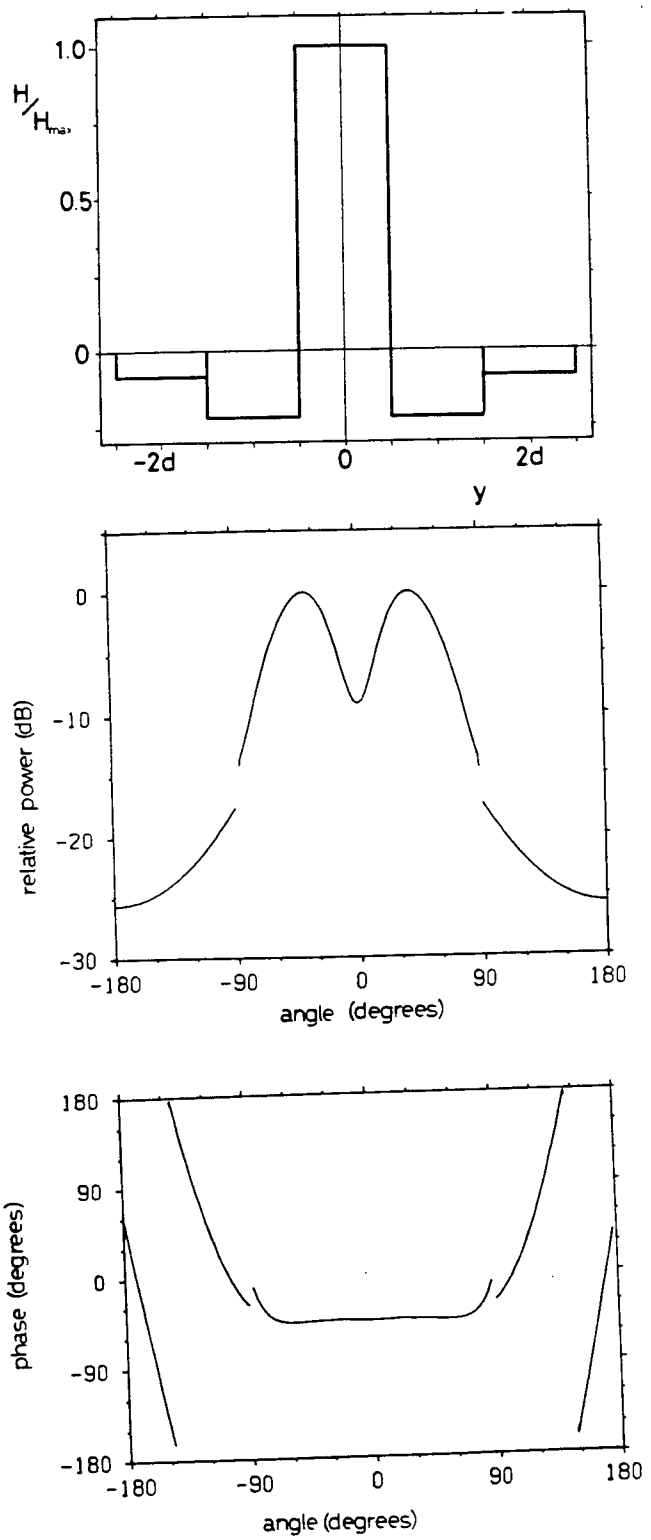

Fig. 7.16 Aperture field and radiation pattern of a five element array A_1=-0.215 A_2=-0.090 d=a=b=0.450λ s_1=0.610λ s_2=0.356λ.

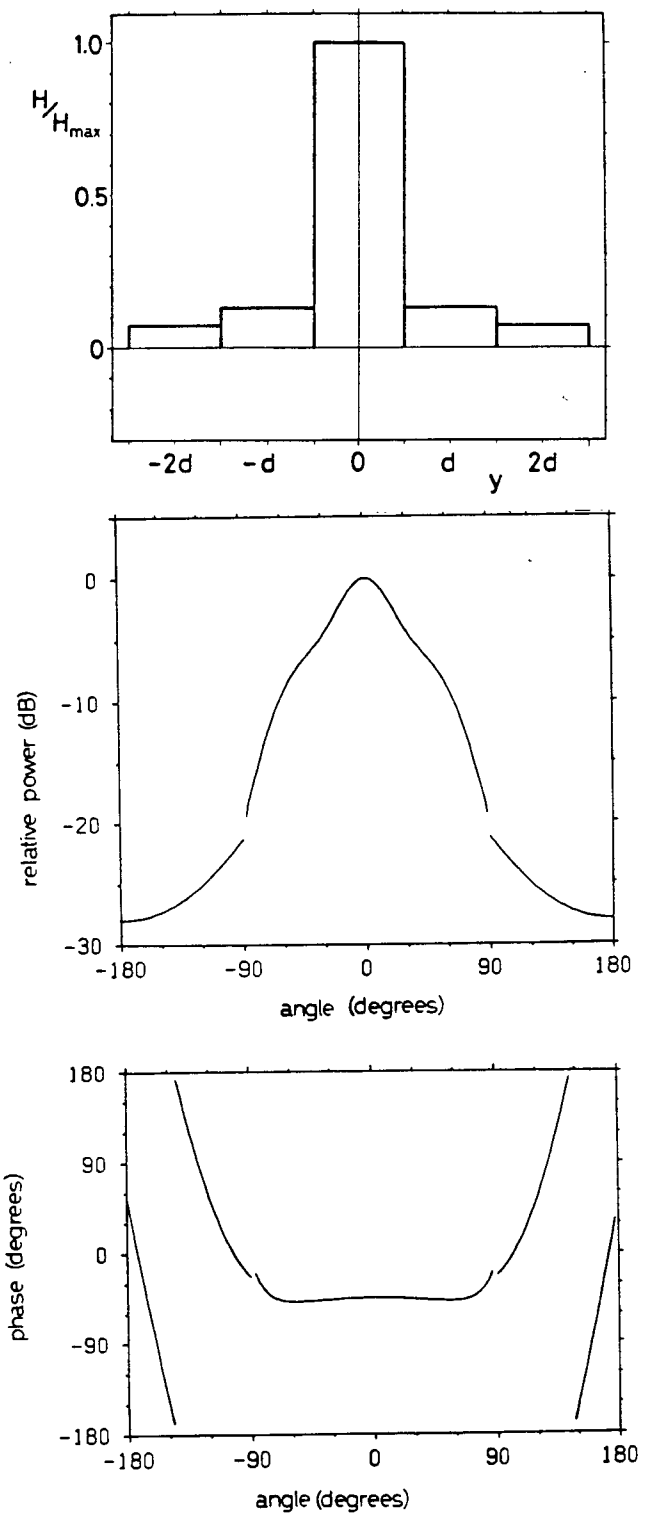

Fig. 7.17 Aperture field and radiation pattern of a five element array $A_1=+0.131$ $A_2=+0.073$ $d=a=b=0.450\lambda$ $s_1=0.857\lambda$ $s_2=0.610\lambda$.

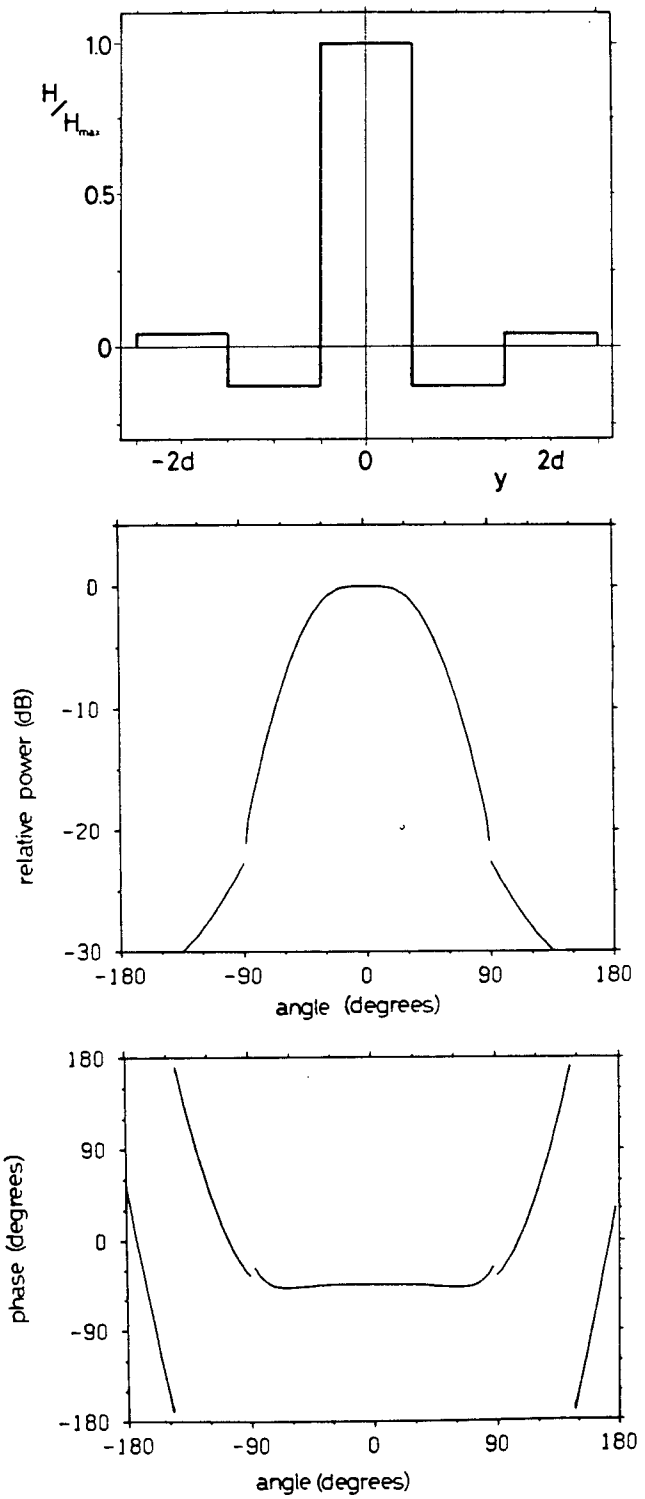

Fig. 7.18 Aperture field and radiation pattern of a five element array A_1=-0.131 A_2=+0.045 d=a=b=0.450λ s_1=0.857λ s_2=0.356λ.

TABLE III

Radiation Pattern Parameters

Figure	A_1	A_2	null(dB)	Beamwidth (degrees)			back radiation(dB)
				-1dB	-3dB	-10dB	
7.8a	0	0	0	39	54	76	-25
7.13a	+0.131	+0.073	0	12	21	64	-28
7.13b	-0.215	-0.090	-9	50	59	78	-26
7.13c	-0.131	+0.045	0	31	43	67	-32

Chapter 8

COUPLING BETWEEN STAGGERED GUIDES

The coupling coefficient for adjacent staggered waveguides (Fig.8.1) will be found in a manner similar to that for reflection and coupling of non-staggered guides. First all possible ray paths up to and including triple diffraction are determined by inspection. The field represented by each ray is calculated from the field of the ray preceding it. The diffraction problems of two successive rays which occur in these ray paths will be solved first to establish the notation used here. The analysis is restricted to the TEM case.

8.1 CANONICAL PROBLEM

In Fig.8.2a an isotropic line source $u_m = E(r)$ located at a distance r_0 from an edge is incident on that edge at an angle θ_0. The diffracted (not the total) field observed at θ such that $\cos(\frac{\theta \pm \theta_0}{2}) \neq 0$ is given by

$$u_{m+1} = G_d(r_0, \theta_0, \theta)E(r) \tag{8.1}$$

at the diffracting edge, where

$$G_d(r_0,\theta_0,\theta) = \frac{e^{-i\pi/4}}{\sqrt{\pi}} \{-e^{-ikr_0 \cos(\theta-\theta_0)} F'[\sqrt{2kr_0} \cos(\frac{\theta-\theta_0}{2})]$$

$$-e^{-ikr_0 \cos(\theta+\theta_0)} F'[\sqrt{2kr_0} \cos(\frac{\theta+\theta_0}{2})]\} , \quad (8.2)$$

$$F'(\alpha) = \begin{cases} F(\alpha) & \alpha > 0 \\ -F(-\alpha) & \alpha < 0 \end{cases} , \quad (8.2a)$$

$F(\alpha)$ is given by (2.4) and $E(r)$ is given by (2.10)

In each case the diffracted field is a line source centred at the diffracting edge.

In Fig.8.2b a plane wave $u_i = e^{-ikr\cos(\theta-\theta_0)}$ is incident on a half-plane edge at angle θ_0. An expression for the diffracted field which is uniformly valid for all angles θ may, from (2.2), be written as

$$u_1 = G'_d(a,\theta_0,\theta)E(r), \tag{8.3}$$

where

$$G'_d(a,\theta_0,\theta) = \frac{G_d(a,\theta_0,\theta)}{E(a)} \tag{8.4}$$

and a is the distance from the edge to the observation point. If ka>>1,

$$G'_d(a,\theta_0,\theta) \sim D(\theta_0,\theta), \tag{8.5}$$

where $D(\theta_0,\theta)$ is given by (2.9).

8.2 CALCULATION OF THE COUPLING COEFFICIENT

Consider two adjacent semi-infinite parallel-plate waveguides consisting of the three perfectly conducting half-planes y=a,z>1, y=0,z>0 and y=-d,z=0, where $\Psi > 0$ is the angle of stagger of the top guide and l=a tan Ψ. We wish to determine the fields coupled from the driven guide (-d<y<0, z>0) into the staggered guide (0<y<a, z>0). As before the incident field

$$u_i = e^{-ikz} \tag{8.6}$$

in the guide is decomposed into two plane waves incident on the half-plane edges y=-d,z=0 and y=z=0 at angles $\theta = 0$ and 2π respectively. Both plane waves have value

$$u_i = \frac{1}{2} \tag{8.7}$$

at the edges.

The singly diffracted field is shown in Fig.8.3a. The incident field u_i given by (8.7) is diffracted at the edge y=z=0. From (2.7) the diffracted field is given by a line source

$$u_1^a = \frac{1}{2} D(2\pi,0)E(r) \tag{8.8}$$

located at the diffracting edge. The contribution to the coupling for single diffraction is found by treating (8.8) as a line source and using (3.11), (3.12) and (3.2). Thus

$$A_S^{(1)} = \frac{\sqrt{\pi}\, e^{i\pi/4}}{2\sqrt{2}\, ka} D(2\pi,0)\,, \tag{8.9}$$

which is identical to (3.17) in the TEM case.

The doubly diffracted fields are shown in Figs.8.5b and c. In Fig.8.3b the incident field u_i given by (8.7), is diffracted at the edge y=z=0. From (8.3), as observed at the edge y=a,z=1 the diffracted field is a line source

$$u_1^b = \frac{1}{2} G_d'(c,2\pi,\frac{\pi}{2}-\Psi)E(r) \tag{8.10}$$

located at the diffracting edge, where $c = \sqrt{\ell^2 + a^2}$ is the distance between the two edges. This field is again diffracted at the edge y=a,z=1 and from (8.1) gives a line source

$$u_2^b = \frac{1}{2} G_d'(c,2\pi,\frac{\pi}{2}-\Psi) G_d(c,\frac{3\pi}{2}-\Psi,2\pi) E(r) . \qquad (8.11)$$

Fig.8.3c shows a ray path which is identical to that shown in Fig.3.2c for a non-staggered guide. Here u_i is given by (8.7), u_1^c is given by (3.34) and u_2^c is given by (3.35). The contribution to the coupling coefficient A_S from double diffraction is given by

$$A_S^{(2)} = \frac{\sqrt{\pi}\, e^{i\pi/4}}{2\sqrt{2}\, ka} [G_d'(c,2\pi,\frac{\pi}{2}-\Psi) G_d(c,\frac{3\pi}{2}-\Psi,2\pi) e^{-ik\ell} + C_0'(d) C_0(d)] . \qquad (8.12)$$

If $\Psi = 0$, (8.12) is equivalent to (3.36) in the TEM case.

The triply diffracted fields are shown in Figs.8.5d and e. Fig.8.3d shows a ray path which is identical to that shown in Fig.3.2d for a non-staggered guide. Here u_i is given by (8.7), u_1^d is given by (3.37), u_2^d is given by (3.38) and u_3^d is given by (3.39) specialized for the TEM case. In Fig.8.3e u_i is given by (8.7), u_1^e is given by (8.10) and u_2^e is given by (8.11) with the final 2π replaced by $\frac{3\pi}{2}-\Psi$. This field is again diffracted at y=z=0 and from (8.1) gives a line source

$$u_3^e = \frac{1}{2} G_d'(c,2\pi,\frac{\pi}{2}-\Psi) G_d(c,\frac{3\pi}{2}-\Psi,\frac{3\pi}{2}-\Psi) G_d(c,\frac{\pi}{2}-\Psi,0) E(r) \qquad (8.13)$$

at the edge.

In Fig.8.3f the incident field u_i given by (8.7) is diffracted at the edge y=-d,z=0. From (8.3) as observed at y=z=0 the diffracted field u_1^f is a line source

$$u_1^f = \frac{1}{2} G_d'(d,0,\frac{\pi}{2}) E(r) \qquad (8.14)$$

located at the diffracting edge. This field is again diffracted at y=z=0 and from (8.1) gives a line source

$$u_2^f = \frac{1}{2} G_d'(d,0,\frac{\pi}{2}) G_d(d,\frac{3\pi}{2},\frac{\pi}{2}-\psi) E(r) \tag{8.15}$$

located at the diffracting edge. This field is again diffracted at y=z=0 and from (8.1) gives a line source

$$u_3^f = \frac{1}{2} G_d'(d,0,\frac{\pi}{2}) G_d(d,\frac{3\pi}{2},\frac{\pi}{2}-\psi) G_d(c,\frac{3\pi}{2}-\psi,2\pi) E(r) . \tag{8.16}$$

In Fig.8.3g the incident field u_i is given by (8.7), u_1^g is given by (8.10) and u_2^g is given by (8.11) with the final 2π replaced by $3\pi/2$. This field is reflected at y=0,z=1 and looks like a line source

$$u_2^g = \frac{1}{2} G_d'(c,2\pi,\frac{\pi}{2}-\psi) G_d(c,\frac{3\pi}{2}-\psi,\frac{3\pi}{2}) E(r) \tag{8.17}$$

at the image point y=-a,z=1, where the notation u_m^x denotes a field in the figure labelled x that has been diffracted m times and also reflected. This field is again diffracted at y=a,z=1 and from (8.1) gives a line source

$$u_3^g = \frac{1}{2} G_d'(c,2\pi,\frac{\pi}{2}-\psi) G_d(c,\frac{3\pi}{2}-\psi,\frac{3\pi}{2}) G_d(2a,\frac{3\pi}{2},2\pi) E(r) \tag{8.18}$$

at the edge. The total contribution to the coupling coefficient from triple diffraction is found by treating (3.39), (8.13), (8.16) and (8.18) as line sources and using (3.11), (3.12) and (3.2). Thus

$$A_S^{(3)} = \frac{\sqrt{\pi}\, e^{i\pi/4}}{2\sqrt{2}\, ka} [\frac{1}{2} C_0'(d) C_0(2d)$$

$$+ G_d'(c,2\pi,\frac{\pi}{2}-\psi) G_d(c,\frac{3\pi}{2}-\psi,\frac{3\pi}{2}-\psi) G_d(c,\frac{\pi}{2}-\psi,0)$$

$$+ \; G_d'(d,0,\tfrac{\pi}{2}) G_d(d,\tfrac{3\pi}{2},\tfrac{\pi}{2}-\Psi) G_d(c,\tfrac{3\pi}{2}-\Psi,2\pi) e^{-ik\ell}$$

$$+ \; G_d'(d,2\pi,\tfrac{\pi}{2}-\Psi) G_d(c,\tfrac{3\pi}{2}-\Psi,\tfrac{3\pi}{2}) G_d(2a,\tfrac{3\pi}{2},2\pi) e^{-ik\ell}]$$

$$+ \; \frac{i}{8ka} [C_0'(d) C_0(d) E(d)] \, . \qquad (8.19)$$

The total coupling coefficient $A_s(d,a)$ up to and including triple diffraction is given by the sum of (8.9), (8.12) and (8.19). Note that (8.19) is not valid for $\Psi = 0$ (non-staggered guides) because of the restrictions which apply to (8.1). If $\Psi = 0$, $A_s^{(3)}$ is given by (3.44).

Note that if the coupled field in the staggered guide is along a shadow boundary the ray-to-mode conversion (3.12) is no longer valid because the coupled field is not a ray field. This difficulty arises when the modal angle θ_n is the complement of the stagger angle Ψ (i.e. $\theta_n = \pi/2 - \Psi$, Fig.8.4). It does not occur in the TEM case here where $\theta_n = 0$, but would arise if other waveguide modes were considered.

8.3 NUMERICAL RESULTS

Numerical values for the coupling coefficient $A_s(d,a)$ calculated as a function of the guide widths a and d and for various angles Ψ are shown in Fig.8.4. As for the non-staggered guides, the single diffraction provides the average behaviour of the coupling coefficient. Addition of the double diffraction terms reveals a fine structure which becomes less pronounced as Ψ is increased.

Exact results for the coupling coefficients are not available for comparison. However, on comparing curves with and without triple diffraction, it appears there is some deterioration in accuracy as the stagger increases.

8.4 SUMMARY

The coupling coefficient between adjacent staggered parallel plate waveguides was found by ray-optical methods. The numerical results show a moderate and gradual change from the non-staggered results as the angle of stagger is increased. These calculations will be useful for calculations involving an array of staggered waveguides.

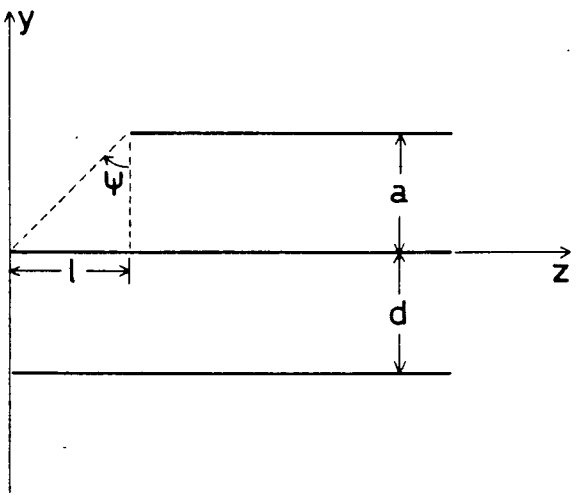

Fig. 8.1

two adjacent staggered
parallel plate waveguides

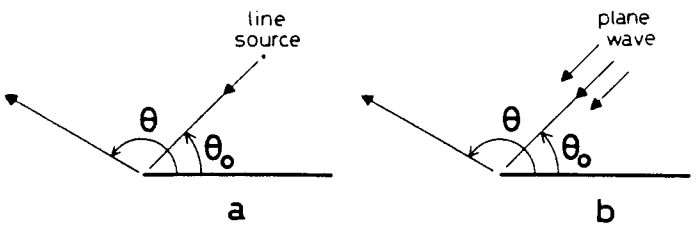

Fig. 8.2
line source and plane wave
incident on a half plane

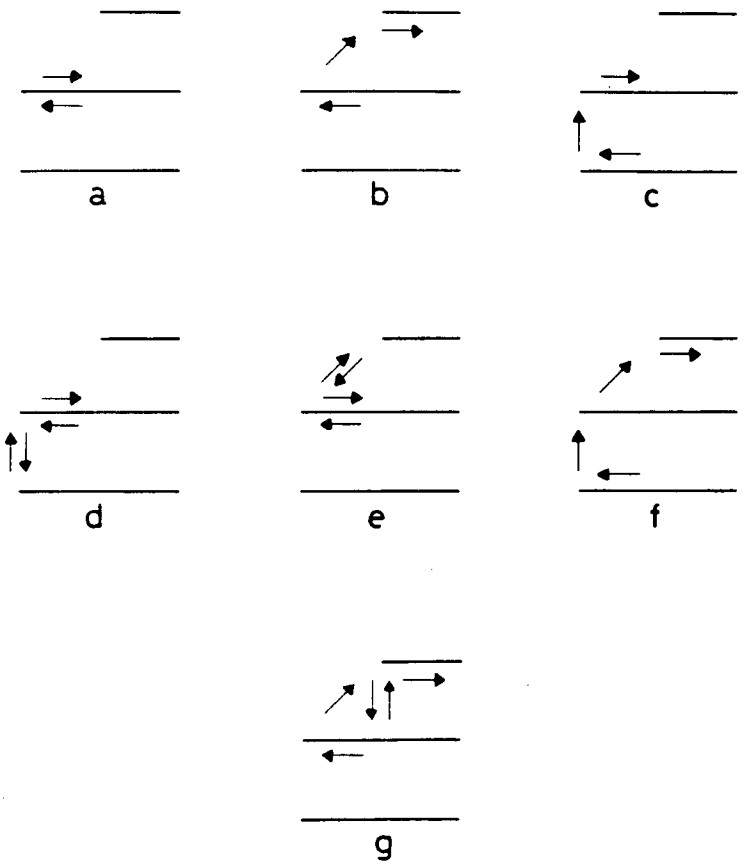

Fig. 8.3
ray paths for coupling coefficient

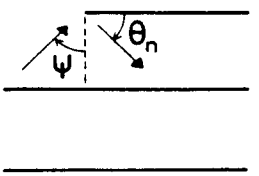

Fig. 8.4
ray path (see text)

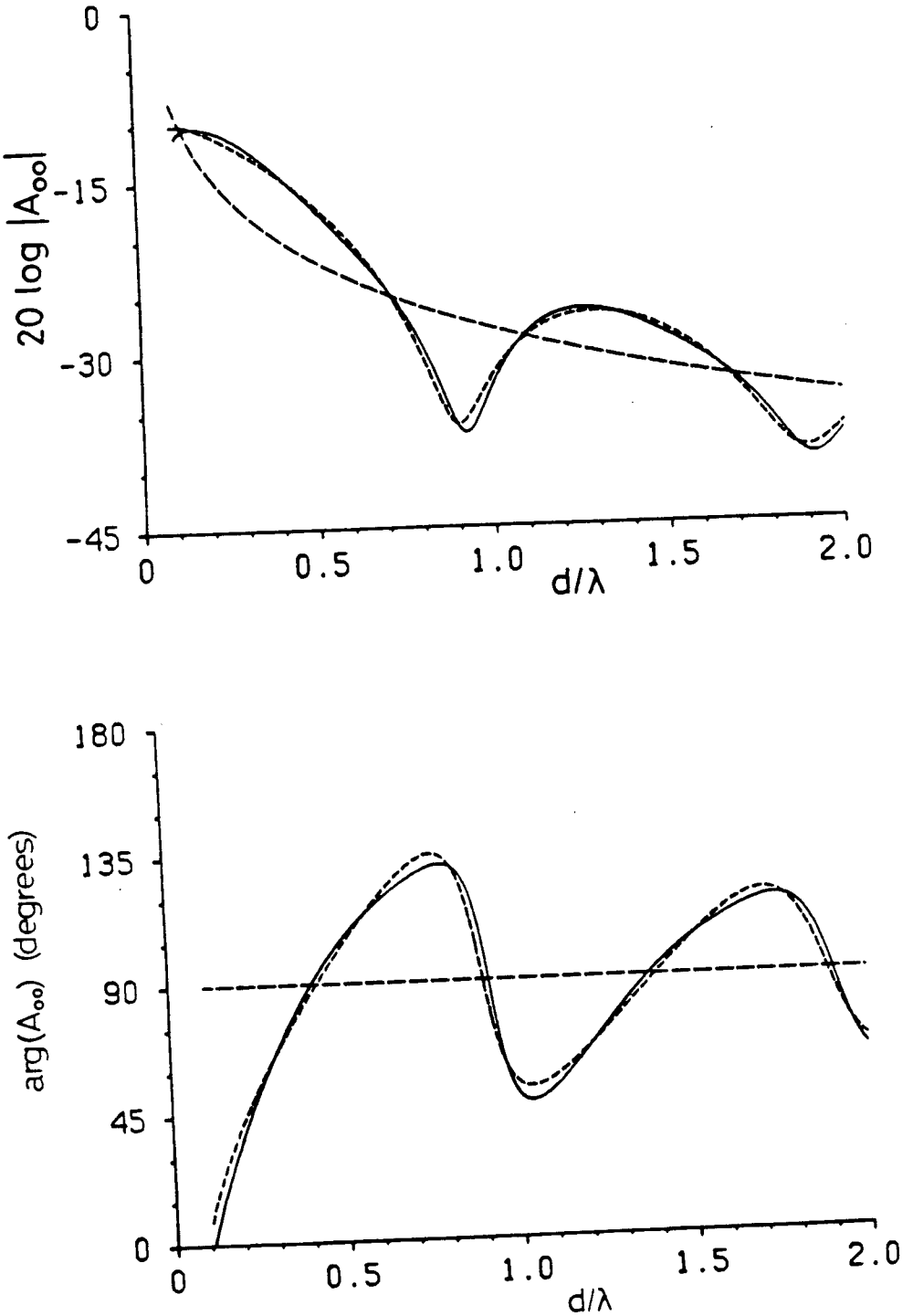

Fig. 8.5a TEM-TEM coupling between staggered waveguides $\Psi=0°$.

—— single diffraction
---- single and double diffraction
—— single and double and triple diffraction

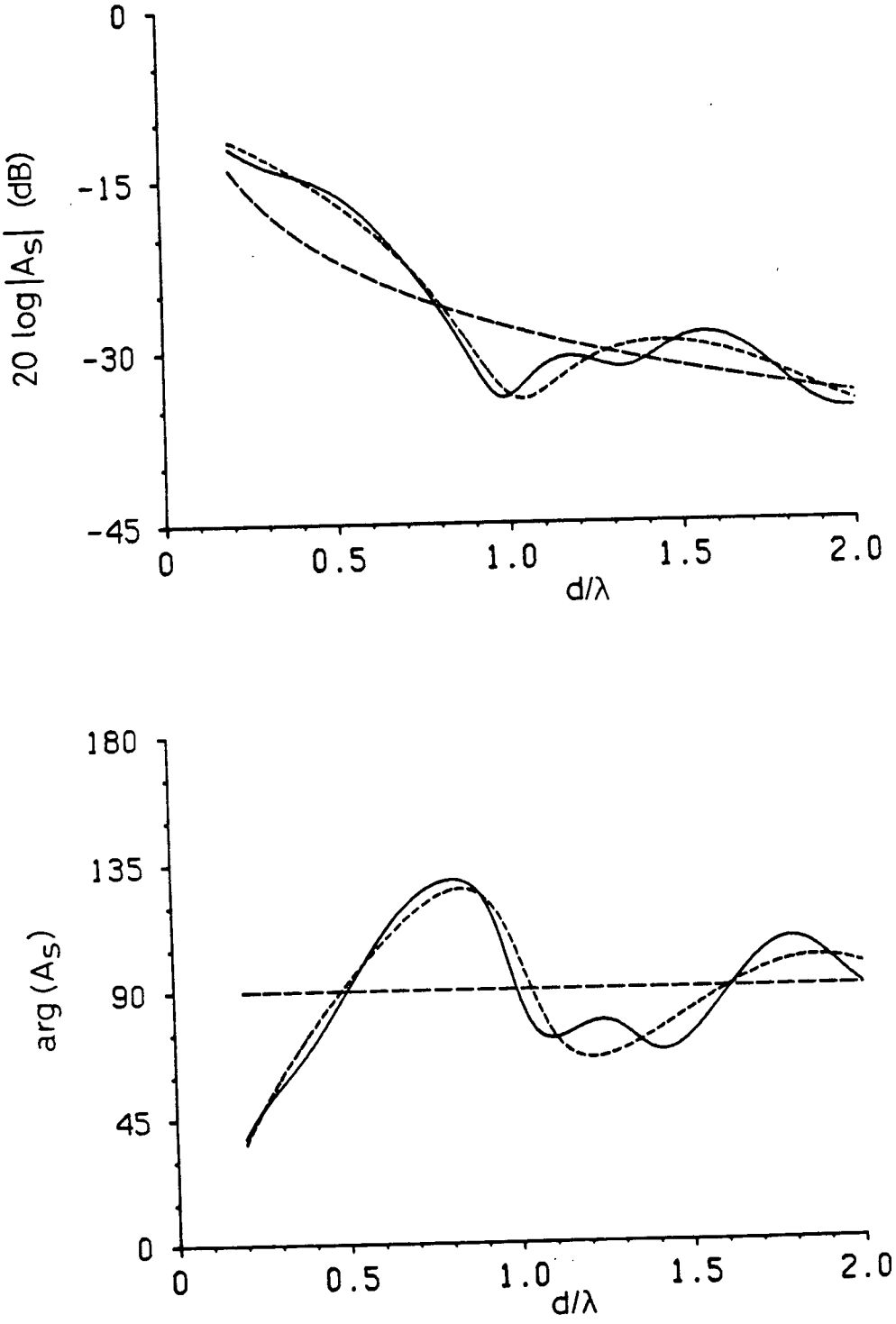

Fig. 8.5b TEM-TEM coupling between staggered waveguides $\Psi=15°$.

— — single diffraction
---- single and double diffraction
—— single and double and triple diffraction

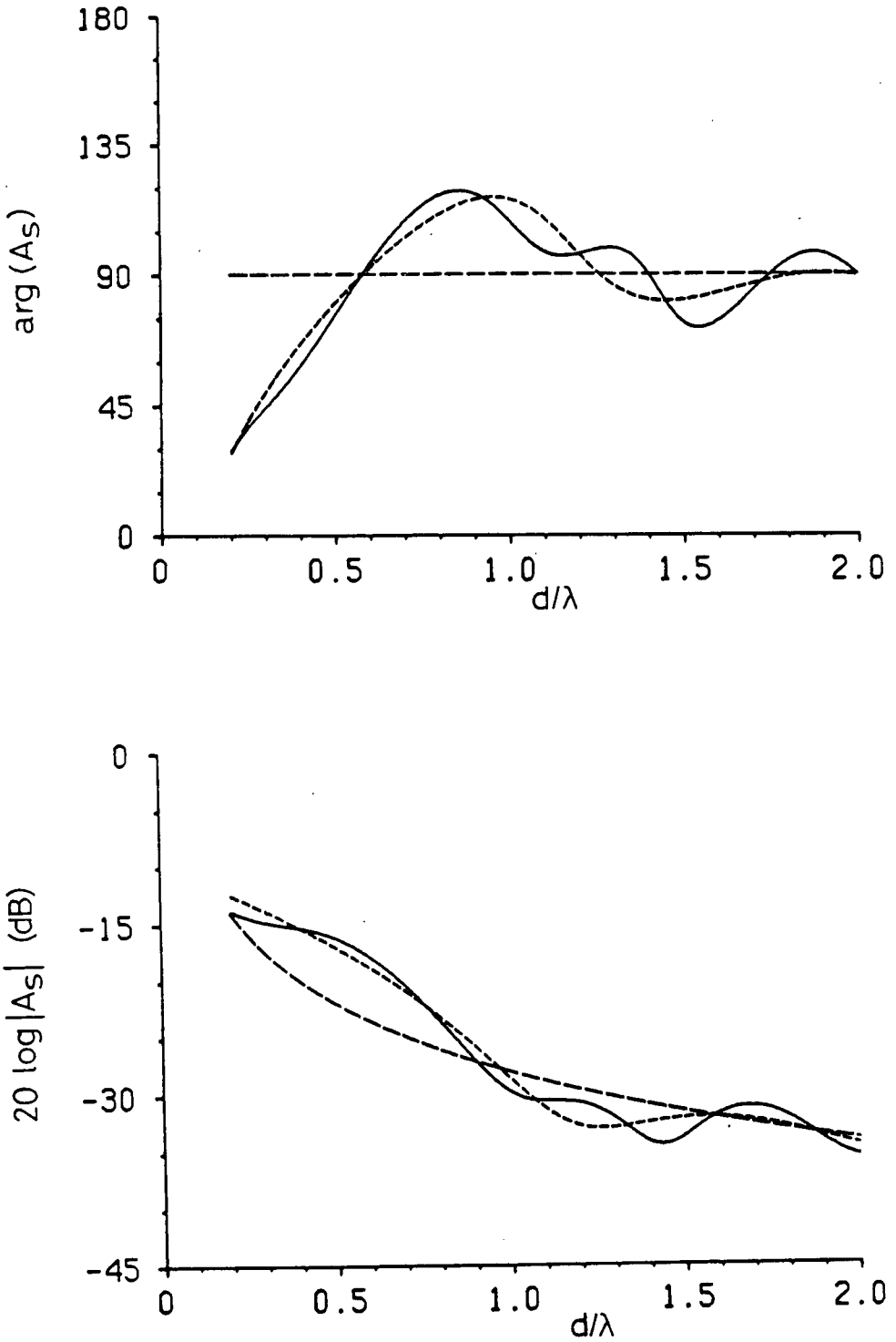

Fig. 8.5c TEM-TEM coupling between staggered waveguides $\Psi=30°$.

—— single diffraction
---- single and double diffraction
—— single and double and triple diffraction

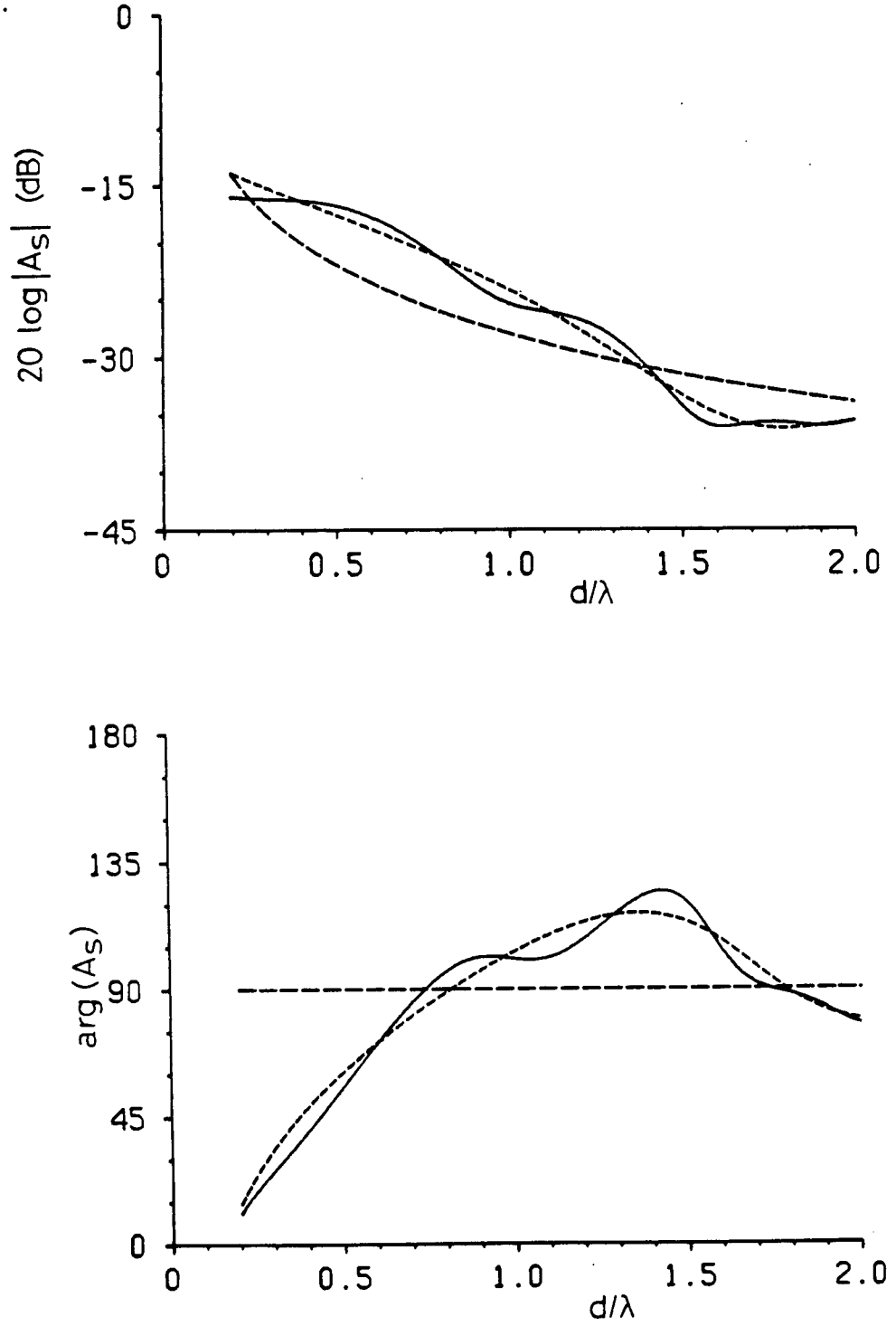

Fig. 8.5d TEM-TEM coupling between staggered waveguides $\Psi=45°$.

— — single diffraction
---- single and double diffraction
—— single and double and triple diffraction

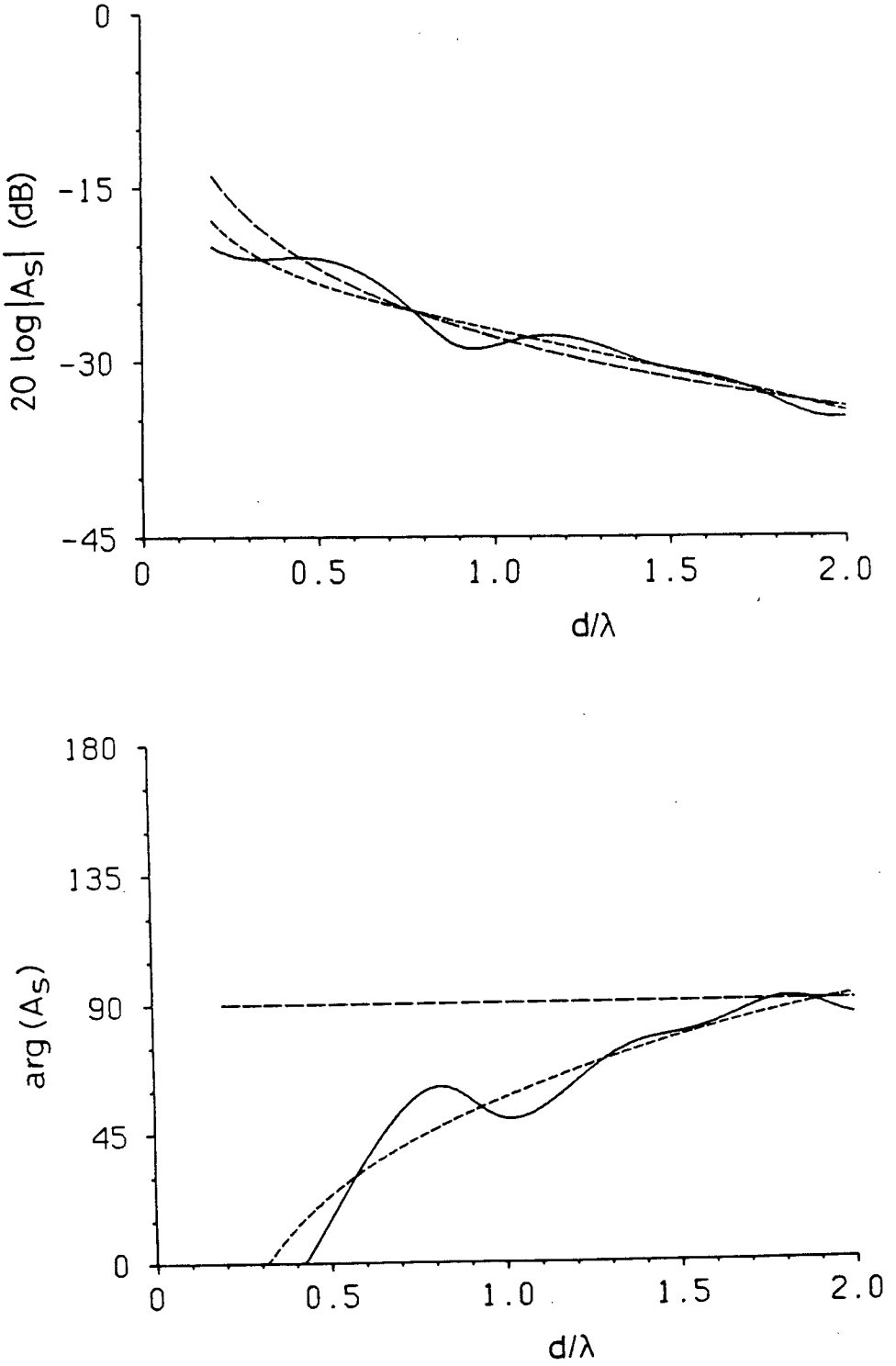

Fig. 8.5e TEM-TEM coupling between staggered waveguides $\Psi=60°$.

— — single diffraction
---- single and double diffraction
—— single and double and triple diffaction

Chapter 9

RADIATION FROM A STAGGERED PARALLEL-PLATE WAVEGUIDE

9.1 FORMULATION

The radiation pattern of a staggered parallel-plate waveguide (Fig.9.1) in the TEM mode is found by ray-optical methods similar to those for a non-staggered guide (Chapter 5). This pattern was found previously by Ryan and Rudduck [42] using edge diffraction theory including terms equivalent to double diffraction only. The ray paths representing the fields considered here are shown in Fig.9.2 up to and including triple diffraction. Note that the staggered guide has many more ray paths for a given order of diffraction then a non-staggered one. The total radiation pattern is made up of the sum of the fields represented by all the ray paths, taking into account that some fields are shadowed and do not contribute in some angular directions. In the following section the fields represented by each ray path will be calculated, and then the total radiation pattern will be found for all angles.

Consider a semi-infinite parallel-plate waveguide of width a consisting of two perfectly conducting half-planes $y=-a/2, z>0$ and $y=+a/2, z=l$, where $\psi>0$ is the angle of stagger and $l=a \tan \psi$. We wish to determine the fields radiated into the space outside the guide.

As before the incident field (8.6) in the guide is decomposed into two plane waves incident on the half-plane

edges. The wave incident on the bottom edge $y=-a/2,z=0$ at $\theta_o=0$ has value (8.7) at that edge. The wave incident on the top edge $y=+a/2,z=1$ at $\theta_o=2\pi$ has value

$$u_i = \frac{e^{-ik\ell}}{2} \tag{9.1}$$

at that edge.

9.2 CALCULATION OF RADIATION PATTERN

The singly diffracted fields are shown in Figs.9.2a and b. In Fig.9.2a the incident field u_i given by (9.1) is diffracted at the edge $y=+a/2,z=1$. From (2.7) the diffracted field is a line source

$$u_1^a = \frac{e^{-ik\ell}}{2} D(2\pi,\theta)E(r) \tag{9.2}$$

at the edge. In Fig.9.2b the incident field u_i given by (8.7) is diffracted at the edge $y=-a/2,z=0$. From (2.7) the diffracted field is a line source

$$u_1^b = \frac{1}{2} D(0,\theta)E(r) \tag{9.3}$$

at the edge. In Fig.9.2c the incident field u_i given by (8.7) is diffracted at the edge $y=+a/2,z=1$. From (2.7) the diffracted field is a line source

$$u_1^c = \frac{e^{-ik\ell}}{2} D(2\pi,2\pi-\theta)E(r) \tag{9.4}$$

located at the diffracting edge. This field is reflected from the lower guide at $y=-a/2,z=1-a\tan\Psi$. The reflected field u_1^c is a line source (9.4) located at the image point

y=-3a/2,z=1. The radiation pattern from single diffraction is formed by the three line sources (9.2), (9.3) and (9.4) located at the two guide edges and the image point respectively.

The doubly diffracted fields are shown in Figs.9.2d-h. In Fig.9.2d u_i is given by (8.7) and u_1^d is found from (8.3). This field is again diffracted at y=+a/2,z=1 and from (8.1) gives a line source

$$u_2^d = \frac{1}{2} G_d'(c,0,\frac{\pi}{2}-\Psi)G_d(c,\frac{3\pi}{2}-\Psi,\theta)E(r) \tag{9.5}$$

located at the diffracting edge. In Fig.9.2e the incident field u_i given by (9.1) is diffracted at the edge y=+a/2,z=1. From (8.1) the diffracted field is a line source

$$u_1^e = \frac{e^{-ik\ell}}{2} G_d'(2d,2\pi,\frac{3\pi}{2})E(r) \tag{9.6}$$

located at the diffracting edge. This field is reflected at the lower half-plane at y=-a/2,z=1 and, as observed at y=+a/2,z=1, u_1^e looks like a line source (9.6) located at the image point y=-3a/2,z=1. This field is again diffracted at y=+a/2,z=1 and from (8.1) gives a line source

$$u_2^e = \frac{e^{-ik\ell}}{2} G_d'(2d,2\pi,\frac{3\pi}{2})G_d(2d,\frac{3\pi}{2},\theta)E(r) \tag{9.7}$$

located at the diffracting edge. In Fig.9.2f u_i is given by (9.1) and u_1^f is found from (8.3). This field is diffracted at y=-a/2,z=0 and from (8.1) gives a line source

$$u_2^f = \frac{e^{-ik\ell}}{2} G_d'(c,2\pi,\frac{3\pi}{2}-\Psi)G_d(c,\frac{\pi}{2}-\Psi,\theta)E(r) \tag{9.8}$$

located at the diffracting edge. In Fig.9.2g u_i is given by

(8.7) and u_1^g is found from (8.3). This field is diffracted at y=+a/2,z=1 and from (8.1) gives a line source

$$u_2^g = \frac{1}{2} G_d'(c,0,\frac{\pi}{2}-\psi) G_d(c,\frac{3\pi}{2}-\psi,2\pi-\theta) E(r) \tag{9.9}$$

located at the diffracting edge. This field is reflected at the lower half-plane at y=-a/2,z=1-a tan θ . The reflected field u_2^g looks like a line source (9.9) located at the image point y=-3a/2,z=1. In Fig.9.2h u_i is given by (9.1) and u_1^h by (9.6). This field is diffracted at y=+a/2,z=1 and from (8.1) gives a line source

$$u_2^h = \frac{e^{-ik\ell}}{2} G_d'(2d,2\pi,\frac{3\pi}{2}) G_d(2d,\frac{3\pi}{2},2\pi-\theta) E(r) \tag{9.10}$$

located at the diffracting edge. This field is reflected at the lower half-plane at y=-a/2,z=1-a tan θ The reflected field u_2^h looks like a line source (9.10) located at the image point y=-3a/2,z=1.

The triply diffracted radiated fields are represented by the ray diagrams in Figs.9.2i-p. Using methods similar to those above, the expressions for the fields can be determined by inspection. In Fig.9.2i the radiated field is a line source

$$u_3^i = \frac{e^{-ik\ell}}{2} G_d'(c,2\pi,\frac{3\pi}{2}-\psi) G_d(c,\frac{\pi}{2}-\psi,\frac{\pi}{2}-\psi) G_d(c,\frac{3\pi}{2}-\psi,\theta) E(r) \tag{9.11}$$

located at y=+a/2,z=1. In Fig.9.2j the radiated field is a line source

$$u_3^j = \frac{1}{2} G_d'(c,0,\frac{\pi}{2}-\psi) G_d(c,\frac{3\pi}{2}-\psi,\frac{3\pi}{2}-\psi) G_d(c,\frac{\pi}{2}-\psi,\theta) E(r) \tag{9.12}$$

located at y=-a/2,z=0. In Fig.9.2k the radiated field is a

line source

$$u_3^k = \frac{e^{-ik\ell}}{2} G_d'(c,2\pi,\tfrac{3\pi}{2}-\psi)G_d(c,\tfrac{\pi}{2}-\psi,\tfrac{\pi}{2}-\psi)G_d(c,\tfrac{3\pi}{2}-\psi,2\pi-\theta)E(r) \qquad (9.13)$$

located at y=-3a/2,z=1. In Fig.9.21 the radiated field is a line source

$$u_3^\ell = \frac{e^{-ik\ell}}{2} G_d'(2a,2\pi,\tfrac{3\pi}{2})G_d(2a,\tfrac{3\pi}{2},\tfrac{3\pi}{2}-\psi)G_d(c,\tfrac{\pi}{2}-\psi,\theta)E(r) \qquad (9.14)$$

located at y=-a/2,z=1. In Fig.9.2m the radiated field is a line source

$$u_3^m = \frac{1}{2} G_d'(c,0,\tfrac{\pi}{2}-\psi)G_d(c,\tfrac{3\pi}{2}-\psi,\tfrac{3\pi}{2})G_d(2a,\tfrac{3\pi}{2},\theta)E(r) \qquad (9.15)$$

located at y=+a/2,z=1. In Fig.9.2n the radiated field is a line source

$$u_3^n = \frac{1}{2} G_d'(c,0,\tfrac{\pi}{2}-\psi)G_d(c,\tfrac{3\pi}{2}-\psi,\tfrac{3\pi}{2})G_d(2a,\tfrac{3\pi}{2},2\pi-\theta)E(r) \qquad (9.16)$$

located at y=-3a/2,z=1.

In Figs 9.1m and n (8.1) is not valid and the contribution from these ray paths is calculated separately. In Fig.9.2o u_i is given by (9.1) and u_1^0 is given by (9.6). The reflected field u_1^0 which appears like a line source at y=-3a/2,z=1 is diffracted at the edge y=+a/2,z=1 and from (3.26) the resultant field is

$$u_2^o = \frac{e^{-ik\ell}}{2} G_d'(2a,2\pi,\tfrac{3\pi}{2})\left[\frac{1}{2}E(2a+r) - \frac{e^{i\pi/4}}{2\sqrt{2\pi}}E(2a)E(r)\right]. \qquad (9.17)$$

The field u_2^0 is made up of two line sources, one centered at y=+5a/2,z=1, the other at y=+a/2,z=1. The reflected field u_2^0 which is made up of two line sources at y=-7a/2,z=1 and y=-3a/2,z=1 is again diffracted at y=+a/2,z=1 and from (8.1)

the resultant field is

$$u_3^o = \frac{e^{-ik\ell}}{4} G_d'(2a,2\pi,\frac{3\pi}{2}) G_d(4a,\frac{3\pi}{2},\theta) E(r)$$

$$- \frac{e^{-ik\ell}}{4} G_d'(2a,2\pi,\frac{3\pi}{2}) \frac{e^{i\pi/4}}{\sqrt{2\pi}} E(2a) G_d(2a,\frac{3\pi}{2},\theta) E(r) . \qquad (9.18)$$

In Fig.9.2p u_3^p , given by (9.8) with θ replaced by $2\pi-\theta$, is reflected at the lower half-plane at $y=-a/2, z=1-a\tan\theta$. The reflected field u_3^p looks like a line source

$$u_3^p = \frac{e^{-ik\ell}}{4} G_d'(2a,2\pi,\frac{3\pi}{2}) G_d(4a,\frac{3\pi}{2},2\pi-\theta) E(r)$$

$$- \frac{e^{-ik\ell}}{4} G_d'(2a,2\pi,\frac{3\pi}{2}) \frac{e^{i\pi/4}}{\sqrt{2\pi}} E(2a) G_d(2a,\frac{3\pi}{2},\theta) E(r) \qquad (9.19)$$

located at the image point $y=-3a/2, z=1$.

The total fields S_0' diffracted from the upper edge $y=+a/2, z=1$ up to triple diffraction are given by the sum of (9.2), (9.5), (9.7), (9.11), (9.15) and (9.18). These fields appear as line sources at the edge. The total fields S_0'' diffracted from the lower edge $y=-a/2, z=0$ up to triple diffraction are given by the sum of (9.3), (9.8), (9.12) and (9.14). These fields appear as line sources at the edge. The total fields S_0''' , given by the sum of (9.4), (9.9), (9.10), (9.13), (9.16) and (9.19), appear as line sources at $y=-3a/2, z=1$, which is the image of the upper edge.

The radiation pattern formed by these apparent line sources for $\frac{\pi}{2} < \theta < \frac{\pi}{2} + \Psi$ is given by

$$S_0 = S_0' e^{-ik\frac{d}{2}\sin\theta} e^{-ik\ell\cos\theta}$$

$$+ \; S_o'' \, e^{+ik\frac{d}{2}\sin\theta}$$

$$+ \; S_0''' \, e^{+ik\frac{3d}{2}\sin\theta} \, e^{-ik\ell\cos\theta} \quad , \tag{9.20}$$

where the exponential terms are the array factors which adjust for the differing path lengths from the line sources to a distant observation point. In other angular ranges, some of the apparent line sources are shadowed and do not contribute to the pattern. There are four shadow boundaries dividing the radiation pattern into five regions which must be considered separately (Fig.9.3). For $0 < \theta < \pi/2 - \Psi$

$$S_0 = S_0' \, e^{-ik\frac{d}{2}\sin\theta} \, e^{-ik\ell\cos\theta} \tag{9.21}$$

For $\frac{\pi}{2} - \Psi < \theta < \frac{\pi}{2}$ and $\frac{\pi}{2} + \Psi < \theta < \frac{3\pi}{2} - \Psi$

$$S_0 = S_0' \, e^{-ik\frac{d}{2}\sin\theta} \, e^{-ik\ell\cos\theta} + S_0'' \, e^{+ik\frac{d}{2}\sin\theta} \tag{9.22}$$

For $\frac{3\pi}{2} - \Psi < \theta < 2\pi$

$$S_0 = S_0'' \, e^{+ik\frac{d}{2}\sin\theta} \tag{9.23}$$

The pattern is clearly not symmetrical about $\theta = \pi$.

At the shadow boundaries $\theta = \frac{\pi}{2} - \Psi, \frac{\pi}{2}, \frac{\pi}{2} + \Psi$ and $\frac{3\pi}{2} - \Psi$ there are discontinuities in the radiation pattern, which may be reduced by taking higher order diffraction terms into account. For example the single diffraction radiation pattern given by (9.2), (9.3) and (9.4) has a discontinuity at $\theta = \pi/2 - \Psi$ because u_1^b is shadowed for $\theta < \frac{\pi}{2} - \Psi$ The addition of double diffraction u_2^d eliminates this discontinuity because it can be shown that (Fig.9.4a)

$$u_1^b\left[\theta=\left(\frac{\pi}{2}-\psi\right)^+\right] e^{+ik\frac{d}{2}\sin\theta} + u_2^d\left[\theta=\left(\frac{\pi}{2}-\psi\right)^+\right] e^{-ik\frac{d}{2}\sin\theta} e^{-ik\ell\cos\theta}$$

$$= u_2^d\left[\theta=\left(\frac{\pi}{2}-\psi\right)^-\right] e^{-ik\frac{d}{2}\sin\theta} e^{-ik\ell\cos\theta} \qquad (9.24)$$

if the asymptotic form (8.5) is used. Similarly the discontinuity at $\theta = \pi/2$ caused by shadowing of u_1^c for $\theta < \pi/2$ can be eliminated by adding u_2^e because (Fig.9.4b)

$$u_1^c\left[\theta=\frac{\pi}{2}^+\right] e^{+ik\frac{3d}{2}\sin\theta} e^{-ik\ell\cos\theta} + u_2^e\left[\theta=\frac{\pi}{2}^+\right] e^{-ik\frac{d}{2}\sin\theta} e^{-ik\ell\cos\theta}$$

$$= u_2^e\left[\theta=\frac{\pi}{2}^-\right] e^{-ik\frac{d}{2}\sin\theta} e^{-ik\ell\cos\theta} . \qquad (9.25)$$

Similarly the discontinuity at $\theta = \frac{\pi}{2}+\psi$ caused by shadowing of u_1^c for $\theta > \frac{\pi}{2}+\psi$ can be eliminated by adding u_2^f because (Fig.9.4c)

$$u_1^c\left[\theta=\left(\frac{\pi}{2}+\psi\right)^-\right] e^{+ik\frac{3d}{2}\sin\theta} e^{-ik\ell\cos\theta} + u_2^f\left[\theta=\left(\frac{\pi}{2}+\psi\right)^-\right] e^{+ik\frac{d}{2}\sin\theta}$$

$$= u_2^f\left[\theta=\left(\frac{\pi}{2}+\psi\right)^+\right] e^{+ik\frac{d}{2}\sin\theta} . \qquad (9.26)$$

Similarly the discontinuity at $\theta = \frac{3\pi}{2}-\psi$ caused by shadowing of u_1^a for $\theta > \frac{3\pi}{2}-\psi$ can be eliminated by adding u_2^f because (Fig.9.4d)

$$u_1^a\left[\theta=\left(\frac{3\pi}{2}-\psi\right)^-\right] e^{-ik\frac{d}{2}\sin\theta} e^{-ik\ell\cos\theta} + u_2^f\left[\theta=\left(\frac{3\pi}{2}-\psi\right)^-\right] e^{+ik\frac{d}{2}\sin\theta}$$

$$= u_2^f\left[\theta=\left(\frac{3\pi}{2}-\psi\right)^+\right] e^{+ik\frac{d}{2}\sin\theta} . \qquad (9.27)$$

However the addition of these double diffraction terms does not completely eliminate discontinuities in the radiation pattern, because the added terms are themselves shadowed in some regions and have discontinuities at the shadow

boundaries. However, the discontinuities in the double diffraction terms is much less then those in the single diffraction terms, so that the overall effect of adding the double diffraction terms is to reduce the discontinuities in the radiation pattern.

Similarly, by adding certain triple diffraction terms, the discontinuities in the double diffraction terms can each be eliminated. Again, the discontinuities which remain in the triple diffraction terms are much less then those in the double diffraction terms. In summary, higher order diffraction terms can be added to reduce the discontinuities at shadow boundaries.

The radiation pattern $\overline{S_0}$ for the staggered guide of Fig.9.5 is calculated in exactly the same way as S_0 . It is found that

$$\overline{S_0}(\theta) = S_0(2\pi-\theta)$$

The ray paths which must be considered to find $\overline{S_0}$ are the mirror image about the z-axis of those shown in Fig.9.2.

9.3 NUMERICAL AND EXPERIMENTAL RESULTS

The radiation pattern of a single staggered parallel-plate waveguide calculated by ray-optical methods is compared with the measured E-plane patterns of the H-plane sectoral horn for a stagger angle of $\Psi = 45^\circ$. The patterns consist of a single asymmetrical lobe with maximum amplitude at about $\theta' = 40^\circ$ off the guide axis ($\theta' = \theta - \pi$) (Figs.9.6a-d). The

discontinuities which might be expected on the four shadow boundaries at $\theta'=-135^\circ$, -90°, -45°, and $+45^\circ$ (Fig.9.3) are very small when the asymptotic form (8.5) is used. If (8.5) is not used there is a discontinuity of about 3dB at $\theta'=+45^\circ$ but all other discontinuities remain small. The phase varies considerably in the forward direction ($|\theta'|<90^\circ$) in contrast to a non-staggered guide where the phase is essentially constant over this range. The experimental patterns generally agreed with the ray-optical theory to within 1 dB except at large angles.

The patterns calculated by Ryan and Rudduck [42] are very similar to those obtained here if only the ray paths 9.1a-h are considered.

Radiation patterns calculated using only single and double diffraction are shown in Fig.9.7. The single diffraction pattern has pronounced discontinuities at the shadow boundaries, but the double diffraction pattern has remarkably small discontinuities and is very similar to the triple diffraction pattern.

The radiation patterns for stagger angles from 0° to 75° at a fixed guide width are shown in Fig.9.8. The pattern changes gradually from that of a non-staggered guide as is increased and becomes more asymmetrical.

9.4 SUMMARY

The radiation pattern of a single staggered parallel plate waveguide is calculated by ray-optical methods. The

discontinuities expected along the four shadow boundaries are very small, even when terms up to and including only double diffraction are considered. The good agreement between this theory and the experimental results gives confidence that both may be applied to more complex geometries.

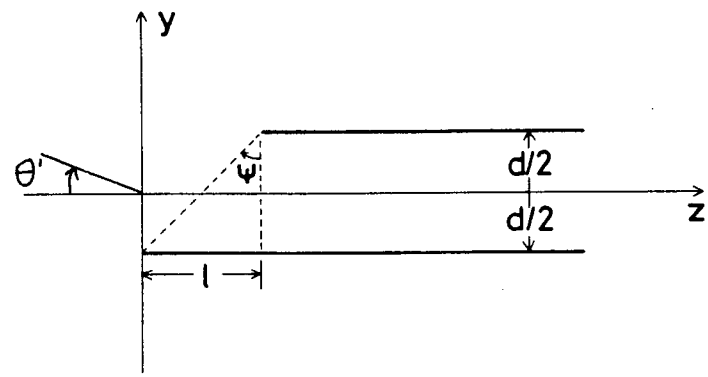

Fig. 9.1
staggered parallel plate waveguide

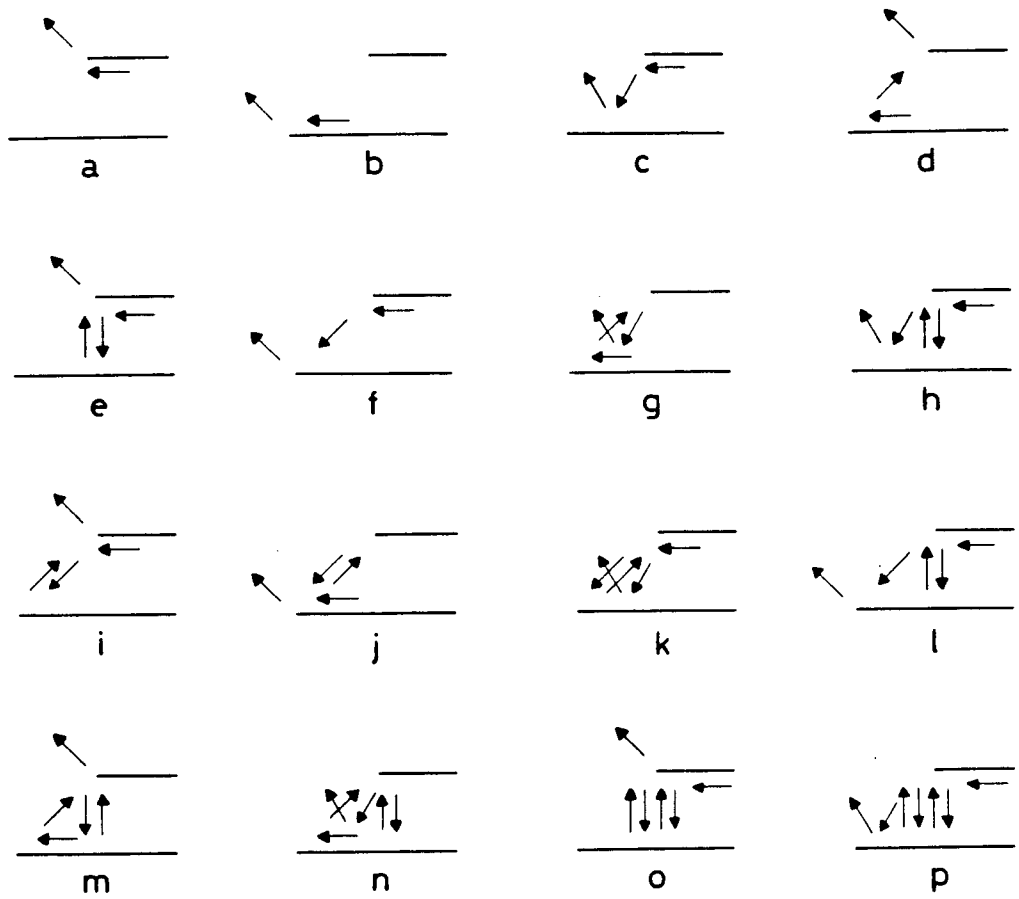

Fig. 9.2
ray paths for radiation pattern calculation

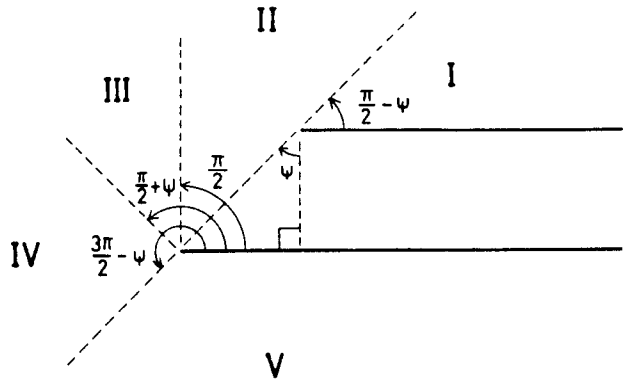

Fig. 9.3
shadow boundaries for staggered parallel plate waveguides

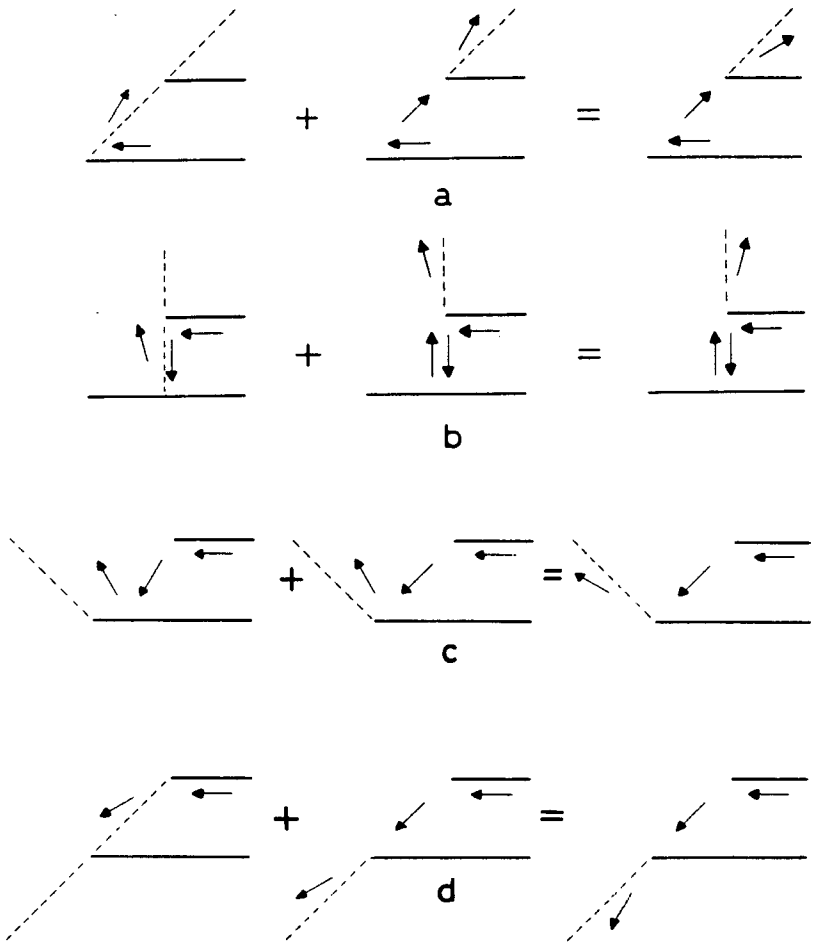

Fig. 9.4
continuity fields across shadow boundaries
see eqns. (9.24) - (9.27).

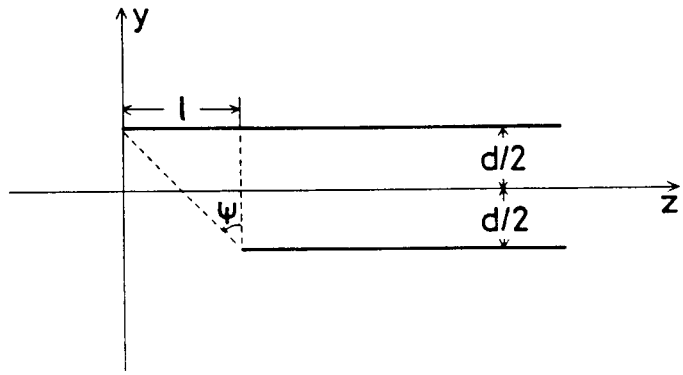

Fig. 9.5
staggered parallel plate waveguide

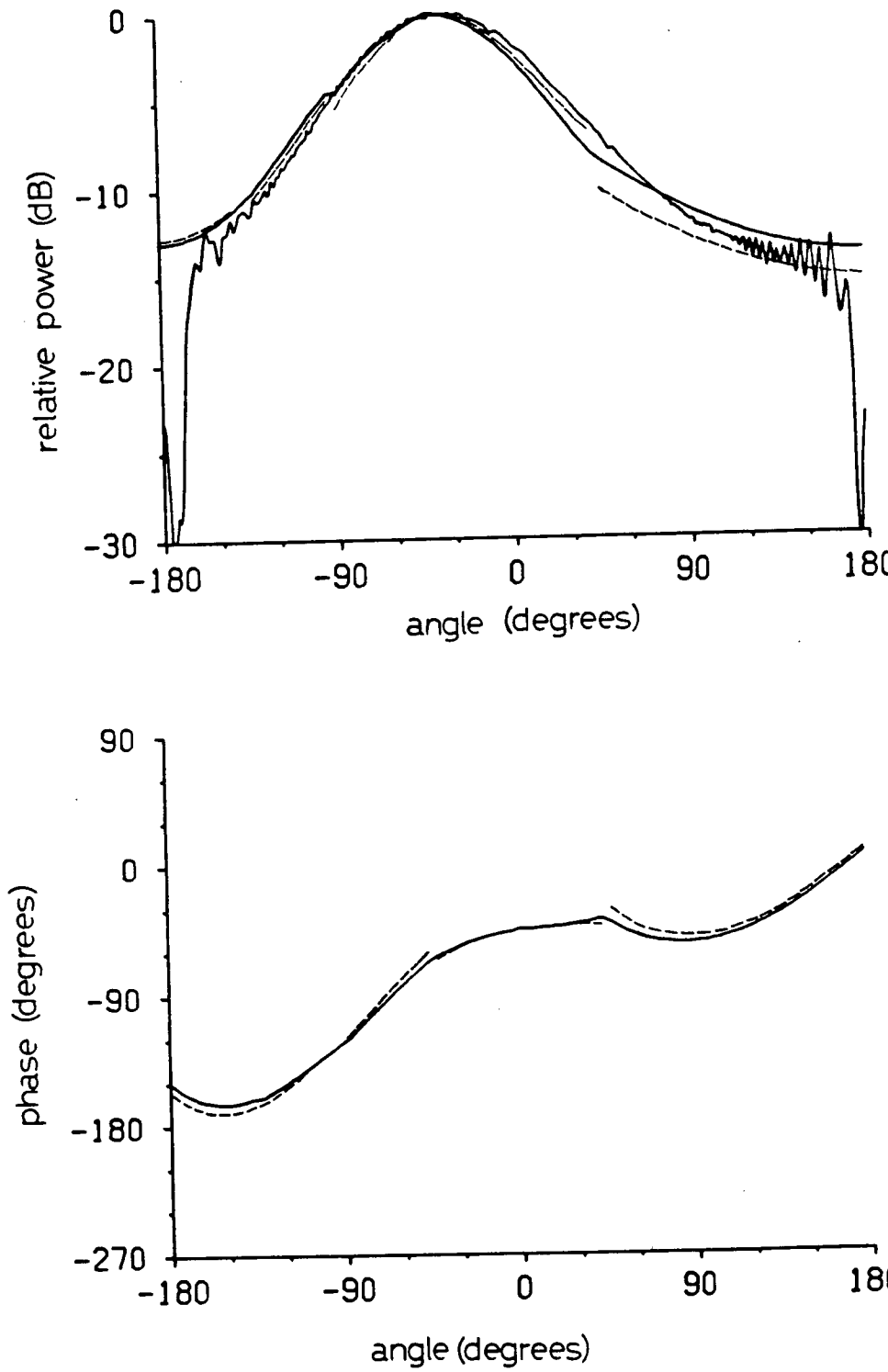

Fig. 9.6a Radiation pattern of staggered waveguide $\Psi=45°$. $d=0.339\lambda$

——— using (8.5)
- - - - - using (8.4)

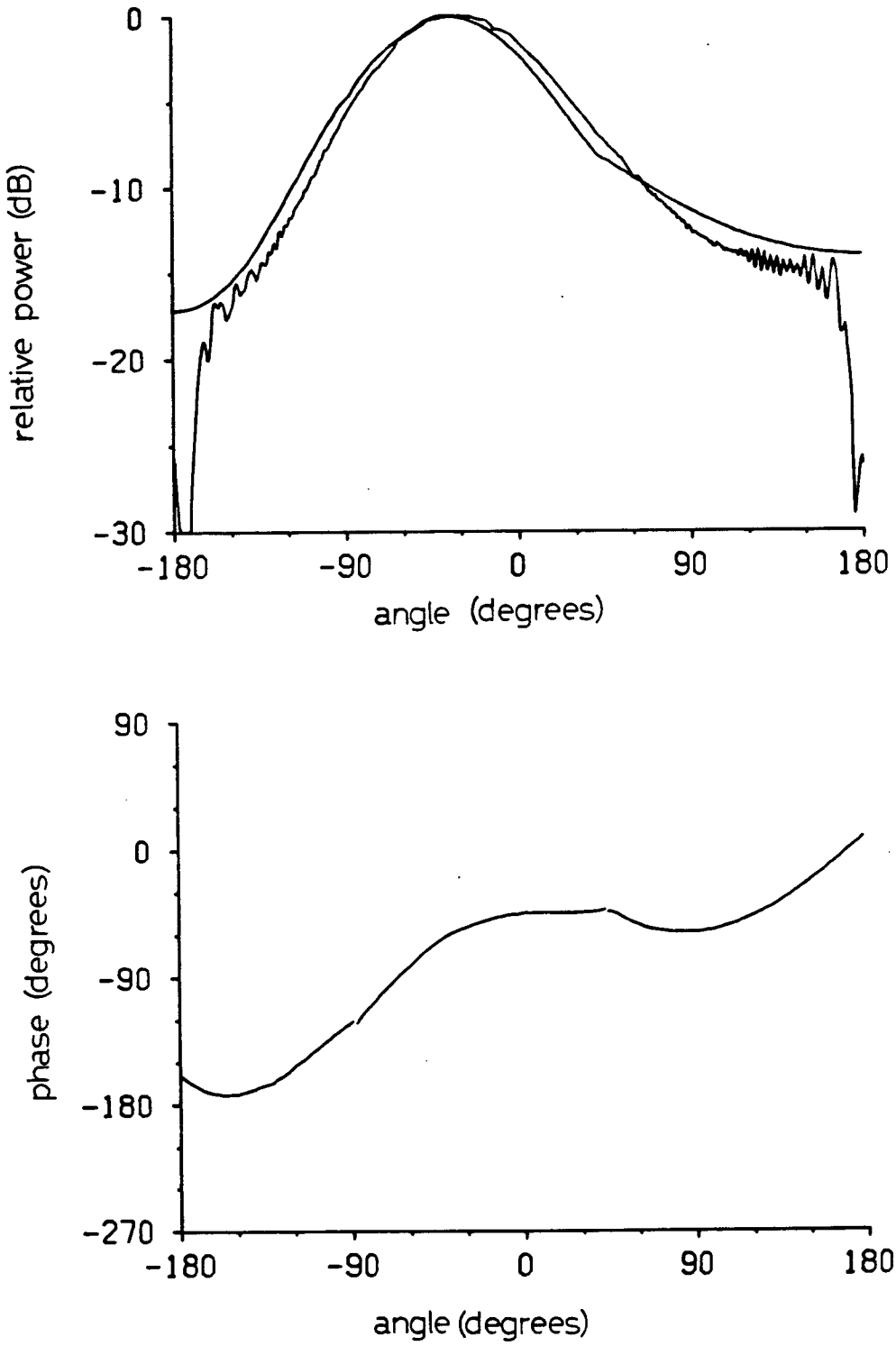

Fig. 9.6b Radiation pattern of staggered waveguide $\Psi=45°$. $d=0.373\lambda$

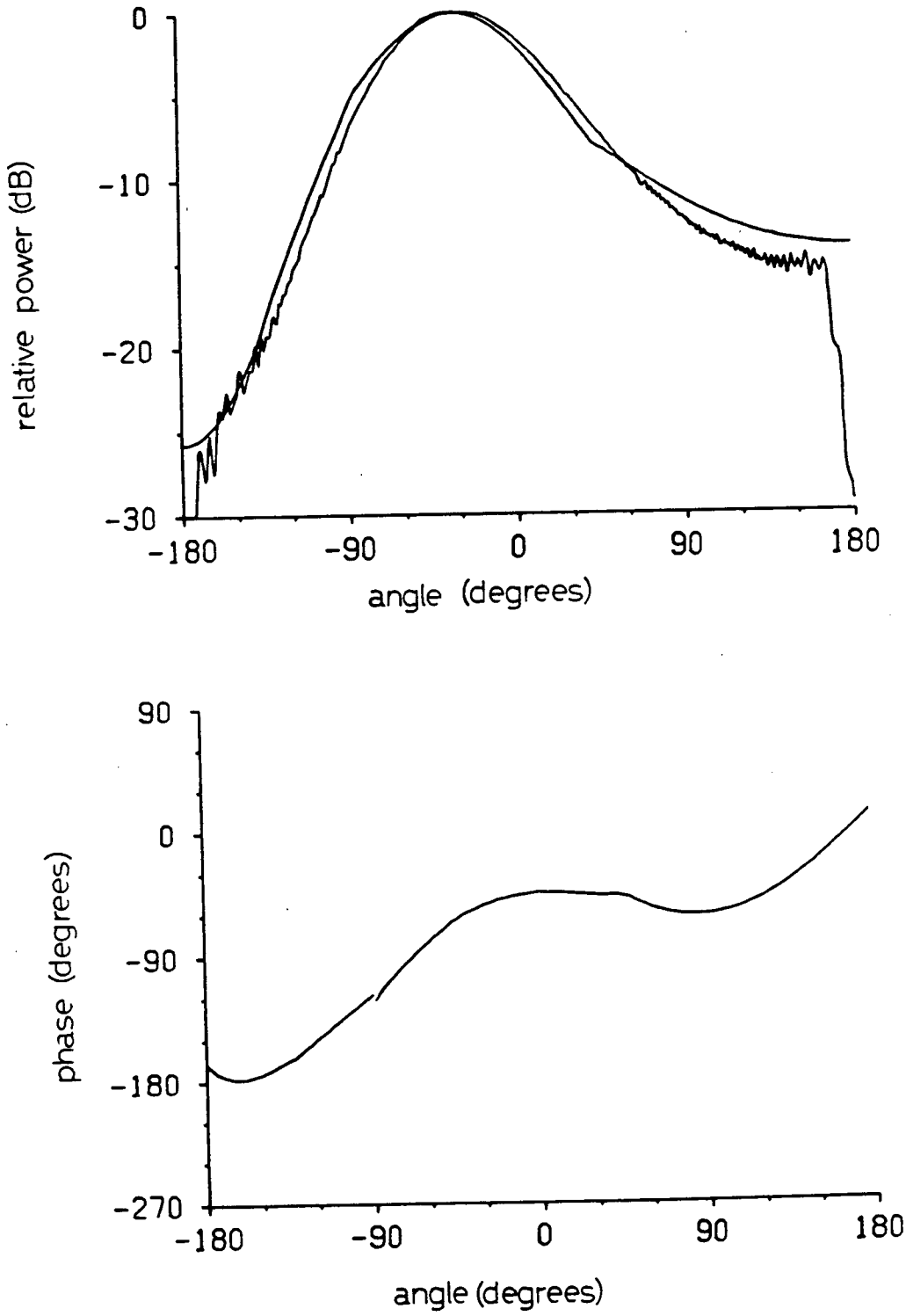

Fig. 9.6c Radiation pattern of staggered waveguide $\Psi=45°$. $d=0.407\lambda$

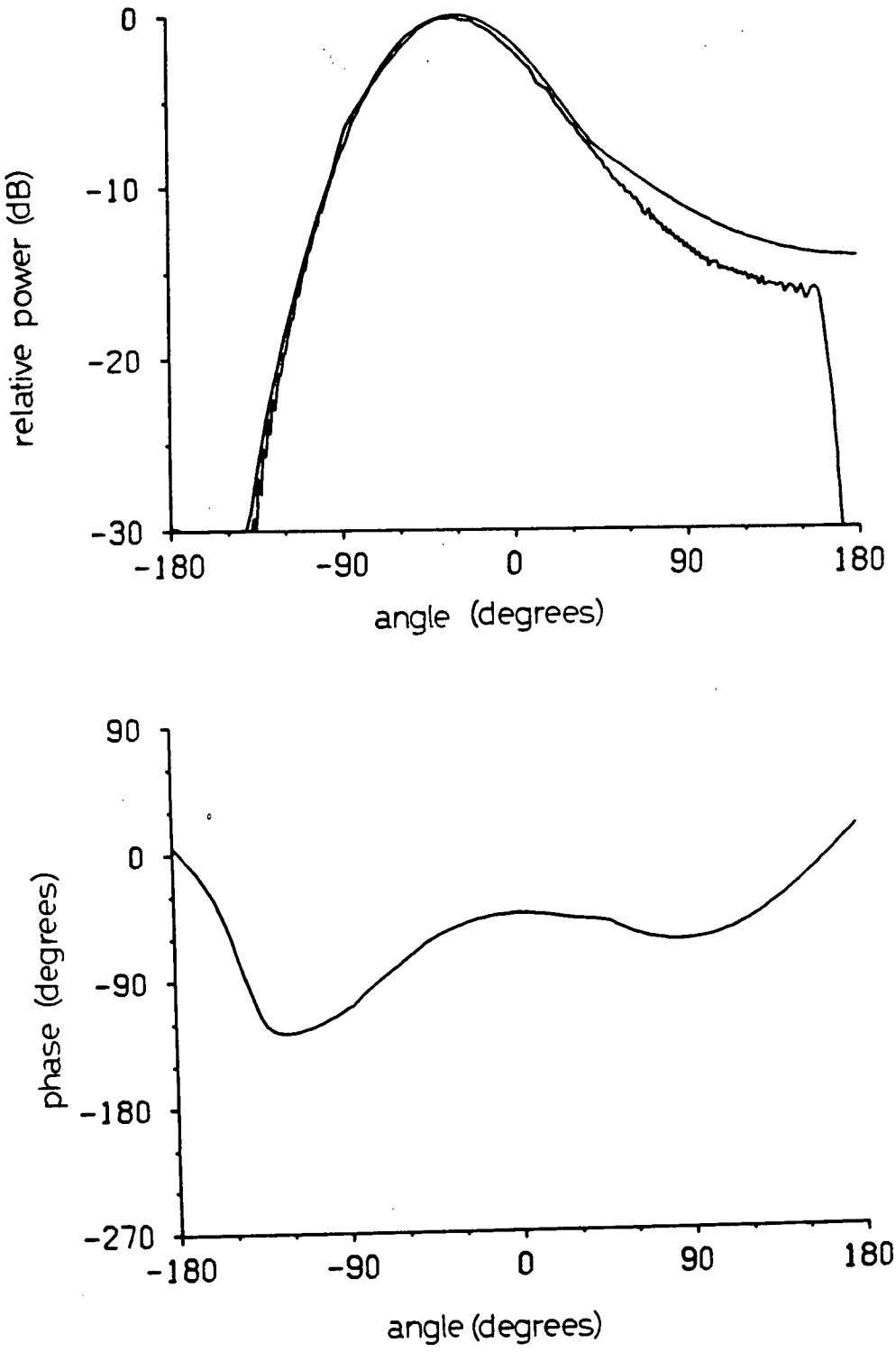

Fig. 9.6d Radiation pattern of staggered waveguide $\Psi=45°$. $d=0.441\lambda$

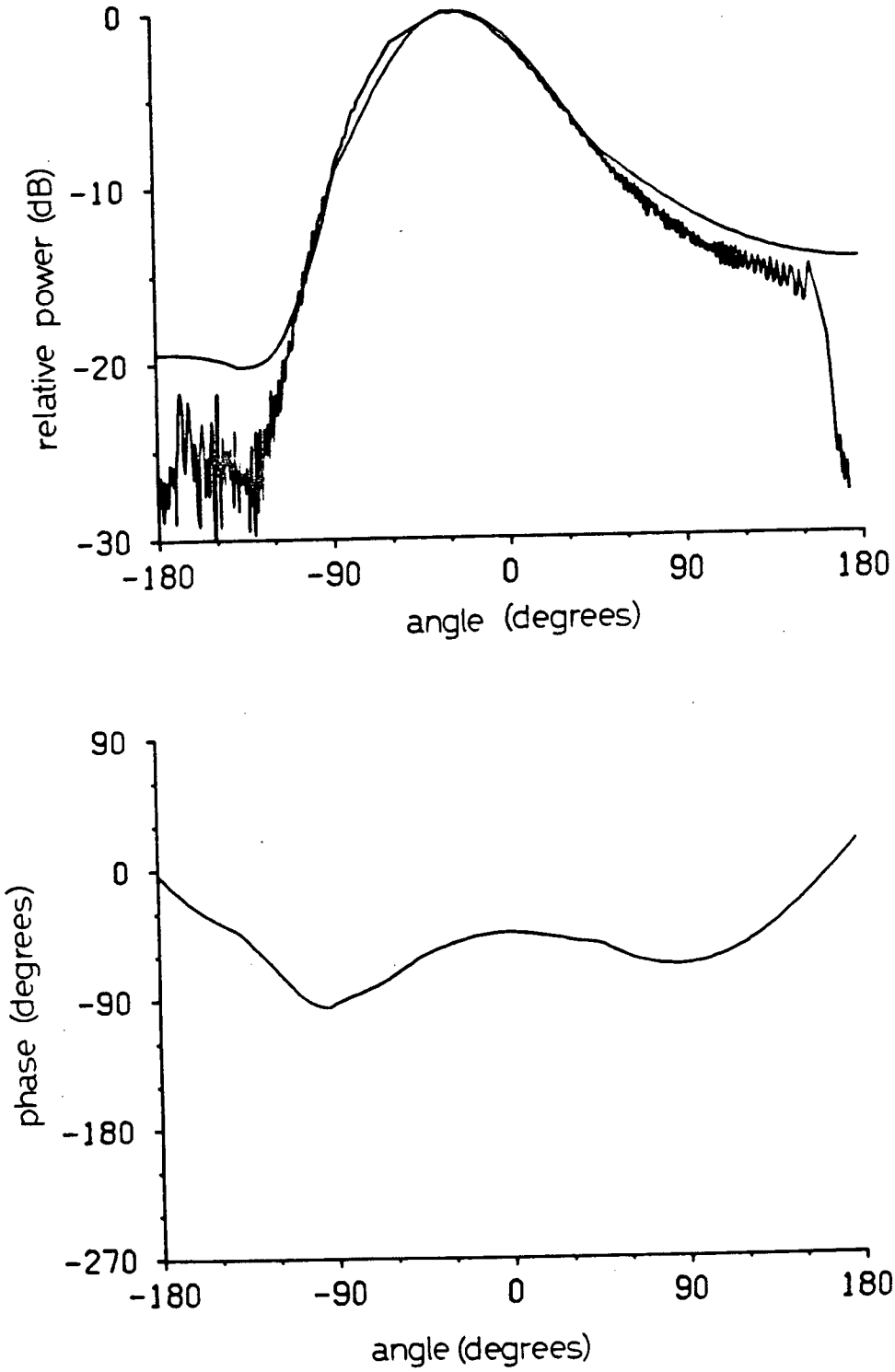

Fig. 9.6e Radiation pattern of staggered waveguide $\Psi=45°$. $d=0.474\lambda$

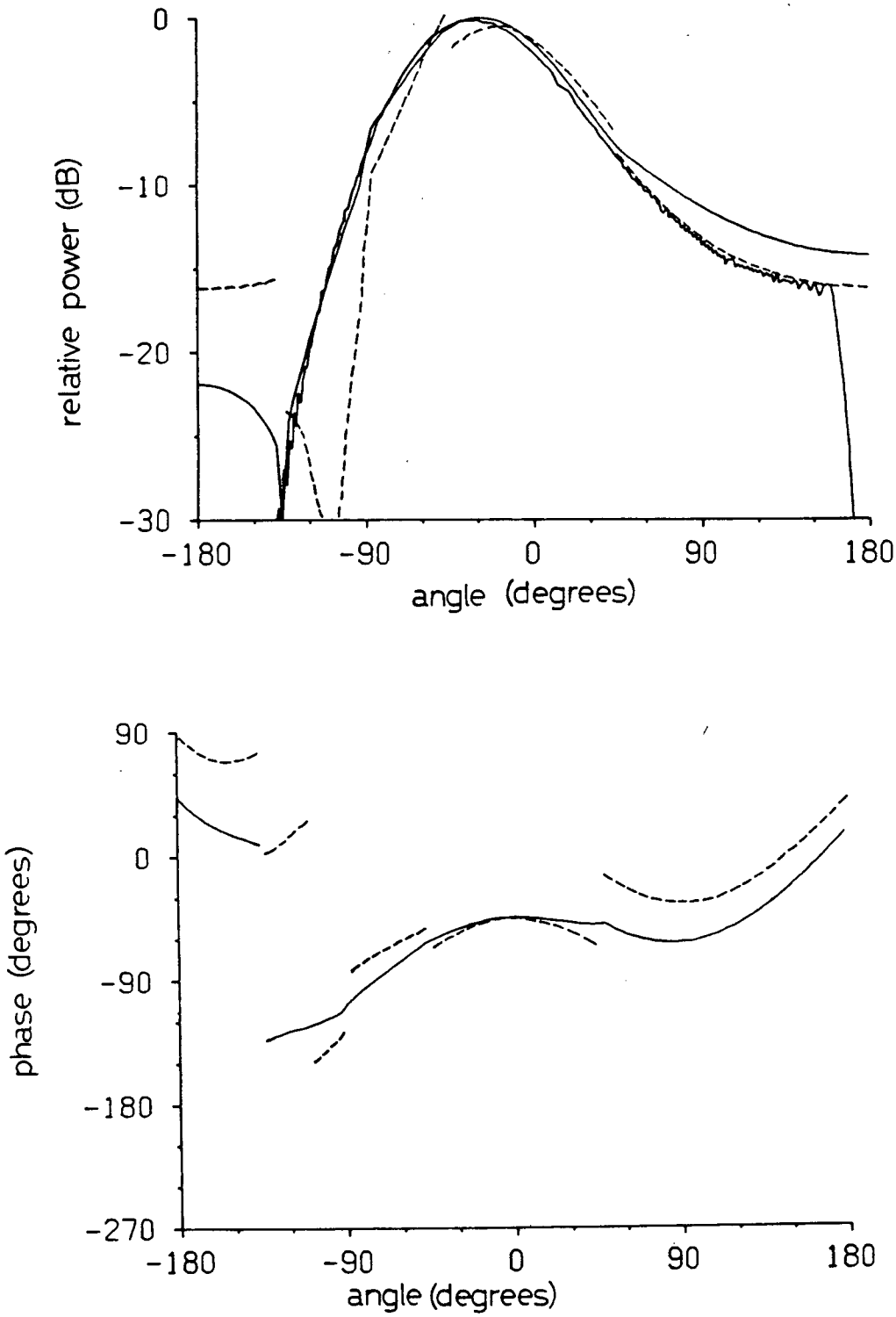

Fig. 9.7 Radiation pattern of staggered waveguide $\Psi=45°$ single and double diffraction only.

$d=0.441\lambda$

---- single diffraction

—— single and double diffraction

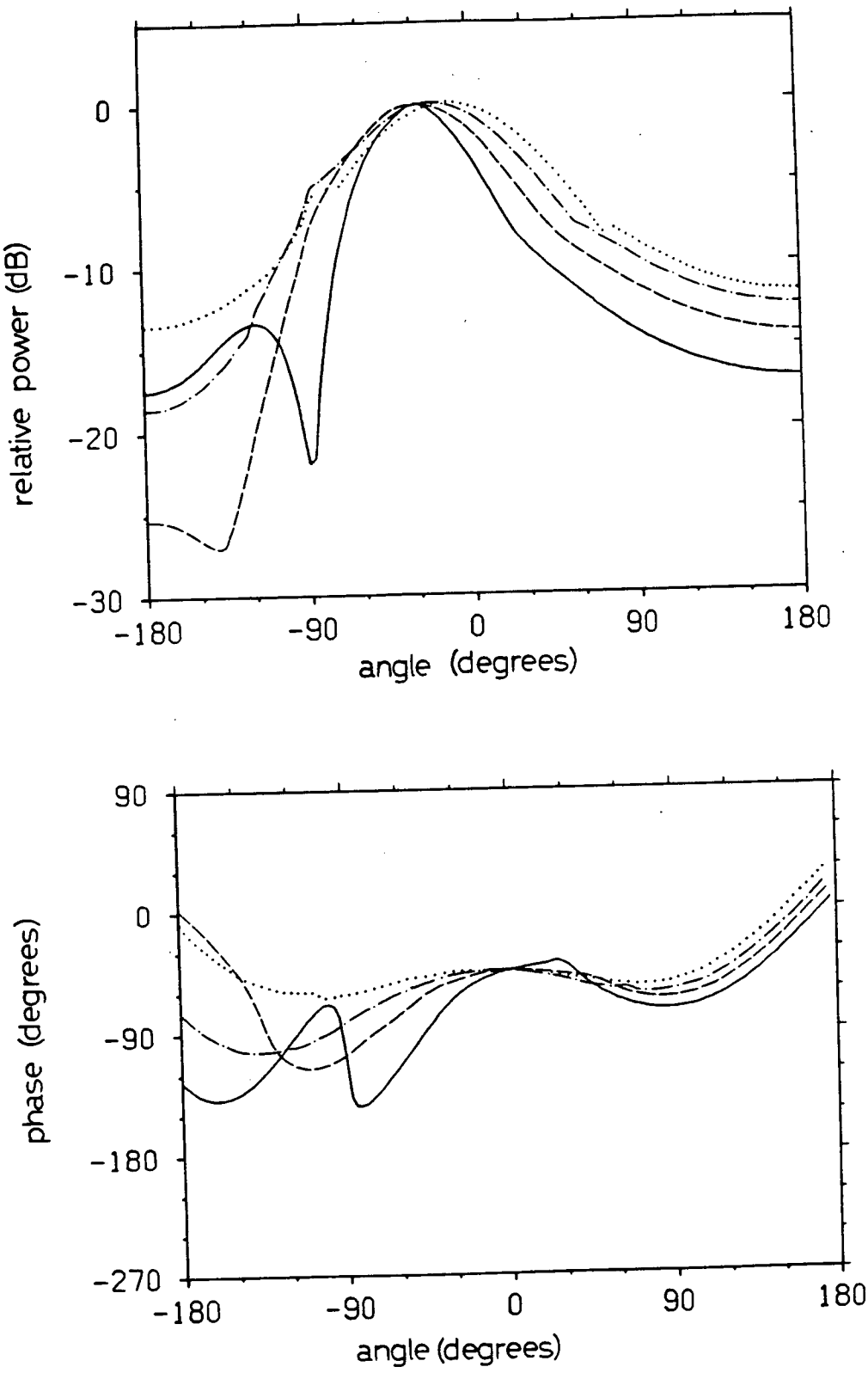

Fig. 9.8 Radiation pattern of staggered waveguide for various stagger angles.

····· Ψ=15° — — — Ψ=45°
—·—· Ψ=30° —— Ψ=60°

Chapter 10

RADIATION FROM MULTI-ELEMENT STAGGERED WAVEGUIDE ARRAY

10.1 INTRODUCTION

The radiation pattern of a multi-element waveguide array (Fig.10.1) with staggered waveguides is found by methods similar to those used for the array of Chapter 6. The main difference between the two arrays is that in the non-staggered array all edges are in the aperture plane, whereas in the staggered array the outer waveguide edges are behind the aperture plane.

The stagger does change the radiation pattern calculation significantly, however. As before the pattern for the case when all guides are of infinite depth is calculated first. The additional fields radiated when the outer guides are shorted are calculated later. The analysis is restricted to the TEM case.

Consider three adjacent semi-infinite parallel-plate waveguides consisting of four perfectly conducting infinitely thin half-planes at $y=-d/2-a, z>1$, $y=-d/2, z>0$, $y=+d/2, z>0$ and $y=d/2+a, z>1$ (Fig.10.2). The incident field (8.6) in the central driven guide $-d/2<y<d/2$ is decomposed into two plane waves each with value (8.7) at the edges $y=-d/2, z=0$ and $y=+d/2, z=0$. These two plane waves are represented by the incident rays in the central guide of Fig.10.2.

10.2 RADIATION WITH OUTER GUIDES OF INFINITE DEPTH

The total radiation pattern S_t of the array of three parallel plate waveguides with only the center guide driven is calculated. The field S_t is made up of the sum of the fields scattered from all the edges and their images. $P_0(d)$ represents the field scattered from the open end of the central guide of width d, S_n (n=1,2,3,4) represents the total field scattered from the nth edge (as labelled in Fig.10.2) not already included in $P_0(d)$ (Fig.10.3,10.4), and $S_{\bar{n}}(n=3,4)$ represents the fields scattered from the nth edge and then reflected from the outer surface of the central guide (Fig.10.5). The fields $S_{\bar{n}}$ appear to emanate from the image of the nth edge . The total radiation pattern must be found separately for each of seven different angular regions (Fig.10.6), because not all edges and images are visible at all angles. The pattern need only be calculated for $0 < \theta < \pi$ because the pattern is symmetrical about $\theta = \pi$.

$0 < \theta < \frac{\pi}{2} - \Psi$ all edges except edge 1 are shadowed and

$$S_t = S_3 e^{-ik(\frac{d+2a}{2})\sin\theta} e^{-ik\ell\cos\theta} . \qquad (10.1)$$

For $\frac{\pi}{2} - \Psi < \theta < \frac{\pi}{2}$

$$S_t = S_3 e^{-ik(\frac{d+2a}{2})\sin\theta} e^{-ik\ell\cos\theta} + S_1 e^{-ik\frac{d}{2}\sin\theta} + P_0(d) . \qquad (10.2)$$

For $\frac{\pi}{2} < \theta < \frac{\pi}{2} + \Psi$

$$S_t = S_3 e^{-ik\left(\frac{d+2a}{2}\right)\sin\theta} e^{-ik\ell\cos\theta} + S_1 e^{-ik\frac{d}{2}\sin\theta} + P_0(d) + S_{\bar{3}} e^{-ik\left(\frac{d-2a}{2}\right)\sin\theta} e^{-ik\ell\cos\theta} + S_2 e^{+ik\frac{d}{2}\sin\theta} . \quad (10.3)$$

For $\frac{\pi}{2} + \Psi < \theta < \pi$

$$S_t = S_3 e^{-ik\left(\frac{d+2a}{2}\right)\sin\theta} e^{-ik\ell\cos\theta} + S_1 e^{-ik\frac{d}{2}\sin\theta} + P_0(d) + S_2 e^{+ik\frac{d}{2}\sin\theta} + S_4 e^{+ik\left(\frac{d+2a}{2}\right)\sin\theta} e^{-ik\ell\cos\theta} . \quad (10.4)$$

The fields P_0 were calculated in Chapter 5. The fields S_1 are calculated using the ray paths in Fig.10.3. The fields S_3 are calculated using the ray paths in Fig.10.4. The fields $S_{\bar{3}}$ are calculated using the ray paths in Fig.10.5. The ray paths used to calculate S_2 and S_4 are the image about the z-axis of those shown in Figs.10.3 and 10.4. The

solutions for the fields represented by all these ray paths are found in a manner similar to that in Chapter 8 and 9.

To calculate s_1 consider the ray diagram in Fig.10.3. Here the radiated field is a line source

$$u_{13} = \frac{1}{2} G_d'(c,2\pi,\frac{\pi}{2}-\psi)G_d(c,\frac{3\pi}{2}-\psi,\frac{3\pi}{2}-\psi)G_d(c,\frac{\pi}{2}-\psi,\theta)E(r) , \tag{10.5}$$

where $c = \sqrt{\ell^2 + a^2}$. To calculate s_3 consider the ray diagram in Fig.10.4. In Fig.10.4a the radiated field u_{32}^a is a line source

$$u_{32}^a = \frac{1}{2} G_d'(c,2\pi,\frac{\pi}{2}-\psi)G_d(c,\frac{3\pi}{2}-\psi,\theta)E(r) . \tag{10.6}$$

In Fig.10.4b the radiated field u_{33}^b is a line source

$$u_{33}^b = \frac{1}{2} G_d'(c,2\pi,\frac{\pi}{2}-\psi)G_d(c,\frac{3\pi}{2}-\psi,\frac{3\pi}{2})G_d(2a,\frac{3\pi}{2},\theta)E(r) . \tag{10.7}$$

In Fig.10.4c the radiated field u_{33}^c is a line source

$$u_{33}^c = \frac{1}{2} G_d'(d,0,\frac{\pi}{2})G_d(d,\frac{3\pi}{2},\frac{\pi}{2}-\psi)G_d(c,\frac{3\pi}{2}-\psi,\theta)E(r) . \tag{10.8}$$

To calculate s_3 consider the ray diagram in Fig.10.5. In Fig.10.5a the radiated field is a line source

$$u_{32}^a = \frac{1}{2} G_d'(c,2\pi,\frac{\pi}{2}-\psi)G_d(c,\frac{3\pi}{2}-\psi,2\pi-\theta)E(r) . \tag{10.9}$$

In Fig.10.5b the radiated field is a line source

$$u_{33}^b = \frac{1}{2} G_d'(c,2\pi,\frac{\pi}{2}-\psi)G_d(c,\frac{3\pi}{2}-\psi,\frac{3\pi}{2})G_d(2a,\frac{3\pi}{2},2\pi-\theta)E(r) . \tag{10.10}$$

In Fig.10.5c the radiated field is a line source

$$u_{33}^c = \frac{1}{2} G_d'(d,0,\frac{\pi}{2})G_d(d,\frac{3\pi}{2},\frac{\pi}{2}-\psi)G_d(c,\frac{3\pi}{2}-\psi,2\pi-\theta)E(r) . \tag{10.11}$$

Similar calculations for the fields s_2 scattered from the

edge y=-d/2,z=0 and S_4 from y=-d/2-a,z=1 show that

$$S_2 = -S_1 , \tag{10.12}$$

$$S_4 = -S_3 . \tag{10.13}$$

These results for S_n and $S_{\bar{n}}$ are now substituted into (10.1), (10.2), (10.3) and (10.4) to give the total radiation pattern of the array of Fig.10.2.

10.3 RADIATION WITH OUTER GUIDES SHORTED

Consider the array of Fig.10.1, which is equivalent to the array of Fig.10.2 except that the outer guides are now of finite depth. The fields coupled into these guides will be reflected from the far end and reradiated. Adjusting the depth of the guides will change the relative phase of their radiation and thus alter the radiation pattern.

The coupling coefficient $A_s(d,a)$ between the central driven guide of width d and the adjacent staggered outer guide of width a has been calculated in Chapter 8. The coupled fields travel down the outer guide and are reflected at the shorted end. The fields then travel towards the open end ,where part is reflected back and part is radiated.

The value A' of the fields in the outer guides at the aperture plane z=0 relative to those from the central driven guide is the sum of a geometric series

$$A' = \frac{A_s(d,a)\, e^{i2ks}}{1-R_s(a)\, e^{i2ks}} , \tag{10.14}$$

where $R_s(a)$ is the reflection coefficient at the open end of the staggered parallel-plate waveguide of width a [40], and s is the depth of the outer guide measured from the aperture plane.

The total radiation pattern of the array of Fig.10.1 is calculated by adding the radiation field caused by the finite depth of the outer guides to the fields radiated from the array of Fig.10.2. The additional fields consist of fields radiated directly from the outer guides, and fields from other edges excited by fields in a shorted guide (Fig.10.7).

Radiation from the outer guides is simply the pattern S_0 (9.19-9.22) of a staggered parallel-plate waveguide multiplied by A' of (10.14). Scattering from other edges due to radiation from the outer guides is calculated by considering the ray paths in Fig.10.7. In Fig.10.7a the field from the edge y=+d/2,z=0 can be written

$$u_{1'2}^{a} = \frac{1}{2} G_d'(d,2\pi,\tfrac{3\pi}{2}) G_d(d,\tfrac{3\pi}{2},\theta) E(r) . \tag{10.15}$$

In Fig.10.7b the field from the edge y=+d/2,z=0 can be written

$$u_{1'3}^{b} = \frac{1}{4} G_d'(d,0,\tfrac{3\pi}{2}) G_d(2d,\tfrac{3\pi}{2},\theta) - \frac{e^{i\pi/4}}{4\sqrt{2\pi}} G_d'(d,0,\tfrac{3\pi}{2}) E(d) G_d(d,\tfrac{3\pi}{2},\theta). \tag{10.16}$$

In Fig.10.7c the field from the edge y=+d/2,z=0 is

$$u_{1'3}^{c} = \frac{e^{-ik\ell}}{2} G_d'(c,0,\tfrac{\pi}{2}+\Psi) G_d(c,\tfrac{3\pi}{2}+\Psi,\tfrac{\pi}{2}) G_d(d,\tfrac{3\pi}{2},\theta). \tag{10.17}$$

In Fig.10.7d the field from the edge y=+d/2+a,z=1 is

$$u_{1'3}^{d} = \frac{1}{2} G_d'(d,2\pi,\tfrac{\pi}{2}) G_d(d,\tfrac{3\pi}{2},\tfrac{\pi}{2}-\Psi) G_d(c,\tfrac{3\pi}{2}-\Psi,\theta). \tag{10.18}$$

In Fig.10.7e the field from the edge y=+d/2-a,z=1 is

$$u_{\bar{3}'3}^{e} = \frac{1}{2} G_d'(d,2\pi,\tfrac{\pi}{2}) G_d(d,\tfrac{3\pi}{2},\tfrac{\pi}{2}-\Psi) G_d(c,\tfrac{3\pi}{2}-\Psi,2\pi-\theta). \tag{10.19}$$

The fields (10.15), (10.16) and (10.17) are added to give the field S_1' from the edge y=d/2,z=0 excited by radiation from the outer guides. Similarly (10.18) gives the field S_3' from the edge y=+d/2+a,z=1, and (10.19) gives the field $S_{\bar{3}}'$ from the image point y=+d/2-a,z=1. Similar calculations of the fields S_2' from the edge y=-d/2,z=0 and S_4' from y=-d/2-a,z=1 show that

$$S_2' = -S_1' \tag{10.20}$$

$$S_4' = -S_3'. \tag{10.21}$$

The additional radiation caused by the finite depth of the outer guides is the array sum of S_0, $\overline{S_0}$, S_n' and $S_{\bar{n}}'$ multiplied by the coefficient A' of (10.14). This radiation is added to S_t in (10.1)-(10.4) to obtain the complete radiation pattern S_{total} for the array of Fig.10.1.

For $0 < \theta < \frac{\pi}{2} - \Psi$

$$S_{total} = S_t + A'S_3' e^{-ik(\frac{d+2a}{2})\sin\theta} e^{-ik\ell\cos\theta} + A'S_0 e^{-ik(\frac{d+a}{2})\sin\theta}. \tag{10.22}$$

For $\frac{\pi}{2} - \Psi < \theta < \frac{\pi}{2}$

$$S_{total} = S_t + A'S_3' e^{-ik(\frac{d+2a}{2})\sin\theta} e^{-ik\ell\cos\theta} + A'S_0 e^{-ik(\frac{d+a}{2})\sin\theta} + A'S_1' e^{-ik\frac{d}{2}\sin\theta} \quad (10.23)$$

For $\frac{\pi}{2} < \theta < \frac{\pi}{2} + \Psi$

$$S_{total} = S_t + A'S_3' e^{-ik(\frac{d+2a}{2})\sin\theta} e^{-ik\ell\cos\theta} + A'S_0 e^{-ik(\frac{d+a}{2})\sin\theta} + A'S_1' e^{-ik\frac{d}{2}\sin\theta} + A'S_{-3} e^{-ik(\frac{d-2a}{2})\sin\theta} e^{-ik\ell\cos\theta} + A'S_2' e^{+ik\frac{d}{2}\sin\theta} + A\overline{S_0} e^{+ik(\frac{d+a}{2})\sin\theta} \quad (10.24)$$

For $\frac{\pi}{2} + \Psi < \theta < \pi$

$$S_{total} = S_t + A'S'_3 e^{-ik\left(\frac{d+2a}{2}\right)\sin\theta} e^{-ik\ell\cos\theta}$$

$$+ A'S_0 e^{-ik\left(\frac{d+a}{2}\right)\sin\theta}$$

$$+ A'S'_1 e^{-ik\frac{d}{2}\sin\theta}$$

$$+ A'S'_2 e^{+ik\frac{d}{2}\sin\theta}$$

$$+ A'\overline{S_0} e^{+ik\left(\frac{d+a}{2}\right)\sin\theta}$$

$$+ A'S'_4 e^{+ik\left(\frac{d+2a}{2}\right)\sin\theta} e^{-ik\ell\cos\theta} \quad . \qquad (10.25)$$

10.4 NUMERICAL AND EXPERIMENTAL RESULTS

The radiation pattern of a three element staggered waveguide array calculated by ray-optical methods is compared with measured E-plane patterns of an H-plane sectoral horn with appendages added to simulate the outer guides. Radiation patterns when the outer guides are of infinite depth are shown in Fig.10.8 for various stagger angles Ψ . As Ψ changes from 0° to 90° the shape of the

pattern changes gradually from that of a three element non-staggered array to that of a single guide, as might be expected. The general effect of increasing ψ is to broaden the pattern.

When the outer guides are of finite depth the patterns are generally similar to those for the three element non-staggered array. The patterns have 3 dB beamwidths ranging from $\pm 20^\circ$ to $\pm 90^\circ$ depending on the frequency (Fig.10.9-10.13). The discontinuities expected along the shadow boundaries at $\theta = \pi/2$ and $\theta = \pi/2 + \psi$ were generally smaller then in the non-staggered case: less then 2 dB at $\theta = \pi/2$ and less then 1 dB at $\theta = \pi/2 + \psi$. This is because there are only two edges along any shadow boundary in the staggered array as compared to four or six edges in the non-staggered arrays of Chapters 6 and 7.

The experimental patterns generally agree with the calculated ones to within 1 dB up to $\theta' = \pm 60^\circ$ and within 3 dB up to $\theta' = \pm 150^\circ$. The patterns at $\theta' = 180^\circ$ could not be measured accurately because of blockage by the antenna mounting arrangement $(\theta' = \theta - \pi)$.

The effect of increasing ψ from 0° to 60° for a fixed guide depth is shown in Fig.10.14. The patterns change gradually from the non-staggered pattern for that guide depth, which has a null on the beam axis, to a pattern with a single lobe with beamwidth considerably narrower then that of a single guide.

10.5 SUMMARY

The radiation pattern of an array of staggered parallel plate waveguides was calculated by ray-optical methods and compared with experimental results obtained using an H-plane sectoral horn with appendages. The calculation is more complex then the non-staggered case because there are more shadow boundaries and more ray paths to be considered. On the other hand, the calculation is simpler because not all edges are in the same plane, thus avoiding the difficulties of multiple edges along a shadow boundary.

The discontinuities observed at the shadow boundaries are generally much smaller then those observed in the non-staggered case. This is not unexpected because only one edge is shadowed at a time when traversing shadow boundaries in the staggered array, as compared to three or five which may be shadowed in the non-staggered array.

The patterns are generally broader then for the non-staggered case, especially for large ψ . The parameters can be adjusted to give a significant reduction in beamwidth as compared to a single guide, however.

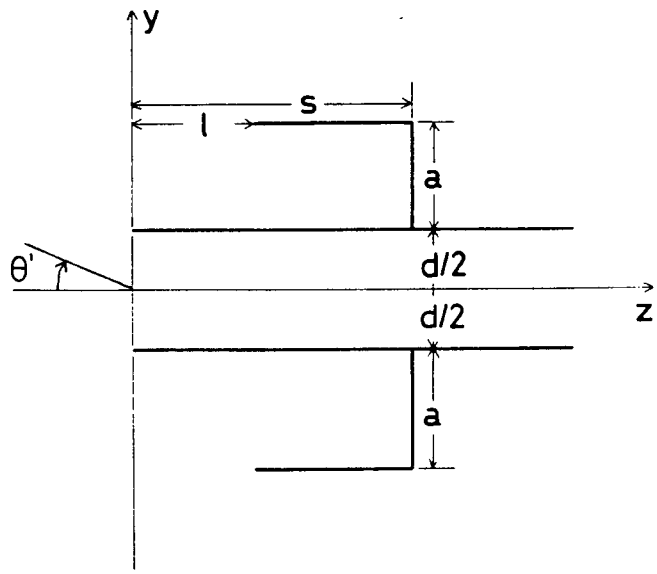

Fig. 10.1
array of staggered parallel plate waveguides with outer guides shorted

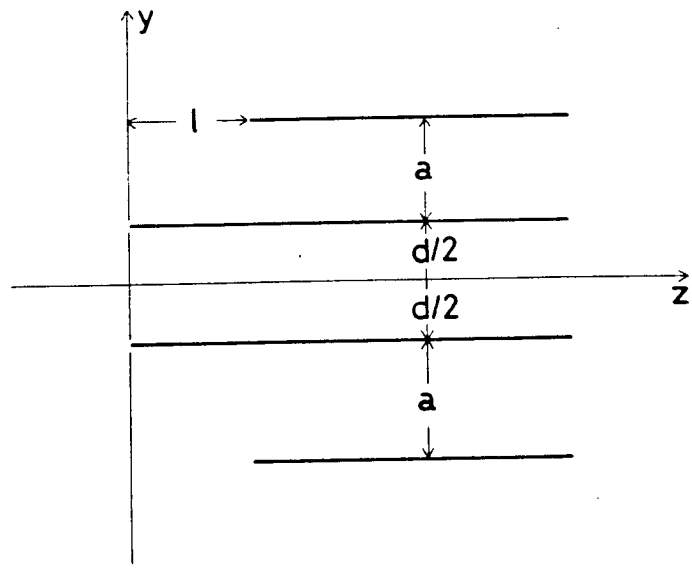

Fig. 10.2
array of staggered parallel plate waveguides with outer guides of infinite depth

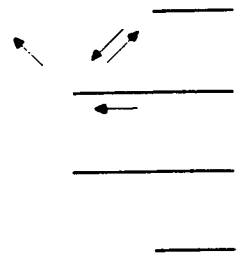

Fig. 10.3
ray path for calculating S_1

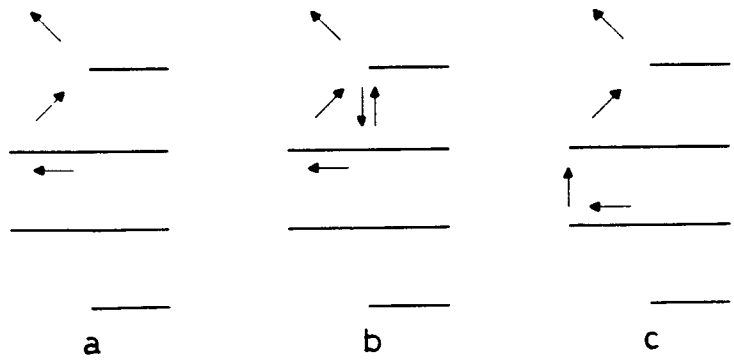

Fig. 10.4
ray paths for calculating S_3

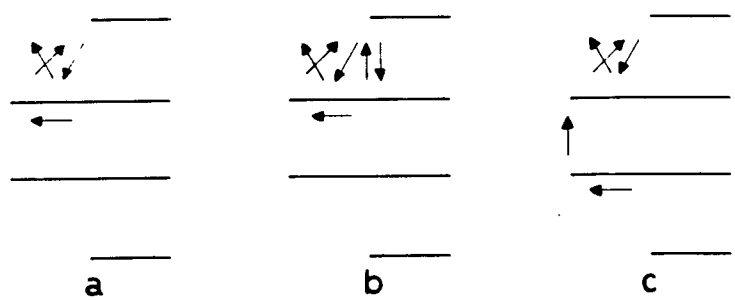

Fig. 10.5
ray paths for calculating $S_{\bar{3}}$

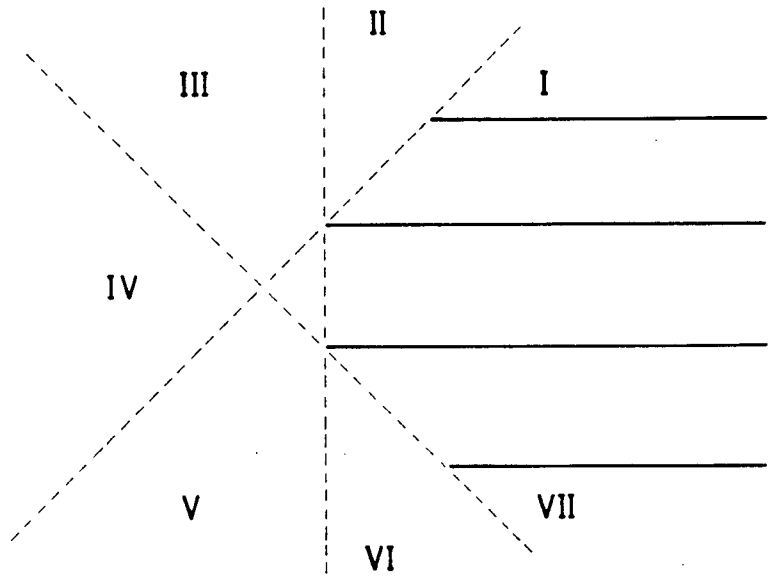

Fig. 10.6
shadow boundaries for an array of
staggered parallel plate waveguides

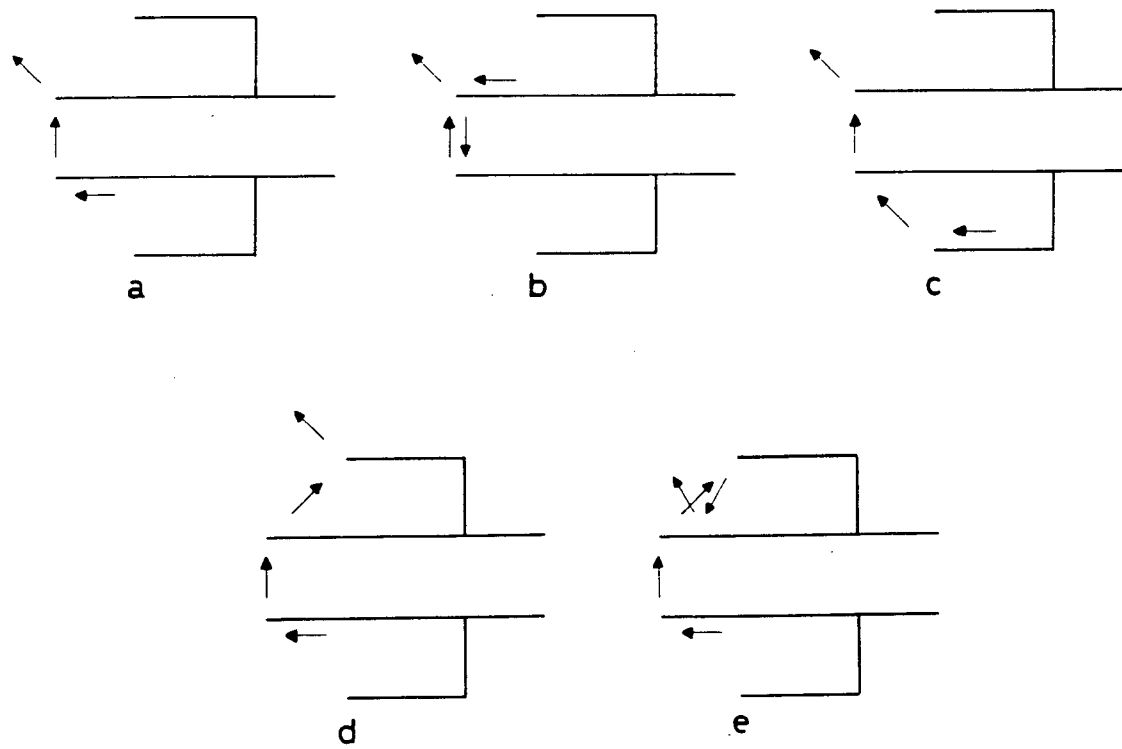

Fig. 10.7
ray paths
(see text)

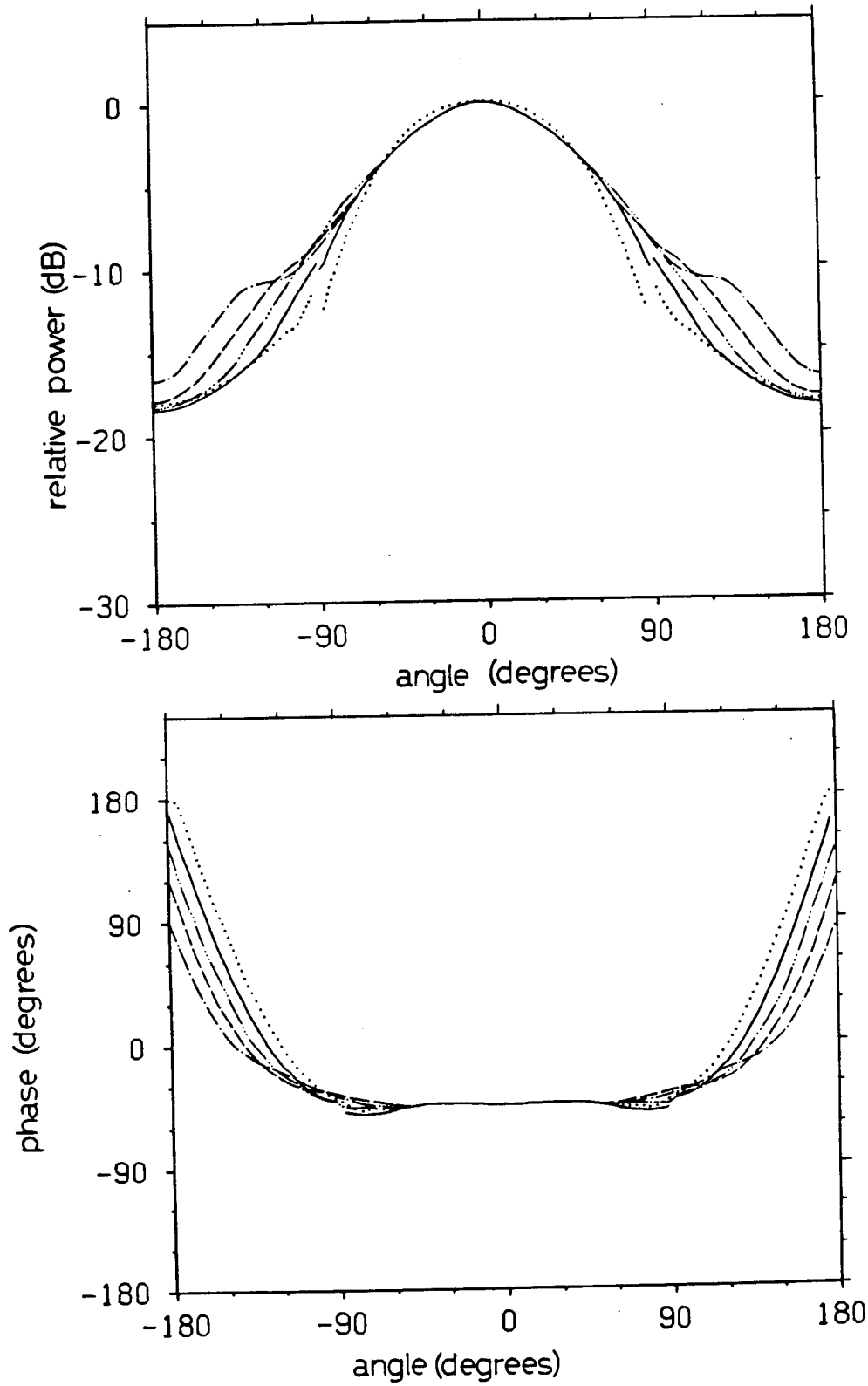

Fig. 10.8 Radiation pattern of staggered waveguide array with outer guides of infinite depth d=a=0.450λ Ψ=45°.

····· Ψ=15° ···—···— Ψ=45° ·—·— Ψ=75°
—— Ψ=30° — — — Ψ=60°

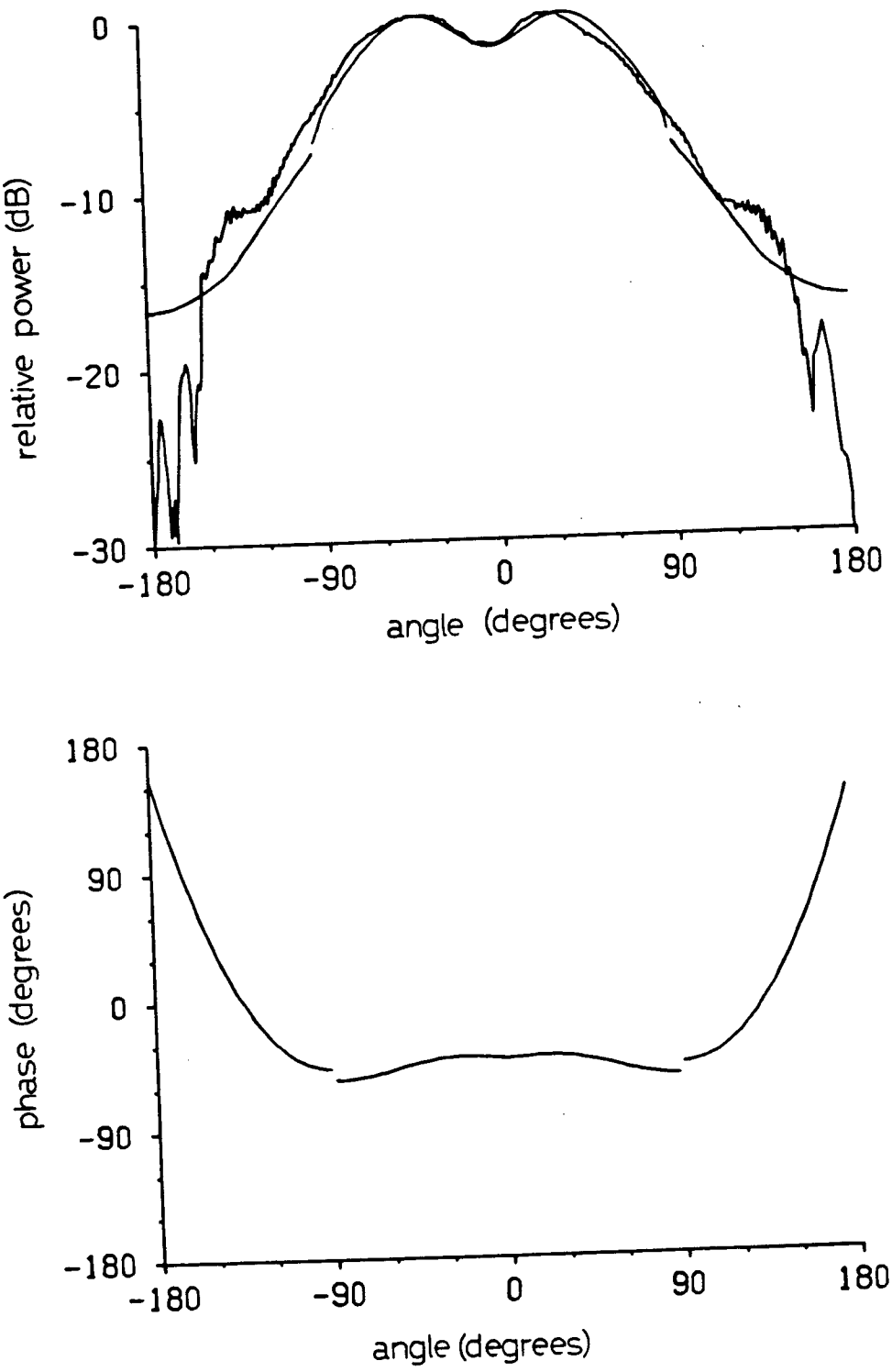

Fig. 10.9 Radiation pattern of staggered waveguide array $d=a=0.474\lambda$ $s=1.166\lambda$ $\Psi=45^\circ$.

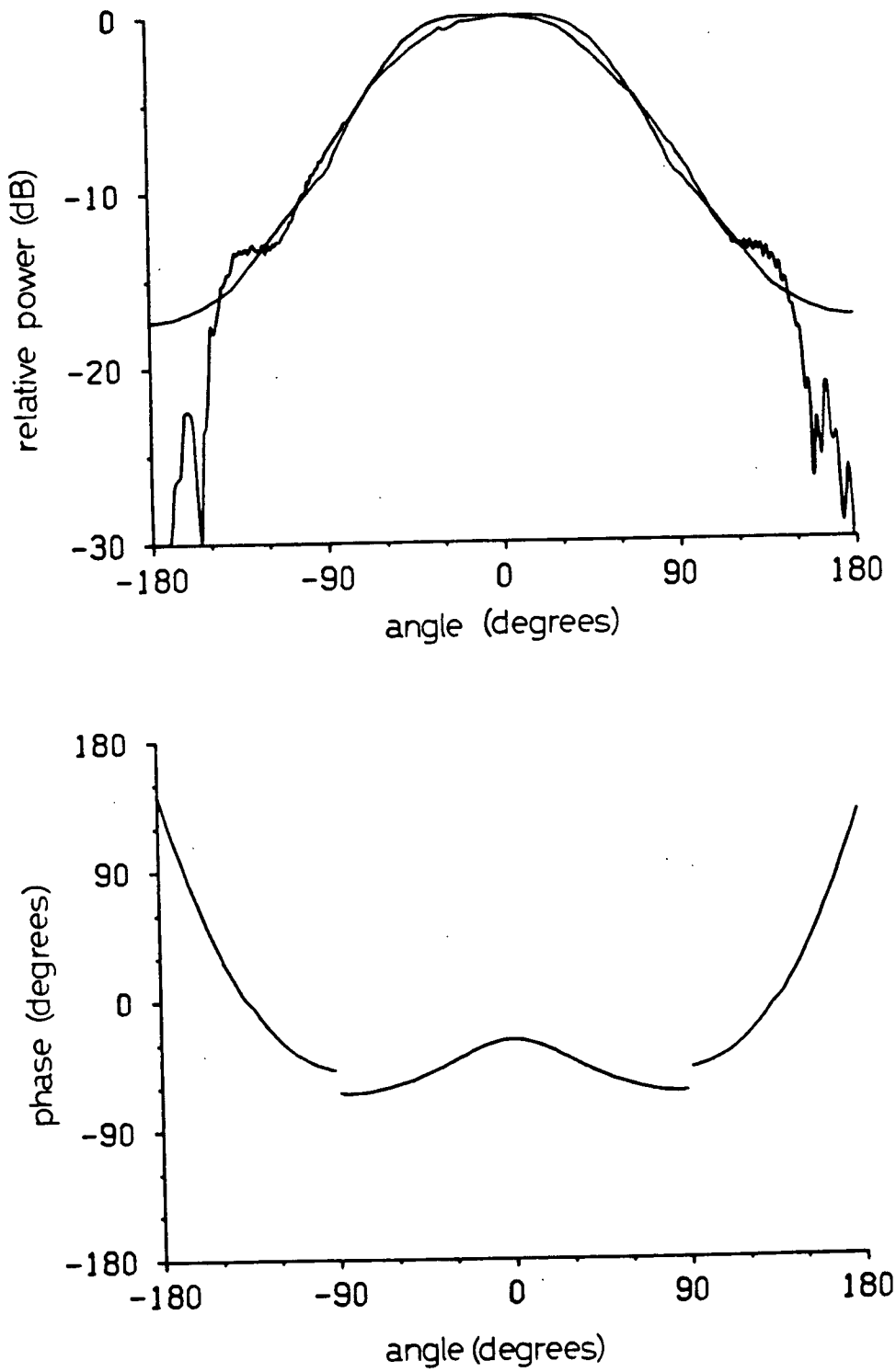

Fig. 10.10 Radiation pattern of staggered waveguide array $d=a=0.441\lambda$ $s=1.083\lambda$ $\Psi=45^{\circ}$.

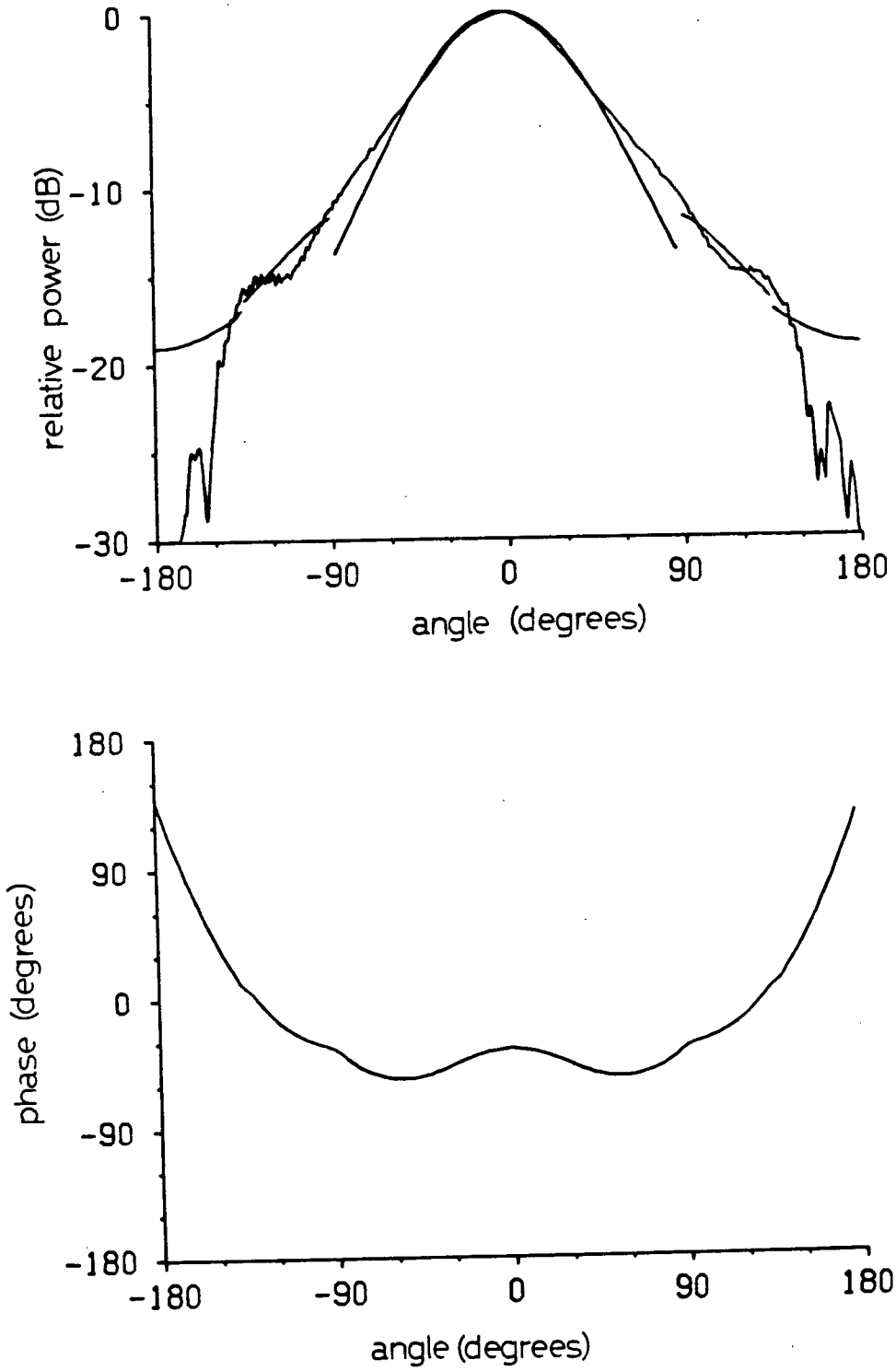

Fig. 10.11 Radiation pattern of staggered waveguide array
d=a=0.407λ s=1.000λ Ψ=45°.

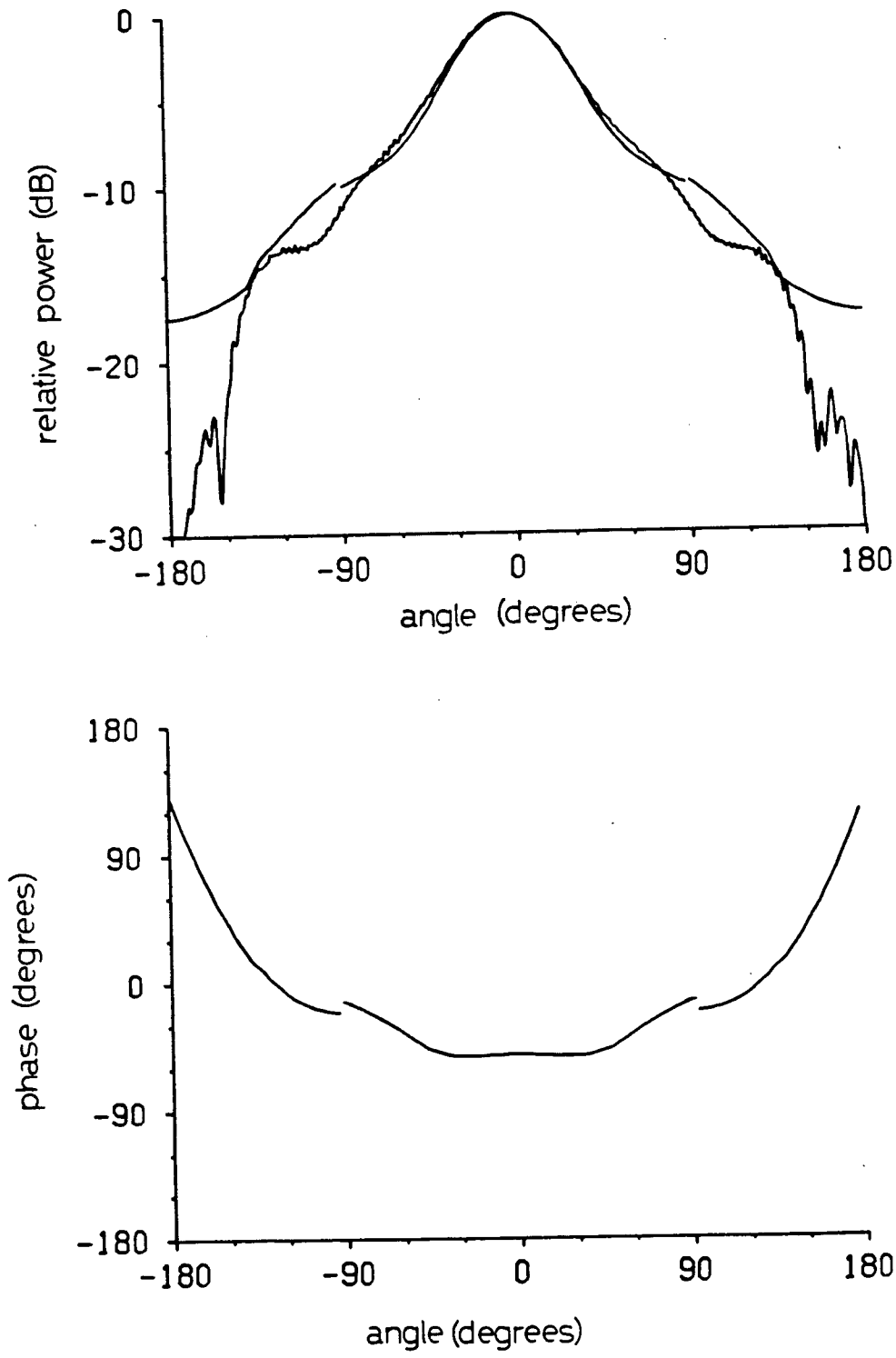

Fig. 10.12 Radiation pattern of staggered waveguide array $d=a=0.373\lambda$ $s=0.916\lambda$ $\Psi=45°$.

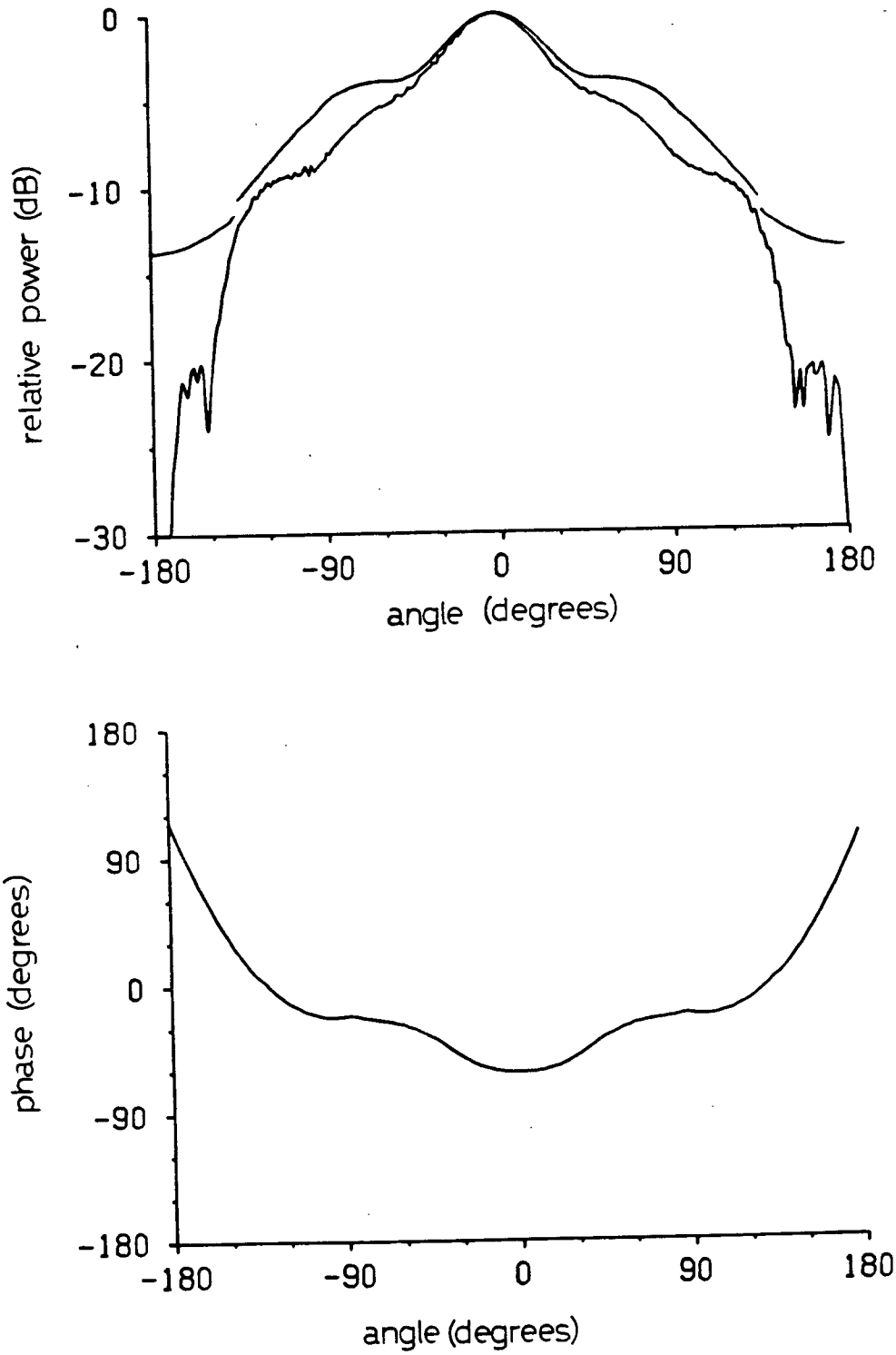

Fig. 10.13 Radiation pattern of staggered waveguide array $d=a=0.339\lambda$ $s=0.833\lambda$ $\Psi=45°$.

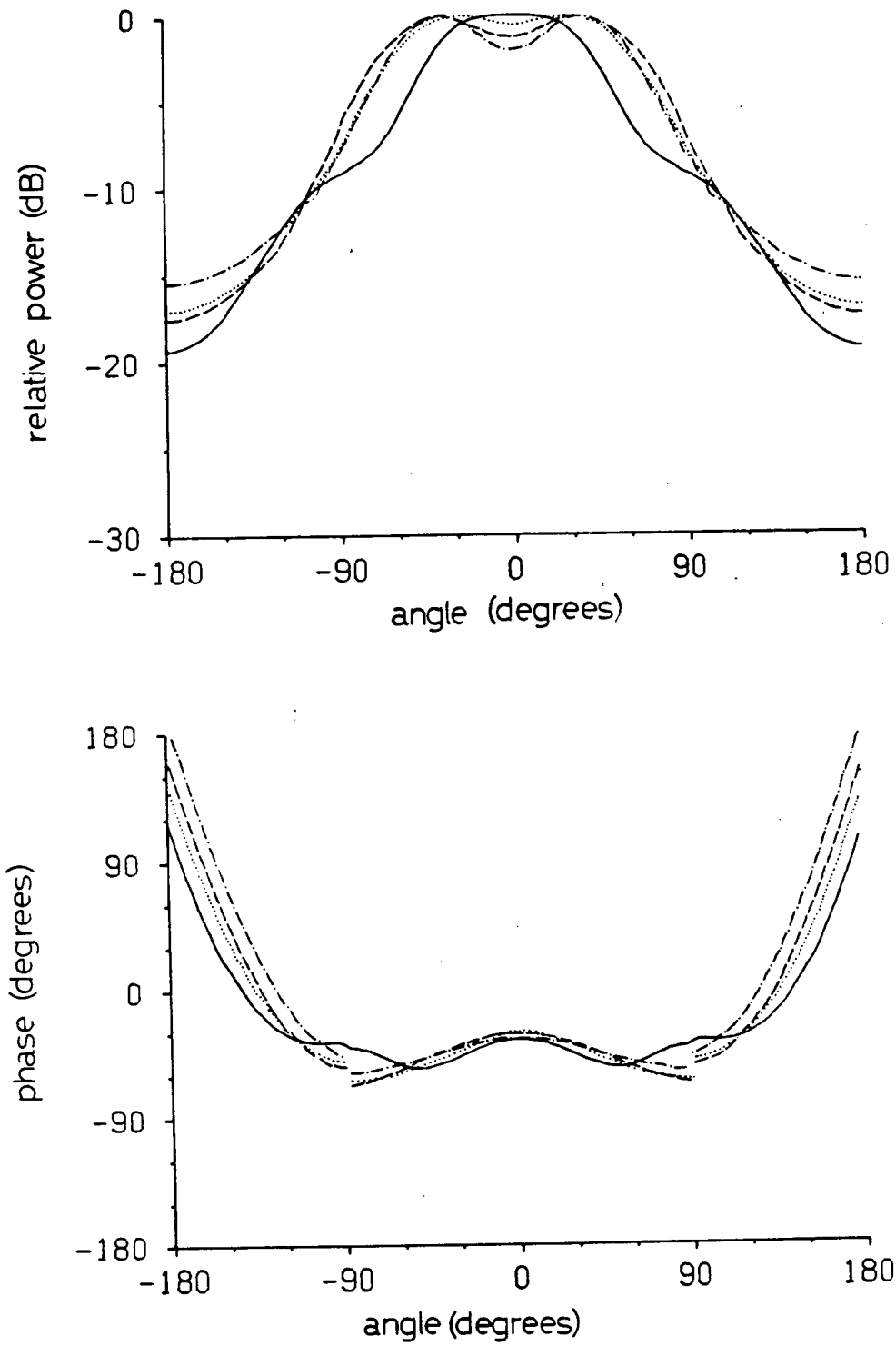

Fig. 10.14 Radiation pattern of staggered waveguide array for various stagger angles Ψ d=a=0.450λ s=1.107λ.

—·— Ψ=15° ····· Ψ=45°
— — Ψ=30° —— Ψ=60°

Chapter 11

GENERAL CONCLUSIONS AND DISCUSSION

11.1 DISCUSSION

Ray-optical methods based on the geometrical theory of diffraction have been used to analyze the fields in coupled parallel plate waveguides. Coupling coefficients between both adjacent and separated waveguides were calculated. Radiation patterns for small arrays, both staggered and non-staggered, were calculated and also measured using an H-plane sectoral horn to simulate the two-dimensional structures.

Ray-optical methods were chosen for this analysis largely because of the good results obtained by others for various simple structures involving half-planes and parallel plate waveguides. The structures considered here, even though considerably more complex, consist of various combinations of parallel plate waveguides. Thus it was anticipated that ray-optical methods might be extended to these more complex structures. The generally good agreement of the ray-optical results obtained here with experimental and other theoretical results where available, indicates that this extension can be successful if the number of diffracting edges is small.

Specifically, the coupling coefficients obtained here agreed quite well with those calculated by other methods in the presence of other guides and/or a simulated groundplane

[29] [38]. Other results for coupling between two adjacent guides in isolation (Fig.3.1) were not available for comparison. Results for coupling between two separated guides in isolation (Fig.4.1) agreed with those obtained using wedge diffraction techniques [17] if the interaction between guides was ignored. The inclusion of this interaction yielded an oscillation in the coupling versus separation curve which was qualitatively similar to that obtained recently in [38] using modified residue calculus, but not in good quantitative agreement. A general lack of sensitivity of the coupling coefficients to the details of the surrounding structure was observed, which gives confidence that these results may be applied directly to more complex structures.

The radiation patterns obtained here for arrays with guides of infinite depth (Fig.7.2) agreed well with those calculated by other methods [29] [38] for the same array in isolation or embedded in a simulated groundplane. The patterns for arrays with outer guides shorted (Figs.6.1,7.1,10.1) showed good agreement with experimental patterns using an H-plane sectoral horn in all cases. Other calculated patterns for these arrays were not available for comparison.

The basic difficulty in applying ray-optical methods to these geometries is that fields diffracted along shadow boundaries are combinations of fields of the same order of k as the incident field and higher order diffracted fields. Consequently, the order of each subsequent diffracted field

is not diminished. Thus one immediate result of extending ray-optical methods to more complex structures is that the number of possible ray paths up to a given order of diffraction which must be considered grows rapidly as more half-plane edges are introduced into the structure from which the rays may diffract. A parallel plate waveguide containing only two edges will require only 2 ray paths to be considered to find the contribution to the reflection coefficient from terms representing n times diffraction. By contrast, two adjacent guides will require many ray paths (depending on n, see Appendix B). Thus ray-optical calculations for simple geometries which require terms including high orders of diffraction become intractable for more complex geometries.

This difficulty is part of the reason why it may be very difficult to use the uniform asymptotic theory (UAT) to accurately calculate the coupling between adjacent waveguides. The UAT is very successful in obtaining excellent agreement with the known exact solution for the reflection coefficient of a parallel plate waveguide. Excellent agreement is obtained even at the mode transition widths, where the exact curve of coupling versus guide width has a cusp with discontinuous first derivative. However, this excellent agreement is only obtained if terms up to n=50 times diffraction are included. The use of UAT with only a few orders of diffraction does not give significant improvement in the reflection case at the mode transition widths over the simpler ray-optical method used here, and

thus would not be expected to significantly improve the coupling coefficient either.

Another result of extending ray-optical methods to more complex structures is that the discontinuities which occur at the shadow boundaries become larger. For a single parallel plate waveguide this discontinuity in the aperture plane is less the 0.5 dB, even when only 6 ray paths up to triple diffraction are taken into account, and may be reduced to an arbitrarily small value by considering more ray paths. For a three element array of non-staggered guides this discontinuity can be up to 3 dB depending on the array parameters, even when 20 ray paths up to quadruple diffraction are considered. It was not possible to reduce this discontinuity further by taking more terms with the method used here. Thus near the shadow boundaries, the accuracy of the ray-optical method decreases as the complexity of the structure increases.

The accuracy away from the shadow boundaries is only slightly affected by the array size, as indicated by the agreement between ray-optical and experimental results, which is about equally good for both simple and more complex arrays.

The basic reason for this difficulty at the shadow boundaries is that the method used to calculate the fields along shadow boundaries is not accurate. If a field represented by a ray in the aperture plane is diffracted, then the resultant field in the aperture plane is not a ray field. Thus when this field is in turn diffracted in the

aperture plane, the ray method used here does not yield an accurate value. This applies to all triply and higher order diffracted fields in non-staggered open-ended parallel plate waveguides calculations by the ray-optical method.

For a single guide this inaccuracy, as measured by the size of the discontinuity in the pattern and comparison with the exact result is quite small. For the waveguide arrays, however, the errors are cumulative, because diffracted fields are repeatedly calculated as if the incident fields are ray fields.

The method used here predicts that the singly diffracted field along the shadow boundary will look like one-half the incident field and the doubly diffracted field will look like one-quarter the incident field. Lee and Boersma [32] showed this to be inaccurate for the case of a plane wave incident on two non-staggered parallel plates and a line source incident on two staggered plates. Thus it may be expected to be inaccurate for the case of a line source incident on two non-staggered plates which arises repeately in the arrays of Chapters 6 and 7.

If a solution for this double half-plane diffraction problem was available, the discontinuities in the radiation patterns in the aperture plane might have been reduced somewhat. However, for better accuracy a solution to the triple half-plane diffraction problem (Fig.4.12) would have been needed also.

When the ray-optical methods used here are extended to more complex parallel plate waveguide structures, the

combination of the large number of ray paths needed and the inaccuracy of the method along the shadow boundaries leads to discontinuities up to ±3 dB in the non-staggered case in the calculated radiation pattern, which cannot be eliminated in a simple manner. However, the radiation patterns away from the shadow boundary in the aperture plane agree quite well with the experimental results so that the ray-optical methods employed here can be useful for predicting the patterns in the angular regions of greatest interest for most applications. Thus ray-optical methods can, within these limits, successfully predict the radiation from coupled parallel plate waveguides.

The radiation patterns of small arrays of parallel plate waveguides are potentially suitable for a variety of applications. A remarkably good sector-shaped pattern with a -10 dB beamwidth of 134° and steep skirts was obtained with a five element array, considering that the aperture size is only slightly more then two wavelengths. A pattern whose amplitude was constant within 0.5 dB over a 120° angular range was obtained with a three element non-staggered array. Other patterns were obtained with nulls on the beam axis.

These results could be applied directly to the design of H-plane sectoral horns with appendages to produce a fan beam with wide angle coverage in the E-plane and a narrow beam in the H-plane. The sector-shaped pattern could be applied directly as a line feed for a parabolic cylinder reflector. If the depth of the parasitic guides could be varied dynamically, e.g. by the reactive loading described

in [35], some beam steering should be possible.

11.2 SUGGESTIONS FOR FURTHER WORK

There are a number of questions which arise from this work that warrant further investigation. An attempt may be made to improve the accuracy of the calculation of the fields along the shadow boundaries of the non-staggered array by using the uniform methods of Lee and Boersma [32], thus avoiding the assumption used here that all fields are ray fields. The problem of a line source normally incident on two parallel plates may be investigated first. The far field may be obtained by a reciprocity argument using the solution for a plane wave on two parallel plates in [32], but the field at all points along the shadow boundary is needed here. The solution for a line source incident on three parallel plates would also be required for both the three and five element non-staggered arrays. However, as the number of edges along the shadow boundary increases, the problem becomes much more difficult, because the number of ray paths to be considered to obtain the desired accuracy grows rapidly. Ray-optical methods may cease to be practical when more then two edges are considered if better accuracy is required than was obtained with the methods used here. Similarly, the coupling coefficient calculations may be improved using uniform methods, particularly near the mode transition regions where cusps are expected, but again the number of ray paths which must be considered for better

accuracy is very large.

Other methods may be used to improve the coupling and radiation pattern results. For coupling between two separated guides, the modified residue calculus method [38] produced the expected cusps at the mode transition widths, and is more accurate than the ray-optical approach used here. This coupling coefficient may be substituted in place of the ray-optical one to improve the radiation pattern calculation of the 5 element array. However, the resulting improvement may not be large, because the coupling coefficient is only about 0.1 (-20 dB), and the field diffracted from the outer edge which is not reradiated from the outer guide is about 0.25 (-12dB) compared to the field in the central guide. Radiation patterns for arrays with outer guides of infinite depth have also been calculated using modified residue calculus, and this method may be extended to the case of shorted outer guides. However, this method becomes more difficult to use for large structures where there are many propagating modes. The reflection coefficient from a single waveguide was calculated with good accuracy using a moment method [48], and this approach may be extended to find coupling coefficients and radiation patterns. Another moment method [35] [36] which has been applied to reactively loaded parallel plate waveguide arrays with walls of finite thickness in a groundplane may also be useful in this context. A combination of ray-optical and moment methods [11] [44] may help to overcome some of the difficulties near shadow boundaries if the moment method is

used near the aperture plane and the ray-optical method away from it.

The results obtained here may also be used as a guide to designing an array of concentric circular waveguides (Fig.1.5). These are known to produce reasonably good patterns by empirical adjustment of the parameters. The TE_{11}-TEM coupling coefficient between open-ended coaxial circular waveguides would be required to predict the radiation pattern. The present work may be considered a first step towards the analysis and optimization of such an array.

11.3 CONCLUSIONS IN BRIEF

Ray-optical methods have been applied to parallel plate waveguide structures with up to six half-plane edges. Theoretical and experimental radiation patterns agree quite well except near shadow boundaries, where discontinuities are observed. The method is not accurate near mode transition regions and shadow boundaries, even when many orders of diffraction are taken into account. Consequently, the accuracy is reduced as the number of half-plane edges along a shadow boundary is increased. However, the regions of greatest interest are most often away from the mode transition regions and shadow boundaries, and here the errors are acceptably small, provided the spacing between edges is at least one-third of a wavelength. Improving the results by using uniform methods is difficult because of the

large number of edge interactions which must be considered. Larger and more complex arrays require higher orders of diffraction than smaller and simpler arrays. A wide variety of patterns is available with a three and five element waveguide array with only the central guide driven by adjusting the width and depth of the outer parasitic guides, including some which could be used to efficiently illuminate a parabolic cylinder reflector.

REFERENCES

[1] D.S.Ahluwalia, R.M.Lewis, and J.Boersma, "Uniform asymptotic theory of diffraction by a plane screen", SIAM J.Appl.Math., vol.16, pp.783-807, 1968.

[2] N.Amitay, V.Galindo and C.P.Wu, "Theory and Analysis of Phased Array Antennas", Wiley, New York, 1972.

[3] J.Boersma, "Ray-optical analysis of reflection in an open-ended parallel-plane waveguide. I: TM case", SIAM J.Appl.Math., vol.29, pp.164-195, 1975.

[4] J.Boersma, "Ray-optical analysis of reflection in an open-ended parallel-plane waveguide. II: TE case", Proc.IEEE, vol.62, pp.1475-1481, 1974.

[5] J.Boersma, "Diffraction by two parallel half-planes", Quart.J.Mech.Appl.Math., vol.28, pp.405-425, 1975.

[6] J.Boersma and S.W.Lee, "High-frequency diffraction of a line source field by a half-plane: Solutions by ray techniques", IEEE Trans.Antennas Propagat., vol.AP-25, 1977.

[7] M.Born and E.Wolf, Principles of Optics, 5th Ed., New York: Permagon Press, 1970.

[8] J.J.Bowman, "Comparison of ray theory with exact theory for scattering by an open waveguide", IEEE Trans.Antennas Propagat., vol.AP-18, pp.131-132, 1970.

[9] J.J.Bowman, "Comparison of ray theory with exact theory for scattering by an open waveguide", SIAM J.Appl.Math., vol.18, pp.818-829, 1970.

[10] W.D.Burnside, E.L.Pelton and L.Peters, Jr., "Analysis of finite parallel-plate waveguide arrays", IEEE Trans.Antennas Propagat., vol.AP-18, pp.701-705, 1970.

[11] W.D.Burnside, C.L.Yu and R.J.Marhefka, "A technique to combine the geometrical theory of diffraction and the moment method", IEEE Trans.Antennas Propagat., vol.AP-23, pp.551-558, 1975.

[12] A.Ciarkowski, "An application of uniform asymptotic theory of diffraction by a plane screen to the analysis of an open-ended waveguide", Acta Physica Polonica, vol.A47, pp.621-631, 1975.

[13] P.J.B Clarricoats, "Some recent advances in microwave reflector antennas", Proc.IEE, vol.126, pp.9-25, 1979.

[14] P.C.Clemmow, "The Plane Wave Spectrum Representation in Electromagnetic Fields", New York: Permagon Press, 1966.

[15] E.Conforti, "A compact feed for short focal length reflectors", M.A.Sc.thesis, University of Toronto, 1978.

[16] P.F.Driessen, "Ray theory of coupling between adjacent parallel plate waveguides", Radio Science, vol.14, pp.969-978, 1979.

[17] R.B.Dybdal, R.C.Rudduck and L.L.Tsai, "Mutual coupling between TEM and TE_{01} parallel-plate waveguide apertures", IEEE Trans. Antennas Propagat., vol.AP-14, pp.574-580, 1966.

[18] L.B.Felsen and H.Y.Yee, "Ray-optical techniques for waveguide discontinuities", IEEE Trans.Antennas Propagat., vol.AP-16, pp.268-269, 1968.

[19] L.B.Felsen and H.Y.Yee, "Multiple interaction by ray optics - some observations and an example", IEEE Trans.Antennas Propagat., vol.AP-16, pp.360-362, 1968.

[20] F.E.Gardiol and P.Haldemann, "Numerical Instabilities of the moment method in waveguide calculations", Elect.Lett., vol.13, pp.694-695, 1977.

[21] R.F.Harrington, Field Computation by Moment Methods, reprinted by R.F.Harrington, 1977.

[22] A.E.Heins, "The radiation and transmission properties of a pair of semi-infinite parallel plates", Quart.Appl.Math., vol.6, part I, pp.157-166, part II, pp.215-220, 1948.

[23] D.S.Jones, "Double knife-edge diffraction and ray theory", Quart.J.Mech.Appl.Math., vol 26, pp.1-18, 1973.

[24] E.V.Jull, "Aperture fields and gain of open-ended parallel-plate waveguides", IEEE Trans. Antennas Propagat., vol.AP-21, pp.14-18, 1973.

[25] K.M.Keen, "Beamwidth variation with aperture diameter of the choked waveguide feed antenna", Elect.Lett., vol 14, pp.406-407, 1978.

[26] J.B.Keller, "Geometrical theory of diffraction", J.Opt.Soc.Amer., vol.52, pp.116-130, 1962.

[27] G.F.Koch, "Coaxial feeds for high aperture efficiency and low spillover of paraboloidal reflector antennas", IEEE Trans. Antennas Propagat., vol.AP-21, pp.164-169, 1973.

[28] R.G.Kouyoumjian and P.H.Pathak, "A uniform geometrical theory for an edge in a perfectly conducting surface", Proc.IEEE, vol.62, pp.1448-1461, 1974.

[29] S.W.Lee, "Radiation from an infinite aperiodic array of parallel- plate waveguides", IEEE Trans. Antennas Propagat., vol.AP-15, pp.598-606, 1967.

[30] S.W.Lee, "Ray theory of diffraction by open-ended waveguides. I. Fields in waveguides", J.Math.Phys., vol.11, pp.2830-2850, 1970.

[31] S.W.Lee, "Ray theory of diffraction by open-ended waveguides. II. Applications", J.Math.Phys., vol.13, pp.656-664, 1972.

[32] S.W.Lee and J.Boersma, "Ray-optical analysis of fields on shadow boundaries of two parallel plates", J.Math.Phys., vol.16, pp.1746-1764, 1975.

[33] S.W.Lee, Y.Rahmat-Samii and R.C.Menendez, "GTD, ray field, and comments on two papers", IEEE Trans.Antennas Propagat., vol.AP-26, pp.352-354, 1978.

[34] R.M.Lewis and J.Boersma, "Uniform asymptotic theory of edge diffraction", J.Math.Phys., vol.10, pp.2291-2305, 1969.

[35] J.Luzwick and R.F.Harrington, "A reactively loaded aperture antenna array", Technical Report No. 3, Dept. Of Electrical and Computer Engineering, Syracuse University, Syracuse, New York, 1976.

[36] J.Luzwick and R.F.Harrington, "A solution for a wide aperture reactively loaded antenna array", Technical Report No. 5, Dept. Of Electrical and Computer Engineering, Syracuse University, Syracuse, New York, 1977.

[37] R.Mittra and S.W.Lee, Analytical Techniques in the Theory of Guided Waves. New York: Macmillan, 1971.

[38] J.P.Montgomery and D.C.Chang, "Electromagnetic boundary value problems based upon a modification of residue calculus and function theoretic techniques", NBS Monograph 164, U.S. Department of Commerce, 1979.

[39] Y.Rahmat-Samii and R.Mittra, "On the investigation of diffracted fields at the shadow boundaries of staggered parallel plates", Radio Science, vol.12, pp.659-670, 1977.

[40] R.C.Rudduck and L.L.Tsai, "Aperture reflection coefficient of TEM and TE_{01} mode parallel-plate waveguides", IEEE Trans.Antennas Propagat., vol.AP-16, pp.83-89, 1968.

[41] R.C.Rudduck and D.C.F.Wu, "Slope diffraction analysis of TEM parallel- plate guide radiation patterns", IEEE Trans.Antennas Propagat., vol.AP-17, pp. 797-799, 1969.

[42] C.E.Ryan, Jr. And R.C.Rudduck, "A wedge diffraction analysis of the radiation patterns of parallel-plate waveguides", IEEE Trans.Antennas Propagat , vol.AP-16, pp.490-491, 1968.

[43] A.Sommerfeld, "Mathematische Theorie der Diffraktion", Math.Ann., vol.47, pp.317-374, 1896.

[44] G.A.Thiele and T.H.Newhouse, "A hybrid technique for combining moment methods with the geometrical theory of diffraction", IEEE Trans.Antennas Propagat., vol.AP-23, pp.62-69, 1975.

[45] L.A.Weinstein, The Theory of Diffraction and the Factorization Method. Boulder, Colorado: Golem Press, 1969.

[46] R.Wohlleben, H.Mathes and O.Lochner, "Simple small primary feed for large opening angles and high aperture efficiency", Elect.Lett., vol.8, pp.474-476, 1972.

[47] C.P.Wu, "Numerical solution for the coupling between waveguides in finite arrays", Radio Science, vol.14, pp.245-254, 1969.

[48] S.L.Wu and Y.L.Chow, "An application of moment methods to waveguides scattering problems", IEEE Trans.Microw.Th.Tech., vol.MTT-20, pp.744-749, 1972.

[49] H.Y.Yee and L.B.Felsen, "Ray-optical techniques for waveguide discontinuities", Electrophys. Dep., Polytechnic Inst. Brooklyn, Farmingdale, N.Y., Rep. PIBEP-68-005, June 1968.

[50] H.Y.Yee, L.B.Felsen and J.B.Keller, "Ray theory of reflection from the open end of a waveguide", SIAM J.Appl.Math., vol.16, pp.268-300, 1968.

APPENDIX A

SCATTERED FIELDS ALONG A SHADOW BOUNDARY

The results (3.26) and (3.29) may be checked by using a symmetry relation for scattered fields

$$u_s(2\pi-\theta) = -\tau\, u_s(\theta) \tag{A.1}$$

which is exact for diffraction by a plane screen [3]. The scattered field by definition includes reflected and diffracted fields, but not the incident field, (3.26) and (3.29) as written do not satisfy (A.1). However, if (3.29) is derived by finding the field at a small angle δ off the shadow boundary (Fig. A.1) and then taking $\delta \to 0$, then (3.29) may be written

$$u_m = + \frac{e^{ik(r+r_0)}}{\sqrt{k(r+r_0)}} - \frac{e^{ik(r+r_0)}}{2\sqrt{k(r+r_0)}} + \tau \frac{e^{+i\pi/4}}{2\sqrt{2\pi}} \frac{e^{ikr_0}}{\sqrt{kr_0}} \frac{e^{ikr}}{\sqrt{kr}} \tag{A.2}$$

If the first term, which is the incident field at the observation point is subtracted out, then the remaining terms representing the scattered field $u_s(\frac{\pi}{2})$ satisfies (A.1), where $u_s(\frac{3\pi}{2})$ is given by (3.26), as is shown below.

Consider a line source E(r) incident on a half plane at $\theta_0=3\pi/2$ (Fig. A.1), the total field observed at $\theta = \frac{\pi}{2} + \delta$ is given, from (2.12) by

$$u_t = \sqrt{\frac{2}{\pi}}\, e^{-i\pi/4} \left\{ \frac{e^{ikR}}{\sqrt{k(r_0+r+R)}}\, F\left[-2\sqrt{\frac{kr_0 r}{r_0+r+R}}\, \sin\frac{\delta}{2}\right] \right.$$

$$\left. +\tau \frac{e^{ikS}}{\sqrt{k(r_0+r+S)}}\, F\left[+2\sqrt{\frac{kr_0 r}{r_0+r+S}}\, \cos\frac{\delta}{2}\right] \right\} \tag{A.3}$$

$$= \sqrt{2}\,\frac{e^{ikR}}{\sqrt{k(r_0+r+R)}} + \sqrt{\frac{2}{\pi}}\,e^{-i\pi/4}\left\{-\frac{e^{ikR}}{\sqrt{k(r_0+r+R)}}\,F\left[+2\sqrt{\frac{kr_0r}{r_0+r+R}}\,\sin\frac{\delta}{2}\right]\right.$$

$$\left. + \tau\,\frac{e^{ikS}}{\sqrt{k(r_0+r+S)}}\,F\left[+2\sqrt{\frac{kr_0r}{r_0+r+S}}\,\cos\frac{\delta}{2}\right]\right\} \qquad \text{(A.4)}$$

where R, S, r, r_0, θ and θ_0 are defined in Fig. 2.3. let $\delta \to 0$, then $R \to r+r_0$, $S \to r-r_0$, and

$$u_t = \frac{e^{ik(r+r_0)}}{\sqrt{k(r+r_0)}} - \frac{e^{ik(r+r_0)}}{2\sqrt{k(r+r_0)}} + \tau\,\frac{e^{-i\pi/4}}{\sqrt{\pi}}\,e^{ik(r-r_0)}\,F[\sqrt{2kr_0}] \qquad \text{(A.5)}$$

If $kr_0 >> 1$ (A.5) = (A.2) QED.

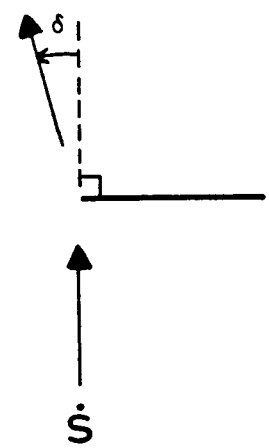

Fig. A.1

APPENDIX B

HIGHER ORDER DIFFRACTION TERMS FOR COUPLING BETWEEN ADJACENT PARALLEL PLATE WAVEGUIDES IN THE TEM MODE

A general expression for TEM-TEM coupling of $0(k^{-\frac{1}{2}})$ between adjacent waveguides is derived for all orders of diffraction. First the equations (3.18), (3.26), (3.29) and (3.30) are specialized to the TEM case and used to calculate the contribution to the coupling for a generalized ray path. All possible ray paths from the driven guide to the parasitic guide are traced systematically and their contributions are added to give the coupling coefficient.

From (3.18) the incident field $u_i=\frac{1}{2}$ in the driven guide excites a diffracted field

$$u_1 = \frac{1}{2}\tau_2 C_0'(r_1)E(r) \tag{B.1}$$

as observed at a point in the aperture plane a distance r_1 away from the diffracting edge, where

$$\tau_2 = \begin{cases} -1 & \text{if } |\theta-\theta_0| = \pi/2 \\ +1 & \text{if } |\theta-\theta_0| = 3\pi/2 \end{cases} . \tag{B.2}$$

This field travels along the shadow boundary and is again diffracted at another edge a distance r_1 away in the aperture plane. The resultant doubly diffracted field of $0(k^{-1/2})$ is from (3.26) or (3.29)

$$u_2 = \frac{\tau_2}{4} C_0'(r_1)E(r_1+r) . \tag{B.3}$$

When the line source u_{m-1} in the aperture plane is diffracted from another

edge the resultant field is

$$u_m = \frac{\tau_2}{2^m} C_0'(r_1)E(r_1+\ldots+r_{m-1}+r) \quad , \tag{B.4}$$

where r_{m-1} is the distance from the line source to the diffracting edge. The field u_m may be diffracted into the parasitic guide at $\theta=0$ or 2π and from (3.30) the resultant field is

$$u_{m+1} = \tau_2\tau_3 \; C_0'(r_1)C_0(r_1+\ldots+r_m)E(r) \tag{B.5}$$

where r_m is the distance from the incident line source to the diffracting edge and τ_3 is given by (B.2)

The field u_{m+1} contributes to the amplitude A_{00} of the mode in the parasitic guide from (m+1) diffraction

$$A_{00}^{(m+1)} = \frac{\sqrt{\pi}\, e^{i\pi/4}}{\sqrt{2}\, ka} \; \frac{\tau_2\tau_3}{2^m} \; C_0'(r_1)C_0(r_1+\ldots+r_m) \tag{B.6}$$

The $0(k^{-1/2})$ contributions to A_{00} for the fields of any ray path are thus dependent only on the signs of τ_2 and τ_3 and on the total path length $r_t = \sum_{n=1}^{m+1} r_n$ in the aperture plane.

All possible ray paths from the driven to the parasitic guide are now traced and the values of τ_2, τ_3 and r_t are evaluated for each ray path. Each ray path in the aperture plane starting and ending at the central edge y=z=0 follows a simple pattern which may be uniquely represented by a binary number (0,1,00,01,10,11,000,001,etc.) where 1 represents a ray going down to y=-d, z=0 and back to centre and 0 represents a ray going up to y=a, z=0 and back to centre. The paths length r_t=S of any ray path starting and ending at the central edge y=z=0 may be written

$$S = \sum_{j=1}^{n} [2a(1-i_{mkj}) + 2d\, i_{mkj}] \tag{B.7}$$

where

i_{mkj} = a binary digit in a binary number representing a ray path,

m = number of digits in binary number,

k = decimal value of binary number,

j = digit number in binary number counting from left to right.

All possible ray paths including at least quadruply diffracted fields contain within them a path starting and ending at the central edge y = z = 0 for which the path length is given by S. The ray paths divide naturally into four groups depending on from which edge in the driven guide (y = 0 or -d) the incident field is first diffracted and from which edge the penultimate ray is diffracted into the parasitic guide (y = 0 or a). The four groups shown in Table B.1.

TABLE B.1 Groups of Ray Paths

Group #	Incident Ray Diffracted at y=	Penultimate Ray Diffracted at y=	Rath Length r_t
1	0	0	S
2	0	a	S + a
3	-d	0	S + d
4	-d	a	S + d + a

The product $\tau_2\tau_3$ is determined by inspection of the ray paths in each group. The quadruple and higher order diffraction contributions to the coupling coefficient are given by terms of the form (B.6). The complete expression is, using the asymptotic form (5.12):

$$A_{00}^{(4-\infty)} = \frac{i}{\sqrt{2}\,ka} \sum_{m=2}^{\infty} \sum_{k=1}^{2^m} \frac{C_0(S)}{2^{2m}} (-1)^{i_{mkl} + i_{mkm} + 1}$$

$$+ \sum_{m=1}^{\infty} \sum_{k=1}^{2^m} \frac{C_0(S+a)}{2^{(2m+1)}} (-1)^{i_{mkl}+1}$$

$$+ \sum_{m=1}^{\infty} \sum_{k=1}^{2^m} \frac{C_0(S+d)}{2^{(2m+1)}} (-1)^{i_{mkm}}$$

$$+ \sum_{m=1}^{\infty} \sum_{k=1}^{2^m} \frac{C_0(S+d+a)}{2^{(2m+2)}} \qquad \text{(B.8)}$$

A general expression for terms of $0(k^{-1})$ was not found. The contribution of these terms beyond six orders of diffraction was not significant, however.

Note that the number of ray paths for each order of diffraction n is given by $2^{n/2}$ for n even and $\frac{3}{2}\, 2^{(n-1)/2}$ for n odd and $n \neq 1$. By comparison there are only two ray paths for each order of diffraction in the calculation of the reflection coefficient.

In the special case of TEM-TEM coupling between guides of equal widths (a=d) the expression (B.8) reduces to

$$A_{00}^{(4-\infty)} = \frac{i}{2\sqrt{2}\, ka} \sum_{\substack{n=4 \\ n \text{ even}}}^{\infty} \frac{C_0(na)}{2^{n/2}} \qquad \text{(B.9)}$$

For ka >> 1, using (3.31) and (3.23)

$$A_{00}^{(4-\infty)} \sim \frac{e^{i3\pi/4}}{2\sqrt{2\pi}\, (ka)^{3/2}} \sum_{\substack{n=4 \\ n \text{ even}}}^{\infty} \frac{e^{ikna}}{2^{n/2}\, n^{1/2}} \qquad \text{(B.10)}$$

Numerical values for the complete coupling coefficient A_{00} using the results of Chapter 3 up to and including triple diffraction and (B.10) for higher orders of diffraction are given in Fig. B.1. Note that the solution is not significantly improved over the triple diffraction results of Chapter 3. The cusps which are expected at the mode transition widths are not obtained.

A comparison of expressions for the $0(k^{-\frac{1}{2}})$ reflection coefficient obtained by Yee et al. [50] and Boersma [3] shows that the UAT solution of [3] may be obtained from the ray-optical solution of [50] by substituting $n^{3/2}$ for $2^{n-1}\, n^{1/2}$ in the denominator of the infinite sum ([3], eqns. (8.3) and (8.9)). It was conjectured that the same substitution might yield an improved expression for the coupling coefficient. Performing this substitution on (B.10) yields

$$A_{00}^{(4-\infty)} \overset{?}{\sim} \frac{e^{i3\pi/4}}{2\sqrt{2\pi}\,(ka)^{3/2}} \sum_{\substack{n=4 \\ n \text{ even}}}^{\infty} \frac{2^{n/2}\, e^{ikna}}{2\, n^{3/2}} \tag{B.11}$$

which may be rewritten, using n=2m

$$A_{00}^{(4-\infty)} \overset{?}{\sim} \frac{e^{i3\pi/4}}{2\sqrt{2\pi}\,(ka)^{3/2}} \sum_{m=2}^{\infty} \frac{2^{m}\, e^{ik2ma}}{2\; 2^{3/2}\; m^{3/2}} \tag{B.12}$$

In the reflection case, this substitution works very well, and the numerical results converge slowly to show a cusp at the mode transition widths, as expected, for $n \overset{>}{\sim} 50$. However, in the coupling case, this substitution does not work at all, because a ratio test shows that the series (B.12) does not converge.

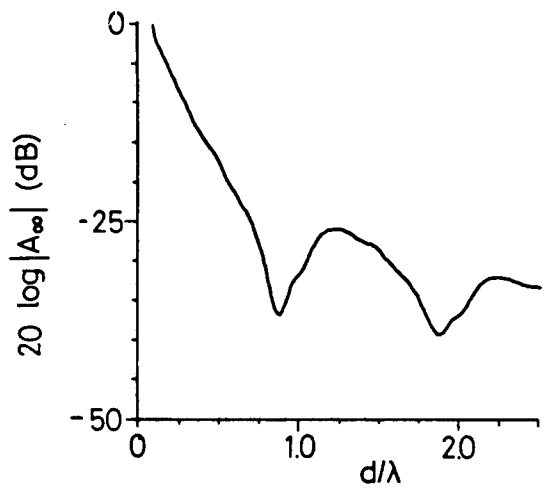

Fig. B.1
coupling coefficient A_{00}

APPENDIX C

CONTINUITY OF FIELDS ACROSS SHADOW BOUNDARIES

The expression (9.24), which shows how a discontinuity in the single diffraction radiation pattern of a staggered parallel plate waveguide is eliminated by adding a double diffraction term, is derived here using (8.2) and the asymptotic form (8.5). It will be shown that (Fig. 9.3a) for $\theta = \frac{\pi}{2} - \Psi$ that as $\delta \to 0$

$$u_1^b(\theta+\delta)\, e^{+ik\frac{d}{2}\sin\theta} + u_2^d(\theta+\delta)\, e^{-ik\frac{d}{2}\sin\theta}\, e^{-ik\ell\cos\theta}$$

$$= u_2^d(\theta-\delta)\, e^{-ik\frac{d}{2}\sin\theta}\, e^{-ik\ell\cos\theta} \qquad (C.1)$$

Note from Fig. 9.1 $\ell^2+d^2 = c^2$; $\cos(\frac{\pi}{2}-\Psi) = \frac{\ell}{c}$; $\sin(\frac{\pi}{2}-\Psi) = \frac{d}{c}$; A, A', A", A"' and B are defined by reference to the previous equation.

$$\tfrac{1}{2} D(0,\tfrac{\pi}{2}-\Psi+\delta)E(r)e^{+ik\frac{d}{2}\sin(\frac{\pi}{2}-\Psi+\delta)}$$

$$+ \tfrac{1}{2} D(0,\tfrac{\pi}{2}-\Psi)G_d(c,\tfrac{3\pi}{2}-\Psi,\tfrac{\pi}{2}-\Psi+\delta)E(r)e^{-ik\frac{d}{2}\sin(\frac{\pi}{2}-\Psi+\delta)}\, e^{-ik\ell\cos(\frac{\pi}{2}-\Psi+\delta)}$$

$$= \tfrac{1}{2} D(0,\tfrac{\pi}{2}-\Psi)G_d(c,\tfrac{3\pi}{2}-\Psi,\tfrac{\pi}{2}-\Psi-\delta)E(r)e^{-ik\frac{d}{2}\sin(\frac{\pi}{2}-\Psi-\delta)}\, e^{-ik\ell\cos(\frac{\pi}{2}-\Psi-\delta)} \qquad (C.2)$$

$$A' e^{+ikd\sin(\frac{\pi}{2}-\Psi+\delta)}\, e^{+ik\ell\cos(\frac{\pi}{2}-\Psi+\delta)} + A"G_d(c,\tfrac{3\pi}{2}-\Psi,\tfrac{\pi}{2}-\Psi+\delta)$$

$$= A"'G_d(c,\tfrac{3\pi}{2}-\Psi,\tfrac{\pi}{2}-\Psi-\delta) \qquad (C.3)$$

$$A' e^{+ikd \sin(\frac{\pi}{2} - \Psi + \delta)} e^{+ik\ell\cos(\frac{\pi}{2} - \Psi + \delta)}$$

$$+ \quad A'' \frac{e^{-i\pi/4}}{\sqrt{\pi}} \left\{ -e^{+ikc \cos\delta} F[\sqrt{2kc} \sin(\tfrac{\delta}{2})] + e^{-ikc \cos(2\Psi - \delta)} F[\sqrt{2kc} \cos(\Psi - \tfrac{\delta}{2})] \right\}$$

$$= A''' \frac{e^{-i/4}}{\sqrt{\pi}} \left\{ +e^{-ikc \cos\delta} F[\sqrt{2kc} \sin(-\tfrac{\delta}{2})] + e^{-ikc \cos(2\Psi + \delta)} F[\sqrt{2kc} \cos(\Psi + \tfrac{\delta}{2})] \right\}$$

(C.4)

let $\delta \to 0$, then $A' = A'' = A''' = A$, and

$$A e^{+ikc} + A \frac{e^{-i\pi/4}}{\sqrt{\pi}} \left\{ -e^{+ikc} F[0] + e^{-ikc \cos 2\Psi} F[\sqrt{2kc} \cos\Psi] \right\}$$

$$= A \frac{e^{-i\pi/4}}{\sqrt{\pi}} \left\{ +e^{-ikc} F[0] + e^{-ikc \cos 2\Psi} F[\sqrt{2kc} \cos\Psi] \right\} \qquad (C.5)$$

$$A e^{+ikc} - \frac{A}{2} e^{+ikc} + B = \frac{A}{2} e^{+ikc} + B \qquad \text{QED.} \qquad (C.6)$$

The expressions (9.24) - (9.26) are derived in a precisely analogous manner.

APPENDIX D

National Research Council of Canada
Division of Electrical Engineering
Antenna Pattern Range

TRANSMITTER

A standard 1 mW signal generator output was fed through a coaxial coupler to a travelling wave tube amplifier with a gain of 30 db. A sample from the coupler was used to monitor frequency, using a digital counter. A low-pass filter was inserted at the output of the amplifier as a safeguard against any harmonics. The signal was then fed through low-loss semi-rigid coax up to the roof. The antenna used to flood the horn under test was a standard X-band horn.

RECEIVER

The other end of the link basically consists of a large turntable on the roof, which is rotatable through 360^{o}, and appropriate receiving instrumentation. Antennas under test are mounted on this turntable, whose angle of rotation is linked by a synchro system to a lab recorder chart drive.

After reception by the horn under test, the R.F. signal was converted to an I.F. of 65 MHz by a waveguide crystal mixer attached to the horn flange. Frequency selective tees within the Scientific Atlanta Series 1600 Wideband receiver, permit the use of a single RG214/U coaxial cable to transfer the L.O. signal from receiver to mixer, and, after harmonic mixing takes place, the I.F. signal from the mixer back down to the receiver. Directly below the turntable, above the lab ceiling, an R.F. rotating joint with mercury contacts, facilitates rotation.

After the CW signal reaches the receiver, and has passed through a series of different conversions,1 KHz modulation is added. This modulation is then detected by a bolometer detector and the output fed to a Scientific Atlanta Rectangular-Polar Pattern Recorder, Series 1580 for plotting.

PATH LENGTH

Transmission path length from the turntable centre of rotation to the adjacent vertical 4"x4" support was 27 feet, 4 inches. Actual aperture to aperture separation was about 12 inches less.

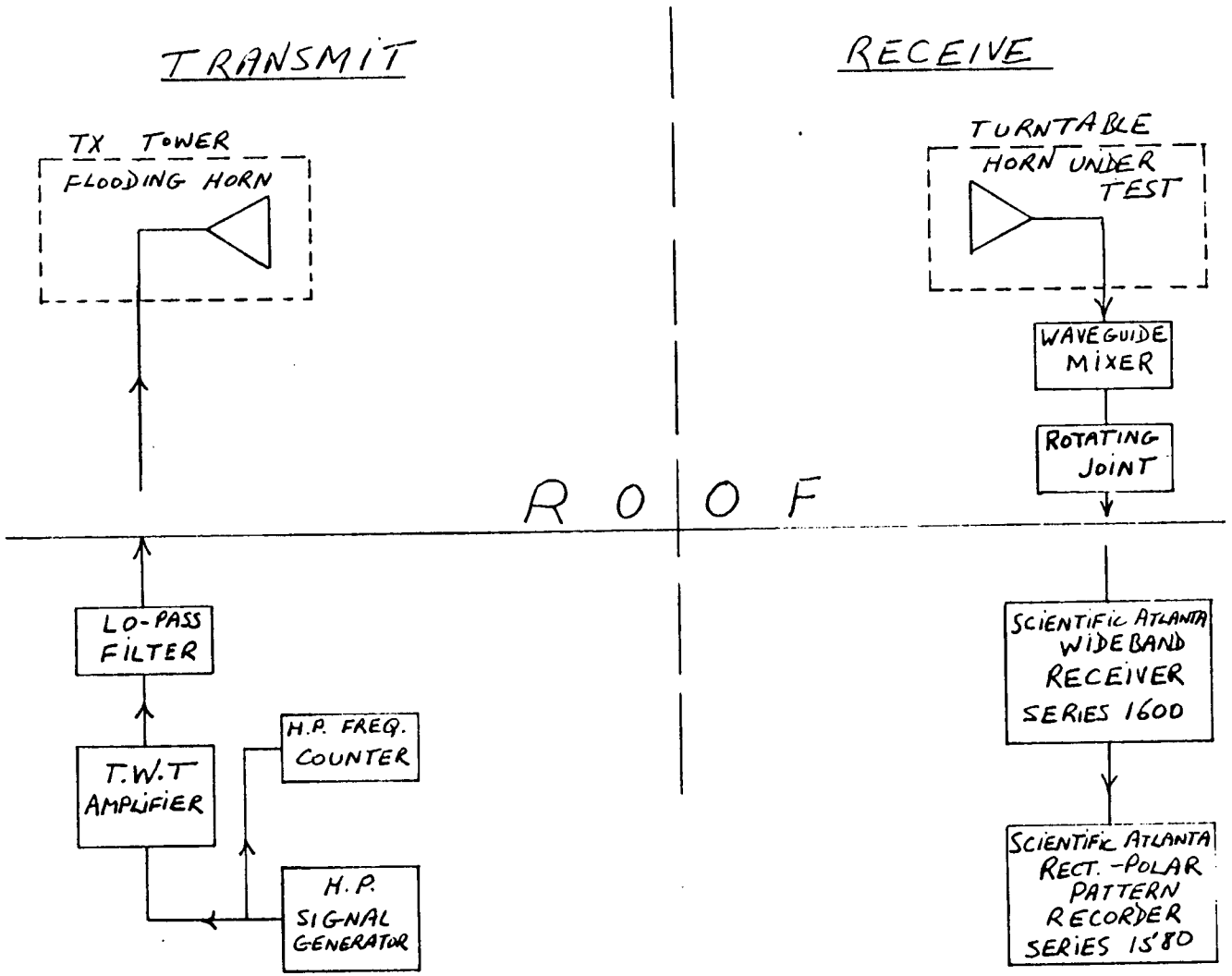

BLOCK DIAGRAM - N.R.C. ANTENNA RANGE